HIGH THROUGHPUT MATERIAL SCIENCE FOR DISCOVERY OF ENERGY-RELATED MATERIALS

A Dissertation

Presented to the Faculty of the Graduate School

of Cornell University

in Partial Fulfillment of the Requirements for the Degree of

Doctor of Philosophy

by

John Mathew Gregoire

February 2010

HIGH THROUGHPUT MATERIAL SCIENCE FOR DISCOVERY OF ENERGY-RELATED MATERIALS

John Mathew Gregoire, Ph.D.

Cornell University 2010

While fuel cells are a promising technology for portable energy conversion, their incorporation into the energy infrastructure is impeded by significant materials issues. The primary issues with the anode catalyst are degradation and slow fuel oxidation kinetics, particularly for direct alcohol fuel cells. This dissertation explains many aspects of a large-scale research project focussed at identifying superior anode catalyst materials. Effective searching of the astronomical number of possible catalysts is achieved through the study of composition spread thin films. A high-throughput electrochemical fluorescence assay is used to evaluate the catalytic activity of the thin films and comparison of these measurements with detailed characterization of the thin film properties is used to establish trends that guide the choice of new materials. The developed characterization methods include the modeling and subsequent calculation of film composition and high-throughput mapping of crystallographic properties with high energy diffraction. Several new catalyst systems are presented, and the ensemble of techniques is also applied to known catalyst systems and shown to reveal important material properties.

BIOGRAPHICAL SKETCH

I was born on May 27, 1982 in Metairie, LA to Dwain and Diane Gregoire who have been great parents my entire life. My older siblings Allen, Julie and Lori and younger sister Christine have been wonderful life companions. We have all done so much together, and some of my fondest memories are from when I was three or four years old and got to join the family fishing and shrimping ventures. In addition to the many things I learned about extracting seafood from the brackish waters of Southeast Louisiana, math and physics lessons started on the shrimping boat.

My grandparents and many cousins, uncles and aunts have also been an important part of my life. My mother's parents, Richard and Helen Schlautman are Nebraska farmers and have taught me many life lessons, most notably the nobility of a strong work ethic and the frivolousness of knowledge attained in the classroom compared to that obtained through experience. My father's mother, Estelle Keller, helped raise me and taught me that if you want to do something that makes sense and feels right then go ahead and don't get hung up on what others think.

I attended St. Angela Merici grade school, Christian Brothers middle school, and Archbishop Rummel High School while living in Metairie, LA. In 2000 I moved to Moorhead, MN and attended Concordia College until entering graduate study at Cornell in 2004. Basically, I learned an academic work ethic and grammar at Christian Brothers, writing and a little math at Rummel, and abstract thinking in the context of math and physics at Concordia. I think I learned how to be an experimentalist by growing up with a family full of questioning minds and then by walking into Bruce's office.

This dissertation is dedicated to my grandmothers Helen and Estelle. I was grateful for their support as I entered graduate school, and I wish they were here to watch me finish.

ACKNOWLEDGEMENTS

I have had a lot of fun working with scientists at Cornell. Much of the research presented in this dissertation was performed with Michele Tague and Maxim Kostylev. I would also like to thank Dr. Mark Prochaska and Dr. Jin Jing who got this research rolling in their graduate careers, and Sara Barron, Jon Petrie and Anna Legard with whom I've collaborated on various projects. Many undergraduates, master's students and other Cornell scientists have made important contributions to this dissertation and I would like to recognize some of these important colleagues: undergraduates Maxim Lobovsky, Valerie Wiesner (Carleton College), José Fonseca (Universidad de Puerto Rico - Río Piedras), Sahr Khan (Wellsley College), Sophie Cahen (École Centrale Paris) and Leo Small; post-doc Akira Muira; CCMR facility managers Maura Weathers, Jon Shu, John Hunt; CHESS scientists Alexander Kazimirov and Darren Dale; and research advisors Bruce van Dover, Frank DiSalvo and Héctor Abruña. I also thank the Dept of Physics and especially my committee members Itai Cohen and Erich Mueller for supporting my research outside the department.

Thank you to Brother Gregory (Christian Brothers teacher) who gave me a strong nudge whenever I got a little lazy and to Dr. James Forde (Concordia Math Dept.) for being an excellent educator and balancing math lessons with reflections on the issues of the world. Thank you to the Cornell Physics (and Astronomy) 2004 incoming graduate students, especially Matt Warkentin, Ryan Shannon, Duane Lo, and Sharon Gerbode, for teaching me physics. Thank you to Paul Bishop and John Sinnot for teaching me how to machine and make lab equipment. Thank you Bruce and Frank for teaching me (very quickly) everything I know about materials and how to play with them.

TABLE OF CONTENTS

LIST OF TABLES

LIST OF FIGURES

CHAPTER 1

INTRODUCTION AND SUMMARY OF RESEARCH

1.1 Structure of dissertation

The first 7 chapters describe various aspects of my primary research project, the study of fuel cell anode catalysts using composition spread thin films (Chapters 8 and 9 discuss other projects). Much of the content in these chapters does not directly relate to fuel cell catalysts; in particular Chapters 3 and 4 present research that is of general interest for high-throughput thin film material science. The discussion is often focused on aspects of the research that are more familiar to me than to anyone else. As such, I have included many details which are not necessary for a presentation of the research project and have not included a catalog of the catalyst results that are available elsewhere. Published work is presented with minor modifications for conformity with the other content of the dissertation and is noted by an $italics$ descriptor in the respective section heading.

1.2 The need for high-throughput studies of fuel cell catalysts

1.2.1 Fuel cells in the energy landscape

I'll start by pointing out that I've not read a single scholarly (research) article concerning models for the supply of humans' energy from renewable sources. I've also never made a polymer electrolyte membrane (PEM) fuel cell. During

my graduate career it evidently became very fashionable for materials-oriented conferences to have special sessions on climate change and renewable energy. So I've acquired a light education and some opinions concerning the importance of fuel cells in the energy landscape.

Short of extracting energy from the moon's gravitational field, about the only other quasi-infinite source of energy is the sun (well I'm not sure about geothermal). The sun's heating of Earth is the ultimate source of wind and waves and we have developed respective devices for converting their mechanical energy to electrical energy. We can let flora take care of the difficult part of solar energy conversion and use the chemical energy in the products. Then there are two really direct methods that are popular. There are photocatalysts for getting fuel (chemical energy) directly from the sun's photons and then there are photovoltaics for translating photons into energetic electrons. All of the above "renewable" energy sources are fantastic, and despite what I commonly hear, they are not in head to head competition with fuel cells. None of these technologies are portable sources of energy. There are plenty of opportunities for the use of fuel cells in stationary configurations but the easiest argument for the need of fuel cells comes from the need for portable energy approach.

There are three main technologies for generating portable energy (that do not involve the hope that the wind is blowing or the sun is shining) and all of them boil down to converting chemical energy into something more useful. Combustion engines convert chemical energy into mechanical motion by burning the chemicals. Batteries use the difference in electron chemical potential between two chemicals to provide a voltage source, and electrons are provided by allowing the chemicals to react at a controlled rate. Fuel cells aren't so different. A

fuel, which could be any molecule that would be put in a thermodynamically favorable state by rearranging the atoms and adding oxygen, is reacted with some oxygen source at a controlled rate. For safety and convenience reasons, it's best to choose a fuel that does not spontaneously oxidize. What this boils down to is the need for catalysts to help overcome reaction barriers. Combustion engines take care of this issue with explosions; catalyst research is the struggle to achieve the goal in a more sophisticated way (technically gasoline could be a fuel cell fuel but the potential barriers to complete oxidation are fantastic at or near room temperature).

There are a handful of fuel cell designs but we'll stick to PEM fuel cells. Once we start getting into the PEM architecture we would wander upon all kinds of material issues so let's stop here and note that we need two catalysts. The anode (or fuel oxidation) catalyst needs to help crack the fuel molecule, crack some other molecule to react with remnants that aren't H^+ (usually split water to provide an oxygen source for carbon) and let all the products go their respective ways. The catalyst implementation must provide pathways for extraction of e^- and H^+, but that is not our topic of interest. The following section illustrates why voltage is a driving force in fuel cell reactions, but the bottom line is that efficient fuel cells require catalysts that provide high reaction rates at low overpotentials. Thus, there are two convenient ways of defining a figure of merit for the oxidation catalyst: the current density provided from the fuel oxidation at a fixed overpotential and the overpotential required to drive the reaction at an appreciable rate. In this dissertation we almost exclusively use the latter and often refer to it as the onset potential.

The generated e^- and H^+ travel through different paths (the electronic one

being the user-defined path) and react with oxygen to form water. We haven't discussed the oxygen source, but to avoid the packaging of an additional chemical it will always be O_2 from air. The cathode catalyst is responsible for dissociating the oxygen so that it can react to form water. Improving the catalyst for this oxygen reduction reaction is very important but makes for painful research because it is difficult to make electronically conducting materials that are stable in acidic media at the high cathode potentials. Catalyst stability is also an important issue in anode catalyst research, the focus of most of this dissertation.

Other than the modestly horrible poisoning and cost issues, Pt is the ideal catalyst when H_2 is the fuel (Poisoning is the term used when catalyst activity is reduced due to the binding of species such as carbon monoxide or sulfur to the surface of the catalyst, blocking fuels from reaching the catalyst surface.). Other than some cost and long-term degradation issues, $Pt_{0.6}Ru_{0.4}$ is a generally fair oxidation catalyst, outperforming Pt for non-H_2 fuels. H_2 is difficult to store and transport so it would be nice to use a different fuel. A front runner is methanol which makes for a so-called direct methanol fuel cell ('direct' as opposed to the original idea of using a methanol reformer as an on-site source of H_2). The very popular Pt-Ru catalyst requires much higher overpotentials for methanol oxidation (about 300mV compared to perhaps 10mV for H_2 oxidation at the same current density). Thus, realization of commercial methanol fuel cells requires the discovery of new catalysts, and that is one driving force for the overarching project of this dissertation.

In summary, there isn't much hope for the long term prevalence of combustion engines. There's a point to be made about Carnot efficiency limitations but let's move on. The most direct competition of the fuel cell is the battery. Bat-

teries have the distinct advantage of being recharged through the very familiar electrical power grid. Fuel cells have the distinct advantage of being recharged through the very familiar fuel station. Time will tell if one dominates or both will be prevalent. Batteries are a well established technology due to decades of academic and industrial research. The current surge in fuel cell basic research may have similar results.

1.2.2 The role of the catalyst and voltage in determining fuel cell current

This section contains a brief description of catalyst kinetics in a half-cell reaction which will provide a picture of how reactions rates can differ greatly depending on the catalyst. The description is based of the treatment of fuel cell thermodynamics and kinetics in $Fuel\ Cell\ Fundamentals$ [118], which includes nice illustrations. Let's consider a simple reaction, $1/2\ H_2 -> e^- + H^+$, taking place on an anode catalyst surface in an electrolyte solution. This reaction may take place in several steps, including the adsorption of the H_2 on the surface and the splitting of the molecule into neutral adsorbed atoms. We will assume that these steps have already occurred and now we have an adsorbed neutral atom (initial state) which will transfer an electron to the catalyst and desorb to become an H^+ in solution (final state). The Gibbs free energy of these states are G_i and G_f, respectively. We will assume that this reaction is thermodynamically favorable such that the energy of the reaction $\Delta G_r = G_f - G_i > 0$.

For treating this problem, typically one would define a reaction coordinate and consider the Gibbs free energy as a function of this coordinate (G_i and G_f

could be the end points in a plot of free energy vs. coordinate). Commonly, this profile would have a peak, which is referred to as the reaction barrier. For the present discussion, we will consider only 3 states of the hydrogen atom, the initial and final states presented above and the "activated" state at the top of the reaction barrier. The Gibbs energy in this state is ΔG_b above G_i. Thus, ΔG_b is the energy barrier for the forward reaction and ΔG_b+ΔG_r is the reaction barrier for the reverse reaction. Statistical mechanics then dictates that the rate of excitation to the activation state is proportional to the respective Boltzman factor. The current density is proportional to the reaction rate and thus we have

$$j_1 \propto e^{-\Delta G_b/k_bT} \tag{1.1}$$

for the forward reaction, and

$$j_2 \propto e^{-(\Delta G_b+\Delta G_r)/k_bT} \tag{1.2}$$

for the reverse reaction. The additional proportionality constants contain product and reaction concentrations and factors for converting reaction probability to current density but we will ignore them and approximate that the proportionality constants in Equations 1.1 and 1.2 are equal.

We have not yet included the "electro-" part of this electrochemical reaction. In the above presentation $j_1 > j_2$, but we can apply a potential to the catalyst with respect to the electrolyte solution and stop the reaction. An electric potential will not change the energy of the initial state because the hydrogen is neutral in this state, but a potential ϕ in the electrolyte with respect to the catalyst will change the energy of the final state by $e\,\phi$, where e is the charge of the H^+. This is the energy per reaction, not the energy per mole (the Chemistry convention). With the above assumptions, if $e\,\phi = \Delta G_r$, then $j_1 = j_2$ and there is no net reaction rate. This is how equilibrium potentials can be calculated. While the net

reaction rate is zero, the rate in both directions is the "exchange current"

$$j_0 \propto e^{-\Delta G_b/k_bT}. \tag{1.3}$$

As you might be able to imagine and we will see below, it is desirable to have the exchange current be as large as possible as thus ΔG_b be as small as possible. The value of ΔG_b is highly dependant on the choice of catalyst and thus the first goal in a search for a good catalyst is to find an electrode that minimizes ΔG_b.

To obtain a net reaction rate we will decrease ϕ below the equilibrium value by an amount η (the "overpotential"). From an electrochemical experiment point of view, we make the voltage of the anode η above the equilibrium potential (which would also be the open circuit potential if there is no other reaction governing the open circuit potential). The energy of the final state is thus shifted by $e\,\eta$ but we do not know the barrier heights anymore because we do not know how much the energy of the activated state changed because we do not know the effective charge of the hydrogen in the activated state. This charge will be larger than the initial neutral charge by some fraction of the final charge; let's call it $\alpha\, e$, where $0 < \alpha < 1$. Thus, our energy barriers are now shifted by $\alpha\, e\, \eta$ and our forward and reverse current densities are

$$j_1 \propto e^{-(\Delta G_b - \alpha\, e\, \eta)/k_bT}, \tag{1.4}$$

$$j_2 \propto e^{-(\Delta G_b + (1-\alpha) e\, \eta)/k_bT}. \tag{1.5}$$

The net reaction rate j=j_1-j_2 is maximized by minimizing ΔG_b and maximizing α, both catalyst-dependent quantities. For small η, $j \propto j_0\, \eta$. After this linear increase with η, j increases by a factor of 10 for every ~60mV increase in η (for a one electron reaction). To optimize power density, fuel cells operate in the high-current (exponential) regime. For a given required current density, the required overpotential η is effectively subtracted from the operational fuel cell voltage.

Roughly speaking, by replacing the anode catalyst by a catalyst with a 10-fold higher j_0, the voltage available for external work at the fuel cell terminals will be increased by 60mV.

1.2.3 The composition spread as a tool for rapid identification of new catalysts

Accepted models of complete oxidation of complex molecules like methanol involve several adsorption and charge transfer steps. These steps are not independent but we can imagine that each step requires particular properties of the catalysts surface atomic and/or electronic structure to proceed efficiently. Elemental metals have been tried and while none of them are very good, Pt is the best. As a result, searches for new catalysts often involve heterogeneous materials, commonly binary, ternary and quaternary metal alloys and ordered intermetallics. Let's limit this broad class of materials to binary and ternary systems that contain Pt and one or two of a set of thirty other elemental metals. This gives us 30 binary systems and 30x29 ternary systems. We'll discuss later how to trim down the list of interesting systems, but for now we are left with the idea of studying 900 chemical systems. If they are to be studied via individual nuggets of material made in a chemistry lab then one has to decide what composition interval to use. For the ternary systems, the phase diagrams are in general unknown so a fairly small interval needs to be used to make sure that all possible phases are explored. Algorithms can be implemented to pick initial compositions wisely but a fairly fine interval would be 5at.%. This corresponds to the need for 282,420 samples. If you could get really efficient and hard work-

ing graduate students to make and test 5 of these nuggets every day of their five year graduate career (no weekends, no vacation) then you only need 31 graduate students. We took a different approach. If you can make all of the compositions on a single wafer and can screen the entire wafer for good catalysts then you only need to make 900 samples. The high-throughput fabrication and testing methods described in this dissertation allow for a graduate student working as hard as the ones described above to make and test 6 composition spreads thin films in a day. At that rate, a single graduate student tests every composition in three months. I'm not that much of a machine, I'm not $that$ hard working and I've done some other things with my days so I have not gotten close to looking at all 900 chemical systems. However, the point is that when the research goal prompts the study of a large number of chemical systems, the composition spread is a phenomenal tool. For the present research topic, throughput is increased be a factor of ~ 1000.

Catalyst-fuel pairings

While methanol has been introduced as a prominent non-H_2 fuel, there are lots of other small organic molecules (SOMs) that could work if the right catalyst is found. The above-mentioned multiple steps to complete oxidation can vary significantly for different SOMs. Figure 1.1, shows that even for catalysts which are very similar in the parameter space outlined above ($Pt_{46}Ru_{34}$ and $Pt_{92}Sn_8$ are both fcc-Pt alloys), testing for the oxidation of different fuels can yield strikingly different results. For the present discussion, this finding demonstrates that knowledge of "good" and "bad" catalysts for one reaction does not significantly reduce the parameter space of possible catalyst for another reaction.

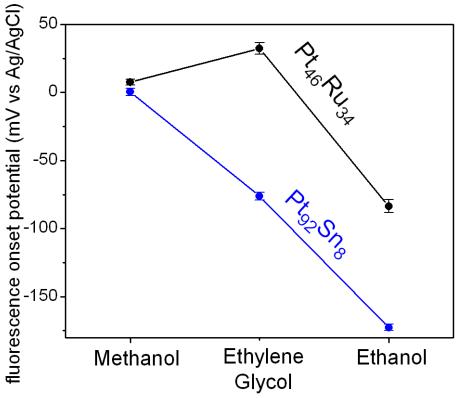

Figure 1.1: The fluorescence onset potential is plotted versus fuel tested for two thin film catalysts, showing that the catalytic activity toward the oxidation of one fuel is a poor predictor for that of another fuel. $Pt_{92}Sn_8$ shows a significant drop in onset potential when tested with different fuels compared to $Pt_{46}Ru_{34}$. It is important to note that the ethanol and ethylene glycol oxidation processes have not been sufficiently investigated to determine if the fuels are being completely oxidized to CO_2 (the catalyst is probably oxidizing these fuels to carbon-containing intermediates).

Our use of high-throughput, combinatorial methods allows us to search the parameter space efficiently for catalyst-fuel pairings that are suitable for fuel cell applications.

1.2.4 The composition spread as a tool for understanding individual catalysts

In the "31-graduate students pumping out metal mixtures" scenario described above, there is a significant potential for sample to sample variations in processing that could confound the systematic study of the catalyst systems. As a simple example, slight variations in the O_2 partial pressure during the growth

of the 18 Pt-Ti nuggets could have significant effects on the nugget purity, which could alter the trends in catalytic activity vs. Ti concentration. In a composition spread thin film all compositions are fabricated in the same chamber at the same time[1]. Combined with a $parallel$ screening (no experiment to experiment variations that could correlate with composition), this approach to material research provides robust identification of good catalysts in small regions of composition or phase space. Also, upon the discovery of active catalysts in a localized region in the composition spread, the characterization of the "good" and "bad" catalysts can provide important insights into the mechanisms of catalysis.

1.2.5 The surface is important

Depending on who you talk to, the first two to ten monolayers of an electrode surface are responsible for catalysis. The surface electronic structure determines how molecules will adsorb, charge will transfer and products will desorb. In this research we will be making measurements of the catalytic activity as a function of $metal$ stoichiometry in a binary or ternary thin films; we have little to no control over the modifications to surface stoichiometry and structure due to film exposure to air or testing solution. The stoichiometry of the catalyst will generally be related to the stoichiometry of the underlying metal film but will almost always contain oxygen and/or hydroxyls; nearly every metal (except Pt, Au and possibly Pd) reacts with O_2 and H_2O even at room temperature. The thickness of the reacted layer will largely be determined by the diffusion rate of the reactive species through the oxidized layer. That is, the oxide layer may quit growing at an appreciable rate due to inability of O_2 to reach underlying metal

[1]Ideally his means that there is no other process parameter that varies with composition. This is not true and is discussed later

(a kinetic limitation).

The importance of the crystal structure of the catalyst is discussed above, but upon oxidation the surface may consist of several different phases, which may be stoichiometric or sub-stoichiometric oxides. The resulting surface structure may or may not be related to that of the underlying crystallites. This dissertation includes the comparison of catalytic properties to thin film characterization data with the goal of understanding which catalyst properties are responsible for improved catalysis. The desired characterization of the catalyst would be measurements of stoichiometry, electronic structure and crystal structure on the film surface in the electrochemical environment. Many surface-sensitive measurements are experimentally challenging and the additional $in\ situ$ requirement makes such experiments prohibitively difficult at present. We will see some examples of using x-ray photoelectron spectroscopy, "bulk" x-ray diffraction and electrochemical characterization to guess what the surface might look like, but this topic notes an area of research at the frontier of materials physics, chemistry and engineering.

CHAPTER 2

A DEPOSITION SYSTEM NAMED TUBBY

2.1 Introducing Tubby

In summer 2005, Profs. van Dover and DiSalvo commissioned the creation of new composition spread deposition system. The existing system, Gilgamesh, was prepared for CFCI research primarily by Mark Prochaska[121] and was also used by Maxim Kostylev to create catalyst libraries, such as those used in [66]. Jon Petrie has also adopted Gilgamesh for his study of oxygen reduction catalysts.

I accepted the task of designing and constructing the new system, which was to be created from the vacuum chamber Tubby. Tubby was a Bell Laboratories chamber which was equipped with three 4 in. AJA magnetron sputter guns and a 6 in. substrate holder with heating and water cooling. One of these sputter guns was retained and the rest of the system was refit with four 2″ magnetron sputter guns (Angstrom Sciences Onyx-2) and a 2.5cm IonTech, Inc. ion gun. The single-substrate holder was replaced by a rotating substrate holder table. The system geometry and features are discussed in the following manuscript and Figure 2.2. A photograph of the system, including its electronics rack, is shown in Figure 2.1.

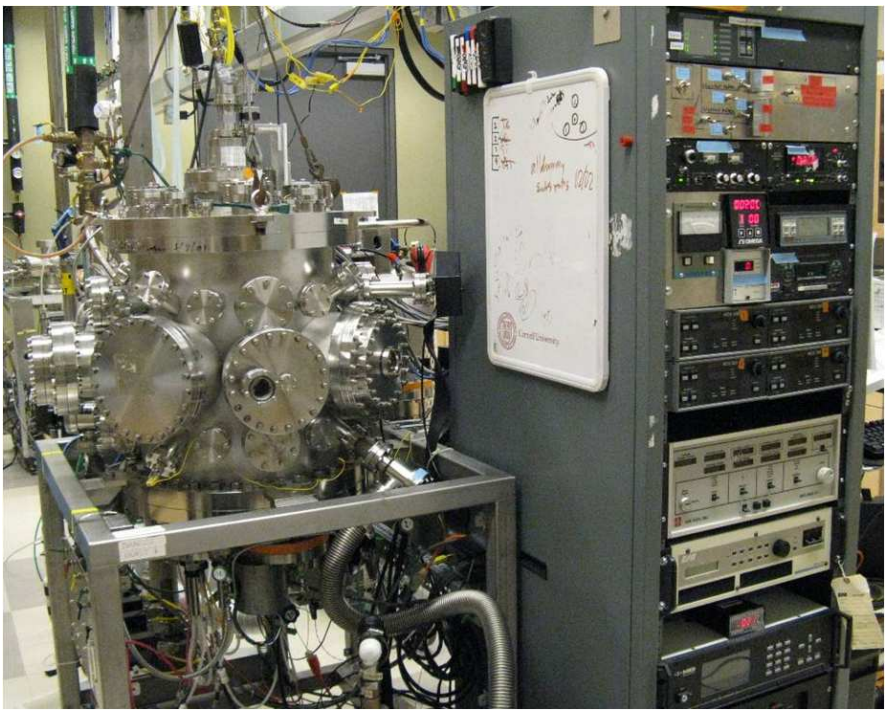

Figure 2.1: Photograph of the Tubby deposition system in Duffield Hall.

2.2 *Manuscript:* Getter Sputtering System for High Throughput Fabrication of Composition Spreads

2.2.1 Abstract

We describe a sputtering system that can deposit composition spreads in an effectively UHV environment but which does not require the high-throughput paradigm to be compromised by a long pumpdown each time a target is changed. The system deploys four magnetron sputter guns in a cryoshroud (getter sputtering) which allows elements such as Ti and Zr to be deposited with minimal contamination by oxygen or other reactive background gasses. The system also relies on custom substrate heaters to give rapid heating and

cooldown. The effectiveness of the gettering technique is evaluated, and example results obtained for catalytic activity of a pseudoternary composition spread are presented.

2.2.2 Introduction

The fabrication of combinatorial libraries of inorganic materials is an increasingly popular technique employed in materials optimization and discovery. The study of continuous composition spreads was developed by Kennedy, et al. [88] in 1965 and, in the context of cosputtering (simultaneous deposition from multiple sputter sources), by Sawatzky and Kay [129] in 1969. In the past few years, several new deposition techniques, such as the printing of salts for discrete composition spreads [107] and the controlled diffusion of gels for continuous composition spreads[81, 82], have been introduced. However, the thin film composition spread has remained an important technique, and the present work contributes to its active development.

The primary inhibition to the widespread use of composition spreads in the decades following their introduction was the lack of sufficiently automated measurement tools for evaluation of the materials. The introduction of computer-assisted evaluation in the 1990's marked an important increase in the use of combinatorial methods [179, 166, 165]. Among these efforts, Xiang et al. [29] developed an alternative to cosputter deposition. Their technique utilizes shutter and/or substrate movement to create a film with a thickness gradient, i.e. a wedge. Sequential deposition of overlapping wedges from any number of sources yields a film that, upon annealing, can form a continuous composi-

tion spread. The main advantage of this technique is control over the shape and steepness of the composition gradients, as these film properties are determined by the computer-controlled shutter and substrate motion. However, while the thickness of each wedge can be made arbitrarily small in principle, the deposited material lacks the intimate, atomic-scale mixing that codeposition provides. While annealing may address this issue, the need to anneal greatly limits the ability to independently control film microstructure and crystal chemistry.

An important concern in any deposition technique is the purity of the fabricated material. In physical vapor deposition, the most common cause of film contamination is the incorporation of reactive gasses in the film. While performing depositions in an ultra-high vacuum (UHV) virtually eliminates this concern, the common UHV practices of using load locks and performing long pumpdowns after system venting are inhibitive for many studies. In particular, for combinatorial, high-throughput studies, the need to frequently change substrates and targets makes UHV highly impractical. In 1964 Theuerer and Hauser [156] introduced a technique for reducing the reactive gas partial pressure in their vacuum chamber capable of reaching a base pressure no lower than 10^{-6} Torr. They enclosed their single sputter source and substrate in a metal can, which during deposition was cooled with liquid nitrogen. Any reactive gases within the enclosure then reacted with material deposited on the enclosure walls and remained there due to the high sticking coefficient created by the cryogenic temperature of the metal. In 1985, van Dover et al.[164] extended this so-called getter sputtering technique to a three-source deposition system for studying linear composition spreads of amorphous transition metal - rare earth alloys. To the authors' best knowledge, the current work is the first to employ the gettering technique in a combinatorial system capable of deposition of

ternary composition spreads. In addition, this work incorporates the gettering technique in a system designed for high-throughput synthesis.

In the context of fuel cell anode catalyst materials, the ability to control the concentration of reactive gasses in a sputtered material is important, for even modest concentrations will affect film microstructure and may inhibit the growth of ordered intermetallic phases. Casado-Rivera, et al.[27, 28] demonstrated that attention to such details is prudent through their discovery of binary ordered metallic phases that show not only high activity for the electro-oxidation of formic acid, but also resilience to poisons commonly found in fuel cell operating environments. It is also worth noting that substrate temperature during deposition is a key parameter in controlling film chemistry and microstructure and thus special attention must be given to substrate heating.

Prochaska, et al. [121] introduced high-throughput, thin-film combinatorial synthesis and evaluation methods to the search for electro-active intermetallics and alloys containing two or three elements. The instrument described in the current work contributes to the search for superior catalyst materials by providing additional thin film fabrication abilities, due most notably to its cryoshroud and custom-made radiative heaters. Also, the system is designed to provide an order of magnitude increase in the rate of composition spread production. In this paper, the main features of the deposition system and deposition techniques are described, followed by experimental results that demonstrate the effectiveness of novel techniques.

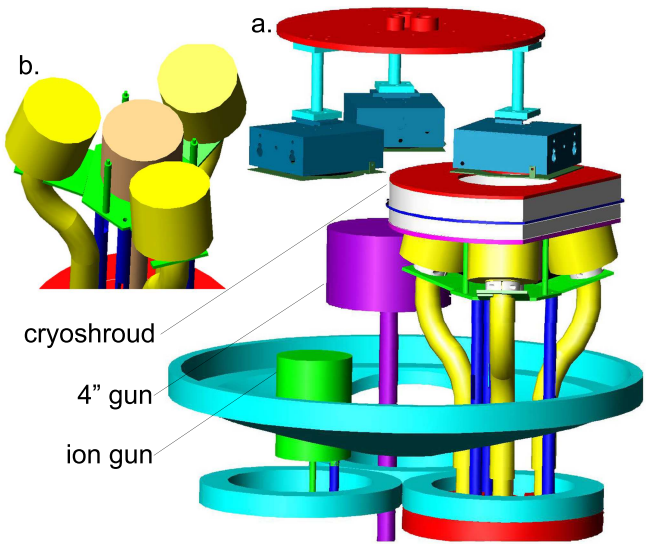

Figure 2.2: a. The three custom substrate heaters on their rotating mounting plate are pictured with the ion gun, 4"gun, and four-gun assembly as positioned in the deposition system. b. A detailed look at the arrangement of the four-gun assembly.

2.2.3 System design

Combinatorial film synthesis

The sputter deposition system contains four 2" magnetron sputter guns (Angstrom Sciences Onyx-2), a 4" AJA, Inc. magnetron sputter gun and a 2.5cm IonTech, Inc. ion gun, all pictured in Figure 2.2a as mounted in the vacuum chamber. Also seen in Figure 2.2a is a round plate that holds three substrate heaters for 3" substrates. The plate is attached to a rotary feedthrough that is geared to a stepper motor. This setup allows for computerized movement that brings any of the three substrates to any of the three film processing positions described in the following paragraphs.

The 4" gun is used for making highly uniform films. Most commonly, it is used for depositing a tantalum adhesion layer on silicon substrates prior to

the deposition of a composition spread. Such uniform metallic layers are also important in substrate heating as will be discussed in section 2.2.3. A stainless steel chimney (not shown) is mounted atop this gun to keep sputtered material from being deposited anywhere other than on the substrate and its holder.

The ion gun is used for substrate cleaning, for example to remove the insulating SiO_2 layer from silicon wafers. In conjunction with the substrate motion, it may also be useful for controlling film microstructure by employing deposition techniques involving alternations between sputtering and ion milling.

The 4-gun assembly (Figure 2.2b) is used for deposition of thin film composition spreads via cosputtering. One of the 2″ guns is centered below the substrate position in a standard on-axis orientation. The remaining three 2″ guns are positioned around the central gun, each with a confocal 15° tilt. In addition to the common binary and ternary composition spreads, this ensemble allows for codeposition of pseudoternary composition spreads: composition spreads containing four elements and covering a region in composition space with the dimensionality of a ternary spread.

The tilt of the three outer guns provides smooth composition gradients as a function of lateral distance on the substrate surface. Without the 15° tilt, sputtered atoms leaving the target would reach the most distant region of the substrate primarily via scattering events with the ambient gas. The resulting angle of incidence at the substrate can be quite sharp for such sputtered material, and unexpected and largely uncontrollable microstructure may ensue. This particular arrangement of the guns was chosen to minimize such effects while also keeping material sputtered in a direction normal to the plane of the target from being deposited on the substrate. This latter geometrical provision is important

for the existence of composition gradients across the entire substrate and is also important in the case of deposition in an oxygen environment, when sputtering of the substrate by O^- commonly occurs.

Between each pair of substrate heaters is a circular aluminum sheet (not pictured) that can be rotated over the 4" gun or 4-gun assembly for presputtering. At the center of one of the sheets is mounted an Inficon crystal deposition monitor that measures the mass accumulation rate at a given point with better than $10 ng/cm^2$ resolution. A direct measure of the profile of deposition rate for each gun can be obtained by incrementally rotating the deposition monitor along an arc above the appropriate gun. For the gun nearest to the center of the chamber, this technique does not provide much information about the deposition profile because the rate remains nearly constant throughout the crystal monitor's path. However, for each of the remaining three guns in the 4-gun ensemble, deposition rates as a function of crystal monitor position are used to fit an empirical form for the deposition profile perceived by a 3" substrate. Since each of the three confocally tilted guns yield an identical deposition profile for a given target with a given applied power, this technique allows the user to quickly calculate the expected composition of an entire composition spread. This method for determining position-dependent film composition is usually accurate to within several atomic percent, rivaling profilometry-based techniques and standardless energy dispersive X-ray analysis. Codeposition of certain sets of elements can yield compositions that differ significantly from those predicted by this method if any of the sputtered elements have a high vapor pressure at the substrate temperature or if the sticking coefficient of any of the elements is compromised by resputtering from the substrate by one of the other elements or by matrix effects in the film. The former of these two conditions cannot be ex-

plored with the deposition monitor because the monitor's temperature cannot be systematically controlled. The deviations from calculated compositions can however be easily anticipated by reviewing the published vapor pressure data. The latter condition will have some dependence on substrate temperature but can be explored at ambient temperature by using the deposition monitor to measure the extent by which the mass accumulation rate achieved by cosputtering a set of elements differs from the sum of the individual rates.

The final item of note in Figure 2.2 is the stainless steel cryoshroud that encloses the region between the deposition sources and the substrate. The walls have four openings on bottom which follow the contours of the three tilted and one central gun and one centered hole on top which allows sputtered material to reach the substrate. It is worth noting that the top hole must be sufficiently large to avoid any shadowing problems. A single loop of 0.25″ stainless steel tubing is welded to the cryoshroud walls and attaches to flexible stainless steel bellows that lead to thermally isolated feedthroughs. While the original getter [156] formed a tight seal except for one argon inlet point, the getter in Figure 2.2 is only loosely sealed with the sputter guns and substrate holder. It simply rests on posts welded to the same plate assembly that holds the four guns. This arrangement in combination with the flexible bellows, allows for quick and easy removal of the cryoshroud during target changes. In fact, the design of this system allows target changes to be performed in less than five minutes.

To start a typical deposition process, three 3″ silicon wafers are mounted in the substrate holders and the system is pumped to the low 10^{-7} Torr range with a CryoTorr8 vacuum pump. The substrates are sequentially brought to the desired deposition temperatures while the tantalum adhesion layer is deposited.

Simultaneously, the cryoshroud is cooled with flowing liquid nitrogen. Typical cryoshroud cooldown times are 10-20 minutes depending on nitrogen flow rate. Once tantalum deposition is complete, the composition spread is deposited. All depositions occur in 5mT argon, regulated with a feedback-controlled angle valve in the high-vacuum pumping line. The deposition monitor is commonly used before and after each deposition to ensure that the deposition sources are performing as expected.

Custom substrate heaters

The three substrate heaters were designed and built in-house. The heater design focuses on providing uniform substrate temperature, rapid warming and cooling cycles, and high heating efficiency, i.e. minimum power required to achieve and maintain a given substrate temperature. These three criteria are superbly met with a design that utilizes three 500W halogen quartz lamps. The use of domestic lamps offers low cost, quick and highly reproducible filament changes, and an enclosed tungsten filament that allows for operation in an oxygen environment.

While single-lamp units for in-vacuum substrate heating are commercially available, no practical installation of such a unit yields uniform substrate heating. Thermodynamic simulations were performed to determine the three-lamp configuration that best meets the need for uniform heating across an entire 3" wafer while maintaining high heating efficiency.

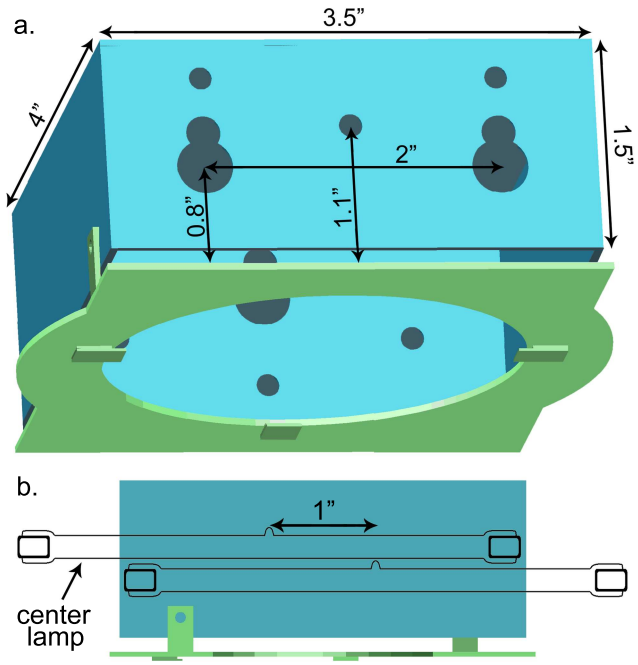

Figure 2.3: a. The custom heater box is shown with substrate holder plate. Dimensions for the heater box and for the positions of the three lamps with respect to the plane of the substrate are given. The lamps are inserted into the larger (“8”-shaped) holes. b. This side view of the heater shows the position of the center lamp with respect to the outer lamps. Inserting the center lamp in the opposite side from the two outer lamps provides a 1” separation between the center of the inner and outer lamps.

Heater design

The heater box and substrate holder, shown in Figure 2.3, are formed from sheets of 0.04” stainless steel. Sheets of 0.002” molybdenum line the interior of the heater box, serving as reflectors. The heater box holds three lamps in the appropriate positions with spring-loaded electrical connections to avoid contact loss due to differential thermal expansion.

The substrate holder plate is attached to the heater box with two small tabs, minimizing thermal contact. With heaters positioned as depicted in Figure 2.2a,

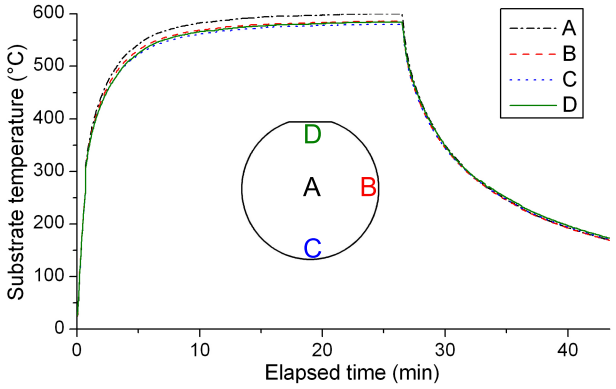

Figure 2.4: The inset shows four points at which thermocouples are cemented to a 3″ silicon wafer. The temperatures obtained from the four thermocouples are plotted as the substrate is heated by a custom heater under 100W applied power. The beginning of the cooling profile is shown after 26 minutes of heating.

the three tabs on the substrate plate are sufficient for holding the substrate. This method of substrate mounting and the low thermal mass of the entire heater assembly allow for rapid substrate cooling.

While the basic design parameters are given in Figure 2.3, CAD drawings, photographs, and further description are available in the online supplementary information and Section 2.3.

Heater performance

Figure 2.4 demonstrates the typical uniformity in substrate heating; maximum temperature variations on a 3″ wafer are limited to a few percent of the deviation from room temperature, up to the maximum tested temperature of 600°C.

A common problem with in-vacuum heating is that heat dumped into the system causes increased outgassing, which raises the partial pressure of reactive gasses. While the situation is improved by performing a heating cycle dur-

ing pumpdown, this time-intensive procedure fails to fully solve the problem. Thus, for a given desired substrate temperature, important heater specifications are the total electrical energy required to bring the substrate to the elevated temperature and the power required to maintain the elevated temperature. For a substrate temperature of 400°C, our custom heaters require 27kJ for a five minute warm-up, compared to the hundreds of kilojoules required for commercially available ohmic heaters, which additionally can require warm up times in excess of thirty minutes. The heaters can maintain the 400°C temperature with only 65W applied power.

An additional attribute of this heater design that makes it particularly appealing to high-throughput studies is exceedingly short cool-down times. The low thermal mass of the heater and the minimal thermal contact to the substrate allows for substrate cooling from 400°C to below 100°C in thirty minutes. The quick decline from high temperatures also shortens the time in which a sputtered film may react strongly with reactive gases in the chamber. The remaining notable feature is a control circuit containing a thermocouple, PID controller, relay, and transformer, which provides automated temperature control to a user-specified setpoint.

It is worth noting that the data on heater performance were obtained using silicon wafers coated with tantalum. Bare silicon and other lightly-absorbing media are not heated as efficiently. When deposition on such substrates is required, the back of the substrate must first be coated with an absorbing material.

2.2.4 Results and discussion

Film purity

Quantifying the effectiveness of the gettering technique in removing reactive gasses from the sputtering environment is difficult. Commonly, the reactive gasses of concern are hydrocarbons, water vapor and diatomic oxygen, and therefore one would like to measure the partial pressure of these gasses within the cryoshroud during sputtering while the absolute pressure is 5mTorr. To gather information on these quantities, we have performed two studies using deposition of the oxyphilic element titanium. The studies are meant to provide information on P_O, the effective partial pressure of all oxygen-containing gasses.

WDS analysis

The first study compared oxygen-incorporation in titanium films with and without the cooled cryoshroud. Film deposition commenced thirty-five minutes after the start of rough pumping, which provided a chamber pressure of 3μTorr in the no-gettering case. During this time, the SiO_2 was ion etched from the silicon substrate, the substrate was brought to the 400°C deposition temperature, and, where applicable, the cryoshroud was cooled for ten minutes. Titanium was deposited from one of the angled 2″ guns onto the silicon substrate creating a film with center thickness 40nm. The film was then capped with 15nm of Pt deposited from the centered 2″ gun to minimize film oxidation upon exposure to air. The film was allowed to cool in vacuum and was analyzed using standard-calibrated wavelength dispersive spectroscopy (WDS). The program GRMFilm [172] was used for electron Monte Carlo and x-ray absorption adjustments to

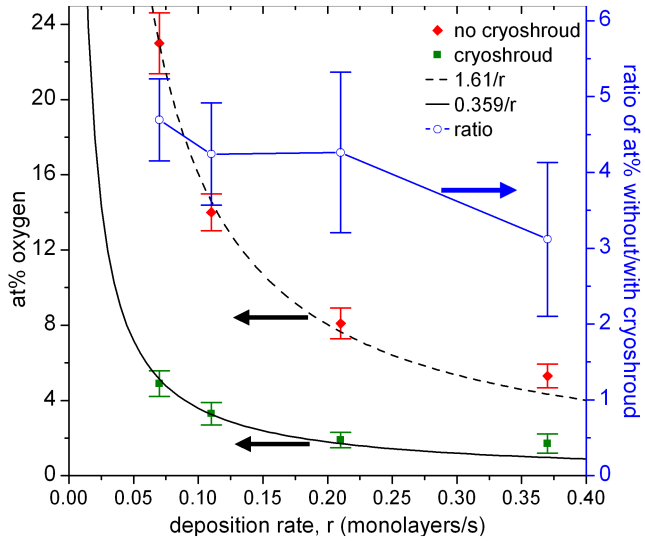

Figure 2.5: The atomic percent oxygen in sputtered titanium films, as determined by WDS measurements, is plotted for depositions both with and without the cryoshroud. The orientation of the gun allows for analysis of a range of deposition rates with a single deposition. Rates are quoted as monolayers of close packed titanium per second. Fitted functions and the ratio of atomic percent oxygen without the cryoshroud to that with the cryoshroud are also plotted.

the WDS raw data, providing the calculated atomic percent oxygen present in the films. Figure 2.5 shows the WDS results as a function of deposition rate. In the limit that the sticking coefficient of oxygen is independent of P_O, the atomic percentage of oxygen present in a sputtered film should be proportional to P_O/r, where r is the deposition rate. The least-squares fit for this functional form is given for each set of data in Figure 2.5. The ratio of the fit parameters suggests that the use of the cryoshroud reduced the effective P_O by a factor of 4.5. This type of analysis was not performed at lower absolute pressures (longer pump-down times) because the signal to noise for the WDS analysis becomes very poor with lower oxygen incorporation.

Film resistivity analysis

To test the effectiveness of the gettering technique for films sputtered in a fully pumped system (absolute base pressure approximately 0.3μTorr), resistivity analysis was performed. The film resistance of a metallic titanium film of given thickness is caused by electronic scattering primarily with phonons, impurity atoms, and titanium grain boundaries. The first of these has a strong temperature dependence while the latter two are independent of temperature. Thus, the ratio of the film resistivity at 300K to that at 5K can be used as a measure of film quality. This resistance ratio has a minimum of unity for films whose resistances are dominated by contaminant atom and grain boundary scattering.

Titanium films were once again deposited at 400°C both with and without the cryoshroud. For each film, the deposition rate was fixed at $\sim$0.5 nm/s. In the gettering deposition, the chamber base pressure during sputtering remained in the mid-10^{-7} Torr range, while this pressure rose to the low-10^{-6} Torr range during the deposition without the cryoshroud. Standard four-point vander-Pauw techniques [162] were used to measure film resistivity of 5mm square substrate pieces. The resistivity of the film deposited with gettering has a resistance ratio of 4.7±0.1, while the film deposited without gettering has a resistance ratio of 3.4±0.1. A film deposited with the same parameters in a deposition system using ohmic heaters which force the chamber base pressure during sputtering to nearly near 10^{-5} Torr has a resistance ratio of 1.2±0.1. We thus conclude that our custom heaters, and to even greater extent the gettering technique, improve the quality of the titanium films deposited in a high-throughput (non-UHV) setting. Quantifying oxygen contamination from the resistance ratio measurements would require numerically distinguishing resistance due to

electron-contaminant atom scattering from that due to electron-grain boundary scattering, which we do not attempt here.

Example electrochemical results from a pseudoternary composition spread

To illustrate other typical film properties, we present the preliminary results of a single pseudoternary composition spread tested for catalytic activity for the oxidation of methanol. The testing method used is the high-throughput fluorescence test described in detail previously [121], which yields images with catalytically active regions marked by their fluorescence. A composition spread was prepared with 250°C substrate temperature with Pb, Co, and Ti in the angled guns and Pt in the centered gun. Deposition rates were chosen such that the center composition would be 50at% Pt and equal atomic ratios among the other three elements. The film composition was calculated using deposition rate techniques described above and the result is given in Figure 2.6b. For ease in determining the optimal Pb:Ti:Co ratios, the fluorescence image result of the electrochemical test, Figure 2.6a, is mapped onto a ternary diagram, Figure 2.6c. The center and low-right active regions of Figure 2.6a have atomic ratios (Pt:Pb:Ti:Co) of approximately 3:1:1:1 and 4:8:0.8:1 respectively. The applied voltage at which fluorescence was first observed indicates that both of these regions have an onset potential for the oxidation of methanol that is approximately 80mV more positive than Pt nanoparticles. The fabrication and testing of this film, which required only a few hours from start to finish, reveals the optimal compositions within the tested region of composition space indicated in Figure 2.6b. While this single experiment did not reveal a breakthrough catalyst, its results direct future investigation of this set of four elements to more

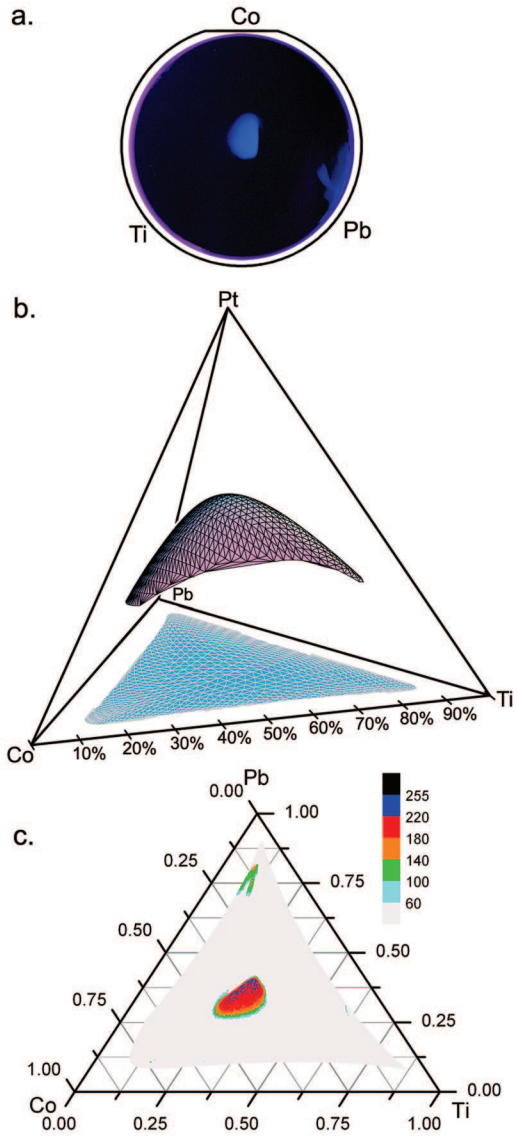

Figure 2.6: a. A fluorescence image taken during electrochemical testing of the film is shown in the outline of the substrate. The image was taken with a potential of 350mV vs. Ag/AgCl applied to the film, revealing catalytically active regions in the center and low-right. The orientation of the three confocally tilted guns is portrayed by the symbols of the target elements. b. The region of composition space covered by the film is the dome-shaped surface in Pt-Pb-Ti-Co composition space. The projection of this surface onto Pb-Ti-Co composition space is also shown. c. The intensity of the fluorescence image is mapped onto a ternary composition plot, showing the optimal Pb:Ti:Co atomic ratios.

Pt-rich composition spreads and to binary and ternary subsets.

2.2.5 Conclusions

We present a deposition system designed for cosputtering composition spread libraries. In addition to exploring ternary composition space continuously, the system includes features for controlling film properties. The primary design focus of this new system is to address the issue of reactive gas contamination in deposited films. While the inclusion of a reactive gas in a material may improve material performance, control over inclusion is necessary to conduct a systematic study. To this end, the composition spread is sputtered in a liquid nitrogen cooled cryoshroud which allows for combinatorial, high throughput studies of materials that may be poisoned by residual gasses at μTorr partial pressures. Such materials include those currently used in the study of shape memory alloys, magnetostrictive materials, semiconductors, and essentially any non-oxide material that includes an oxyphilic element.

2.2.6 Acknowledgments

The authors wish to thank Mark Prochaska, Maxim Kostylev, Sara Barron, Sharon Gerbode, Paul Bishop and John Sinnot for helpful conversations and general assistance in the construction of the deposition system. The WDS analysis was made possible by the Cornell Center for Materials Research Facilities supported by the National Science Foundation under Award Number DMR-0520404. Primary funding for this work is provided by the Department of En-

ergy, Grant No. DE-FG02-03ER46072.

2.2.7 Comments on system updates

The Phillips corporation has started selling new bulbs which have a shorter coiled filament length so the latest rebuild of the heaters included installation of a new brand of lamps which lost most of their ceramic end caps upon operation for 550°C substrate temperature.

The cryoshroud was stainless steel before October 2008 and copper thereafter. The copper shroud also has gas ports for supply of sputter gases at an individual source, but these have never been used.

The use of ion gun for controlling film microstructure has yet to be tried, but I will note that simultaneous operation of the ion gun and sputter guns would be important. The ion beam does not like to start at sputter pressures but may be started at 0.1 mT and continually operated as the pressure is slowly increased (I think). Also, use of the above-mentioned intra-shroud gas inlets would create a higher pressure in the sputter region than near the ion gun.

2.3 Additional notes on substrate heaters

In designing a substrate heater, we considered several desired properties: stable operation in high oxygen partial pressures, control of substrate temperatures from 100 to 600 °C, rapid heat-up and cool-down time (10 min.), low thermal mass, modest thermal contact between substrate and heater body, form factor

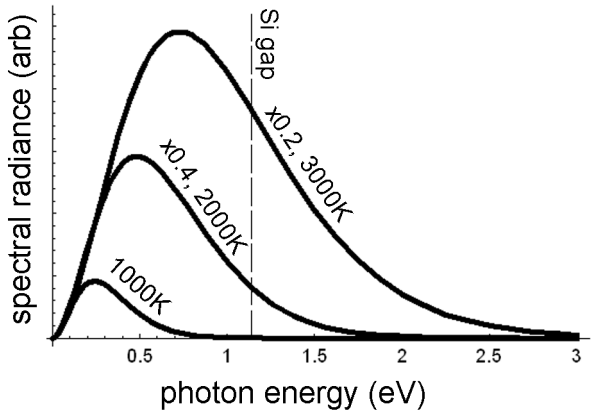

Figure 2.7: To investigate Si absorption of filament radiation, the filament is modeled as a blackbody emitter whose emission spectrum is plotted for three temperatures. The Si band gap is also plotted for comparison.

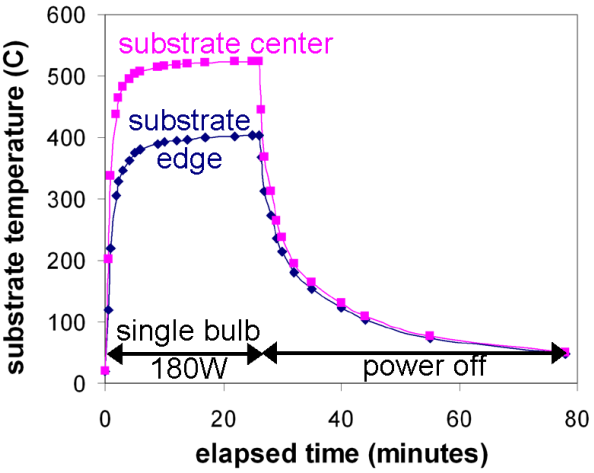

Figure 2.8: The temperature of the substrate surface as measured by cemented thermocouple is measured during heating and cooling for two substrate positions: center and edge of 3″ wafer.

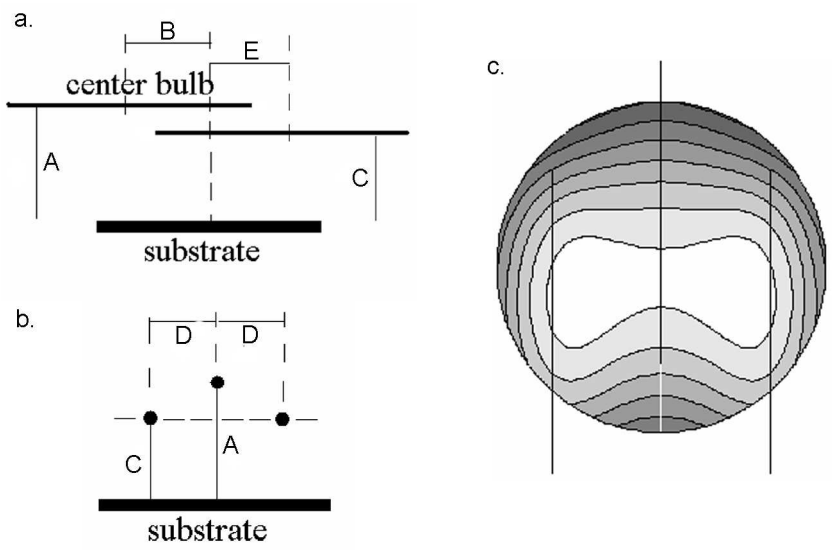

Figure 2.9: a. and b. Side views showing the geometric relation of the three bulbs with respect to the substrate. The model bulb layout used to build the heaters is that of a. and b. with A to E 27, 12, 20, 24 and 12 mm, respectively. c. A contour map of the power density from direct (not reflected) photons plotted inside the outline of a 3" substrate. The positions of the three bulbs are shown by vertical black lines.

compatible with US Inc. ohmic heaters. To give all of these properties, we chose a radiative heating approach using domestic quartz halogen bulbs (these are simply tungsten filaments in a vacuum-tight seal filled with inert gas and a halogen to help redeposit evaporated tungsten on filament). These bulbs are obviously not meant to operate at 500°C in vacuum, but we tried and the bulbs have been operated for years without failure.

Many substrate materials (silicon, quartz, sapphire) don't absorb much blackbody radiation from filaments at typical filament temperatures. Figure 2.7 shows blackbody spectra for 3 temperatures along with the Si bandgap, demonstrating that modest absorption of the emitted photons is only obtained for filament temperatures $\gtrsim$3000K, beyond the typical operating temperature of

tungsten filaments. Thus, all substrate heating measurements were made with Si substrates with a film of at least 100nm of Ta on the front surface. The use of a metal coating on the back side of wafers seems to be less effective due to reflection of incident radiation.

Simple thermodynamic modelling was performed to assist in the design of radiative heaters. Considering a filament to be a 1-D radiation source, geometry and integration can be used to calculate the intensity of radiation experienced at every point on a substrate. We considered only the incidence flux of energy as a function of substrate position. The different light bulbs considered in this investigations were PHILIPS 250W, 300W and 500W quartz halogen bulbs. The only quantities specific to the different types of bulbs in this treatment are the length of the filament and the linear (radiated) power density. The radiated power densities of the bulbs were measured with an applied voltage of 30V and assumed to be emitted uniformly from the coiled parts of the filament.

More than a dozen different 1-,2-,3-, and 4-bulb configurations were considered. The contour plots of the radiation intensity provide numerical information on the heating of the substrate due to photons that collide with the substrate directly. The contour plots also allow semi-quantitative analysis of the temperature gradients that would exist with no thermal conductivity in the substrate. Thus, one is able to make educated guesses concerning the extent to which temperature variations resulting from this model will be suppressed by thermal conductivity in the substrate. The final thermodynamics to keep in mind is that the heater design will include a reflector box that will add an approximate uniform radiation intensity to the entire substrate. It is worth noting that the filament from a 500W lamp is considered to be only the coiled portion of the

wire and is thus significantly shorter than the entire lamp assembly.

The modelling indicated that with a single bulb, the center of the substrate received twice as much radiation intensity as the edge of the substrate. The effect was also observed experimentally as shown in Figure 2.8. The optimal bulb configurations were 4-bulb ensembles with complicated geometry that would not make for practical manufacturing. There are some nice theoretical configurations that involve perpendicular bulbs, but they cannot be realized due to finite bulb thickness. A set of ensembles of three parallel 500W bulbs offer a compromise between ease of manufacture, uniformity of substrate radiation, and fraction of radiated light incident directly onto the substrate.

The bulb arrangement and an example contour image are shown in Figure 2.9. The three identical bulbs are parallel with the center bulb at a height A above the substrate, shifted away from center along the axis of the bulb a distance B. The two other bulbs are symmetric about the center bulb a distance C above the substrate, separated by $2D$, and shifted away from center a distance E in the opposite direction from the center bulb shift.

CHAPTER 3

MODELING DEPOSITION RATES AND OTHER PROPERTIES OF COSPUTTERING

3.1 The importance of calculating composition in high throughput research

In this chapter I present the methods used to build a model for the high-throughput determination of Tubby deposition profiles and subsequent calculation of film composition. For combinatorial material science in general and catalysis studies in particular, the ability to reliably calculate film composition without measurements on the film is an important, powerful tool.

The most common method for composition mapping of a composition spread thin film is via an electron microprobe. Typically, the probe is equipped with a programmable translation stage which reduces the effort required for creating a composition map. However, the entire process from substrate mounting to data analysis is costly in time and effort. Many films created in a high-throughput search will not exhibit a sufficiently high figure of merit to warrant detailed characterization. Thus, composition mapping could be delayed until after acquisition of property data. However, for catalysis or other electrochemical studies, the possibility of leaching of labile elements can lead to changes in the bulk concentration of the film, thus confounding the measurement of the as-deposited composition map. The calculation of film composition from pre-determined deposition profiles is a very high-throughput characterization technique. For films suspect of leaching, composition measurements can be

made after testing and compared to the as-deposited, calculated compositions. I would note that for very interesting catalysts, composition measurements are prudent "just to be sure."

3.2 Measurement of Deposition Profiles

3.2.1 Relating crystal monitor data to deposition profiles

The movable crystal monitor, introduced in 2.2.3, is used to collect data on the deposition profile of the targets sputtered from guns in the 4-gun assembly. The following discussion demonstrates that crystal monitor data taken from an arc across the deposition region can be used to calculate deposition rates for an entire 3" substrate. Remember that gun 1 and gun 3 are symmetric in the gun-crystal monitor geometry. Also remember that the moving crystal monitor provides little information concerning the profile from gun 2. The orientation of gun 4 makes its deposition profile the easiest to determine and thus it will be left out of this discussion. The crystal monitor arc is shown in Figure 3.1, which includes an illustration of the geometric parameters defined below.

For this study, I first needed to measure the thickness profile of a film deposited using a single angled gun source. While several techniques exist for measuring the thickness of a film, few techniques offer high density of data on a metal thickness spread with a reasonable data acquisition time. For films with known optical properties, reflectometry or ellipsometry can be used to measure film thickness with a high DAQ rate. The same is true for capacitance measurements on a film of know dielectric strength. In principle, resistivity measure-

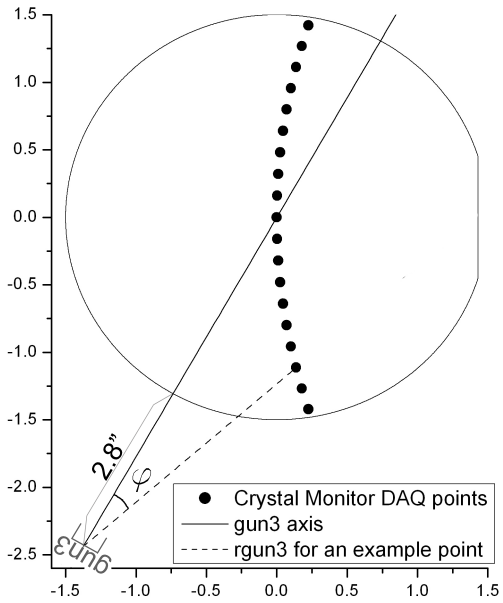

Figure 3.1: The deposition region is outlined by the shape of a 3″ wafer. This is a bird's eye view in Tubby so this would be the $back$ side of the wafer. The position of gun 3 is shown as well as the projection of the gun 3 axis in the substrate plane. The crystal monitor positions commonly used for deposition profiling are shown. These substrate positions are parameterized in polar coordinates in the substrate plane with the origin determined by projecting the gun center in the direction normal to this plane.

ments would work, but the sensitivity of film resistivity to deposition parameters makes this approach less attractive. The remaining traditional technique is profilometry, which requires patterning the film by either depositing through a shadow mask or using the black wax technique for post-deposition film removal. For single point or deposition profiling in one dimension, this is the most attractive option. However, for collecting data at a high density of points across an entire wafer, the film processing requirements become prohibitive. I found that an untraditional application of Wavelength Dispersive Spectroscopy (WDS) provided the dynamic range and resolution I needed for thickness profiling.

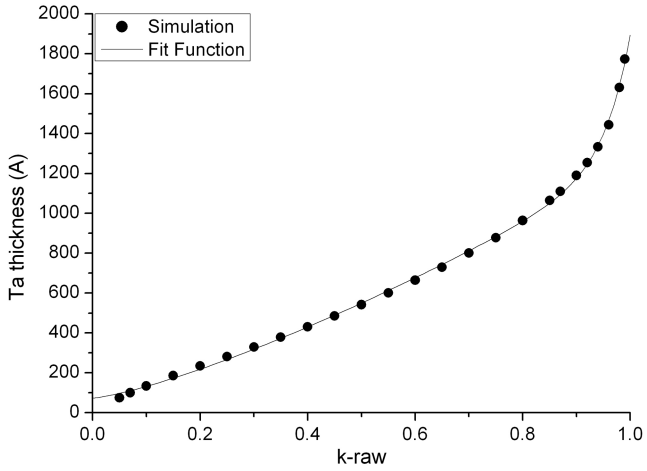

Figure 3.2: Ta thickness as a function of WDS k-raw values as determined by the program GMRFilm [172] and my fitted function.

As film thickness increases from zero thickness, the number of inelastic electron - film atom scattering events increases, leading to the generation of a greater number of x-rays in the film. However, x-rays generated in the film escape to the detector with a probability determined by the x-ray absorption properties of the film. For pure element films, Monte Carlo simulations for electron trajectories combined with mass absorption corrections can yield very accurate determination of the film thickness as a function of x-ray yield. In WDS, x-ray yield is quantified by the measured quantity k-raw. Taking my Ta film measurements as an example, k-raw is the ratio of the number of Ta M_α x-rays detected per second to that from a bulk (infinitely thick) Ta sample. Figure 3.2 gives simulation results for Ta film thickness as a function of k-raw. My empirical fitted function used in the data analysis below is also plotted. At k-raw$<$0.05, counting statistics are poor, and as can be seen in the figure 160nm$\approx \infty$. Therefore, this technique can be used to analyze Ta film thickness over approximately one order of magnitude. This dynamic range is much smaller than conventional thickness determination techniques, but is suitable for Tubby single-element films.

Deposition profiles from a given gun will have the same general form for any metal target sputtered under DC power. The gun-substrate geometry, gun magnet strength, and deposition atmosphere are the main parameters that determine the general form of the deposition profile. The mission is to find a functional form that describes the general deposition profile which has parameters that will take on unique values for each (metallic) target element. My proposed functional form for the deposition profile across a substrate is given by

$$f\left(rgun\right)\sqrt{cos\left(\varphi\right)}, \tag{3.1}$$

where

$$f\left(rgun\right)=\left(a\,e^{-b\,x}+c\,rgun^{2}\right), \tag{3.2}$$

and where a, b, and c are parameters (excluding the overall magnitude of the deposition rate, parameter space is actually two-dimensional). The two variables $rgun$ and φ are depicted in Figure 3.1. Both variables are defined in the plane of the substrate and are referenced to a given gun's position ($rgun1$, $rgun2$, and $rgun3$ are the gun-specific variables). For a given point on the substrate, $rgun$ is calculated by considering the vector from the target to the substrate point and taking the length of that vector's projection in the substrate plane.; φ is the point's angular separation from the projection of the gun axis in the substrate plane. Over an entire 3" substrate, $rgun$ varies between 2.3" and 4.3", and φ has a maximum value of 32.4°. The φ dependence of the deposition profile (Equation 3.1) is weak, at most changing the deposition rate by 8.1%. Also, it has no dependence on the target material. It is a purely geometrical term, leaving the element-specific component of the profile a function of a single variable. This property is highly desirable for both ease and accuracy of fitting crystal monitor data and subsequently inferring deposition rates over the entire substrate.

To verify this deposition profile model and develop techniques for determining profile parameters from crystal monitor measurement, Ta and Pt were sputtered from all three angled guns: crystal monitor scans were performed and films were prepared and analyzed by the WDS method. The results and discussion are included in the Appendix.

The following sections demonstrate the calculation of film composition using the deposition profiles models. While co-deposition of some sets of elements affords composition calculation by the intuitive arithmetic, phenomena unique to codeposition may result in film compositions which differ significantly from these "expected" compositions.

3.3 *Manuscript:* Resputtering phenomena and determination of composition in codeposited films

3.3.1 Abstract

The use of standard characterization techniques to determine elemental compositions in composition spread thin films is time-intensive. Combinatorial, high-throughput studies of thin film materials demand high-throughput determination of film composition. We discuss the possibility of calculating codeposited film compositions from deposition profiles obtained during single-source sputtering. In the context of DC magnetron sputtering, we find that while this technique is appropriate for the Pd,Pt,Ti system, it yields atomic ratios in a Pt, Pb composition spread thin film that vary significantly from values measured

with wavelength-dispersive x-ray spectroscopy. A model for resputtering during codeposition is presented to account for these discrepancies, and the model is used to calculate resputter rates during Pt, Pb codeposition. We also employ our model to estimate the resputtering susceptibility of commonly sputtered elements.

3.3.2 Introduction

The synthesis of combinatorial libraries of inorganic materials is an increasingly popular technique employed in materials optimization and discovery. Deposition of thin film composition spreads from multiple sources is an attractive technique for creating such libraries as it allows for fabrication of the libraries in a high-throughput regime [71, 167]. We discuss the ability to determine elemental compositions in the thin film while minimizing the use of traditional characterization techniques that compromise the high-throughput nature of the study. Our discussion is carried out in the context of magnetron sputtering, which is an attractive deposition technique in combinatorial studies as it offers constant, comparable deposition rates for many elements [167].

The deposition of the composition spread thin films can be performed by sequential [30] or simultaneous [167] deposition of the constituents. Given deposition rates and profiles for the constituents, the elemental composition of a film sputtered in sequential layers can be easily calculated provided that the individual layers are sufficiently thick. The thickness of each layer must be large enough that the deposition of a layer does not significantly alter the just-deposited layer. With decreasing layer thickness and in the ultimate limit of

simultaneous deposition (codeposition), interactions among the deposited material and projectiles from the deposition sources may cause the stoichiometry of the film to differ from that which is calculated using deposition rates from individual sources. We note that the codeposition regime is desirable as it yields films that are intimately mixed in the as-deposited state.

The said interactions will differ with deposition technique (PLD, CVD, etc.). Chemical interactions among the deposited species will be relatively independent of deposition technique while interactions such as the removal of film material by bombarding species will be negligible for evaporated films but may be significant for deposition techniques involving higher energy species. The current work discusses such interactions in the case of codeposition from single-element targets using DC magnetron sputtering in an inert atmosphere and we note that the phenomena discussed are of equal interest for the case of ion beam sputtering.

Resputtering

In the deposition scenario at hand, an inert gas ion (e.g. Ar^+) is accelerated across the cathode dark space and bombards a biased metal target (cathode). The collision may eject target atoms, and with some probability the inert gas atom reflects as an energetic neutral atom. Positively charged ions that reflect from the target are decelerated across the cathode dark space and thus do not contribute to resputtering. The net result is a flux of target atoms and reflected gas atoms impinging the substrate. We are interested in the arrival rate and energy of each species at the substrate as well as the accumulation rate of the deposited (metal) species during both single-source and multi-source sputter-

Table 3.1: Symbols used for the various molar rates at a given point on the substrate and for given sputtering parameters.

symbol	molar rate
${}^{a}\mathrm{R}$	arrival at substrate
${}^{s}\mathrm{R}$	accumulation during single-source sputtering
${}^{c}\mathrm{R}$	accumulation during cosputtering
${}^{c}\mathrm{r}$	effective resputter rate due to phenomena unique to cosputtering

ing. Table 3.1 gives the symbols used for these molar rates. Subscripts of these symbols will indicate the species whose rate is being referenced. All values of ${}^{a}\mathrm{R}$ for species from a given source are assumed to be independent of the operation of other sources.

During deposition from a single source, the deposited metal is partially resputtered from the substrate by reflected gas neutrals and self-sputtering. These phenomena, collectively referred to as *intrinsic resputtering*, result in a positive intrinsic resputtering fraction $({}^{a}\mathrm{R} - {}^{s}\mathrm{R})/{}^{a}\mathrm{R}$.

Hoffman [76] asserted that, in the absence of projectile scattering with a background gas, this fraction is well parameterized by the target-projectile atomic mass parameter,

$$\mu = \frac{M_{target} - M_{projectile}}{M_{target} + M_{projectile}}. \tag{3.3}$$

He mapped this parameterization with thirty measurements of intrinsic resputtering for a particular geometry in an ion beam deposition system. For the sputtering of Pt by 1keV Ar, the intrinsic resputtering was measured to be about 16% of the Pt arrival rate: 12% from resputtering by reflected Ar and 4% from Pt self-sputtering. Since, for example, the mass parameter μ for Pb sputtered by Ar is roughly equivalent to that of Pt by Ar, the intrinsic resputtering fractions should be approximately the same.

In addition to this intrinsic resputtering, when targets are powered simultaneously, one depositing species can be resputtered by the other depositing species or by Ar neutrals reflected off the other target(s). Also, resputter rates from intrinsic phenomena may be significantly altered by the coexistence of multiple species on the growing film's surface. These phenomena do not occur in single-source deposition and result in cosputter accumulation rates ${}^{c}\mathrm{R} = {}^{s}\mathrm{R} - {}^{c}\mathrm{r}$.

Limited control of resputtering can be achieved by use of ion sources (ion-assisted deposition) and substrate bias (especially in reactive sputtering). We do not discuss such techniques as we are interested in the codeposition analogue of intrinsic resputtering. We do however note that these techniques have spawned studies of resputtering of multicomponent films, such as the measurements and models of Harper and Gambino [73].

Resputtering from growing multicomponent films has also been previously studied in the context of deposition from a single alloy target [46, 17, 72, 134, 135, 153]. Eisenmenger-Sittner, et al. and Bauer, et al. [46, 17] studied resputtering effects of Cu and Pb sputtered from a single target with low Pb loading. They simulate six resputter phenomena: Ar, Cu and Pb each impinging on Cu and on

Pb. This work and that of Shah and Carcia [135], which addresses resputtering in the ion beam sputtering of an alloy target, are of particular interest as they note variations in resputtering with differing substrate position (relative to the target).

Bruce, et al. [23] studied resputtering in the sequential deposition of W and Si from separate magnetron sources. Their sputter geometry involves substrate movement such that each source deposits in the standard planar face-to-face geometry. They find that as the sequentially deposited layers become increasingly thin, the resputtering of the just-deposited layer by the next layer's source results in measurably different bulk compositions. Similar resputtering effects have been observed in pulsed laser deposition from a multicomponent target, which is well described as the sequential deposition of thin layers. Resputtering in this context are observed and modelled by Sturm and Krebs [153].

Resputtering in the codeposition of Ti and W has been modelled with TRIM calculations by Bergstrom, et al. [20]. Their simulations revealed that the primary cause of resputtering is energetic Ar reflected from the W target, a result that is in agreement with the present work.

In multi-source sputtering, inert gas atoms reflected from different sources must be treated as different projectiles as their energy distributions will depend on the target material and cathode voltage. Thus, with codeposition from n single element sources, n species accumulate on the substrate with $2n^2$ resputtering phenomena occurring at the growing film's surface. While intrinsic resputtering occurs at a film surface with unity surface concentration, the film surface in cosputtering has a finite concentration of all n elements. Thus, cosputtered films will never have compositions equal to those calculated from single source

accumulation rates. We demonstrate that the differences are negligible in some instances while significant in others.

3.3.3 Measurements of film composition and deposition rates

EDS and WDS measurements

Energy Dispersive x-ray Spectroscopy (EDS) analysis of a ternary Pd,Pt,Ti composition spread was performed using a JEOL 8900 EPMA Microprobe. Quantization of elemental concentrations were calculated with NORAN System SIX software using the Pd L, Pt L and Ti K x-ray counts.

Wavelength-Dispersive x-ray Spectroscopy (WDS) analysis of Pt, Pb binary composition spreads were performed using the same instrument. PbS and Pt polycrystalline bulk samples were used as standards, and M_α x-rays were counted after diffraction through a TAP crystal. The raw data was then corrected for absorption and thin film effects using GMRFilm [172], providing Pb:Pt atomic ratios used for analysis.

These standards and GMRFilm were also used to measure the thickness of pure element thickness spread films by exploiting the dependence of x-ray counts on film thickness.

In-situ measurements of single source deposition profiles

The deposition system, described previously [67], contains a crystal deposition monitor which can be moved across the deposition region, measuring mass ac-

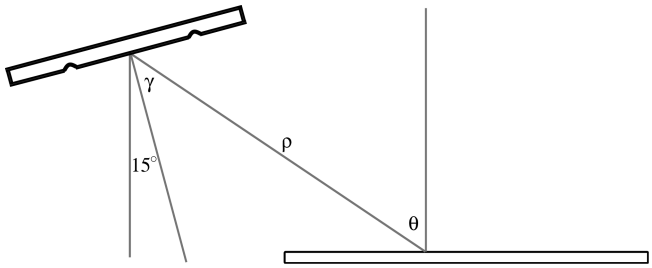

Figure 3.3: The relative position of the 3in. substrate (bottom) and one of the 2in. targets (upper-left) in the deposition system is shown. The important geometrical variables for a given point on the substrate are noted. The figure is drawn approximately to scale.

cumulation rates at different positions. The corresponding ${}^{s}\mathrm{R}$ values are fit to an empirical function for the deposition rate from the given source as a function of substrate position. To establish the validity of this method, fitted profiles were compared to film thickness measurements performed on a thickness spread thin film using WDS. The crystal monitor data and fitting routines were found to produce the WDS thickness values to within a few percent.

3.3.4 Deposition Geometry

Composition spread films are sputtered from two or three sources positioned such that the targets are centered 8.3cm from substrate center, 4.2cm out of the substrate plane and also confocally tilted 15° from substrate parallel (Figure 3.3). While the majority of sputtered material is ejected from the ring whose cross section is drawn on the target, we approximate that atoms leave the target at an angle γ, travel a distance ρ to a substrate point and impinge at an angle θ=γ+15° from substrate normal.

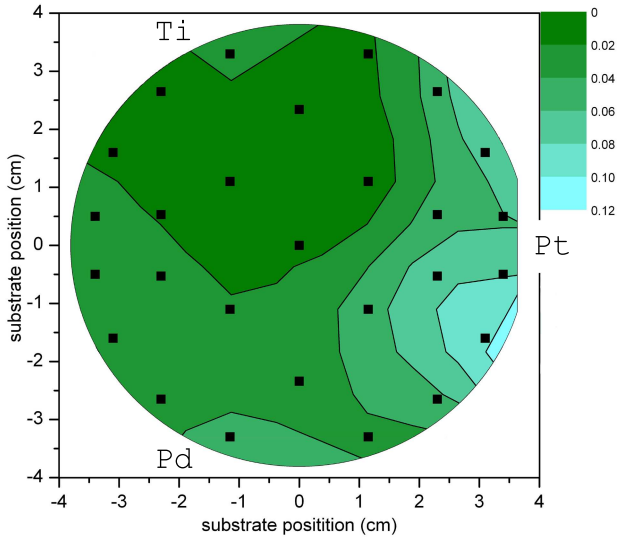

Figure 3.4: For the Pd,Pt,Ti composition spread, the error (Equation 3.5) in determining EDS-measured film compositions using crystal monitor data is interpolated across the substrate. The orientation of the three targets is noted by the element symbols and the substrate positions of the EDS measurements are plotted.

3.3.5 High-throughput determination of compositions in a Pd,Pt,Ti composition spread thin film

A Pd,Pt,Ti ternary composition spread was deposited on a 3in. Si wafer. The single thin film covers approximately the central half of the ternary composition space; that is, the three elemental concentrations each vary from approximately 10% to 80%. The elemental concentrations were measured by EDS at 27 substrate positions and compared to those inferred from single-source profiles (Sec. 3.3.3).

At a given substrate position, the normalized atomic ratios Pd:Pt:Ti=a:b:c are described by

$$c = 1 - a - b,\ a \in \{0, 1\},\ b \in \{0, 1 - a\}. \tag{3.4}$$

A reasonable quantification of the difference between two normalized ternary atomic ratios a_1:b_1:c_1 and a_2:b_2:c_2 is the distance between the two points in the partial plane described by Equation 3.4,

$$\left[\left((a_1 - a_2)^2 + (b_1 - b_2)^2 + (c_1 - c_2)^2\right)\right]^{1/2}. \tag{3.5}$$

For standardless EDS measurements of the absolute ratios, 10% is a reasonable value for this quantity. Figure 3.4 shows that the above techniques for crystal monitor-based profiling of the ternary composition spread produces the EDS values to within the absolute accuracy of the measurement.

The only significant deviations between inferred and measured compositions occur for the lowest Pd concentrations, where crystal monitor data provides a higher Pd concentration than EDS detects. Regardless of absolute compositions, EDS measurements of relative changes in elemental concentrations are accurate to an atomic percent. Thus, our comparison of crystal monitor and EDS compositions suggest a systematic, preferential decrease in the accumulation of Pd near the Pt source. In the following section we explore this phenomenon quantitatively for a two element system in which the effect is more pronounced.

3.3.6 Resputtering phenomena in the codeposition of Pb and Pt

Film deposition

Thin film composition spreads containing Pt and Pb were deposited onto one substrate held at 60°C and one held at 200°C. Depositions were carried out in 5mT Ar with Pt and Pb target potentials -370V and -320V with respect to cham-

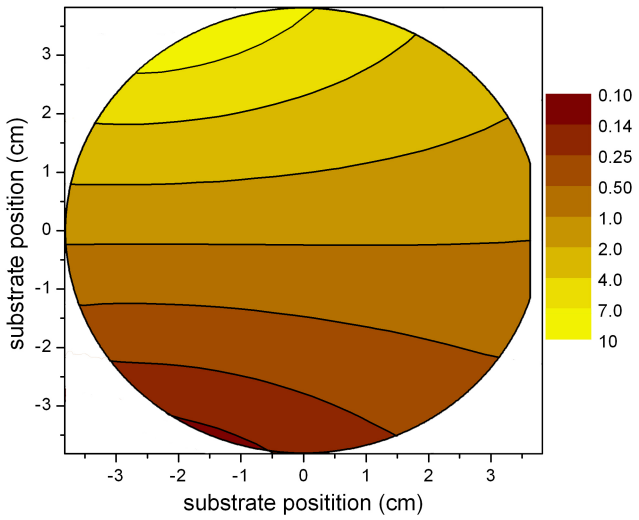

Figure 3.5: The map of atomic ratio Pb:Pt for the binary composition spread is inferred from crystal monitor profiles.

ber ground. The molar deposition rate at substrate center from each target was measured before film deposition with the crystal monitor; the individual rates were measured again after film deposition and found to be unchanged, demonstrating the stability of the sputter sources. These rates for Pt and Pb were 2.0 and 2.3 nmoles/s/cm^2 respectively. Given these rates and measured deposition profiles, the Pb:Pt ratio inferred from crystal monitor data is given in Figure 3.5. A film with this composition profile could be made by sequential deposition of sufficiently thick layers, as discussed in section 3.3.2.

A model for calculation of resputtering rates

Given relations among the rates in Table 3.1, single-source depositions rates can be used to calculate resputtering rates and thus compositions of cosputtered films. In this section we develop a model of resputtering in the Pb, Pt system which provides such relations. While the accumulation of Ar in the growing

film is neglected (${}^{s}\mathrm{R}_{Ar} = {}^{c}\mathrm{R}_{Ar} = 0$), the arrival rates of reflected Ar neutrals, ${}^{a}\mathrm{R}_{Ar-Pt}$ and ${}^{a}\mathrm{R}_{Ar-Pb}$ are included, where the hyphenation indicates the target responsible for Ar reflection. As presented in section 3.3.3, the crystal monitor accurately measures ${}^{s}\mathrm{R}$. The atomic ratios Pb:Pt measured by WDS are ${}^{c}\mathrm{R}_{Pb}/{}^{c}\mathrm{R}_{Pt}$.

Define ${}^{s}\chi$ to be the bulk atomic ratio Pb:Pt for a film sputtered sequentially from the two targets (Figure 3.5). Define ${}^{c}\chi$ to be this ratio for a codeposited film,

$$ {}^{c}\chi = \frac{{}^{s}\mathrm{R}_{Pb} - {}^{c}\mathrm{r}_{Pb}}{{}^{s}\mathrm{R}_{Pt} - {}^{c}\mathrm{r}_{Pt}}. \tag{3.6} $$

The error of cosputtered compositions inferred from single-source profiles is meaningfully quantified by the fractional deviation from the true cosputtered ratio,

$$ \frac{{}^{s}\chi - {}^{c}\chi}{{}^{s}\chi}. \tag{3.7} $$

Reflection of Ar neutrals: The dynamics of reflection of Ar neutrals are not calculated here but are extracted from semi-quantitative data in [17], which includes analysis of the DC sputtering of a Pb target with 500V applied. This work presents results of TRIM calculations of the fraction of Ar reflected from the Pb target and the energy spectrum of the reflected Ar as a function of reflection angle. For a given scattering angle within the scope of our substrate (see Figure 3.3), the energy profile (in units of the bombarding Ar energy) is approximately given by Figure 3.6. This scaled energy profile is used for Ar reflected from both Pb and Pt targets. The assumption that the energy spectrum from a Pt target will be similar to that of a Pb target follows from the argument that reflection ener-

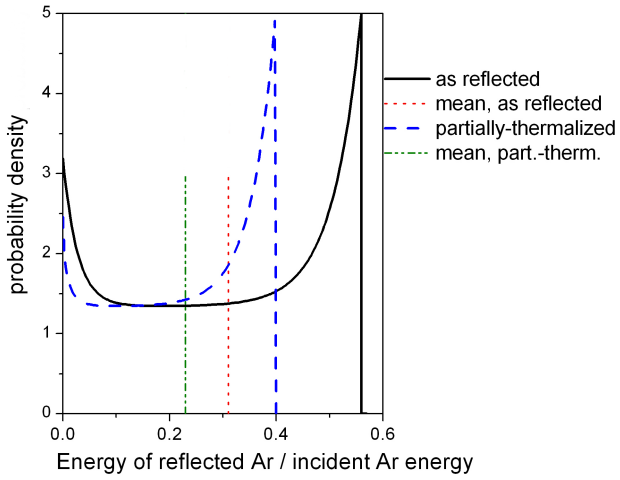

Figure 3.6: The probability density function of reflected Ar energy is plotted both at the surface of the target responsible for reflection and 5.3cm from the target, where the Ar has been partially thermalized by collisions with the background 5mT Ar. The mean energies of the two distributions are also noted.

getics are similar for any target with mass much greater than the inert projectile [45].

In the absence of scattering with a background gas, the ratio of energetic Ar departing the target at an angle γ to that of Pb ejected into γ is equal to the ratio of arrival rates at a corresponding substrate position,

$$ {}^{a}\mathrm{R}_{Ar-Pb} = \beta_{Pb}\, {}^{a}\mathrm{R}_{Pb}. \tag{3.8}$$

The simulation of Bauer, et al. [17] provides a total reflected Ar to sputtered Pb ratio (averaged over angles γ) of 0.247. While this value certainly varies with ejection direction γ, we invoke an isotropic approximation, using Equation 3.8 with β_{Pb}=0.247. We note that comparison of the semi-quantitative data for the Ar flux [17] and our measured Pb flux as functions of γ indicate that this approximation is reasonable for $25^\circ < \gamma < 55^\circ$, the approximate range that encloses our substrate. Despite the difference in sputtering voltage, we assume

that this value and the appropriately scaled distribution of Figure 3.6 sufficiently describe Ar reflection from our Pb target.

Simulations performed by Eckstein and Biersack [45] suggest that the reduced energy (Equation 3.17) and mass ratio parameterize both the probability for energetic reflection of incident Ar and the fraction of energy retained upon reflection. Their work indicates that the change in these parameters from our sputtering of Pt to that of Pb results in changes in the reflection probability and fraction of reflected energy that are less than 10%. Ignoring these small changes, since the sputter yield of Pt by Ar is a factor of 3.3 lower than Pb by Ar for the relevant operating voltages, the arrival rate of Ar at the Pt target must be higher than at the Pb target by this factor to remove an equal number of target atoms. We thus approximate β_{Pt}=3.3β_{Pb} and

$$ {}^{a}\mathrm{R}_{Ar-Pt} = \beta_{Pt}\, {}^{a}\mathrm{R}_{Pt}. \tag{3.9} $$

Energy spectra of sputtered Pb and Pt: The energy spectra of sputtered Pb and Pt (as they leave their respective targets) are assumed to be well described by the semiempirical energy distributions set forth in [157]. With Ar impinging at energy E_{Ar}, the probability density function for the energy E of sputtered atoms is proportional to

$$ \left(1 - \left(\frac{E_b + E}{m\, E_{Ar}}\right)^{1/2}\right) / \left(E^2 + \left(1 + \frac{E_b}{E}\right)^3\right), \tag{3.10} $$

where m is the energy transfer factor from collision theory and E_b is the binding energy of the sputtered materials. While the validity of this equation has not been extensively verified for Pb and Pt sputtered by Ar, it yields a most probable energy 3.8eV for Pt sputtered by 370eV Ar, which is a reasonable value given measured data in [151]. For comparison, the most probable energy for Pb sputtered by 320eV Ar is 2.2eV.

The distribution of Equation 3.10 allows for finite probability density at arbitrarily large E. We use a cutoff energy [17]

$$E_{max} = m\ E_{Ar} - E_b, \tag{3.11}$$

the maximum energy that could be transferred to a sputtered atom by an impinging atom according to linear cascade theory.

Thermalization of sputtered material and reflected Ar: As sputtered Pb and Pt atoms and reflected Ar travel from the targets to the substrate, collisions with the background Ar gas cause thermalization of these super-thermal species. This phenomenon has been treated by Monte Carlo simulations [112] that model collisions by picking the energy loss of the energetic atom and the scattering angle from appropriate distributions. For ease in calculation, we use the continuous energy loss model for gas phase scattering [60]. This model includes an energy loss per distance traveled that is proportional to the projectile velocity. Treating thermalization as the zero-point of projectile energy, the energy of a projectile a distance ρ away from the target is

$$E = (1 - \rho/\rho_{max})^2\ E_0 \tag{3.12}$$

where E_0 is the energy of the projectile leaving the target and ρ_{max} is the distance traveled by the projectile before thermalization,

$$\rho_{max} = AE_0^{1/2}. \tag{3.13}$$

For a given temperature T in K, Ar pressure p in Pa and Ar to projectile mass

number ratio M,

$$A = 0.012 \left(\frac{1 + 1/M}{M_{Ar}} \right) \left(1 + M^{2/3} \right)^{3/4} \frac{T}{p} \frac{cm}{eV^{1/2}}. \tag{3.14}$$

The scattering angles of Pb and Pt, which are much more massive than the thermal constituents (Ar), will be small. Thus, the continuous energy loss approximation, which neglects scattering angles, is reasonably applied to Pt and Pb. While the neglect of scattering angle is less appropriate for the thermalization of energetic Ar, the mean free path of Ar in our system is greater than the target-substrate distance. The implications of these approximations for the results of the following calculations are discussed in section 3.3.8.

The convolution of the above energy profiles, Equation 3.10 and Figure 3.6, with Equation 3.12 provides the energy distribution for the projectiles, $\Xi(E, \rho)$, where ρ is the distance from the appropriate target (see Figure 3.3). This distribution has a maximum energy $E_{max}(\rho)$ easily calculated with Equations. 3.11 and 3.12. It is worth noting that convolution of a probability distribution with Equation 3.12 does not preserve probability. The continuous energy loss model mandates that at non-vanishing ρ, some fraction of the projectile population has thermalized, and thus, the distribution describes only the fraction that remains energetic. Or equivalently, the full energy distribution is taken to be an energetic fraction

$$\int_0^{E_{max}(\rho)} \Xi(E, \rho) \; dE_B \tag{3.15}$$

and the (remaining) thermalized fraction that diffuses in the 5mT Ar atmosphere.

Figure 3.6 shows the evolution of the reflected Ar energy profile after thermalizing through 5.3cm travel from the target. At this point 29% of reflected Ar have thermalized and the remaining 71% have a mean energy significantly lower than the mean energy at ρ=0.

Sputter yields at the substrate: For the eight sputter yields of interest, we use the semi-empirical model set forth by Matsunami, et al. [105, 104] and recently discussed by Seah, et al. [132]. For an atom A with binding energy E_b, the threshold energy $E_{t,AB}$ for sputtering by projectile species B is

$$E_{t,AB} = E_b[0.08 + 0.164\,(M_A/M_B)^{0.4} + 0.0145(M_A/M_B)^{1.29}]. \tag{3.16}$$

The reduced energy ϵ for a collision by a projectile with energy E is given by

$$\epsilon = \frac{0.03255}{Z_A Z_B \left(Z_A^{2/3} + Z_B^{2/3}\right)^{1/2}} \frac{M_A}{M_A + M_B} E. \tag{3.17}$$

For the A-B combinations of interest, the sputter yield Y is given by

$$Y_{AB} \propto \frac{1}{E_{b,A}} \left(1 - \left(\frac{E_{t,AB}}{E}\right)^{1/2}\right)^{2.8}, \tag{3.18}$$

where the proportionality constant is a function of the reduced energy, elemental properties of A and B, and empirically determined coefficients. The proportionality constants used in this study were taken from [68].

Angle of substrate incidence: The above sputter yields (Equation 3.18) assume normal incidence. Neglecting changes in trajectory due to gas phase scattering, the angle of impact at a given substrate position is θ as drawn in Figure 3.3. While no data concerning the angular variation in sputter yields with Pb or Pt projectiles could be found in the literature, for Ar impinging on metal surfaces

with $\theta < 60°$, the yield has been shown to vary as $(\cos\theta)^{-1}$ [117]. This functional form for angular dependence is used for all sputter yields.

Effective sputter yield and resputter rates: While the yield of a projectile with known energy is given by Equation 3.18, the average yield of a projectile with energy distribution Ξ at substrate position (ρ, θ) is

$$\Upsilon_{AB}(\rho,\theta) = \int_{E_{t,AB}}^{E_{max}(\rho)} Y_{AB}(E)\ \Xi(E,\rho)\,(\cos\theta)^{-1}\,dE. \tag{3.19}$$

Then the arrival rate of X (X=Pt or Pb) is given by

$${}^{a}\mathrm{R}_X = {}^{s}\mathrm{R}_X\left(1 - \Upsilon_{XX} - \beta_X\,\Upsilon_{XAr-X}\right)^{-1}. \tag{3.20}$$

Using this equation, the molar rates determined by crystal monitor measurements are adjusted for intrinsic resputtering to provide arrival rates of Pt and Pb. Arrival rates for reflected Ar can then be obtained with (Equations. 3.8 and 3.9).

Surface concentration: The resputter rate of a given species at the substrate will be proportional to the probability P_X that an approaching projectile will impinge on that species. We approximate that the cross section for collision of the (low energy) projectiles and a Pt, Pb alloy monolayer is sufficiently high that sputtering of the Pt, Pb film occurs only from the first monolayer. The relative cross-section for collision with X in the first monolayer will be proportional to the concentration of X in that layer. Given the similar masses and atomic radii of Pb and Pt, we approximate the proportionality constant to be unity.

As alluded to in section 3.3.2, the surface concentrations of deposited species are not unity during codeposition. Neglecting the reflection of (low energy) Pb and Pt from the substrate surface, as a gas-phase metal atom approaches the

substrate, the probability P that it is a Pb atom is

$$ {}^{a}\mathrm{P}_{Pb} = \frac{{}^{a}\mathrm{R}_{Pb}}{{}^{a}\mathrm{R}_{Pb} + {}^{a}\mathrm{R}_{Pt}}. \tag{3.21} $$

This atom becomes a surface atom and remains so until it is covered by the next monolayer of material, at which point, in our approximation, it can no longer be resputtered. At this time, the probability that it is a Pb atom is given by

$$ {}^{c}\mathrm{P}_{Pb} = \frac{{}^{c}\mathrm{R}_{Pb}}{{}^{c}\mathrm{R}_{Pb} + {}^{c}\mathrm{R}_{Pt}}. \tag{3.22} $$

If the accessibility of the atom to projectiles is constant over the time spent as a surface atom, the time-averaged probability of a given projectile impinging on Pb and Pt are

$$ \mathrm{P}_{Pb} = \left({}^{a}\mathrm{P}_{Pb} + {}^{c}\mathrm{P}_{Pb}\right)/2, \ \mathrm{P}_{Pt} = 1 - \mathrm{P}_{Pb}. \tag{3.23} $$

Cosputtering resputter rates: The resputter rate of X from a given projectile is the product of P_X (Equation 3.23), the effective yield of the projectile (Equation 3.19), and the arrival rate of the projectile (Equations. 3.8,3.9,3.20). The absolute resputter rate of X is the sum of the sputter rates from each projectile:

$$ {}^{a}\mathrm{R}_X - {}^{c}\mathrm{R}_X = \mathrm{P}_X \sum, \text{ with } \sum = \sum_B \Upsilon_{XB} \, {}^{a}\mathrm{R}_B. \tag{3.24} $$

For X=Pb, the solution is

$$ \begin{aligned} 2 \, {}^{c}\mathrm{R}_{Pb} = {}^{a}\mathrm{R}_{Pb} - {}^{c}\mathrm{R}_{Pt} - (1 + {}^{a}\mathrm{P}_{Pb}) \sum \\ + \Bigg[\left({}^{c}\mathrm{R}_{Pt} - {}^{a}\mathrm{R}_{Pb} + (1 + {}^{a}\mathrm{P}_{Pb}) \sum \right)^2 \\ - 4 \left({}^{a}\mathrm{P}_{Pb} \sum - {}^{a}\mathrm{R}_{Pb} \right) \Bigg]^{1/2}. \end{aligned} \tag{3.25} $$

The equation for ${}^{c}\mathrm{R}_{Pt}$ is given by interchanging the element symbols. This system of equations can be solved in closed form, yielding expressions for the accumulation rates during cosputtering.

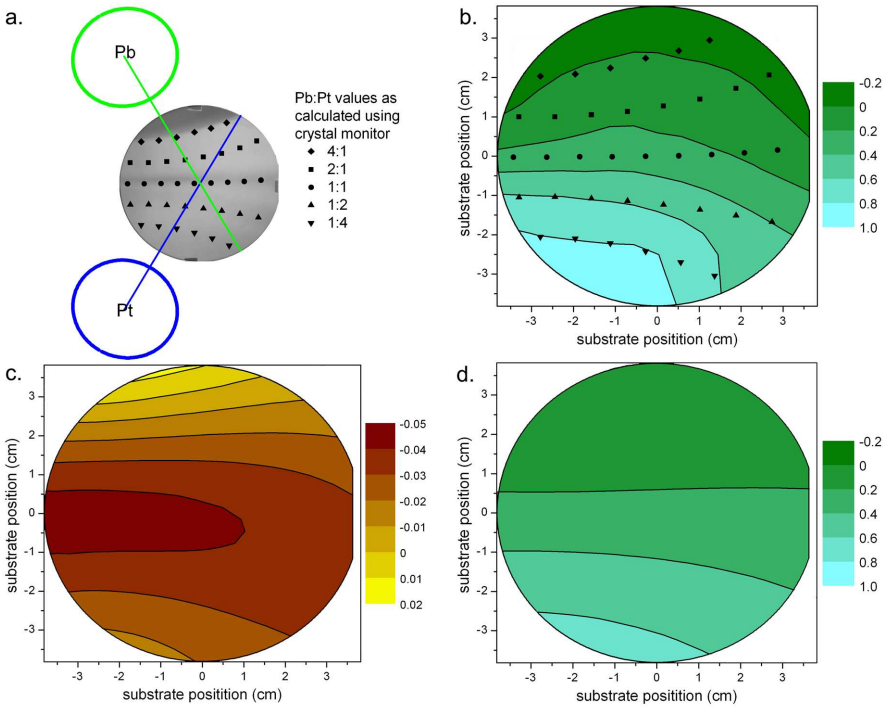

Figure 3.7: a. The positions of the 27 WDS measurements on the Pt, Pb composition spread are shown and categorized by the nominal stoichiometries determined from crystal monitor data. The substrate image is a photograph of the sputtered composition spread. Dark regions indicative of surface roughness coincide with compositional contours. The positions of the two 2in. targets are also shown as well as their axes in the substrate plane. b. The fractional difference in atomic ratio Pb:Pt between crystal monitor measurements and WDS measurements (Equation 3.7) is plotted in the outline of the substrate. c. The fraction of Pt single-source accumulation rate that becomes resputter rate due to codeposition is calculated and can be compared with d. Negative values correspond to cosputter accumulation rates that exceed those of single-source sputtering. d. Using calculated values of ${}^{c}\chi$ (see section 3.3.6), values of Equation 3.7 are plotted for comparison with b.

Results of calculated resputter rates in Pt, Pb codeposition

The calculated cosputter accumulation rates (Equation 3.25) and crystal monitor data are used to calculate the fractional loss in Pb:Pt due to cosputtering (Equa-

tion 3.7), yielding the contour plot of Figure 3.7d. For the 21 data points with highest Pb concentration (excluding the bottom row of points in Figure 3.7a), our simulations produce the WDS measured Pb:Pt values with an average absolute error of 13%, compared to the error of 45% using the raw crystal monitor data. For the six points with crystal monitor Pb:Pt values of 25%, the calculations predict a Pb:Pt value of 12% while the measured value is 6%. That is, the calculations correctly predict that a large fraction of the Pb will be resputtered from the film during codeposition, but the magnitude is not large enough to correctly produce WDS values.

Relative yields of different projectiles: The effective yields (Equation 3.19) of the four projectiles on both pure Pb and Pt surfaces are given as a function of substrate position in Figure 3.8. Our calculations indicate that the Ar projectiles have far higher yields, but we note that arrival rates are not included in this comparison.

The WDS data of Figure 3.7b clearly suggests that Pb is being preferentially removed from the substrate in a way that correlates to distance from the Pt source. A question of interest is whether Pt projectiles or Ar reflected from Pt are the cause for this removal. The ratio of the Pb resputter rates of these two projectiles is given in Figure 3.9, which shows that Pb resputtering due to Ar reflected from Pt is dominant.

Enhancement of accumulation rate due to codeposition: The effective resputter rate due to cosputtering, ${}^{c}\mathrm{r}$, can be negative. Suppose the projectiles from the source of element X are the dominant resputter projectiles in codeposition. Due to the reduced probability for projectile collision with X on the growing film's surface (compared to the unity probability of single source deposition), codepo-

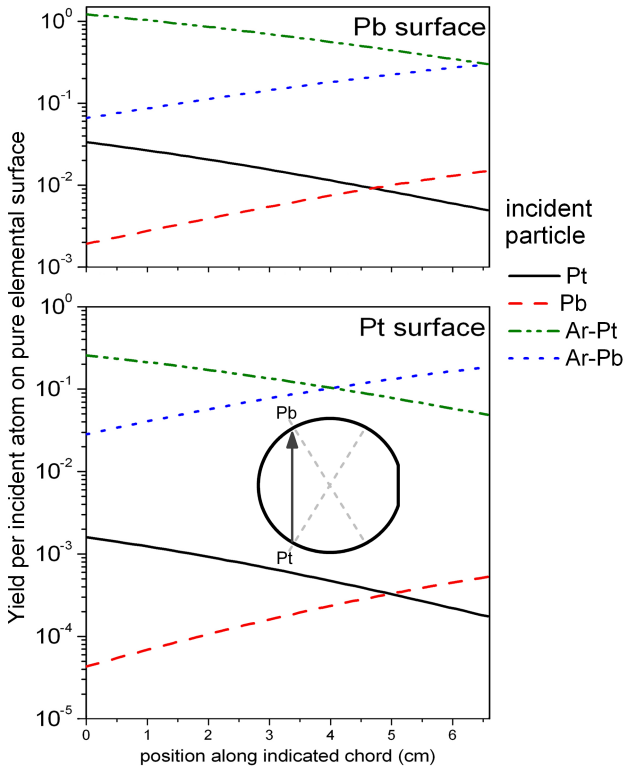

Figure 3.8: The effective yields (Equation 3.19) for the four projectiles in Pt, Pb codeposition are shown for both pure Pb and pure Pt surfaces. The yields are plotted as a function of position on the substrate line connecting the point closest to the Pt target and point closest to the Pb target. The inset gives a graphical representation of this line.

sition may result in a higher accumulation rate of X, that is ${}^{s}\mathrm{R}_X < {}^{c}\mathrm{R}_X < {}^{a}\mathrm{R}_X$. In our Pt, Pb codeposition, the calculations indicate this is the case for Pt over most of the substrate. A contour plot of ${}^{c}\mathrm{r}_{Pt}/{}^{s}\mathrm{R}_{Pt}$ is given in Figure 3.7c.

Note on Pb resputter fraction: Figure 3.7c demonstrates that

$$\left| \frac{{}^{c}\mathrm{r}_{Pt}}{{}^{s}\mathrm{R}_{Pt}} \right| \ll 1, \tag{3.26}$$

i.e. cosputtering with Pb has little effect on the net accumulation of Pt. In this

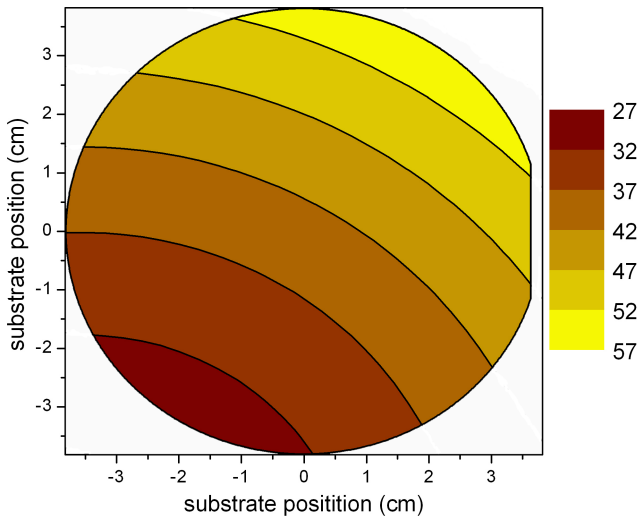

Figure 3.9: The ratio of the resputter rate of Pb by Ar-Pt during the Pt, Pb codeposition to that of Pb by Pt is plotted across the substrate, demonstrating that Ar-Pt is the projectile more responsible for Pb depletion in the film.

limit, Equation 3.7 can be written in an illuminating form,

$$\frac{{}^{s}\chi - {}^{c}\chi}{{}^{s}\chi} = 1 - \frac{1 - {}^{c}\mathrm{r}_{Pb}/{}^{s}\mathrm{R}_{Pb}}{1 - {}^{c}\mathrm{r}_{Pt}/{}^{s}\mathrm{R}_{Pt}} \approx \frac{{}^{c}\mathrm{r}_{Pb}}{{}^{s}\mathrm{R}_{Pb}}. \tag{3.27}$$

That is, ignoring the changes in the resputtering of Pt due to cosputtering, Figures 3.7b and 3.7d give values of the fraction of single-source Pb accumulation that is resputtered due to codeposition. Figures 3.7c and 3.7d can thus be compared to demonstrate the extent to which the magnitude of codeposition-specific resputtering of Pb exceeds that of Pt.

Temperature dependence of resputtering phenomena in codeposition: Figure 3.10 indicates that increasing the substrate temperature from 60°C to 200°C results in negligible differences in resputtering phenomena over most of the substrate. The measured differences do not monotonically correlate with the arrival rate of any of the projectile species in our model. We note that a modification

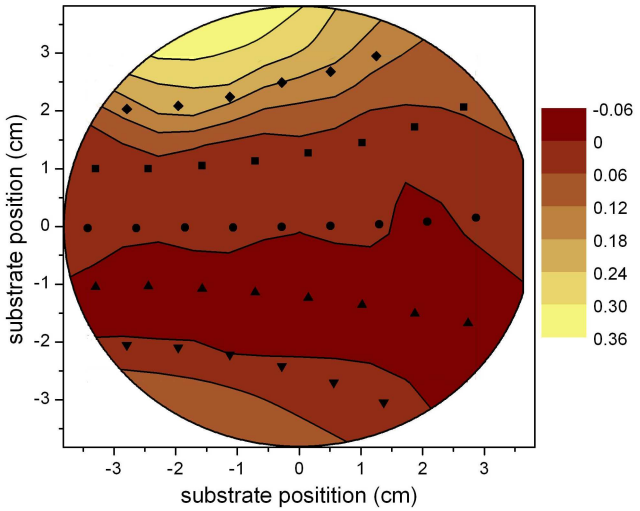

Figure 3.10: WDS-determined values for Equation 3.7 for a Pt, Pb composition spread film deposited on a 200°C substrate are subtracted by the data in 3.7b. and plotted in the outline of the substrate. The magnitude of this difference is indicative of the importance of increased substrate temperature in codeposited film composition for our Pt, Pb system. The negative values correspond to an increase in Pb concentration with elevated substrate temperature but are within the measurement error and reproducibility limits of sputter conditions.

of our model to explain higher temperature depositions may be necessary, especially for Pb-rich film compositions. While we do not offer an alteration to the model here, we suggest that the cause for a temperature dependence in this temperature range is due to an increase in the probability of surface Pb atoms to have an appreciable thermal energy (vis a vis the threshold for sputtering) as governed by Boltzman statistics. That is, as the rate of spontaneous desorption (evaporation) becomes significant, even low energy projectiles can stimulate desorption (resputtering). While the yields for fcc polycrystalline targets were found to be independent of substrate temperature with ion bombardment in the keV range [25], the thermal energy effect will be amplified for lower energy projectiles. Further discussion of temperature dependence in resputtering

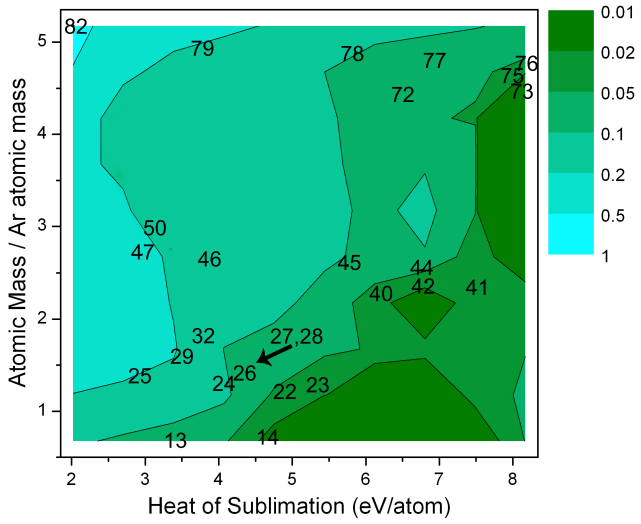

Figure 3.11: Using the resputtering model of Sec. 3.3.6, the effective yield (Equation 3.19) of Ar-Pt impinging the substrate center is plotted in contours as a function of mass ratio and heat of sublimation for 27 commonly sputtered elements. The atomic numbers of the elements are used to identify their approximate positions on the graph.

from multicomponent films can be found in [20, 72, 46].

3.3.7 Resputter Yield of Ar reflected from Pt for 27 elements

To illustrate significant parameters in determining the magnitude of resputtering phenomena in codeposition, the total sputter yield $\Upsilon_{Ar-Pt,X}$ was calculated for 27 commonly sputtered elements X. The energy spectra, gas scattering, etc. of section 3.3.6 were used and Equation 3.19 was evaluated at substrate center. The results are plotted in Figure 3.11 which shows that the heat of sublimation of the elements is a governing factor in determining susceptibility to resputtering. This figure can be used as an indicator of the inability of the crystal monitor (or other single-source sputter profile) data to predict stoichiometry of

codeposited films when the deposition includes an element with Ar reflection dynamics similar to those of Pt.

3.3.8 Discussion

Pd,Pt,Ti composition spread

The Pd,Pt,Ti system can be treated in the same detail as the Pt, Pb system upon determining an energy spectrum and probability for the reflection of Ar from Pd and Ti targets. The simulations of Eckstein and Biersack [45] can be used to estimate the reflection probability and average reflected energy of Ar from the respective targets. With its lower mass and slightly higher reduced energy for comparable molar deposition rates, the reflection probability of Ar from Pd should be less than 70% and the average reflected energy less than 50% of the values for Pt. Also, the yield of Pd by Ar is higher than the yield of Pt at the respective operating voltages, so the number of Ar impinging the respective targets will be lower for Pd for a given equal (single source) molar deposition rate.

Although the reduced energy (Equation 3.17) required to achieve the desired molar rate from Ti is high due its low sputter yield by Ar, the low Ti to Ar mass ratio results in an estimated Ar reflection probability of 20% of that of Pt and an average absolute reflected energy of 0.1%.

Using the same Pt energy spectrum as above, we calculate the total yields (Equation 3.19) for Pt sputtering Pd and Ti to be $< 10^{-3}$ and $< 10^{-5}$ across the substrate. The other metal-metal resputtering phenomena in this system are

equally insignificant and thus we conclude that for the Pd,Pt,Ti system, the only significant resputtering phenomena are those with Ar-Pt as projectile.

We calculate the total yields for Ar-Pt sputtering Pb to be about 3 times higher than for Pd and 17 times higher than for Ti and thus conclude that resputtering phenomena associated with cosputtering are far less important for this system compared to the Pt, Pb system, as the EDS and WDS measurements confirm.

In the Pd-rich region (see Figure 3.4), the point with the largest deviation (Equation 3.5) is one for which crystal monitor data provides a Pd:Pt:Ti of 10.7:75.6:13.7 while the measured EDS values are 7:80:13. Adjusting crystal monitor data by including Ar-Pt sputtering of Pd with Pd surface sputter probability (Equation 3.23) approximated by crystal monitor Pd concentration gives Pd:Pt:Ti=8.5:77.4:14.0. While the error (Equation 3.5) of the crystal monitor data in producing this EDS measurement is 5.8%, this single adjustment reduces the error to 3.2%. We thus conclude that our model of resputtering phenomena in codeposition reliably describes the observed shortcomings of the determination of film compositions using crystal monitor data in the Pd,Pt,Ti system.

Implications of resputter model approximations in the Pt, Pb system

As noted in section 3.3.6, the mean free path for nearly the entire Ar projectile energy spectrum exceeds all target-substrate distances. The application of the continuous energy loss model eliminates the substrate impingement by the highest energy Ar projectiles. These projectiles have significant yields for both Pt and Pb and we expect that as a result, the data in Figure 3.8 are an underes-

timate for the effective Ar resputter yields. We also note that the magnitude of this effect varies with substrate position due to changing target-substrate distance.

Our use of the Thompson model [157] for the energy distribution of atoms ejected from the target neglects any variation with ejection direction. Stuart, Wehner, and Anderson [151, 152] found an increase in ejection energy with increasing ejection angle. The simulations of Mahieu, et al. [101] for Zr sputtered by 400eV Ar showed that the most probable ejection angles for the highest energy sputtered material are between 35° and 60°, the range of sputtering angles that cover our substrates. An upward shift in Pb and Pt energy distributions would increase the yields from these projectiles. However, the yields would remain much smaller than those of Ar projectiles (see Figure 3.8).

The energy spectrum of reflected Ar also changes as a function of angle γ from target normal. The calculations of Bauer, et al. [17] show that, for large γ, this energy spectrum has a higher density near the maximum energy shown in Figure 3.6.

The model for the energy threshold for sputtering (Equation 3.16) assumes normal incidence. Wehner [175] finds that the threshold energy for sputtering decreases with more oblique incidence. While we neglect this θ dependence, it may significantly increase the effective sputter yields for all projectiles by widening the interval of integration in Equation 3.19.

While the combination of these approximations may affect the magnitude of resputtering, the collective potential of neglected anisotropies to alter the gradients of resputter rates across the substrate is more significant. Thus the higher

density of contour lines in the measured data of Figure 3.7b compared to the calculated data of Figure 3.7d is not surprising.

Our final note on approximations is that the absolute sputter yields obtained from [105, 68] carry significant yet unquantified uncertainties. Our calculated resputter rates are directly proportional to these yields and thus our calculated results carry these significant uncertainties.

Interactions in the growing film

Other phenomena in codeposition that could be important for resputtering are diffusion of species in the film to the film surface as it is deposited and shifts in the binding energy of surface atoms due to atomic interactions in the film. While we do not include these phenomena in the above model, notes on their significance in the Pt, Pb system and in general codeposition are provided as supplemental information 3.4. These notes include discussion of the negative values of Figure 3.7b and additional resputter calculation data. The role of diffusion has previously been discussed in the context of resputtering [72, 46, 20].

Applicability to other deposition systems

Since the sputter geometry plays such an important role in resputter phenomena, the absolute resputter rates will vary significantly amongst deposition systems. Our treatment of resputtering and the overall calculated susceptibility to resputtering (Figure 3.11) are more system independent.

Beyond deposition geometry, other deposition parameters (e.g. type and

pressure of inert gas, target voltages in magnetron sputtering or accelerating voltages in ion beam sputtering) can significantly affect resputtering phenomena. These parameters are included in the model outlined in section 3.3.6. Provided availability of a sputter yield for each projectile-film constituent combination (or proportionality constant in Equation 3.18) and initial energy distribution for reflected inert neutrals, this model can be applied to estimate resputtering rates in any codeposition experiment. While the profile used in the present work (Figure 3.6) was obtained from TRIM calculations of [17], targets with different reflection dynamics [45] may require similarly calculated profiles.

3.3.9 Conclusions

Single-source profiling can be an effective tool for determining compositions in multi-gun sputtering. This is particularly useful for high-throughput studies, in which measurements of composition of every location on a composition spread film would be expensive in time and effort. For the codeposition of some sets of elements, modeling film growth as the simple addition of individual rates can lead to significant errors. We have demonstrated that resputtering phenomena account for most of these errors and have developed a model that incorporates the most important effects. While our model includes several approximations which can easily be improved, it provides sufficiently accurate results to demonstrate the primary causes of resputtering in the Pt, Pb system and to provide a framework for determining the importance of these phenomena in other codeposition systems. With the use of this model, compositions can be calculated with an accuracy of a few atomic percent, which is comparable to the best routine absolute composition measurements for thin films.

3.3.10 Acknowledgments

The WDS analysis was made possible by the Cornell Center for Materials Research Facilities supported by the National Science Foundation under Award Number DMR-0520404. Primary funding for this work is provided by the Department of Energy, Grant No. DE-FG02-03ER46072.

3.4 *Supplementary information:* Resputtering phenomena and determination of composition in codeposited films

3.4.1 Shifts in binding energy

Multi-component resputtering with immiscible elements involves a film surface that microscopically is either one pure metal or the other. The failure of the metals to alloy leaves their binding energies unchanged from bulk values. While alterations in binding energy are excluded from the above calculations, we note their importance for resputtering phenomena.

Shifts in binding energies can be calculated using Miedema [106, 114]. The Miedema models provide the enthalpy of formation of a bulk intermetallic phase starting from the individual bulk solids. The change in binding energy of a single X atom is the enthalpy of formation of the product intermetallic phase divided by the number of X atoms required to form that product.

If sputtered material form the thermodynamic equilibrium phases as they are deposited, the binding energies of surface atoms will shift. A projectile will

impinge on a crystalline grain with probability determined by the concentration of that crystalline phase (see Figure 3.12). Within that grain, the probability of hitting an atom of a given type is determined by the stoichiometry of that ordered phase. With the product of these probabilities, the sputtering yield can be calculated using the binding energy for the species of interest in that phase.

To demonstrate the potential impact of these shifts in binding energy, calculated resputter rates of Pb by Ar-Pt are presented in Figure 3.13. The binding energies of Figure 3.12 used in Figure 3.13 are for bulk ordered phases. Since binding energy shifts of surface atoms in a given ordered structure are less than those of bulk atoms, Figure 3.13 demonstrates an upper limit on the shift in resputter rates due to binding energy shifts.

In the main paper we present WDS data that, for a small region of the film, indicates an increase in Pb concentration due to cosputtering (negative region of Figure 6b). While a number of measurement errors could have caused these negative values, their existence may be explained by our resputtering model appended by the above discussion on binding energy. In this region, Figure 7 (in the main paper) shows that Ar-Pt and Ar-Pb have comparable yields for sputtering Pb, but the arrival rate of Ar-Pb is much greater due to proximity to the Pb target. Thus, sputtering of Pb by Ar-Pb is dominant in this region and is also present in single-source sputtering. The presence of 10at% Pt in this region may form Pb_4Pt crystallites, increasing the binding energy and reducing the sputter yield for a significant fraction of the Pb being deposited. The result is a slight enhancement in the accumulation rate of Pb in this region compared to single-source sputtering.

3.4.2 Diffusion

The arguments used to determine surface concentration in section VB7 (in the main paper) assume zero diffusion of bulk sputtered species to the surface. With cosputtered species that have different surface energies and in the limit of low deposition rate compared to diffusion rate, this diffusion can significantly alter relative resputter rates.

Since Pb and Pt are fcc metals with lattice constant $a \approx 4.4\mathring{A}$, the nominal inter-plane spacing is $a/4^{1/3}$ and the nominal area per atom is $a^2/4^{2/3}$. With a deposition rate of 4 nmoles/s cm^2, the diffusion constant necessary for the diffusion rate to equal the film growth rate is 1.5 10^{-15} cm^2/s.

The surface energy of pure Pb is lower than any of the thermodynamic equilibrium phases or phases mixtures in the Pt, Pb system. Thus, if Pb is able to diffuse to the surface, it will tend to remain there, making the surface Pb rich. This increases the Pb resputter rate and decreases the Pt resputter rate, making the bulk film more Pt rich.

While the 60°C polycrystalline bulk diffusion constant of Pb is a factor of a 100 smaller than the nominal critical value of 1.5 10^{-15} cm^2/s, the value at 200°C is a factor of 1000 larger [140]. Thus, while diffusion is appropriately excluded from our calculations, it may be an important phenomenon in determining film stoichiometry in some deposition scenarios. We also note that alloying and formation of ordered phases as discussed in the previous section will increase the activation energy for diffusion and greatly reduce diffusion rates.

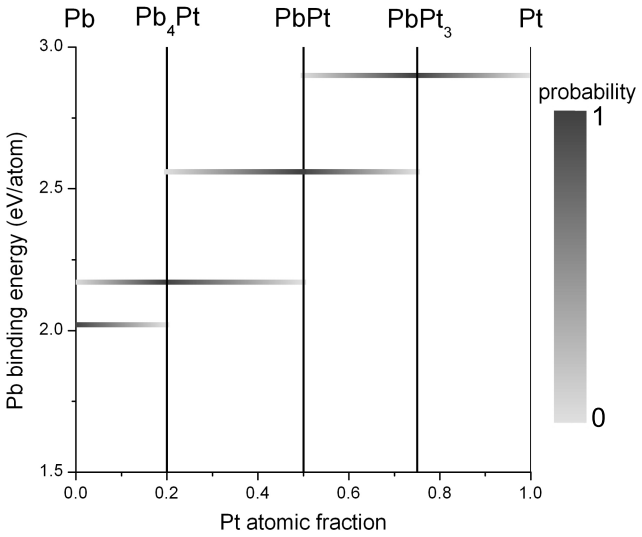

Figure 3.12: The binding energy of Pb in bulk Pt, Pb alloy in thermodynamic equilibrium. Multiple values at given stoichiometry are due to different Pb binding energies in coexisting phases. The binding energy plots are drawn in grayscale representing the concentration of the appropriate Pb-containing phase at the given stoichiometry

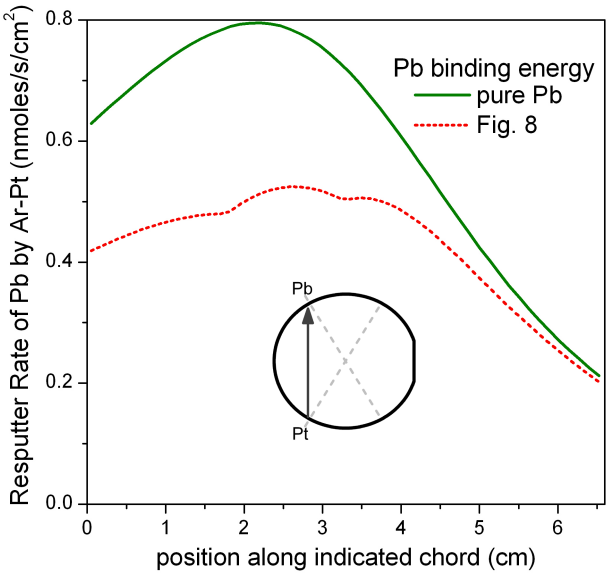

Figure 3.13: The total molar resputter rate of Pb from the substrate during codeposition is shown as a function of substrate position using the binding energy of pure Pb and the binding energy of Pb in the composition-dependent bulk equilibrium phase.

3.5 *Manuscript:* A model for calculating resputter rates in codeposition

3.5.1 Abstract

The ability to calculate composition in composition spread thin films is a powerful tool in combinatorial research. This ability is pivotal in high throughput studies, where the time and effort required to determine elemental compositions using standard techniques can be prohibitive. Calculating codeposited film composition from single-source deposition profiles requires a model for film growth in codeposition. In DC magnetron sputtering, modeling film growth as the simple addition of individual rates can lead to significant errors, primarily due to resputtering of film atoms by energetically reflected gas atoms. We develop a model which includes the definition of a resputter coefficient that is used to calculate resputtering rates in the codeposition of an arbitrary number of sources. The accuracy of the model is demonstrated for the codeposition of Pt and Pb. In the development of the model, useful parameterizations of fundamental quantities of sputter dynamics are presented, and we also present tabulated values of the resputter coefficient for 27 commonly sputtered elements at select voltages.

3.5.2 Introduction

The synthesis of combinatorial libraries of inorganic materials is an increasingly popular technique employed in materials optimization and discovery. Depo-

sition of thin film composition spreads from multiple sources is an attractive technique for creating such libraries as it allows for fabrication of the libraries in a high-throughput regime [71, 167]. In this paper we discuss the ability to determine elemental compositions in the thin film while minimizing the use of traditional characterization techniques that compromise the high-throughput nature of the study. Our discussion is carried out in the context of magnetron sputtering, which is an attractive deposition technique in combinatorial studies as it offers constant, comparable deposition rates for many elements [167].

In [62] we have presented a model for resputtering in the codeposition of Pt and Pb, discussed the applicability of our model to other deposition techniques, and placed our model in the context of the existing literature. The present work generalizes the model of [62] for codeposition of any set of metals.

In the deposition scenario at hand, an inert gas ion (e.g. Ar^+) is accelerated across the cathode dark space and bombards a biased metal target (cathode). The collisions eject target atoms and with some probability, the inert gas atom reflects as an energetic neutral atom. Positively charged ions that reflect from the target are decelerated across the cathode dark space and thus do not contribute to resputtering. The net result is a flux of target atoms and reflected gas atoms impinging the substrate. The surface dynamics of the accumulating (metal) species with the impinging species determines the bulk film composition, and to assist in the discussion of these interactions, we define symbols for the relevant molar rates in Table 3.1. Subscripts of these symbols will indicate the species whose rate is being referenced. All values of ${}^{a}\mathrm{R}$ for species from a given source are assumed to be independent of the operation of other sources.

During deposition from a single source, the deposited metal is partially re-

sputtered from the substrate by reflected gas neutrals and self-sputtering. These phenomena, collectively referred to as *intrinsic resputtering*[76], result in a positive intrinsic resputtering fraction $({}^{a}\mathrm{R} - {}^{s}\mathrm{R})/{}^{a}\mathrm{R}$.

In addition to this intrinsic resputtering, when targets are powered simultaneously, one depositing species can be resputtered by the other depositing species or by Ar neutrals reflected off the other target(s). Also, resputter rates from intrinsic phenomena may be significantly altered by the coexistence of multiple species on the growing film's surface. These phenomena do not occur in single-source deposition and result in cosputter accumulation rates ${}^{c}\mathrm{R} = {}^{s}\mathrm{R} - {}^{c}\mathrm{r}$. In [62] we demonstrated that the metal-metal resputtering is small, and thus in the present work we consider only the reflected gas atom contribution to ${}^{c}\mathrm{r}$.

Inert gas atoms reflected from different sources must be treated as different projectiles as their energy distributions will depend on the target material and sputtering voltage. Thus, with codeposition from n single element sources, n species accumulate on the substrate with n^2 resputtering phenomena (involving reflected inert gas) occurring at the growing film's surface. While intrinsic resputtering occurs at a film surface with unity surface concentration, the film surface in cosputtering has a finite concentration of all n elements. Given these considerations, we develop a model for calculating the resputter rates of the n^2 phenomena, assuming single-element sputter targets and an Ar sputter gas.

3.5.3 Deposition geometry and in-situ measurements of single source deposition profiles

The deposition system, described previously [67], contains three 2 in. magnetron sources positioned symmetrically with respect to the substrate such that the targets are centered 8.3cm from substrate center, 4.2cm out of the substrate plane and also confocally tilted 15° from substrate parallel (Figure 3.3). For the source depicted in the figure, the majority of sputtered material is ejected from the ring whose cross section is drawn on the target. For ease in calculation, we approximate that atoms leave target X at an angle γ_X, travel a distance ρ_X to a substrate point and impinge at an angle θ_X=γ_X+15° from substrate normal.

During the operation of a single source, a crystal deposition monitor can be moved across the deposition region, measuring mass accumulation rates at different positions. The corresponding ${}^{s}\mathrm{R}$ values are fit to an empirical function, providing the single-source deposition profile for the given target-source combination. To establish the validity of this method, fitted profiles were compared to film thickness measurements performed on a thickness spread thin film using wave dispersive spectroscopy (WDS). The crystal monitor data and fitting routines were found to reproduce the WDS thickness measurements to within a few percent.

3.5.4 A model for resputtering by reflected Ar in codeposition

For commonly sputtered elements X, the yield $Y(E)$ of Ar projectiles with energy E have been tabulated [68]. The yield is zero below a threshold energy

$E_{t;X,Ar}$ and will have a dependence on Ar incident angle θ (usually taken to be $1/\cos\theta$) [117] that we ignore at this time. If the Ar energy has a probability distribution Ξ with vanishing probability for energies above E_{max}, we define the effective yield of X by Ar,

$$\Upsilon_{X,Ar} = \int_{E_{t;X,Ar}}^{E_{max}} Y_{X,Ar}(E)\, \Xi(E)\, dE. \tag{3.28}$$

The primary position dependences in this equation arise from the fact that Ar arriving at a given substrate position will have a unique energy distribution due to both variations in reflected energy as a function of angle from target normal and scattering with the Ar sputter atmosphere. The sputtering of X by $Ar - X$ in single-source sputtering corresponds to an arrival rate of X that exceeds the accumulation rate. Given the ratio β_X such that arrival rate of $Ar - X$ is

$${}^{a}\mathrm{R}_{Ar-X} = \beta_X\, {}^{a}\mathrm{R}_X, \tag{3.29}$$

the arrival rate of X can be written in terms of the single-source accumulation rate,

$${}^{a}\mathrm{R}_X = {}^{s}\mathrm{R}_X \left(1 - \beta_X\, \Upsilon_{X,Ar-X}\right)^{-1}. \tag{3.30}$$

We note that β_X has a substrate position dependence that we discuss in Sec. 3.5.4.

In the codeposition of A and B, A arriving at the substrate can be resputtered by both $Ar - A$ and $Ar - B$. The Ar impinging the substrate will strike A with a probability P_A, resulting in a total resputter rate of A

$${}^{a}\mathrm{R}_A - {}^{c}\mathrm{R}_A = \mathrm{P}_A \left(\Upsilon_{A,Ar-A}\, {}^{a}\mathrm{R}_{Ar-A} + \Upsilon_{A,Ar-B}\, {}^{a}\mathrm{R}_{Ar-B}\right). \tag{3.31}$$

Using Equations. 3.29, 3.30 and 3.31, the effective resputter rate of A due to codeposition with B is

$${}^{c}\mathrm{r}_A = {}^{s}\mathrm{R}_A - {}^{c}\mathrm{R}_A = {}^{s}\mathrm{R}_A \frac{-\left(1 - \mathrm{P}_A\right)\Upsilon_{A,Ar-A}\beta_A}{1 - \Upsilon_{A,Ar-A}\beta_A} + {}^{s}\mathrm{R}_B \frac{\mathrm{P}_A \Upsilon_{A,Ar-B}\beta_B}{1 - \Upsilon_{B,Ar-B}\beta_B}. \tag{3.32}$$

The first term of Equation 3.32 is the difference in the resputter rate of A by $Ar-A$ between single-source and multi-source deposition. Due to codeposition collision probability P_A that is less than the unity value of single-source deposition, this type of intrinsic resputtering is mitigated in codeposition. This term will vary as a function of substrate position primarily due to varying values of ${}^s\mathrm{R}_A$ and P_A. The values of $\Upsilon_{A,Ar-A}$ and β_A vary as functions of ρ_A and θ_A, which we treat by a single multiplicative function Ω_A=$\Omega\left(\rho_A, \theta_A\right)$. The second term of Equation 3.32 is the resputter rate of A by $Ar-B$ and carries analogous position dependences with respect to ρ_B and θ_B. The position dependence in each term is governed by system geometry (Figure 3.3) and scattering of reflected Ar with the background Ar atmosphere. Given the symmetric placement of the sources and similar Ar-Ar scattering dynamics over the energy range of interest, we assume the position dependence in the second term has the same form as that of the first term, Ω_B=$\Omega\left(\rho_B, \theta_B\right)$. This function is discussed further in Sec. 3.5.4.

Given Equation 3.32, it is useful to define the resputter coefficient

$$\Gamma_{A,B} = \frac{\Upsilon_{A,Ar-B}\ \beta_B}{1 - \Upsilon_{B,Ar-B}\ \beta_B}, \tag{3.33}$$

a nonnegative, unitless measure of the capacity of Ar reflected from B to resputter A. Equation 3.32 can then be rewritten

$${}^c\mathrm{r}_A = -\,{}^s\mathrm{R}_A\Omega_A\left(1-\mathrm{P}_A\right)\Gamma_{A,A} + {}^s\mathrm{R}_B\Omega_B\mathrm{P}_A\Gamma_{A,B}, \tag{3.34}$$

where we have included the additional position dependences discussed above.

Reflection of Ar neutrals: Simulations performed by Eckstein and Biersack [45] suggest that the probability for energetic reflection of Ar impinging target X ($_N\eta_X$) and the fraction of energy retained upon reflection ($_E\eta_X$) are well parameterized by the reduced energy of the collision (ϵ) and mass ratio. In [45],

plots of ${}_N\eta_X$ and ${}_E\eta_X$ resulting from TRIM calculations are presented as functions of these two parameters. We present the following closed form expressions for these parameterizations:

$$
\begin{aligned}
{}_N\eta_X &= 0.698\left(\frac{M_X}{M_{Ar}}\right)^{0.2} - 0.877\frac{\epsilon^{0.044}}{(M_X/M_{Ar})^{0.0428}} \\
{}_E\eta_X &= 0.0207\frac{M_X}{M_{Ar}} - 0.225\left(\frac{M_X}{M_{Ar}}\right)^{0.938}\epsilon^{0.0144}.
\end{aligned}
\tag{3.35}
$$

For the elements X of interest, $M_{Ar} < M_X < 5.5M_{Ar}$. For Ar energies between 200eV and 1000eV, this mass range implies 7x10$^{-4} < \epsilon < 10^{-2}$. For these ranges, Equations. 3.35 produce the calculated values to within 10%.

Assume that applying a voltage V_X (below chamber ground) to target X results in impingement by Ar of energy $e\,V_X$. This energy, and the mass of X give the energetic reflection probability ${}_N\eta_X$ (Equation 3.35). For a given substrate position, an arrival rate ${}^a\mathrm{R}_X$ requires a target impingement rate of ${}^a\mathrm{R}_X/Y_{X,Ar}(V_X)$. The probability distribution of the ejection direction of X and of the reflection direction of $Ar - X$ were found to have similar forms over the directions of interest for our substrate, with the probability density of Ar reflection into this angular range greater than that of X emission into this range [62, 17]. We thus approximate that the distributions differ only by a multiplicative factor, which for consistency with [62], we take to be 2.35. The arrival rate of X at position (ρ_X, θ_X) is proportional to the corresponding ejection probability for direction γ_X, allowing Equation 3.29 to be rewritten

$$
\beta_X = \frac{{}^a\mathrm{R}_{Ar-X}}{{}^a\mathrm{R}_X} = 2.35\,\frac{{}_N\eta_X}{Y_{X,Ar}(V_X)}. \tag{3.36}
$$

We note that the neglected differences in the ejection distributions of X and $Ar-X$ corresponds to a neglected θ_X dependence of β_X. Also, since scattering with the background gas alters the angle γ_X between substrate normal and substrate

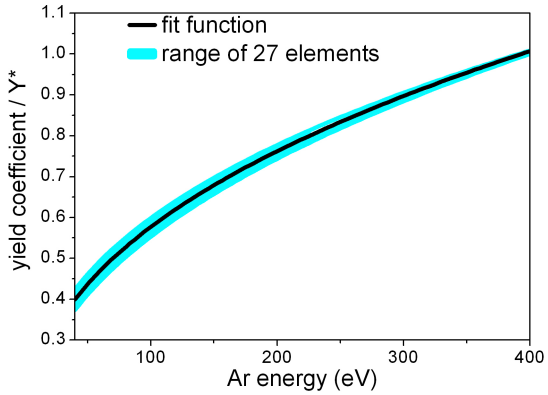

Figure 3.14: The range of values of Equation 3.40 for 27 commonly sputtered elements is represented by the shaded region. The best fit function $0.906E^{0.402}$ is overlaid.

impingement, differences in the scattering dynamics of X and Ar result in ρ_X and θ_X dependences that are ignored in Equation 3.36.

While ${}_E\eta_X$ (Equation 3.35) gives a nominal value for the fraction of energy retained by Ar upon reflection, the importance of the energy distribution of reflected Ar is noted in [62]. While this distribution will vary with target material X, we assume a functional form (Figure 3.6) used in [62] which is derived from the simulated reflection of Ar from a Pb target [17]. The free parameter in this distribution is the maximum energy, which we approximate

$$E_{max} = 0.56\, V_X \frac{{}_E\eta_X}{{}_E\eta_{Pb}}. \tag{3.37}$$

The constant prefactor follows from the calculated E_{max} in [17], the V_X factor follows from our assumption that the maximum Ar energy scales with the accelerating voltage and the ${}_E\eta$ ratio captures the changes in reflection dynamics for other elements X.

Effective yield: The sputter yield of X by Ar with energy E is given by

$$Y_{X,Ar} \propto \left(1 - \left(\frac{E_{t;X,Ar}}{E}\right)^{1/2}\right)^{2.8}, \tag{3.38}$$

where the proportionality constant is a function of the reduced energy, elemental properties of X and Ar, and empirically determined coefficients [105, 104]. The functional form of this proportionality (which includes expressions for stopping energies and the binding energy of X) is sufficiently complicated that for ease in calculation we offer the following parameterization of the sputter yield:

$$Y_{X,Ar} = 0.906\, Y_X^*\, E^{0.402} \left(1 - \left(\frac{E_{t;X,Ar}}{E}\right)^{1/2}\right)^{2.8}, \tag{3.39}$$

where Y_X^* is a coefficient chosen such that Equation 3.39 gives the tabulated value for the sputter yield of X by 400eV Ar. The values of this coefficient are easily obtained from Equation 3.39 and published sputter yield data [68]. This parameterization suggests that given the impinging element (Ar), the function

$$\frac{Y_{X,Ar}}{Y_X^* \left(1 - \left(\frac{E_{t;X,Ar}}{E}\right)^{1/2}\right)^{2.8}} \tag{3.40}$$

has a universal dependence on the impinging energy. Figure 3.14 demonstrates this universality and that Equation 3.39 produces yields to within a percent of tabulated values for the energy range of interest.

Given Equation 3.39, Equation 3.28 can be written as

$$\Upsilon_{X,Ar} = 0.906\, Y_X^* \int_{E_{t;X,Ar}}^{E_{max}} E^{0.402} \left(1 - \left(\frac{E_{t;X,Ar}}{E}\right)^{1/2}\right)^{2.8} \Xi\,(E)\, dE, \tag{3.41}$$

where E_{max} is given by Equation 3.37 and Ξ by Figure 3.6. The integral is well parameterized by

$$236\, e^{-\left(20.9 + E_{t;X,Ar}\right)^{0.529}} \left(E_{max}^{0.425} - 5\right)^{0.701 + 0.0328\, E_{t;X,Ar}}. \tag{3.42}$$

Resputtering of X is prominent in determining film composition when $E_{t;X,Ar}$ is small and E_{max} large. Figure 3.15 demonstrates that for the region of interest,

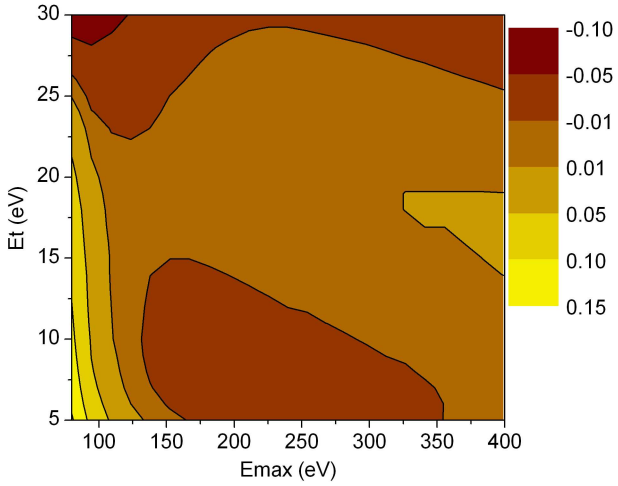

Figure 3.15: The fractional error of Equation 3.42 in producing the integral of Equation 3.28 is plotted in contours as a function of the two parameters. The error is negligible in the range of interest (high E_{max}, low E_t

.

this parameterization produces the numerical integration result to within a few percent.

Collision probability: Detailed analysis of the collision probability P_A, introduced in Equation 3.31, may lead to a functional expressions that includes properties of the cosputtered elements (see Sec. 3.5.6). We approximate this probability by the most intuitive function of single-source sputter rates:

$$\mathrm{P}_A = \frac{\mathrm{P}_A}{\sum_X \mathrm{P}_X}, \tag{3.43}$$

where the sum is over all elements X being codeposited.

Resputter coefficients

The resputter coefficient (Equation 3.33) can be written as a closed form function of basic elemental properties of A, B, and Ar; sputter yield constants $E_{t;A,Ar}$, Y^*_A,

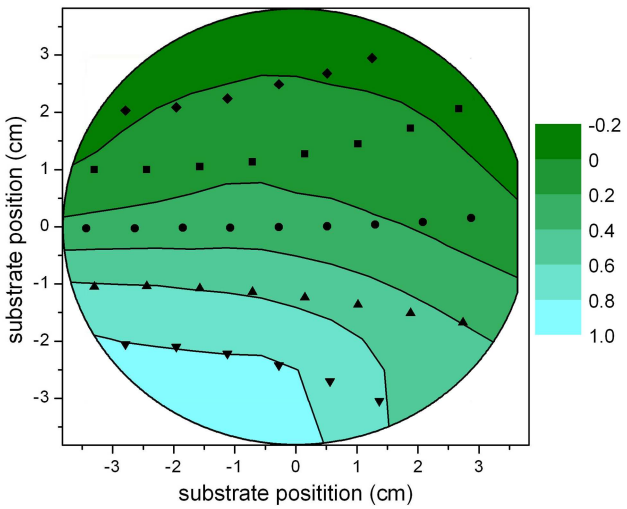

Figure 3.16: Using crystal monitor and WDS measurements, the fractional resputter rate of Pb due to codeposition with Pt is plotted within the outline of the wafer [62]. The atomic ratio is near unity at substrate center, and the WDS measurement locations are noted by the black points.

$E_{t;B,Ar}$ and Y_B^*; and the voltage applied to target B. Thus, given the target voltage, the susceptibility of resputtering of A when codeposited with B is quantified by the resputter coefficient $\Gamma_{A,B}$. Resputter coefficients for 27 commonly sputtered elements are given at two example target voltages in Table 3.2. A program for calculating the resputter coefficients at any target voltage is available [1].

Resputter rate variations as a function of substrate position

The remaining task is to quantify the variations of resputter rate with substrate position that not described by Equation 3.32, i.e. to find the function Ω of Equation 3.34. For the position dependences that need to be addressed, both ρ and θ are physically relevant variables. While these are independent variables, their relation over the region of space covered by the substrate (Figure 3.3) suggests

Table 3.2: Values of the resputter coefficient (Equation 3.33) for 18 commonly sputtered elements with the 8 targets with highest Z values are presented for target voltages of 250V (The published version contains 27 elements and additional 500V data). Resputter coefficients at these voltages for the 19 other targets are almost all less than 0.10.

resputtered	target at 250V							
element	Hf	Ta	Re	Os	Ir	Pt	Au	Pb
Cu	0.64	0.95	0.64	0.61	0.53	0.52	0.33	0.19
Ge	0.36	0.54	0.36	0.35	0.3	0.3	0.19	0.11
Zr	0.11	0.17	0.12	0.11	0.1	0.1	0.06	0.04
Nb	0.1	0.16	0.11	0.11	0.09	0.09	0.06	0.03
Mo	0.11	0.17	0.12	0.11	0.1	0.1	0.06	0.04
Ru	0.22	0.33	0.22	0.22	0.19	0.19	0.12	0.07
Rh	0.27	0.4	0.27	0.27	0.23	0.23	0.14	0.08
Pd	0.56	0.83	0.56	0.53	0.46	0.45	0.28	0.16
Ag	1.06	1.57	1.04	1.0	0.85	0.84	0.53	0.3
Sn	0.37	0.55	0.37	0.35	0.3	0.3	0.19	0.11
Hf	0.13	0.2	0.14	0.13	0.11	0.11	0.07	0.04
Ta	0.08	0.12	0.08	0.08	0.07	0.07	0.04	0.03
Re	0.13	0.19	0.13	0.13	0.11	0.11	0.07	0.04
Os	0.14	0.21	0.15	0.14	0.12	0.13	0.08	0.05
Ir	0.2	0.3	0.21	0.2	0.17	0.17	0.11	0.06
Pt	0.25	0.37	0.25	0.25	0.21	0.21	0.13	0.08
Au	0.58	0.86	0.58	0.55	0.47	0.47	0.29	0.17
Pb	1.71	2.52	1.67	1.58	1.35	1.33	0.83	0.47

that the position dependences may be well quantified as a function of a single variable.

To determine $\Omega(\rho)$, we use the example Pb, Pt system of [62]. The primary resputtering event in the codeposition of Pb and Pt is the removal of Pb from the growing film by incident reflected Ar. We thus apply the above discussion with A=Pb and B=Pt. The atomic ratio Pb:Pt of a codeposited binary composition spread was determined by WDS measurements at 27 substrate positions. For a given measurement,

$$ {}^{c}\chi = \frac{{}^{c}\mathrm{R}_{Pb}}{{}^{c}\mathrm{R}_{Pt}} \approx \frac{{}^{s}\mathrm{R}_{Pb} - {}^{c}\mathrm{r}_{Pb}}{{}^{s}\mathrm{R}_{Pt}}. \tag{3.44} $$

Values of the single-source accumulation rate are obtained from single-source deposition profiles (Sec. 3.5.3), allowing for the calculation of ${}^{c}\mathrm{r}_{Pb}$ at 27 substrate positions. The measured fractional Pb resputter rate (${}^{c}\mathrm{r}_{Pb}/{}^{s}\mathrm{R}_{Pb}$) is plotted in Figure 3.16b. The linear fit for $\Omega(\rho)$ that minimizes the mean squared difference between the data in Figure 3.16b and the Pb resputter fraction calculated using Equation 3.34 is

$$ \Omega = 1.91 - 0.155\rho/\mathrm{cm}. \tag{3.45} $$

Least squares fitting with higher order polynomials yields neither insight into the physics nor significantly reduced fitting error.

Numerical results

The Pb:Pt ratio (${}^{c}\chi$) and at%Pb can be directly inferred from single-source profiles,

$$
\begin{aligned}
{}^{c}\chi &= \frac{{}^{s}\mathrm{R}_{Pb}}{{}^{s}\mathrm{R}_{Pt}} \\
\mathrm{at\%Pb} &= \frac{{}^{s}\mathrm{R}_{Pb}}{{}^{s}\mathrm{R}_{Pb} + {}^{s}\mathrm{R}_{Pt}},
\end{aligned}
\tag{3.46}
$$

or corrected for resputtering of Pb using Equations. 3.34 and 3.45,

$$
\begin{aligned}
{}^{c}\chi &= \frac{{}^{s}\mathrm{R}_{Pb} - {}^{c}\mathrm{r}_{A}}{{}^{s}\mathrm{R}_{Pt}} \\
\mathrm{at\%Pb} &= \frac{{}^{s}\mathrm{R}_{Pb} - {}^{c}\mathrm{r}_{A}}{{}^{s}\mathrm{R}_{Pb} - {}^{c}\mathrm{r}_{A} + {}^{s}\mathrm{R}_{Pt}}.
\end{aligned}
\tag{3.47}
$$

For producing the WDS values of ${}^{c}\chi$, Equation 3.46 has an average absolute error of 96% which is reduced to 8.6% by using Equation 3.47. These errors are dominated by regions of the film with low Pb content for which Equation 3.46 overestimates Pb content by a maximum factor of 5.1 while Equation 3.47 overestimates by a maximum factor of 1.1. The average absolute difference in at%Pb values from WDS measurements and from Equation 3.46 is 8.4at% with a maximum difference of 18.7at%. Equation 3.47 reduces these differences to 1.1at% and 4.2at%, respectively.

3.5.5 Algorithm for calculating film composition in many-source deposition

In codeposition from n targets B, for each film constituent A, resputtering may significantly alter film composition given an appreciable value of any of the resputtering coefficients $\Gamma_{A,B}$. Given m resputter coefficients Γ_{A_i,B_i} ($1 \leq i \leq$

$m \leq n^2$) that are ordered from largest to smallest, we propose the following calculation for the accumulation rates ${}^c\mathrm{R}_A$:

With initial state ${}^c\mathrm{R}_A = {}^s\mathrm{R}_A$, for each i update the accumulation rate of A_i,

$$
\begin{aligned}
{}^c\mathrm{R}_{A_i} = {}^c\mathrm{R}_{A_i} - {}^c\mathrm{R}_{B_i}\Omega_{B_i}\mathrm{P}^*\,\Gamma_{A_i,B_i},\ \mathrm{P}^* = \mathrm{P}_{A_i} \text{ if } A_i \neq B_i, \\
\mathrm{P}^* = \mathrm{P}_{A_i} - 1 \text{ if } A_i = B_i,
\end{aligned}
\tag{3.48}
$$

and use the new ${}^c\mathrm{R}_{A_i}$ value to calculate the P^* of the next iteration. The ratios of the resulting ${}^c\mathrm{R}_A$ values are the atomic ratios of codeposited film.

The current model allows ${}^c\mathrm{R}_A$ to attain negative values. Physically, the product $\Omega_B\Gamma_{A,B}$ must be positive and less than unity. This issue can be addressed by placing an upper limit on Ω ($\Omega < 1/\Gamma$ for the largest Γ that will be used) or by attenuating this product as it approaches unity. This issue is most important in the deposition of a dilute concentration of A with an element B. In this extreme case, $\Omega_B\Gamma_{A,B}$ is the fraction of A that is resputtered.

3.5.6 Discussion

Experimental confirmation of the model

The results of Sec. 3.5.4 demonstrate the accuracy of the model in accounting for resputtering in the codeposition of Pt and Pb. Figure 3.45 shows that for the region of the substrate where resputtering of Pb is most prominent, the values of Equation 3.44 are of order unity. That is, the position dependence correction is a smoothly varying function that does not drastically change the resputter rates from the nominal value given by our model for resputtering. This result

confirms our model and the approximations within. For example, an unreasonable value of the corrective factor in Equation 3.36 would have made the values of Equation 3.44 unreasonable or not of order unity.

Uncertainty of resputter coefficients

The primary uncertainty in the calculation of the resputter coefficients (Equation 3.33) is due to the estimation of β (Equation 3.36). The denominator of Equation 3.33 could be replaced by a different expression for intrinsic resputtering fraction if a more appropriate expression is found. Hoffman [76] gives values for intrinsic resputtering with very low uncertainties, but these values are given for a particular geometry that is significantly different from that of magnetron sputtering.

The other primary source of uncertainty in Equation 3.33 is due to the significant but rarely cited uncertainties in the tabulated values of sputter yields, which (as indicated by Equation 3.41) correspond to significant uncertainties in our resputter coefficients. Given these notes, we allow the reader to determine whether the uncertainties of Equation 3.33 are appropriate for the individual application.

Geometry

The calculations of resputter rates require knowledge of the deposition geometry (i.e. an expression for Ω). In our simple treatment of the position dependence, we suggest that the geometrical factor $\Omega(\rho, \theta)$ needs to be determined only once for a given deposition system. The calculations of [62] indicate that in

our system, the physics captured by Ω is primarily the scattering of reflected Ar with the background gas, the variation in sputter yield with angle of incidence, and the neglected variations in the energy distribution and reflection probability of Ar. While the geometrical factor Ω is linear for our system, it may assume more complicated forms, particularly if the substrate assumes a different range of angular displacements from the target (γ).

The denominator of the resputter equation (Equation 3.33) is the enhancement of the arrival rate over the single source deposition rate. The substrate dependence of β and Υ cannot be mathematically written as multiplicative factor, such as is suggested in Equation 3.34. Deposition geometries may exist in which these position dependences are more important and must be treated in a more appropriate manner.

Collision probability

The expression for collision probability (Equation 3.43) suggests that Ar-metal collision probabilities are equivalent to metal surface concentrations. This approximation may not be equally valid for all metal alloys. Furthermore, Equation 3.43 assumes that single-source deposition rates directly determine codeposition surface concentrations. In [62], we incorporated a more elegant treatment of this probability by addressing the evolution of the surface stoichiometry from the arrival (gas-phase) stoichiometry to the bulk film stoichiometry. This evolution may also have an element-specific component if there is significant surface segregation of a particular species on the time scale of a monolayer deposition. While these details should be addressed if higher accuracy is desired, we note that a moderate error in the calculation of this probability corresponds to a small

error in the resulting film stoichiometry.

A related concern is that of shifts in binding energy of film constituents upon alloying. These shifts correspond to shifts in the sputter yields and thus resputter rates. The importance of these shifts is discussed in [62].

Parameterizations

The parameterizations offered in Equations. 3.35, 3.37, 3.39 and 3.42 are not particular to resputtering and may be useful in other calculations of sputtering phenomena. We do note that these equations assume units of eV for all energies.

3.5.7 Conclusions

Single-source profiling can be an effective tool for determining compositions in multi-source sputtering. This is particularly useful for high-throughput studies, in which measurements of composition of every location on a composition spread film would be expensive in time and effort. For the codeposition of some sets of elements, resputtering of film constituents can significantly alter film composition. We propose a model of resputtering that defines a metric for the magnitude of resputtering for any set of codeposited elements and have demonstrated that this model sufficiently describes resputtering in the codeposition of Pt and Pb. We assert that with the use of this model, compositions can be routinely calculated with an accuracy of a few atomic percent, which is comparable to the best routine absolute composition measurements for thin films.

3.5.8 Acknowledgements

The WDS analysis was made possible by the Cornell Center for Materials Research Facilities supported by the National Science Foundation under Award Number DMR-0520404. Primary funding for this work is provided by the Department of Energy, Grant No. DE-FG02-03ER46072.

3.6 Thoughts on resputtering in reactive atmospheres

The above resputter calculations assume a sputter atmosphere of 5mT Ar. At higher pressures, gas-phase scattering would be increased and thus resputtering reduced. The use of a different inert gas would require determination of the different reflection profile and sputter yield as a functions of target material. If the atmosphere is not inert, several important phenomena may lead to deviations from the above model.

In a reactive atmosphere, the film surface being resputtered may have a different sputter yield than that of the target elements, but this is similar to formation of intermetallics issue already discussed for the cosputtering of metals. In reactive sputtering, the $target$ surface may also be partially reacted with atmosphere. In this case, the operating voltage required to obtain the same deposition rate as that of an inert atmosphere is usually different. The gun voltage is a parameter in the above model, but this voltage change corresponds to a change in sputter yield similar to that arising at the film surface. Additionally, the gas reflection profiles and probabilities would be a surface stoichiometry-weighted average.

Perhaps more important than all the above effects is the different species present in the sputter atmosphere in reactive sputtering. For Ar sputtering, the accelerated ion is almost exclusively Ar^+ and resputtering happens largely by reflected neutral Ar. Sputtering in CH_4 would result in several different charged species to consider and some may be negatively charged and this accelerate away from the target. In O_2 sputtering, the primary charged species are O^- and O^{-2}, both of which are accelerated away from the target and depending on the plasma potential may obtain energies much larger that of reflected Ar. Thus, resputtering may be even more pronounced in reactive sputtering. However, reactive sputtering, especially with O_2, is seldom performed in a face-to-face geometry. Orthogonal off-axis sputtering is more common, but we will discuss sputtering in the Tubby tilted-gun geometry. The measurements discussed below suggest that negatively charged species accelerate along the gun axis and are mostly contained to the cylindrical region obtained by projecting the target surface along the gun axis. This cylindrical region does not intercept the substrate and thus the possible large increase in resputtering with reactive atmospheres is avoided.

3.6.1 Langmuir probe analysis in deposition region

A crude Langmuir probe was temporarily installed in Tubby by taking a ≈3mm copper disc, soldering a wire to the back, insulating the wire and mounting the disc in the plane of the substrate. Outside the vacuum chamber, the wire was connected to the chamber ground through a voltage supply and ammeter. The voltage supply provided a bias with respect to ground and the resulting current measured.

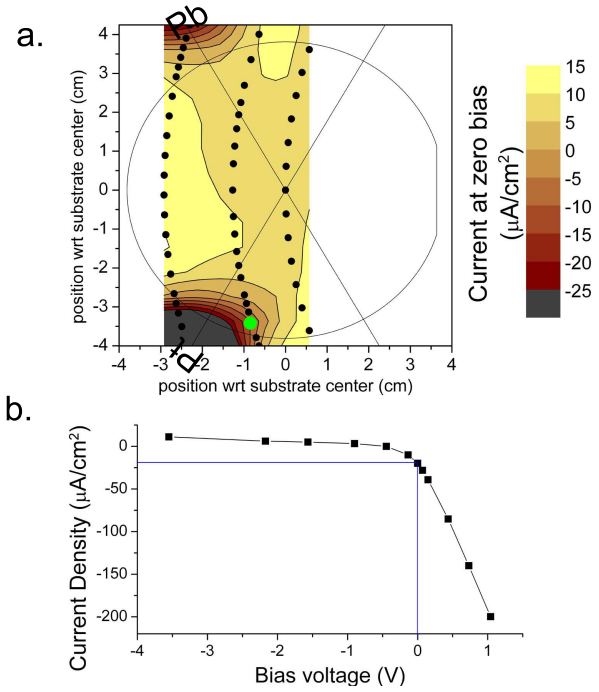

Figure 3.17: a. Current density measured by Langmuir probe at zero bias as a function of substrate position in the cosputtering of Pt and Pb. The black points denote measurement positions and the substrate outline is shown. b. For the green point shown in a., the probe current as a function of bias with the zero-bias point marked.

Pt and Pb were cosputtered in 5mT Ar and the probe swept through arcs similar to those used in crystal monitor deposition profiling. Three different sweeps were performed by venting the chamber and moving the probe to a different radius. The absolute positioning resolution of the probe is a couple mm.

In deposition of metals on Si, the film surface is grounded through contact with the substrate heater. Thus, to gather the most applicable data, most measurements were made with zero bias. A contour map of the zero-bias current is shown in Figure 3.17a. Several spots were measured multiple times with good reproducibility in the profile but ≈20% variations in the absolute current value.

Current densities below -30μA/cm^2 were very noisy, but reached mean value well below -100μA/cm^2. These highly negative currents are likely due to e^- bombardment. (For discussion of charge concentration and potential profile in magnetron sputter plasmas, see a standard physical vapor deposition text.)

Most of the deposition region within the substrate outline experiences a small positive current. The rapid decay in e^- bombardment suggests that it is negligible for most of the substrate and thus these currents are mostly due to bombardment by positive ions. My best guess is that metal atoms passing through the plasma may ionize at a position where the plasma potential is near ground and thus are not decelerated by the gun voltage and continue to the substrate. The important result is that in the deposition of a film, the substrate is largely free of e^- bombardment. Large spatial gradients in e^- bombardment over the substrate would correspond to nonuniform substrate heating. In general, it is best to have composition be the only strongly varying parameter as a function of substrate position.

Figure 3.17b shows that bias on the order of 1V can greatly effect substrate bombardment by charged species. In the deposition of oxides or other insulating films, this may be important. Possibly the bombardment profile of negative ions in reactive sputtering may be similar to the e^- profile inferred from Figure 3.17a and thus do not present a significant concern for unwanted substrate variations in resputtering or effective reactivity with the gas.

As a final note, both the Pt and Pb were operated near 300V during the acquisition of data for Figure 3.17a. Evidently, the e^- bombardment is a strong function of target material.

CHAPTER 4

HIGH ENERGY X-RAY CHARACTERIZATION

4.1 *Manuscript in preparation:* High Energy XRD/XRF for High-Throughput Analysis of Composition Spread Thin Films

The previous chapter describes the calculation of film composition, which through comparison with electrochemical results allows for determination of the composition range of active catalysts in a given chemical system. A more detailed understanding of the active catalyst is attained by also comparing the electrochemical results to the phase map of the composition spread. This map also tells you which phases have been tested, and in the event that there are known phases in the chemical system, let's you know if you've tested all the phases you are interested in. This map must be measured (it cannot be calculated), and high throughput crystallography of inorganic samples is an important tool for combinatorial research that is being developed by several groups, including mine. NOTE: In the following discussion and that in the Appendix, the fiber texture angle is denoted as χ but this may not be in agreement with accepted nomenclature.

4.1.1 Introduction

Analysis of inorganic libraries is an increasingly popular technique for materials discovery and optimization, as evident in the number and variety of recently

published methods for combinatorial materials research[155, 170]. We have recently presented methods for high throughput screening of continuous composition spread thin films for fuel cell oxidation catalysis[121, 66]. In this research, binary or ternary continuous composition spreads are sputter deposited onto Si substrates from elemental metal targets. The entire composition spread is then evaluated as a catalyst (e.g., for the oxidation of methanol) and the catalytically active regions determined. The catalytic activity of a material is a strong function of its surface electronic structure and we anticipate that the three bulk properties that vary as a function of position in the composition spread and will best correlate with trends in catalytic activity are film composition, crystalline phase, and fiber texture. The goal is thus to measure (in a single experiment) these properties as a function of substrate position and correlate the results with the measurements of catalytic activity. This type of analysis is at the frontier of combinatorial materials research. For example, principle component analysis has recently been applied to the problem of heterogeneous catalysis using only composition variables as components[136]. The ability to include crystalline phase and fiber texture in this type of analysis would greatly facilitate the discovery of new materials for not only catalysis but also the broad range of applications conducive to investigation with combinatorial methods. We present a simple configuration for simultaneous measurement of these films properties using 60keV synchrotron radiation.

Synchrotron radiation has been employed for mapping the composition[171] and structure[32] of inorganic libraries. These techniques have recently been combined in a single experiment[178]. For detection of all Bragg reflections, films that exhibit fiber texture require the analysis of orientational degree of freedom either through sample rotation during data acquisition or mapping of

both the fiber texture angle and scattering angle. Several techniques for fiber texture analysis have been developed with high energy x-ray diffraction (XRD) and area detectors[86]. Recently, Kukuruznyak et al.[92] have adopted this type of experiment for the analysis of ternary oxide composition spreads. The diffraction data acquired at many positions in the composition spread was used to determine not only the phase behavior but also the regions exhibiting an epitaxial relation to the underlying substrate. We present data processing techniques which afford simplifications of the diffraction experiments of [92]. The simplified setup also allows for ease in detection of x-ray fluorescence (XRF) from the thin film such that film composition, crystalline phase and fiber texture are simultaneously mapped.

Batch analysis of the large datasets acquired during characterization of composition libraries is an active area of research. Barr et al. demonstrated significant advancements in the analysis of powder XRD patterns from organic libraries using principal-component analysis, metric multidimensional scaling, and clustering techniques[13, 14]. These techniques have been adapted for the analysis of inorganic libraries[99], but several properties of inorganic phases pose significant problems for these algorithms. One particular challenge is their automated detection of phases in multi-phase samples. As detailed below, the use of high x-ray energy affords detection of high order Bragg reflections which will facilitate phase identification. Also, in the analysis of fiber textured films, phase identification via comparison to known powder patterns is confounded by the absence of peaks in the measured diffraction spectra. The peaks are commonly not detected due to inadequate sampling of reciprocal space, which is addressed in the present work by designing the diffraction geometry to provide detection over a wide range of fiber texture angles.

4.1.2 Experimental

Thin film deposition

Thin film composition spreads are prepared by magnetron cosputtering in a deposition system that has been described previously[65]. The composition spread discussed in this work was prepared using a prime grade Si substrate (76.2mm diameter, 350μm thick, (100) orientation, single-side polished). A uniform 7nm Ti adhesion and heating layer was deposited on the substrate, followed by co-deposition of Pt and Ru in an atmosphere of 0.67Pa Ar. The independent Pt and Ru dc power sources were operated at 129mA, 353V and 162mA, 355V respectively. The Pt and Ru rates were independently measured to be $2{\cdot}10^{-9}$mol/s/cm^2 at substrate center using a quartz crystal monitor, and the substrate was maintained at 400°C during the 420s deposition.

XRD/XRF apparatus

The XRD/XRF experiments were performed at the A2 line of the Cornell High Energy Synchrotron Source (CHESS). A schematic of the experimental layout is given in Fig. 4.1. The diffraction images were measured in transmission geometry with a MAR345 image plate detector oriented normal to the incident beam. An X-flash detector was displaced by 90° from the incident beam, and the substrate was oriented such that the thin film faces the MAR345 and X-flash detectors.

The sample to MAR345 distance was 0.55m and calibrated using a Si powder mounted at the film position. The center of the detector is intentionally

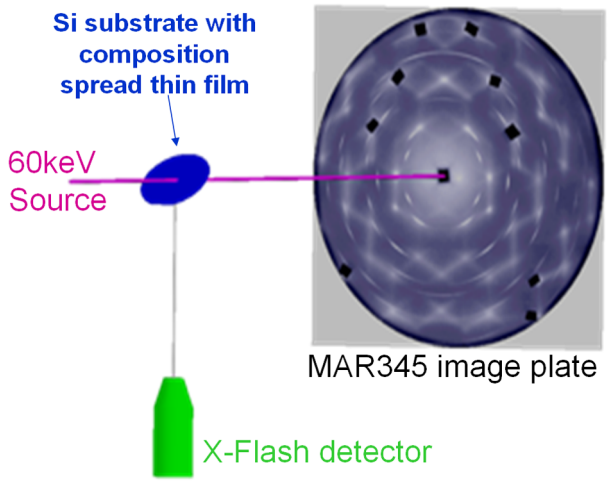

Figure 4.1: Schematic of the XRD/XRF equipment in the CHESS A2 hutch. The schematic is approximately to scale, and the MAR345 image shown in the outline of the detector is a typical diffraction image acquired on a composition spread thin film.

displaced from the beam axis so that artifacts associated with image plate erase issues are easily identified. In this geometry, the 60keV x-ray energy provides detection of Bragg reflections with d-spacings ranging from 0.05nm to 0.5nm, the primary range of interest for inorganic materials.

A goniometer provides α=46° substrate tilt with respect to the incident beam, and a translation stage mounted to the goniometer provides positioning of the composition spread thin film with respect to the incident beam. Data acquisition is performed by defining a rectangular grid of substrate positions and employing an automated data acquisition system which acquires diffraction images and fluorescence spectra at the subset of positions within the bounds of the composition spread. The collimated incident beam has a 1.2mm square footprint on the tilted substrate, and thus each measurement is an average over a ≈1at.% composition range of the composition spread thin film[65].

A 4.8mm-thick Al plate is mounted on the front of the detector and serves as

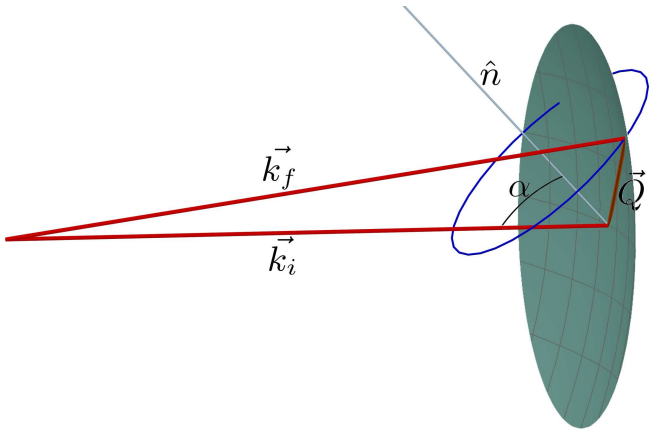

Figure 4.2: The reciprocal space geometry for the diffraction experiment is shown with the substrate normal $\hat{n}$ displaced α=46° from the initial wave vector $\vec{k_i}$. The green spherical section denotes the section of the Ewald sphere intersected by the image plate detector. A scattering vector $\vec{Q}$ which intercepts the Ewald sphere is shown along with the corresponding final wave vector $\vec{k_f}$. The fiber texture ring formed by procession of $\vec{Q}$ about $\hat{n}$ is shown in blue.

a passive high-pass x-ray energy filter, which is particularly helpful in reducing detection of isotropically emitted x-ray fluorescence. As discussed in Section 4.1.3, the diffraction images contain thermal diffuse scattering from the Si substrate. The diffraction geometry is designed to avoid detection of Si Bragg reflections, but the thermal diffuse scattering is more intense than typical film Bragg reflections at some detector regions. To avoid saturation of the image plate in these positions, small Pb pieces were taped onto the Al plate. The substrate holder is machined to provide nearly identical mounting of each substrate. As a result, data acquisition for each composition spread results in a fairly constant Si thermal diffuse scattering profile so that the Pb pieces never need to be moved. The substrate is secured with tape to avoid stressing the Si, which would result in substantial variation in the thermal diffuse scattering profile as a function of substrate position.

The substrate is not rotated during acquisition, precluding the study of single crystalline films. The films are assumed to be either equiaxed or fiber textured, a common property of metal thin films deposited onto a polycrystalline underlayer. The reciprocal space geometry of the experimental configuration is presented in Fig. 4.2. For a given (hkl) of a single-phase fiber textured thin film, the set of (hkl) reciprocal lattice vectors of the crystalline grains (which have an isotropic azimuthal distribution) lie on a circle in reciprocal space, as depicted in the figure for fiber texture along substrate normal. If the substrate normal $\hat{n}$ were coaxial with the incident wave vector $\hat{k_i}$, the texture ring depicted in Fig. 4.2 would not intersect the Ewald sphere.

Fiber texture is analyzed as a function of the angular displacement χ of the scattering vector with respect to substrate normal. In the presented geometry, the α=46° provides detection of the range 48°$< \chi <$140°, although this range does vary slightly with the scattering vector magnitude $|\vec{Q}|$. For a fiber textured film of a given phase, the goal is to detect at least one reflection from each family of Miller indices hkl which give rise to appreciable intensity in powder diffractometry. The necessary range of χ detection depends on the crystal symmetry and fiber texture direction, but for the case of cubic symmetry, any continuous χ range in excess of 90° is sufficient. Thus, the geometry presented above provides detection of nearly all diffraction peaks necessary for phase identification. We do note that due to the detection of a subset of the reflections in the family hkl, the relative peak intensities of powder patterns derived from the diffraction images may differ from those of indexed powder diffraction patterns.

4.1.3 Data processing, results and discussion

As discussed above, non-interactive analysis of characterization data is an active field of research in combinatorial material science. For processing of the XRD/XRF data, we have combined established algorithms with new analysis techniques into a software platform written in the Python programming language.

XRF-determined composition and thickness

We previously presented algorithms for calculating film composition from measured deposition profiles which include a model for resputtering in codeposition [63, 64]. For the Pt-Ru composition spread, the estimated accuracy of the calculated composition x in Pt_xRu_{1-x} is 5at.% or less. The model also provides calculation of the molar film thickness. For this manuscript we assume that the cosputtered film density is the weighted average of bulk Pt and Ru densities, which allows for calculation of the film thickness not only from the deposition profiles but also from the XRF data, as described below. The estimated uncertainty in the calculated film thickness is 10%, due primarily to uncertainty in the absolute deposition rate in our deposition profiles.

For the set of XRF spectra from a given composition spread, the XRF analysis is configured with the data acquisition parameters, including incident x-ray flux, sample geometry, element list (e.g. Pt, Ru, Ti, Si, etc.). Then, the analysis of each spectrum proceeds non-interactively, employing routines from the PyMCA software package[160]. Each spectrum is independently fit using a model that accounts for Compton scattering as well as fluorescence each ele-

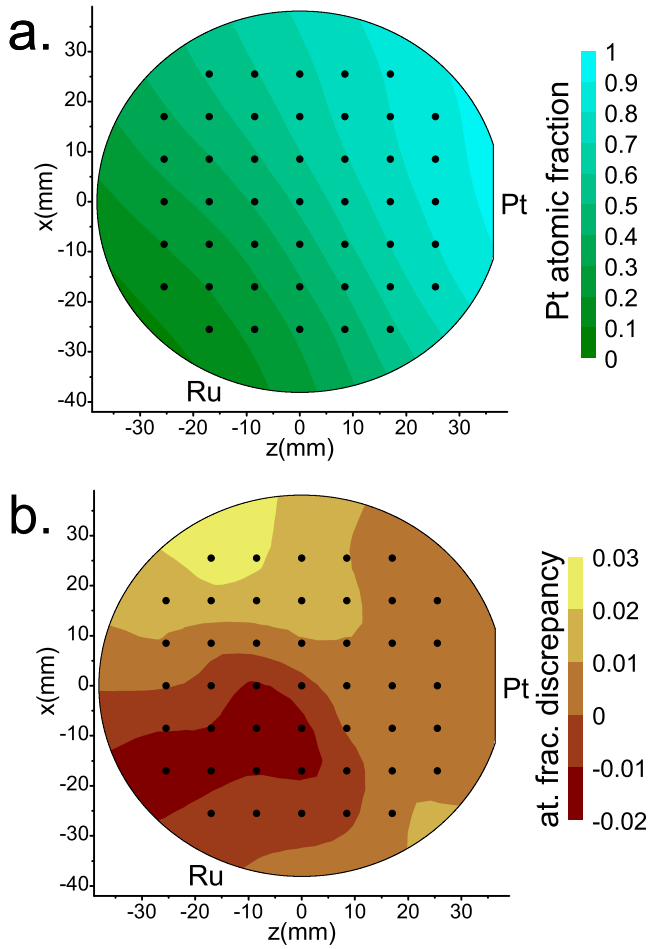

Figure 4.3: Interpolated contour plots show the XRF-determined profile of the atomic fraction Pt (a.) and its deviation from that of the deposition profile calculations (b.) for the Pt-Ru composition spread thin film. The plots are within an outline of the Si-substrate and the element symbols denote the orientation of the respective deposition source with respect to the substrate. The black points show the substrate positions used in high energy XRD/XRF data acquisition.

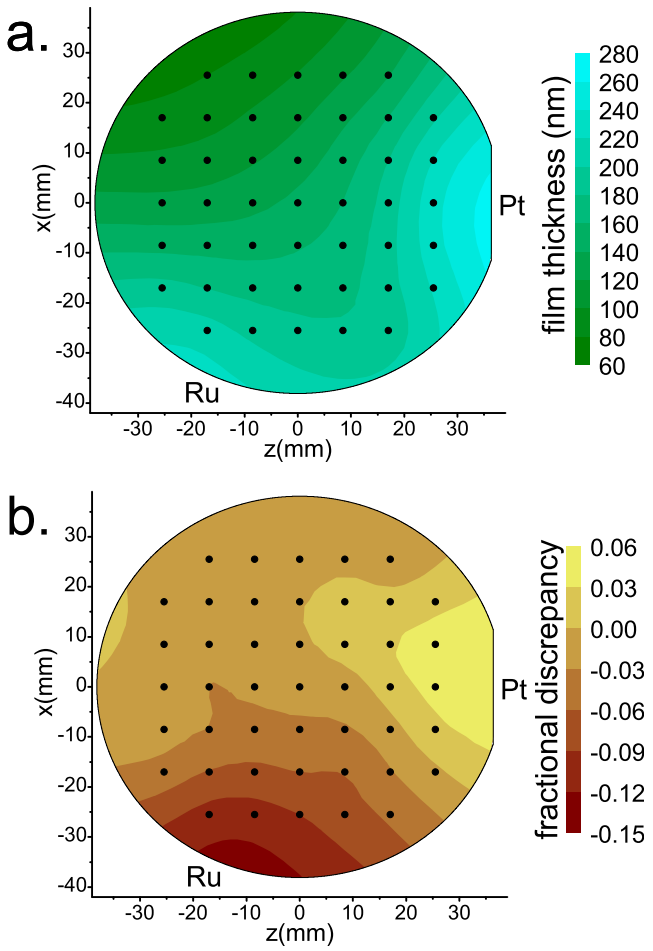

Figure 4.4: In the format of Fig. 4.3, interpolated contour plots show the XRF-determined profile of the Pt-Ru film thickness (a.) and its fractional deviation from that of the deposition profile calculations (b.).

ment. The absolute and relative intensities of the characteristic peaks of the elements of interest characteristic (e.g. Pt-M and Ru-K) are then used in an iterative procedure which simultaneously solves for a self-consistent estimation of the absolute mass and relative mass fraction. While the deposition profile calculations can be used to seed the iterative routine, we found that the same results we obtained by seeding each spectrum with arbitrarily chosen 50at.% concentrations and 100nm thickness. Additionally, the routine converged within $\lesssim$10

iterations for each spectrum.

For the Pt-Ru composition spread, the compositions calculated using this algorithm are plotted in Fig. 4.3a and the thicknesses in Fig. 4.4a. The smoothness of the interpolated contours in these plots are indicative of the negligible uncertainties in the calculated intensities of the fluorescence peaks. Thus, the only error in the calculated film properties are due to possible shortcomings of the data processing model and its implementation. The strong agreement between the XRF-calculated parameters and those of the deposition profiles (Figs. 4.3b and 4.3b) demonstrate the validity of the data processing algorithm. The region of the composition spread in which the discrepancies between XRF and deposition profile calculations are largest is the Ru-rich region. As previously discussed[65], the highest uncertainties in our crystal monitor-measured deposition profiles are in this highest rate region. Compared to the results of the XRF analysis, the deposition profile calculations predict lower Pt concentrations and lower thicknesses in this region, which are consistent with an underestimated Ru deposition rate in this region. Thus, the XRF experiment and analysis techniques provide robust measurements of composition and thickness with estimated uncertainties of 5at.% and 5%, respectively.

XRD image processing and line profile analysis

As described above, the diffraction images contain thermal diffuse scattering from the Si substrate which should be removed during data processing to facilitate comparison of the diffraction data to indexed powder patterns. Similarly, the diffraction images contain unwanted intensity due to x-ray scattering with air and the underlayer film, although the underlayer is weekly scattering

in the Pt-Ru sample discussed in this manuscript. The experiments of Kukuruznyak et al.[92] involve background subtraction using diffraction images obtained on substrate regions without deposited material. For the composition spread thin film deposition, the inclusion of such a region in each composition spread would require either a deposition mask or post-deposition film removal. The common use of elevated substrate temperature during deposition inhibit deposition masking and both techniques would impede upon the high-throughput nature of the research. Instead, a background subtraction image is calculated from the set of diffraction images acquired on a composition spread. The algorithm assumes that for every detector pixel, there will be at least one diffraction image in the dataset that contains no diffraction intensity from the composition spread thin film. This assumption is commonly met in composition spread thin films due to lattice constant shifts and phase changes as a function of film composition.

Since each diffraction is acquired under a pre-determined x-ray dose, any scatterer that is common to every sample analyzed in a dataset (the set of points in Fig. 4.3) will provide the same the diffraction pattern and intensity in every image. The intensity of a given pixel in the calculated background image is the minimum intensity obtained by that pixel in the set of all diffraction images acquired on the composition spread. That is, we exploit the fact that by sampling the thin film over a wide range of compositions, we ensure that any Bragg reflections from the thin film are not in every diffraction image. This simple algorithm has been sophisticated by excluding low-intensity outliers in the intensity distribution of each pixel and smoothing the background image. Also, the calculated background image is inspected for inclusion of film Bragg reflections which may exist in the event that the above assumptions are not realized.

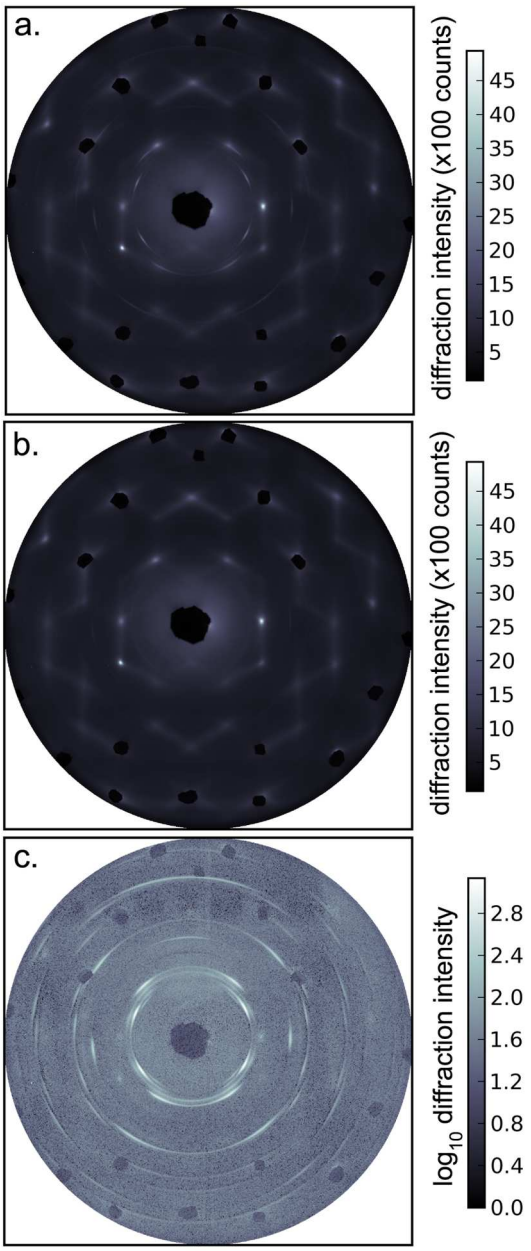

Figure 4.5: The background subtraction for the diffraction image acquired at substrate center is illustrated. The raw diffraction image (a.) is plotted with the same intensity scale as the background image (b.), which is common to the entire dataset. The difference image (c.) is plotted in a logarithmic intensity scale to show the effectiveness of the background subtraction and presence of many faint Pt and Ru Bragg reflections.

In this case, these problematic regions are calculated by interpolation of the surrounding data. While this background-correction routine is not automated, it requires user analysis of only one diffraction image per composition spread.

For the center point in the Pt-Ru composition spread, Fig. 4.5 shows the raw diffraction image, the calculated background image and the difference image that is used in subsequent analysis. The incomplete arcs in Fig. 4.5c indicate that the film is fiber textured. Azimuthal integration of this image (with appropriate $\mathrm{d}|\vec{Q}|\mathrm{d}\chi$ weighting) yields the analogue of a powder line profile which is then processed to the final spectrum used for phase identification (Fig. 4.6b). Although not depicted in Fig. 4.5, we note that the detector regions immediately surrounding the Pb blocks are excluded from analysis.

Fiber texture analysis

The fiber texture of the film is determined by analysis of the χ distributions of identified Bragg reflections in the line profiles. As demonstrated in Fig. 4.7, the peaks in the χ distributions may deviate from the values calculated under the assumption that the fiber texture direction is substrate normal. While anisotropic film stress will give rise to such deviations, the more dominant effect in the fcc-Pt portion of the Pt-Ru composition spread is that of oblique deposition. In the deposition system, the axis of the Pt source is displaced from substrate normal in the direction of α tilt in Fig. 4.1. The resulting alteration of the film growth direction corresponds to a shift in the fiber texture direction and thus the χ distributions. The direction of fiber texture with respect to substrate normal can also be analyzed through comparison of the χ distributions calculated from the left hand side and right hand side of the detector. Unlike the Pt

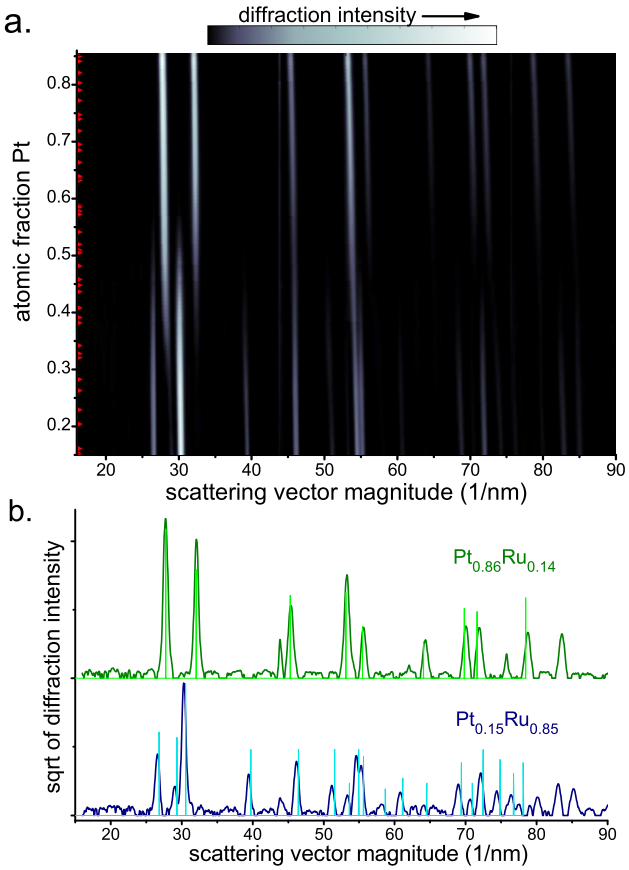

Figure 4.6: a. The diffraction line profiles from the 45 measurements on the Pt-Ru composition spread are plotted with interpolation along the composition (vertical) axis. The XRF-determined compositions of the measured samples are noted by red markers along the vertical axis. Each line profiles is normalized by the respective XRF-determined thin film mass. The alloying of the two elements is evident in the slope of the diffraction peaks as a function of composition, and the two-phase region is easily identified. b. The line profiles of the most Pt-rich and Ru-rich samples are plotted along with the indexed powder patterns for fcc Pt-(top) and hcp-Ru (bottom)[3]. The peak shifting due to alloying is evident, and the line profiles show high-order peaks in the high scattering vector range not included in the indexed patterns.

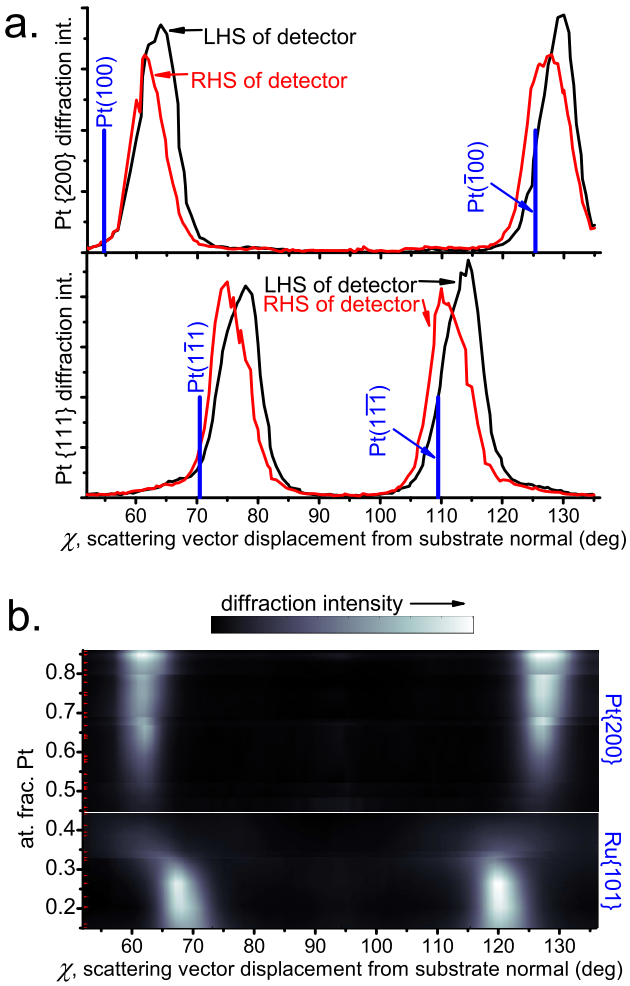

Figure 4.7: The diffraction intensity profiles of the Pt{200} (a.) and Pt{111} (b.) Bragg reflections are plotted as a function of the scattering vector angular displacement χ from substrate normal. Analysis of these distributions reveals that the film is fiber texture about Pt(111). Different distributions are plotted for left hand side (LHS) and right hand side (RHS) of the detector, which correspond to the sampling of reciprocal space on different sides of the plane defined by $\vec{k_i}$ and $\hat{n}$ (see Fig. 4.2. c. Using only the right hand side of the 45 diffraction images, the χ distributions of the Pt{200} and Ru{101} are plotted as a function of the atomic fraction of Pt. The Pt{200} (Ru{101}) distribution is shown over the composition range where the fcc-Pt (hcp-Ru) phase is dominant. Following the fiber texture analysis of a. and b., the plot indicates that fcc-Pt maintains Pt(111) fiber texture over its entire composition range. Similarly, the plot demonstrates that hcp-Ru maintains Ru(001) fiber texture.

source, the axis of the Ru source in the deposition system is not in the substrate tilt plane, and correspondingly, careful analysis of the Ru reflections in Fig. 4.5 reveal that the axis of left-right symmetry is tilted from vertical.

4.1.4 Conclusions

We present a high-energy XRD/XRF experiment for analysis of composition spread thin films. We also present data processing algorithms that provide mapping of the film composition, diffraction line profiles and diffraction χ-distributions as a function of position in the composition spread. The phase behavior of the chemical system is determined through combination of the composition mapping with the analyzed diffraction line profiles. Thus, the primary bulk properties of the composition spread are determined in a single experiment. The reduced data can then be compared with independently determined property data to reveal important trends. For example, we have recently performed such analysis to better understand the mechanisms of methanol oxidation catalysis in the Pt-Ta system (being prepared for a separate publication).

4.1.5 Acknowledgments

This work was supported by the Cornell Fuel Cell Institute funded by the Department of Energy (ER06-02-13022-11751-11792). The experiments were conducted at the Cornell High Energy Synchrotron Source (CHESS) which is supported by NSF award DMR-0225180. The authors thank Michele Tague, Anna Legard and Taro Naoi for assistance in data acquisition.

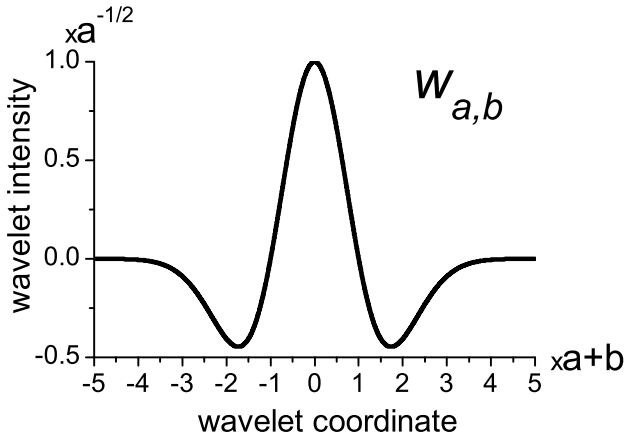

Figure 4.8: The Lorentzian of Gaussian wavelet (Equations 4.3 and 4.1) is plotted as functions of the scale parameter a and translation parameter b.

4.2 Algorithms for high-throughput XRD analysis

Processing the large quantity of data acquired via the methods of the previous section requires high-throughput analysis. As discussed above, the development of such algorithms is an active field of research. In this section we explore a new approach to XRD analysis involving wavelet transforms. Some additional algorithms are described in the Appendix. That discussion includes a re-presentation of some ideas from the previous section in a more formal notation, which may also be useful in the interpretation of the associated Python code.

4.2.1 Wavelet-based analysis of diffraction line profiles

Introduction

Fourier analysis is commonly used to express spectral data in terms of frequency components and associated phases. While transformation into this frequency-phase space is useful for many data analysis practices, the most intuitive transformation space for peak identification is a peak width-peak position space. In the formalism of wavelet analysis, such a transform can be built by appropriate choice of a mother wavelet $w(x)$ such that peak width and position are accessed through dilation and translation of this wavelet,

$$w_{a,b}(x) = a^{-1/2} w(\frac{x-b}{a}). \tag{4.1}$$

Dilation and translation are dictated by what are hereto forward referred to as the wavelet scale and position parameters a and b, respectively. Given a 1-D function (e.g. spectral data) $f(x)$ and assuming both w and f are real-valued functions, the wavelet transformation of f is given by

$$T_{a,b} \propto \int w_{a,b}(x)\, f(x)\, \mathrm{d}x. \tag{4.2}$$

A common choice of mother wavelet is the Lorentzian of a Gaussian (LoG, also known as the Mexican hat) wavelet (see Fig. 4.8),

$$w(x) \propto (1-x^2) Exp[-x^2/2]. \tag{4.3}$$

Variation in the wavelet scale a provides "multiresolution" analysis, which has been incorporated into analysis of x-ray differential correlation functions by Ding, et al. [40]. In this work, LoG wavelets with different widths probe ordering on different length scales, and analysis of the wavelet transformed data

provided insights into the structure of silica glass vis a vis crystalline counterparts.

Wavelet-based data compression and filtering algorithms are analogous to their counterparts built upon Fourier transformations. In x-ray diffraction analysis, wavelet-compressed powder spectra have been used for increased computation efficiency[143] and for crystalline phase identification via comparison with wavelet transforms of pure phase spectra[16].

Wavelet denoising algorithms have been implemented in data processing algorithms for several varieties of spectral data, including powder x-ray diffraction[144]. The denoised data is typically transformed back into its original (1D) coordinate space for further analysis.

Algorithms for the extraction of peak positions and properties from the 2D wavelet transform surface have recently been developed; these algorithms demonstrate high sensitivity and low false detection rate for peak identification in low signal-to-noise spectra. Du et al. [44] developed such an algorithm for analysis of mass spectrometry data using the LoG wavelet transform. A similar algorithm has been implemented using the derivative-of-Gaussian (or Ridger) wavelet to analyze low signal-to-noise signals from Contactless Electrophoresis measurements [174].

In the present work, we adopt the algorithm of [44] for the analysis of powder diffraction spectra of composite Pt-TaC thin films. In particular, the wavelet transform is used to identify the Bragg peaks in spectra with a large "background" component. In these spectra, the background signal is not high frequency noise that could be filtered by conventional (e.g. Fourier) algorithms.

The wavelet-based algorithm identifies the Bragg peaks and additionally provides estimates of peak parameters which are subsequently used in local profile fitting.

Thin film fabrication

The metal thin films analyzed by x-ray diffraction were sputter deposited in a combinatorial magnetron sputter deposition system described previously[65]. Single crystalline silicon wafers (350μm thick, (100)-orientation) were coated with a uniform 12nm Ti layer which serves as a diffusion, adhesion, and heating layer. A radiation heater brings the substrate to 400°C, a temperature that is maintained during film deposition. The Pt-TaC composition spread thin film was deposited in an atmosphere of 5mT of 7.5% CH_4 in Ar.

X-ray diffraction

High energy x-ray diffraction was performed in transmission geometry with a 60keV x-ray beam at the Cornell High Energy Synchrotron Source. The 2-D diffraction images (MAR345 image plate detector) contain not only Bragg reflections from the metal thin film but also a strong thermal diffuse scattering from the silicon substrate. The beam is moved to various positions across the thin film such that diffraction images are obtained at various film compositions present in the composition spread thin film. The majority of the substrate signal is removed by subtracting from each image that which is common among all images from the same substrate. Details of the extraction of powder patterns from the 2-D images and of the experimental apparatus were described previ-

ously. Powder diffraction spectra are obtained through azimuthal integration of the 2-D diffraction images.

Wavelet modification and design parameters of transformation

While a variety of mother wavelets could be used to identify peaks in diffraction spectra, the current work only involves the use of LoG family of functions $w_{a,b}$ given by Equations. 4.3 and 4.1). The data f is assumed to be a 1D set of measurements performed on a grid of positions X with regular spacing δx in the measurement coordinate x. The wavelet transform is essentially a discrete convolution of data f with $w_{a,b}$ and can thus be performed either in the coordinate space of the data (the discrete counterpart of Equation 4.2) or in its reciprocal coordinate space through multiplication of the discrete Fourier transforms of f and $w_{a,b}$. In both approaches, artifacts in the calculation result may arise due to the finite spacing in X and "edge" effects due to the termination of the data at the extreme values of X. We present an algorithm to circumvent these issues in the direct transform calculation.

The LoG wavelet has no zeroth or first moment, and thus in the support region of the wavelet ([-5a, 5a]), constant and linear components of f do not contribute to transform intensity. However, the discrete wavelet obtained by evaluating $w_{a,b}$ on X may have a finite zeroth and first moments, especially when a is comparable to δx. This undesirable property also arises when b is within $\sim$5a of the extremes of X. This latter issue is commonly addressed by artificially extending the dataset through interpolation or reflection of f about the boundary. However, we suggest that both problems are remedied by modi-

fication of the discrete wavelet:

$$W_{a,b}(x) = \{ \quad \alpha\, w_{a,b}(x) \text{ if } w_{a,b}(x) \geq 0 \qquad \beta\, w_{a,b}(x) \text{ if } w_{a,b}(x) < 0\}, \tag{4.4}$$

where α and β are chosen such that $W_{a,b}$ has no zeroth or first moment and has wavelet energy equal to that of the mother wavelet,

$$\Sigma_X\, W_{a,b}^2\, \delta x = \int w_{a,b}^2 \mathrm{d}x. \tag{4.5}$$

That is, the basic properties of the wavelet are restored by an asymmetric (vertical) stretch. The energy conservation improves comparability among wavelet transform coefficients. However, significant modification of the wavelet through Equation 4.4 will reduce comparability. The extent of wavelet modification that should be allowed will vary with the exact form of f and the desired result of the wavelet transform, but we have found that reasonable results are obtained if the unmodified wavelet has an energy within 5% of the continuous wavelet energy. Otherwise, the measurement grid X is considered to be insufficient for the calculation $T_{a,b}$. While not utilized in the present work, we note that this technique may also be useful for cases of missing data (holes in X due to missing or corrupted measurements) or non-grid data (such as randomly spacing in X). In these cases, δx in Equation 4.5 must be replaced with the effective cross section of each measurement.

Given a mother wavelet, the primary design parameters of a wavelet transform are the choices of a and b. For convenience, the set B of values for the position parameter b is taken to be X. Transformations that use constant spacing in the set A of scale parameters are loosely defined as $continuous$ wavelet transforms. Such wavelet sets are used in the peak searching algorithms of

[44] and [174], but as is explained below, constant spacing in A results in oversampling of the large scale features. Data compression algorithms based on $discrete$ wavelet transforms commonly employ dyadic spacing in the scale parameter. However, for peak identification of diffraction spectra we find that using wavelet scales with $\log_{1.3}$ spacing allows for straightforward identification of the peak ridges while maintaining high computational and memory efficiency.

The remaining wavelet transform design parameter is the range of A. Using the above wavelet modification scheme, the minimum value of A is chosen to be the measurement spacing δx. The maximum value of A is practically chosen to be larger than the value of a that maximizes the wavelet transform of the widest peaks in f. The maximum LoG wavelet transform of a unit half-width at half-maximum peak is achieved with scale parameter of 2.9 for a Lorentzian peak and 1.9 for a Gaussian peak. For the high-energy diffraction example below, we expect crystalline grain dimensions no smaller than 3nm. The Scherrer half-width for high energy x-ray diffraction peaks from such a grain is approximately 1/nm, and thus A is extended to 4.5/nm.

Ridge and peak identification

The algorithm for extracting peak positions from the 2-D wavelet transform surface $T(a, b)$ is based on that of [44].The guiding principles of the algorithm are that given a peak in f at position x the wavelet transform $T(a, b)$ will have local maxima with respect to b at $b = x$ and the intensity of the maxima will be slowly-varying with a (slowly-varying compared to that of any super-linear background in the data). An example application of the wavelet peak detection

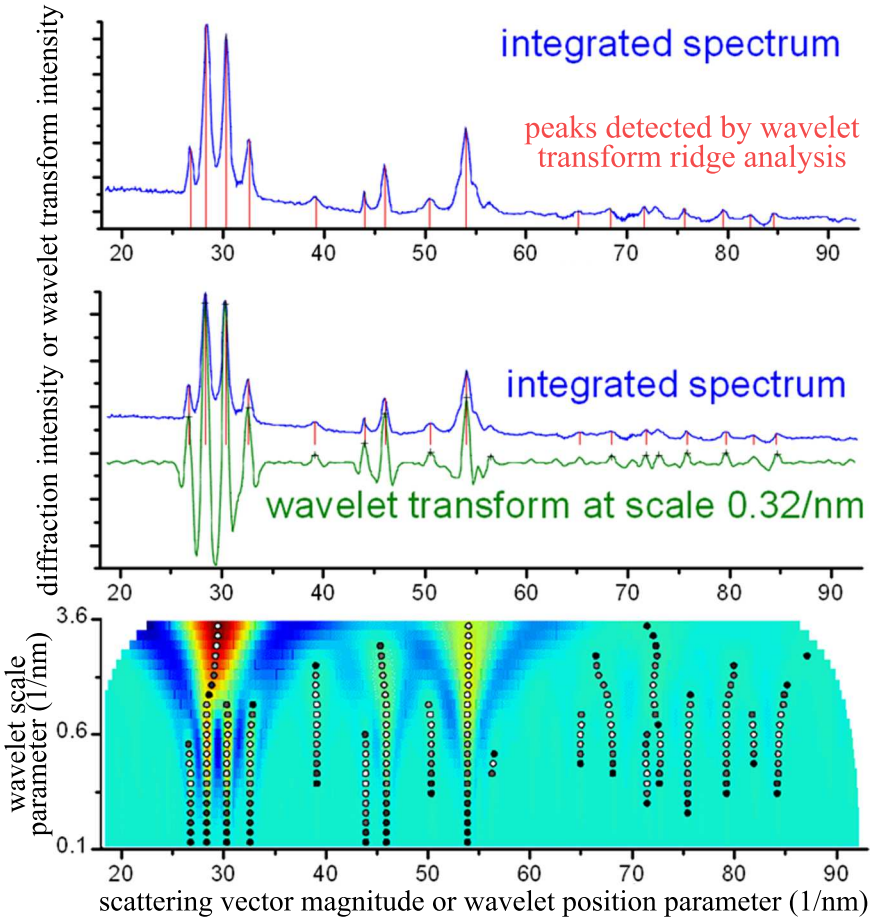

Figure 4.9: The wavelet-based analysis of a the diffraction line profile obtained for a Pt-Ru thin film sample. The center plot shows the line profile as well as its wavelet transform at a select wavelet scale. In the bottom plot, the wavelet transform is plotted (color scale) for several values of wavelet scale. The maxima above a critical value are denoted by grayscale dots. These maxima are grouped into ridges and given plotted in a grayscale representation of the relative intensity of the wavelet transform within the ridge. The ridges are used to identify peak positions in the original data, which are shown in the top two figures.

algorithm is given in Figure 4.9.

Further processing and profile fitting

While the aggressive background subtraction algorithm presented in the Section 4.2 is very effective at removing most of the intensity outside of the film Bragg peaks, it often creates artificial peaks in the background-subtracted spectrum g which are not easily distinguished from the true Bragg reflections. Identification of the peak positions in f allows for profile fitting g without concern for the inclusion of peaks which are artifacts of data processing. Obtaining the final peak parameters from profile fitting of the peaks in g reduces the consequences of false-positive peak detection in the wavelet transform algorithm. While this multi-step process makes for a complicated data analysis program, the program requires no user interaction and remains computationally efficient.

Profile fitting for peak parameter extraction involves three fit parameters for each peak (assuming symmetric peaks). Profile fitting algorithms commonly involve simultaneous optimization in each parameter and often with a variable number of peaks and with additional parameters for simultaneous fitting of the background profile. For the fitting of many peaks in a large set X, such profile fitting can be computationally expensive. The wavelet peak identification algorithm provides a fixed number of peaks with near-optimal starting parameters. In the absence of simultaneous background fitting, the dataset g over X can be also segmented for rapid fitting. To assure proper fitting of overlapping peaks, data segments are created by considering the set of windows formed by symmetrically expanding the peaks in P so that each window extends three peak widths in X. The ranges of X that are not in any window are not included in

profile fitting and the remaining segments are fitted individually.

Wavelet-based analysis of diffraction images

The ultimate goal is to apply the above algorithms to analysis of diffraction $images$. In this case, the wavelet transform space is 4-dimensional (scale and translation parameters for both the scattering vector coordinate and fiber texture coordinate). The formation of the wavelet basis set is also tricky because "physically correct" analysis of fiber textured diffraction peaks requires a different $d\psi$ normalization at each diffraction image pixel. The wavelets should also be modified as described in Section 4.2.1 when the wavelet intersects masked regions of the diffraction images (see discussion of mask image $\mathbb{K}$ in Section 4.2). For these reasons and the fact that mathematicians have not delivered FFT and inverse FFT algorithms for polar coordinates, the wavelet transform of raw diffraction images is computationally challenging (we don't have results yet).

CHAPTER 5

ELECTROCHEMICAL EVALUATION METHODS

5.1 Fluorescence assay apparatus for thin film electrochemistry

The parallel screening of thin film compositions spreads using pH-dependent quinine fluorescence was developed by Jing Jin and Mark Prochaska[121] based on earlier work published by Reddington et al.[127]. The basic configuration is shown in Figure 5.1. In 2007 I made a new testing system based on their PTFE cell design. The system contains a glass bottle for each solution to be used during testing. The bottle are deaerated with N_2 bubbling and kept under positive N_2 pressure. Solution is pumped into the cell by independent peristaltic pumps controlled by relays to permit computer-controlled filling. A peristaltic pump is also used to drain the cell so that experiments can be performed without opening the cell, which means that the cell can be sealed and kept under controlled atmosphere. Atmosphere control is essential to keep the composition spread thin film under inert atmosphere after an electrochemical pretreatment. The pretreatment is designed to remove oxides and contaminants on the surface of the metal film due to exposure to air. As we will see, the pretreatment can have significant effects on catalytic activity.

The basic test for catalytic activity is to fill the cell with a solution containing a fuel, quinine and a supporting electrolyte (for solution conductivity) in deionized water. The potential of the composition spread is then increased from some low potential (where no fuel oxidation occurs) at 5mV/s. At substrate positions where fuel oxidation occurs, the H^+ ions released into solution quickly drop the pH to 4, activating the UV-excited protonation of quinine which results in flu-

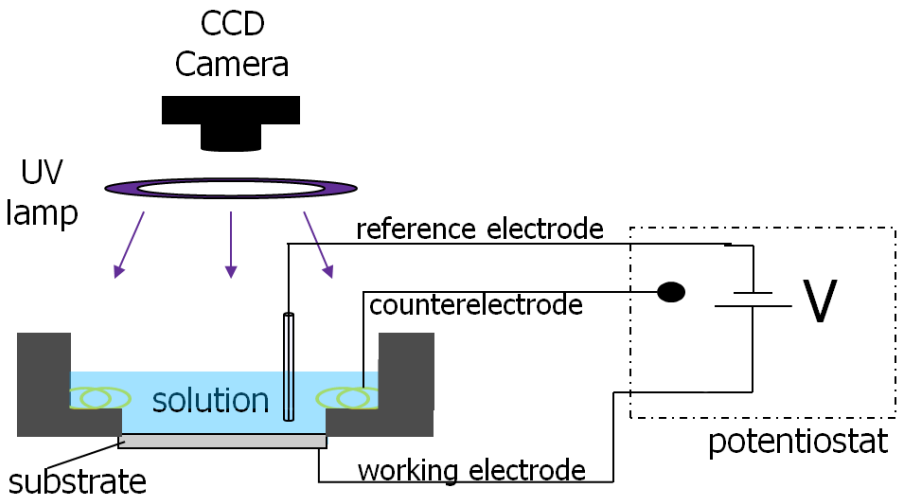

Figure 5.1: An illustration of the apparatus for fluorescence-based electrochemical testing thin film composition spreads.

orescence emission at 450nm. The intensity of the blue channel of CCD images of the film is a fairly high signal-to-noise measure of the fluorescence intensity. The variations in fluorescence intensity with substrate position and working electrode potential contain a lot of information concerning catalytic activity of the chemical system manifested in the composition spread thin film.

5.1.1 Partial oxidation of fuels

The fluorescence test, even after removal of false positives, is sensitive to any fuel oxidation. For example, ethanol could be partially oxidized to acetic acid, CH_3-CH_2-OH + H_2O $->$ CH_3-CO_2-H + $4H^+$, releasing protons and inducing fluorescence. This reaction is of little interest to the fuel cell community (maximum energy extraction occurs when all C ends up as CO_2), but if a catalyst drives this reaction at a low overpotential then the catalyst can be included in follow-up studies. For the ethanol case, the follow-up studies could include

the study of acetic acid oxidation or the study of ethanol catalyst by differential electrochemical mass spectroscopy to determine the reaction products. Neither of these techniques are currently being routinely performed, but the plan is to instate them in the testing cycle sometime soon. A similar situation exists with ethylene glycol and oxalic acid.

5.1.2 Subtleties

There are lots of subtleties to the fluorescence apparatus and its operation that are not pivotal for recognizing a home run catalyst but must be considered in trying to use the fluorescence testing to do science. I'll mention a few here that are not discussed elsewhere:

. The intensity of the fluorescence signal is roughly proportional to the intensity of the UV illumination on the substrate. The previous method of placing a UV lamp on the side of the cell does allow for detection of fluorescence everywhere but if one is to compare fluorescence intensity profiles from different substrate regions, the UV illumination needs to be more uniform (or at least calibrated). In my apparatus, this is achieved by using a circular black light from a party store, placing a white sheet of paper in the substrate position, and finding a geometry that makes the blue channel of images of the paper uniform.

. The reference electrode (required for attaining an absolute voltage scale for the composition spread working electrode) is Ag/AgCl and contains Cl^- ions that may diffuse slowly through a semi-permeable membrane. If the reference electrode is left near a film, the Cl^- will locally poison the surface.

. The counter electrode is the current collector. Any current passing through the $36cm^2$ of thin film must also pass through the counter electrode and the

potentiostat will apply whatever voltage necessary to drive some reaction at the appropriate rate on the counter electrode surface. Pt is a common choice for counter electrode but to save money we use Au. At high potentials, the counter electrode material may leach into solution and plate onto the working electrode (this is very bad). Michele and I have found that the Au plating onto a Pt film is undetectable when using low-O_2 solution, but in O_2-saturated 0.1M H_2SO_4 solution this is a big problem.

. The limited dynamic range of economical CCDs require that the aperture and gain be carefully set to provide low-noise measurements of faint fluorescence and measurement of fluorescence intensity over a wide voltage range without saturation (the fluorescence intensity typically increases exponentially over a 150mV interval).

. Every year we unveil another false mechanism of false positive fluorescence: H^+ release after pretreatment, reversible surface oxidation, surface area effects of stable but previously dealloyed thin films. This last mechanism gets its own manuscript.

5.2 *Manuscript:* High Throughput Evaluation of Dealloyed Pt-Zn Composition Spread Thin Film for Methanol Oxidation Catalysis

5.2.1 Abstract

While the high energy density of methanol makes it a promising fuel for low-temperature fuel cells, the lack of an oxidation catalyst with sufficiently fast kinetics limits the commercial implementation of these fuel cells. The numerous adsorption and charge transfer steps associated with complete methanol oxidation make metal alloys likely candidates for superior catalysts. Combinatorial searches employing metal thin film libraries are well suited for methanol oxidation catalyst studies, and we have developed experimental techniques to strengthen the evaluation of such libraries in a high-throughput regime. In particular, we employ catalyst pretreatment methods and linear sweep voltammetry with a ferrocene redox couple to determine the area and thus the specific activity of kinetically stable alloy catalysts. Particular attention is given to the relevance of the assessment to fuel cell operating conditions. These methods combined with established techniques provide both a rapid semi-quantitative map of methanol oxidation activity and enable a detailed quantitative analysis of the most active compositions. The efficacy of these techniques is demonstrated through the evaluation of Pt-Zn continuous composition spread thin films of varying thickness. The detailed characterization of the thin films is presented and discussed in the context of the electrochemical analysis.

5.2.2 Introduction

Proton exchange membrane fuel cells (PEMFCs) are promising energy conversion devices. Commercial viability of PEMFC technologies relies upon materials optimization of several PEMFC components in order to achieve significant improvements in energy conversion efficiency and materials cost. PEMFCs that utilize liquid fuels, such as methanol and ethanol, are of particular interest because liquid fuels offer high energy density and mitigate the storage and transportation issues associated with hydrogen fuel. One of the main obstacles in the implementation of such fuel cells is the lack of an anode catalyst that can effectively overcome the kinetic barriers associated with the oxidation of complex molecules. Accepted models of complete oxidation involve several adsorption and charge transfer steps[52, 94] which are optimized by unique properties of the catalyst's surface atomic and electronic structure. As a result, searches for new catalysts often involve heterogeneous materials, commonly binary, ternary and quaternary metal alloys and ordered intermetallics.

In the last decade, a number of publications have presented combinatorial high throughput methods for efficient exploration of this wide range of possible anode catalysts for direct methanol fuel cells (DMFCs)[35, 39, 83, 84, 98, 121, 127, 142, 150, 149, 177]. These collective works offer several different electrochemical methods for catalyst evaluation which compromise between the conflicting requirements of high-throughput and validity for operating fuel cells[141]. We discuss here several experimental techniques that conform to both of these requirements. The techniques can be used in conjunction with the existing testing methods and allow for better quantitative evaluation of the specific activity of prospective catalysts.

The study of alloy and intermetallic catalysts presents several challenges for evaluation methods. A solid solution of two or more elements may dealloy under electrochemical conditions in which one of the elements is thermodynamically unstable. Since Pt and Au are the only pure metals which are thermodynamically stable in the electrochemical environment of a PEMFC, dealloying is an important issue in combinatorial studies of heterogeneous catalysts. Electrochemically-induced dealloying has been discussed in literature with respect to catalyst stability[10, 21], as a potential fabrication technique for high surface area electrodes[181], and as a fabrication technique for novel catalyst materials[91]. In the context of catalyst discovery, important effects of dealloying include significant changes in catalyst composition and surface area. As labile atoms leach from the alloy, the material becomes porous with a surface that is enriched with the more noble element[47, 119]. The structure of the post-leaching material, passivation mechanisms during leaching, critical potentials of dealloying, and critical stoichiometries for bulk leaching are active topics of research[48, 137]. These works indicate that bulk leaching of binary alloys occurs when the atomic concentration of the labile element is nearly equal to or exceeds that of the noble element, a result that we rapidly acquire for the Pt-Zn system through our use of composition spread thin films. In fact, our characterization of the Pt-Zn films demonstrates the value of our techniques for the rapid assessment of all of these dealloying parameters, and we note that the composition spread technique may be particularly useful for dealloying studies of higher order (for example, ternary or quaternary) systems. However, in this manuscript we present and discuss the techniques solely in the context of catalysis experiments. We focus our discussion on the surface area effect of dealloying, for it affects the measurement of the specific activity of the catalyst.

The dealloying of Ag from a Au-Ag film that is initially planar[48, 181] results in nanostructured Au with pore size in excess of 20 nm. For a 50 nm film with this structure, the surface area increases by a factor of approximately 2 to 3. The low surface diffusivity of Pt (compared to Au) affords much finer feature sizes in porous Pt; for example, pores as small as 3.5 nm have been reported for dealloyed Pt-Cu[122]. Such high porosity may result in a much higher increase in surface area. We report a surface area increase of a factor of 50 due to dealloying of a 50 nm Pt-Zn film. Since specific current density is the most common measure of catalytic activity, it is essential for any catalyst discovery method to account for dealloying-induced changes in the surface area available for catalysis.

We employ our previously published[121] and improved combinatorial catalyst discovery method to analyze binary Pt-Zn thin film composition spreads for MeOH oxidation. In the conditions used in our electrochemical pretreatment and screening tests, Zn is predictably labile. As a result, exposure of Zn-rich film regions to moderate anodic potentials in an acidic environment results in bulk leaching of Zn until a stable stoichiometry of ca. 55 at% Zn is reached. The leaching of Zn occurs in the methanol oxidation potential range and confounds the interpretation of catalytic activity. Thus, only the stable or dealloyed compositions are evaluated for methanol oxidation. The dealloyed films have high porosity and the increased surface area results in both an improved apparent onset of methanol oxidation as determined by a fluorescence screening technique and a higher methanol oxidation current at a given overpotential. We use a ferrocene redox reaction as a simple and fast technique to determine the approximate surface area accessible by small molecules such as MeOH during oxidation. This measured specific surface area facilitates the interpretation of

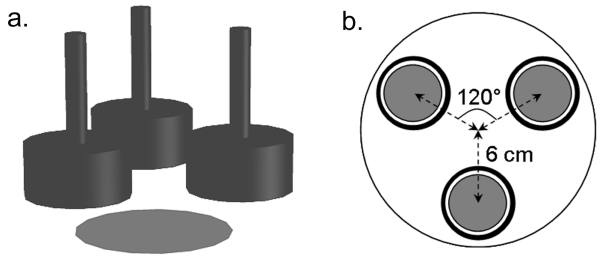

Figure 5.2: a. The three sputter gun ensemble for the deposition of composition spread thin films is shown with 3-in. substrate shown in gray. b. A view of the gun assembly from the viewpoint of the substrate is shown to illustrate the deposition geometry. (Note: this is the cartoon of Gilgamesh).

the oxidation test results by providing a surface area normalization factor.

5.2.3 Experimental

Sputtering of composition spread thin films

A detailed description of our combinatorial high throughput method, including composition spread synthesis and testing was presented previously[121]. The deposition system contains an ensemble of three 2-in. DC-magnetron sputter sources (Figure 5.2) for deposition of binary or ternary composition spreads. The sources are powered simultaneously to ensure intimate mixing of the film constituents. The vacuum chamber base pressure is typically in the mid-10^{-5} Pa range and thin films are deposited onto 3-in. Si wafers in an atmosphere of 1.3 Pa of high purity Ar. Prior to deposition of the continuous composition spread, a uniform 25 nm Ta film is deposited to promote film cohesion, prevent chemical reaction between the film and substrate, and ensure adequate lateral conductivity for electrochemical testing. To promote the formation of equilibrium

intermetallic phases, the substrate is typically maintained at an elevated temperature (up to 600°C) during the film deposition with a US Inc. ohmic heater. Deposition rates are determined for individual sources with an Inficon crystal deposition monitor, and films of differing thickness are made in sequential depositions by varying deposition time and keeping deposition rates constant.

Electrochemical testing

The evaluation of the thin film catalysts includes electrochemical pretreatment, cyclic voltammograms, and optical fluorescence screening. The 3-in. wafer with thin film is mounted in a Teflon® cell with ca. 7 cm inner diameter, which defines the region of the composition spread that is exposed to the testing solution. Three electrical contacts are made to the film surface at the perimeter of the substrate (not in contact with the solution). Two-point electrical measurements (typically 1 Ω) ensure sufficiently conducting film contact. All electrochemical tests involve a standard three-electrode configuration with the thin film as the working electrode. A gold wire in solution serves as the counter electrode.

For testing of the entire composition spread, the testing cell is sealed with a quartz lid to allow for control of the testing atmosphere, even during optical measurements. The apparatus includes glass storage vessels for the testing solutions which are bubbled with nitrogen and kept under nitrogen pressure to minimize the concentration of dissolved oxygen. Peristaltic pumps are used for automated filling, draining, and rinsing of the cell without removal of the lid such that the testing atmosphere is constantly controlled, most commonly with flowing nitrogen.

Electrochemical catalyst pretreatment: For composition spread thin films that contain elements that are labile over a subset of the voltage range of interest for the methanol oxidation screening (for example Zn in a Pt-Zn film), many voltage sweeps may be necessary to acquire a stable surface. Holding the film at a fixed potential above the critical potential for dealloying allows the film to obtain a stable surface more efficiently. Electrochemically stable Pt-Zn films were attained by a 10 minute constant potential pretreatment at 0.6 V vs Ag/AgCl in a pH 2 aqueous H_2SO_4 solution.

As a standard step for preparing the surface of the composition library for catalytic activity assessment, a pretreatment step is applied consisting of a linear voltage sweep from 0 mV to -800 mV vs. Ag/AgCl in an aqueous solution of 0.01M H_2SO_4 with 1M Na_2SO_4 (supporting electrolyte). The goal of the pretreatment procedure is to provide a reproducible surface and to replicate testing under fuel cell stack start-up conditions. During the procedure, the surface is exposed to mild to moderate reducing conditions under which many metal surface oxides are reduced. For select alloys, the surface oxide reduction is witnessed through visible changes to the film's surface, and in many cases hydrogen is evolved on the film surface and the resulting bubbles are visible. We hypothesize that the critical voltage marking a sharp increase in reduction current followed by the appearance of the hydrogen bubbles gives a measure of the activation energy for hydrogen evolution, which will be further discussed in a separate publication.

This type of pretreatment procedure is common practice in the fuel cell industry where anodes are often polarized to negative potentials so as to desorb anions and reduce surface oxides, yielding a clean and reproducible surface.

Likewise, the "break-in" procedure of H_2-air PEMFCs involves exposing the anode to a reducing environment before the first load is applied to the fuel cell. The hypothesized result is that all but the most tenuous surface oxides on the catalyst (or composition library) are reduced to a metallic state. In all cases, it is unclear what the exact nature of the resulting reduced material is. Relevant to pretreatment on composition libraries, studies are underway to determine whether this procedure regenerates the material to the metallic state that existed prior to oxidation (e.g., an alloy or ordered intermetallic phase) or results in a mixture of partially and fully reduced metals as discrete "islands" on the surface. This pretreatment combined with the controlled atmosphere and deoxygenated testing solutions allow for the testing of the catalyst with a surface state more representative of that which would exist in an operating PEMFC. We also note that this pretreatment, henceforth referred to as hydrogen evolution pretreatment, virtually eliminates sample to sample variability caused by differing lengths of air exposure while maintaining the high-throughput capability of the original method. For example, fluorescence assays of Pt-Ru composition spread thin films without this pretreatment have resulted in onset potentials varying from 390 mV to more than 530 mV vs SHE. However, after pretreating these films, the fluorescence onset potentials are consistently within 20 mV of 390 mV.

Fluorescence assay: The primary evaluation of a composition spread thin film is performed with a parallel-screening fluorescence assay that was developed by Reddington et al.[127] and adapted for the evaluation of continuous composition spread thin films[121]. The potential of the film (working electrode) is swept positive of the open circuit potential at 5mV/s, typically to 200 mV vs the saturated Ag/AgCl reference electrode. The aqueous testing solution of 5M

methanol, 2mM quinine and 0.1M potassium triflate (supporting electrolyte) is initially pH neutral. At a given film location, the methanol oxidation proceeds at accelerating rates due to the increasing overpotential, releasing protons into solution and resulting in a rapid local pH drop below pH 5. For a given applied potential, this pH drop corresponds to a decrease in thermodynamic overpotential by 59.1mV per pH unit for the single electron reaction, and oxidation rate decreases as dictated by the Tafel equation. As the voltage sweep continues and the reaction proceeds, the decreasing pH activates the protonation of the dissolved quinine, which then fluoresces under UV illumination. The potential at which fluorescence is detectable in images acquired with a charge-coupled device (CCD) camera is hereby referred to as the fluorescence onset potential and serves as a semi-quantitative measure of the catalytic activity for methanol oxidation. The mm-scale spatial resolution afforded by proton diffusion (see Sec. 5.2.4) corresponds to near at.% resolution in identifying the bulk composition of active catalysts. Methanol oxidation is one of several surface reactions that leads to a local decrease in pH and thus fluorescence. To identify false positive fluorescence results, a scan is performed with the same scan parameters in a solution without methanol. This high-throughput parallel screening points the investigator to the most active regions of the composition spread.

Localized evaluation of composition spread subsets: While the fluorescence assay quickly determines the presence of promising methanol oxidation catalysts, further testing is required to better understand the activity of the fluorescence-active subset of the composition spread. Localized testing of the thin film is achieved by employing a smaller Teflon® cell with 1 cm internal diameter. We note that the mounting of the smaller cell on the composition spread thin film requires the removal of the quartz lid and thus air exposure of

the film. With the smaller cell, a Ag/AgCl reference electrode is used for some tests. However, the proximity of the reference electrode and the film surface introduces the problem of Cl poisoning of the film surface and thus for methanol oxidation tests, a reversible hydrogen electrode (RHE) is prepared.

The most conventional characterization using the smaller cell is the acquisition of cyclic voltammograms in an aqueous solution of 5M methanol and 0.1M H_2SO_4. This test confirms that catalysts found to be active near neutral pH in the fluorescence test are also catalytically active at pH 1, the approximate pH encountered in operating fuel cells. While this test gives the methanol oxidation current as a function of overpotential, a measure of the specific surface area is needed to provide the current density, which is the most meaningful descriptor for a potential fuel cell catalyst. The surface area measurement is performed by linear sweep voltammetry with a ferrocene redox couple in an aqueous solution of 0.2mM ferrocene monocarboxylic acid with 0.1M Na_2SO_4 (supporting electrolyte). The monocarboxylic acid functional group increases aqueous solubility of the ferrocene. The ferrocene redox couple is chosen due to its low electrode adsorption, easily accessible redox potential in the range of interest for catalysis, fast kinetics which result in readily measured currents, and general insensitivity of the kinetics toward electrode composition. For the single electron redox reaction, given the ferrocene concentration C, sweep rate v, diffusion constant D of ferrocene monocarboxylic acid, and peak oxidation or reduction current i_p, the electrode surface area accessed by ferrocene molecules is given by rearrangement of the Randles-Sevcik equation,

$$A = 3.72\,10^{-6}\,i_p\,v^{-1/2}\,D^{-1/2}\,C^{-1}. \tag{5.1}$$

Other common methods for surface area measurements include H_2 and CO

adsorption. These methods are ill-suited for analysis of heterogeneous catalysts as the gas adsorption varies with electrode surface composition. In particular, a promising oxidation catalyst may weakly adsorb CO, an intermediate in the oxidation of methanol. Also, H_2 adsorption for electrochemically dealloyed films may measure a specific surface area that significantly differs from the methanol oxidation surface area. Electrode surface atoms in sub-nm pores will not fully participate in methanol oxidation due to size exclusion of the methanol molecule, but such surface atoms may adsorb H_2. The ferrocene monocarboxylic acid molecule is larger than the methanol molecule and has different diffusion dynamics into the small pores of an electrochemically dealloyed film, but the ferrocene-determined surface area serves as a semiquantitative measure of the level of porosity resulting from dealloying.

Repeated testing: Repetitions of the above tests are commonly performed to ensure reproducibility. After air exposure of the film and especially after the film has been stored in air for several days, the hydrogen evolution pretreatment is typically performed. After the 1 cm cell tests, a fluorescence assay is performed and compared to the initial assay to ensure that the 1 cm tests did not significantly alter the film morphology.

Composition, structure, and surface morphology

Surface images of the composition spreads were obtained using a Leo 1550 Scanning Electron Microscope (SEM). Energy Dispersive x-ray Spectroscopy (EDS) analysis was performed using the same instrument in conjunction with a Bruker AXS XFlash 3001 Silicon Drift Detector. Quantization of elemental concentrations were calculated with Bruker Espirit 1.8 software using the Pt M and Zn L

x-ray counts. X-ray diffraction (XRD) spectra were obtained with a Bruker AXS General Area Detector Diffraction System (GADDS).

5.2.4 A model of fluorescence evolution and its dependence on the electrode specific surface area

Consider an approximately homogeneous region of a composition spread electrode with specific surface area to geometric surface area ratio r (hereafter referred to as the specific area ratio). Electrochemical characterization of this electrode as a methanol oxidation catalyst consists of the measurement of the fluorescence intensity F and geometric current density I as a function of electrode potential E using a linear voltage sweep at rate v. Subsequently, the specific surface area current density J is determined. At a given potential in the sweep, a total coulombic charge Q per geometric surface area gives the number of protons that have been released into solution. The distribution of these protons in the solution is governed by diffusion and solution flow. In an initially static solution, we assume that for low Q the distribution is diffusion limited. Relevant nominal diffusion times are 10s for detectable fluorescence and 100s for an entire fluorescence experiment. Assuming a proton diffusion constant of 10^{-4} cm^2s^{-1}[128], the corresponding diffusion lengths are approximately 0.03 cm and 0.1 cm, respectively. Thus, the lateral spatial resolution of the fluorescence experiment is 0.1 cm. Also, at the fluorescence onset potential, the fluorescent layer is confined to a 0.03 cm thick layer above the electrode. Both of these dimensions agree well with experimental observations. Near the onset of fluorescence, the thickness of the fluorescent layer is on the order of the diffusion

length, which is much larger than the structural features of the electrode. With the assumption that the electrode microstructure permits rapid diffusion of released protons to the geometric electrode surface, F is uniquely determined by the magnitude and spatial distribution of Q (*geometric* charge density).

During a fluorescence experiment, Q and F increase and the pH above the electrode decreases monotonically, with fluorescence intensity reaching a detectable value due to a critical charge density Q^* at the fluorescence onset potential E^*. The injection of charge at rate J (*specific* current density) and the flow of charge due to curvature in the charge profile (chemical diffusion) determine the spatial distribution of Q. These electrode-specific variations in charge profile as a function of distance from the electrode may result in variations in the value of Q^* required for detectable fluorescence. We neglect these variations and approximate that Q^* has a fixed value for a given apparatus.

Nernstian fluorescence onset potential

Assuming Nernstian behavior of the oxidation reaction, the oxidation current as a function of electrode potential is given by

$$J = \frac{J_l}{1 + \mathrm{Exp}\left(f^{-1}\left(E_{1/2} - E\right)\right)}, \tag{5.2}$$

where J_l is the mass transport limit of the current density, $E_{1/2}$ is the half-wave potential for the process under consideration and f=59.1mV at ambient temperature. For low current densities, we ignore the effect of microstructure on mass transport and assume that J_l is proportional to the accessible electrode surface area. For a linear voltage sweep starting at a voltage $E_{-\infty}$ at which J is negligi-

bly small, the accumulated geometric charge density Q at time t is given by

$$Q = r \int_{-\infty}^{t} \mathrm{d}t' \, J, \tag{5.3}$$

where the prefactor r is for conversion from specific surface area to geometric surface area. In our approximations J is a measure of the specific activity of the catalyst electrode. Substitution of Eq. 5.2 into Eq. 5.3 yields the released coulombic charge as a function of electrode potential,

$$Q = r J_l \, f \, v^{-1} \, \ln\left(1 + \mathrm{Exp}\left(\left(E - E_{1/2}\right)/f\right)\right). \tag{5.4}$$

It follows that for a given value of Q^*, the fluorescence onset potential as a function of area ratio is

$$E^* = E_{1/2} + f \, \ln\left(\mathrm{Exp}\left(Q^* \, v \, f^{-1} \, r^{-1} \, J_l^{-1}\right) - 1\right). \tag{5.5}$$

5.2.5 Results and Discussion

According to their Pourbaix diagrams, many transition metals are thermodynamically labile in an electrochemical environment relevant for acidic PEMFCs. On the other hand, Pt is insoluble at all pH and, other than the formation of a thin Pt-O surface layer, is unreactive up to approximately 1.2V vs. SHE. As a result, when Pt-M alloys (where M is an unstable metal) are subject to an acidic environment and moderate positive potentials, M may leach out into solution, leaving behind a porous Pt-enriched alloy. De-alloying of Pt-M alloys has significant implications for the discovery and characterization of new catalytic materials for PEMFCs. Selective leaching of one component of an alloy can dramatically increase the surface area of the catalyst. To compare the current (and power) density at a given potential, it is necessary to account for the

change in the fuel-accessible surface area caused by dealloying. In particular, according to its Pourbaix diagram, Zn is oxidized and is soluble in an acidic environment at PEMFC anode potentials[120]. As a result, if Zn in Pt-Zn alloys is not coated by surface Pt or stabilized through the enthalpy of mixing with Pt, it is likely to leach into solution under typical PEMFC anode conditions. While this dealloying complicates the evaluation of the catalytic properties of Pt-Zn alloys, we present both physical and electrochemical characterization of Pt-Zn composition spread thin films to deduce catalytic activity. Three Pt-Zn composition spreads with thicknesses 10, 50, and 200 nm were prepared by co-sputtering the metals from two of the sources depicted in Figure 5.2. The depositions were performed at 250°C and the deposition rates were chosen to provide a near 1:1 stoichiometry at substrate center. The films were pretreated and analyzed for catalytic activity toward methanol oxidation as discussed in Sec. 5.2.3. EDS, XRD and SEM characterization of the films were performed both before and after the electrochemical tests to provide physical characterization of the dealloying effects.

Structure and composition characterization

EDS and XRD characterization of the films indicate that at a given substrate position, all three films shared the same bulk composition and structure both before and after electrochemical testing and thus we present only the representative results from the 200 nm film. The Zn content of the as-deposited compositions spreads varied from ca. 90 at.% to less than 5 at.% and decreased upon electrochemical testing as shown in Figure 5.3. These measurements of bulk stoichiometry indicate that Zn-rich areas of the film dealloyed throughout

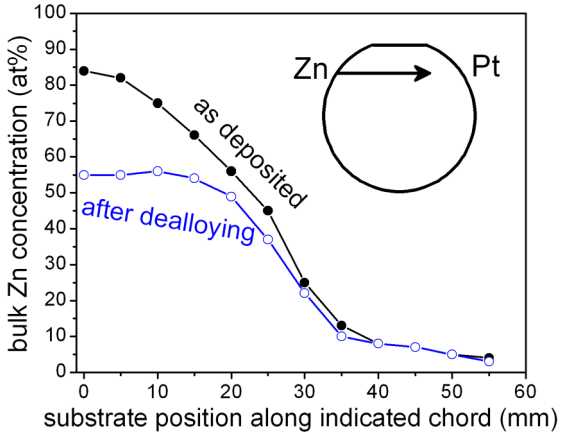

Figure 5.3: EDS measurements of film stoichiometry are shown as a function of substrate position for the 200 nm Pt-Zn film both as-deposited and after electrochemical testing. The inset shows a depiction of the substrate with the orientation of the two deposition sources denoted by the element symbols. The chord corresponding to the graph's substrate position axis is depicted by the black arrow. We note that the measurements on the thinner composition spread films yielded nearly identical results.

the bulk of the film, resulting in a stabilized film with ca. 55 at.% Zn. Bulk dealloying did not occur in areas where the initial Pt concentration was greater than 50 at%. Figure 5.4 shows the pre- and post-electrochemistry XRD patterns for the 200 nm film in the region with as-deposited composition 70 at.% Zn. The only identifiable phase in the region is PtZn, which has a tetragonal, AuCu ($L1_0$) structure type. Although a significant amount of Zn leached out from the bulk of the alloy during testing, essentially the same diffraction pattern was obtained after testing, indicating that the material did not undergo a major crystal structure change. The accepted lattice constants for $Pt_{0.53}Zn_{0.47}$ in this phase are 0.4015 nm, 0.0349 nm[116]. The lattice constants calculated with Jade (Materials Data Inc.) for the pre- and post-electrochemistry spectra are 0.403(2) nm, 0.353(2) nm and 0.401(3) nm, 0.351(2) nm respectively (see Section 5.3.1 for further information). The small shift in lattice constant and the similarity of the

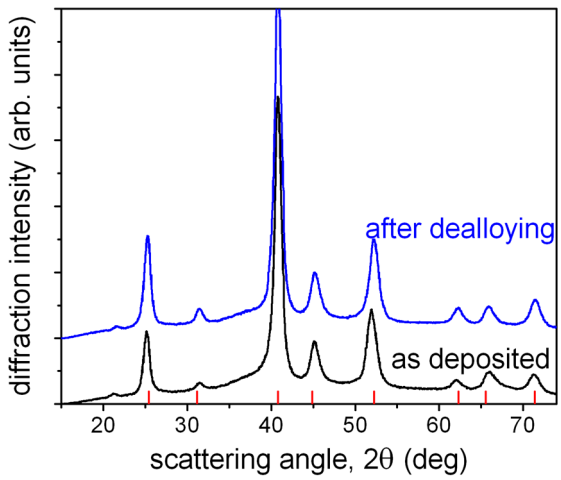

Figure 5.4: XRD patterns acquired for the 200 nm Pt-Zn film are shown for both the as-deposited and electrochemically tested film. The substrate position is that of Figure 2 with as-deposited composition of 70 at.%. The pattern for the dealloyed film is offset along the intensity axis for clarity. The red markers along the scattering angle axis note the known values for the tetragonal ($L1_0$) PtZn ordered intermetallic [116]. We note that the measurements on the thinner composition spread films yielded nearly identical results.

Pt and Zn atomic radii preclude the interpretation of composition changes in this phase. Post-electrochemistry XRD patterns obtained at several other substrate positions with initially high Zn concentration reveal the same PtZn ordered structure, demonstrating the stability of this structure with ca. 55 at.% Zn.

As deposited, the Pt-Zn films consisted primarily of tightly packed grains, with SEM images (Figure 5.5a) demonstrating the absence of gaps, cracks or other features that may be penetrated by an electrolyte solution. However, dealloying in the Zn-rich region of the film to the extent demonstrated by the composition data in Figure 5.3 results in a highly porous material[47, 119]. Evidence of such porosity can be observed by the post-electrochemistry SEM image in

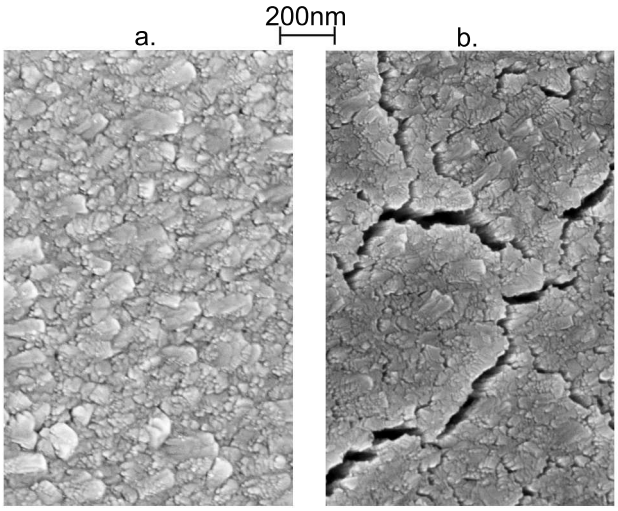

Figure 5.5: SEM images of the 200 nm Pt-Zn film surface are shown for both the as-deposited (a.) and electrochemically tested (b.) film at the same substrate position of Figure 3. The electrochemically tested film has cracks as large as tens of nm wide and hundreds of nm long which appear to extend throughout the thickness of the film. Similar cracks are visible in SEM images of the thinner films.

Figure 5.5b, which reveals the presence of many large and small cracks due to the compressive stress caused by the leaching of Zn. In accordance with the composition data of Figure 5.3, the cracks observed in the SEM images penetrate the bulk of the film, and thus correspond to a significantly increased surface area available for catalysis. The porous microstructure also made the film appear visibly dark due to increased roughness and porosity on the scale of the wavelength of visible light. While the as-deposited films were nearly planar (regardless of thickness), the bulk leaching resulted in a specific surface area that increases with film thickness. Hence, upon dealloying, the ratio of the available catalytic surface area to the geometric surface area of the tested region increased with film thickness. In the following section we quantify these changes in film morphology through electrochemical methods.

Electrochemical characterization

Ferrocene voltammetry for porous vs. planar films: A cyclic voltammogram at a scan rate of 50 mV/s for the ferrocene redox reaction on a planar Pt film is shown in Figure 5.6. As expected for a reversible reaction and freely diffusing species on a planar electrode, the forward and backward scans are symmetric with a ΔE_p of ca. 60 mV shift between current peaks. The (sweep rate normalized) forward scans for ferrocene oxidation on a 200 nm dealloyed Pt-Zn film are also shown for three scan rates. Although all of these scans were performed on the same geometric area of film, the much higher peak current at lower scan rates indicates a much higher specific surface area. The wide distribution of pore sizes in the dealloyed film corresponds to diffusion dynamics beyond the planar electrode model and thus symmetry in the forward and reverse scans is lost. Also, the peak oxidation current depends on scan rate in a manner that differs significantly from the model of Eq. 5.1. The effective electrode surface area decreases with increasing scan rate as slower scan rates afford ferrocene diffusion into small pores. This phenomenon is accentuated by the low concentration of ferrocene in the test solution. A systematic study of this variation could be used to probe the pore size distribution but is beyond the scope of the present work. For measurement of the electrode area, we use only peak currents from forward scans of 5mV/s voltage sweeps, the same sweep rate used for acquisition of methanol oxidation voltammograms.

Evaluation of methanol oxidation activity of Pt-Zn alloy catalysts: The three dealloyed, stable Pt-Zn composition-spread thin films were each evaluated for methanol oxidation catalytic activity through several fluorescence assays followed by local testing of the region with lowest fluorescence onset potential.

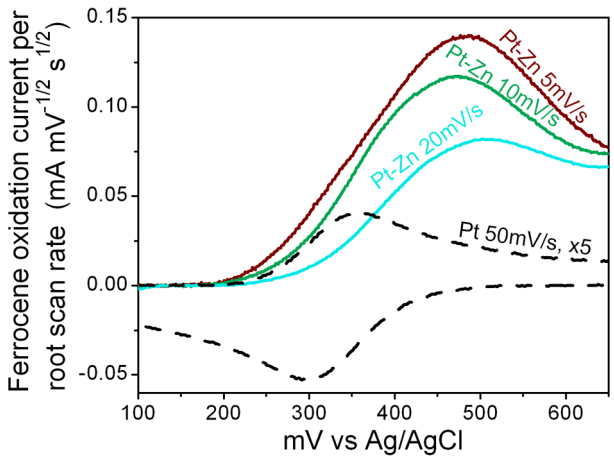

Figure 5.6: Measured ferrocene redox currents, scaled by the square root of the sweep rate, are plotted for different thin film electrodes using the same geometric testing area. The height of a given redox peak is proportional to the electrode surface area (Eq. 5.1). The cyclic voltammogram (dotted line) acquired at 50 mV/s on a planar Pt film is scaled by a factor of 5. The peak heights of the forward and reverse scans are symmetric and with peak currents offset by ~60 mV. The forward scans (ferrocene oxidation waves) are shown for three scan rates with a porous 200 nm Pt-Zn film. The systematic decrease in peak height with increasing scan rate indicates departure from the model of Eq. 5.1 and reflects the fine pore structure of the film. The area calculated from Eq. 5.1 for the Pt voltammogram is in good agreement with the 0.73 cm^2 area of the small testing cell. The corresponding specific surface areas for the Pt-Zn scans are tens of cm^2. The Pt-Zn film used for this study is not one of the three films discussed throughout the remainder of the manuscript.

The local testing included both methanol oxidation voltage sweeps and the measurement of the electrode specific surface area.

Analysis of each fluorescence assay provided a map of fluorescence onset potential for the entire composition spread thin film. This map is given for the 200 nm film in Figure 5.7a. for all three Pt-Zn films, the fluorescence assays indicated that the entire half of the film that was visibly changed by dealloying had a lower fluorescence onset potential than the Pt-rich half of the composition

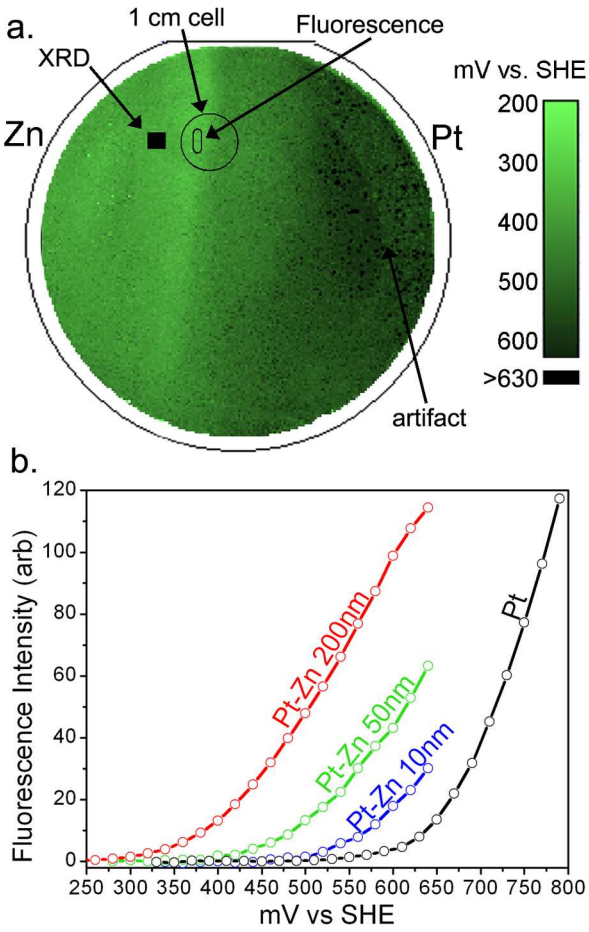

Figure 5.7: a. The fluorescence onset potential is mapped for the dealloyed 200 nm Pt-Zn film in an outline of the substrate. The elemental symbols denote the relative positions of the two deposition sources, and the variation in composition with horizontal position is given in Figure 5.3. The approximate positions of the point analyzed by XRD (Figure 5.4), region analyzed with the 1 cm cell, and the region used for the fluorescence intensity plot in b. are noted. The "artifact" label notes an annulus in the most Pt-rich region with average fluorescence onset less than 500 mV. This fluorescence onset is an artifact of the optics in the setup and is due to the extreme brightness of the most fluorescent regions at these potentials. The true fluorescence onset in this region is that of the neighboring Pt-rich region, ca. 600 mV vs SHE. b. The fluorescence intensity averaged over the region of interest is shown for the fluorescence assays of the three Pt-Zn films. The fluorescence profile for a planar Pt film is also shown. Each data point is calculated from a CCD image taken at 20 mV intervals during the 5mV/s voltage scan.

spread. For the present discussion, we refer only to the fluorescence intensity in the region noted in Figure 5.7a, which is plotted as a function of applied potential in Figure 5.7b. The fluorescence intensity plots in Figure 5.7b show that onset potential decreases significantly with increasing film thickness. This trend is also seen in Figure 5.7a through analysis of the vertical band of lowest onset potential. The onset potential increases with increasing distance from the deposition sources. This is a region of constant as-deposited composition but with film thickness decreasing with increasing distance from the deposition sources. Figure 5.8 demonstrates the relation between the fluorescence onset potential and the specific area ratio. As indicated by Figure 5.7b, the increased film thickness (and thus specific surface area) provides a higher local proton concentration throughout the voltage sweep and fluorescence becomes detectable at an earlier potential. For comparison, the fluorescence onset potential of a planar Pt film is also plotted in Figure 5.8.

Local testing of the composition library was performed in a 0.73 cm^2 region straddling the boundary of bulk leaching in the film (as noted in Figure 5.7a). The total surface area of the 10 nm, 50 nm, and 200 nm films were measured to be 3.5, 13, and 29 cm^2 (±20%) respectively. For each film, this measured area is used to determine the area ratios of the porous region in the 0.73 cm^2 testing area, as described in Section 5.3.1 and plotted in Figure 5.8. Also, the same 0.73 cm^2 region was used to measure methanol oxidation currents at pH 1, and these currents were scaled by the ferrocene-determined surface areas to yield the specific oxidation current densities plotted in Figure 5.9. The geometric current densities are also shown, dramatically illustrating the importance of the surface area measurements for comparing catalytic activity to that of planar Pt. For example, the required overpotential for 20μA per geometric cm^2 is 120 mV less for

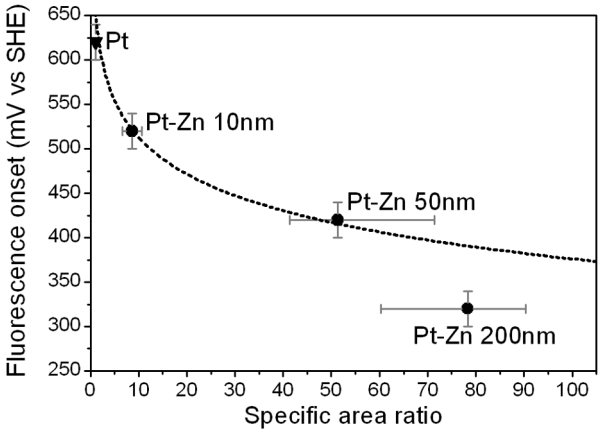

Figure 5.8: The Pt-Zn fluorescence onset potential determined from Figure 6 is shown as a function of the specific surface area ratio measured by the ferrocene linear voltammetry technique. For comparison, the fluorescence onset potential of a planar Pt film is shown at unity surface area ratio. Eq. 5.5 with parameters determined from the electrochemical characterization of the 10 nm Pt-Zn film is also plotted (dashed line). A discussion of measurement error is included in the supplementary material (Section 5.3.1).

the 200 nm film compared to the 10 nm film, but the overpotentials for 20μA per specific cm^2 are within 35mV for all three films. Above 650 mV vs SHE, the increased current densities of Pt-Zn compared to Pt are not due to differences in mass transport and thus indicate improved reaction kinetics, possibly due to an improved tolerance of the surface Pt in PtZn toward catalyst poisons such as CO. However, at low overpotential, the current density measurements indicate that the three Pt-Zn films have similar reaction kinetics both among themselves and compared to planar Pt.

We use the model of Sec. 5.2.4 to further analyze the fluorescence onset potentials of the catalysts. Least squares fitting of the specific current density of the 10 nm Pt-Zn film (Figure 5.9) to Eq. 5.2 gives J_l=0.45 mA/cm^2 and $E_{1/2}$=760 mV vs. SHE. Application of Eq. 5.5 with the measured area ratio and fluores-

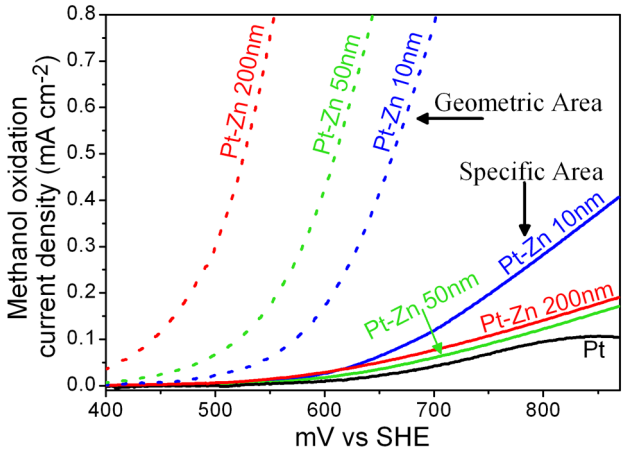

Figure 5.9: Using the 0.73 cm^2 cell, the methanol oxidation current was measured at pH 1 with a 5 mV/s scan rate. The geometric area (0.73 cm^2) current density of each Pt-Zn catalyst is plotted (dashed lines). The specific area current density calculated using the surface areas from the ferrocene linear voltammetry measurements is plotted for the three porous Pt-Zn films as well as for a planar Pt film (solid lines).

cence onset for this film (Figure 5.8) gives Q^*=0.74 mC/cm^2. With these values, the variation in fluorescence onset potential for a catalyst with surface area ratio r and equal specific catalytic activity is given by Eq. 5.5 and is plotted in Figure 5.8. Comparison of the 50 nm Pt-Zn and planar Pt data demonstrates that these catalysts have nearly identical specific activity to the 10 nm Pt-Zn film at low total released coulombic charge. The >60 mV discrepancy between the 200 nm Pt-Zn datum and the 10 nm Pt-Zn model suggests that the 200 nm film contains a catalyst with improved specific activity. However, we presume that the discrepancy is related to the high porosity and relatively large thickness of the 200 nm film, which may transgress the simple mass transport model of Sec. 5.2.4.

The similarity of the materials properties of the three Pt-Zn films determined by traditional characterization techniques (Figures 5.3 and 5.4) suggests that the films contain the same active catalyst. This conclusion is also readily met by

employing our collection of high-throughput electrochemistry methods. The electrochemical characterization provides the additional direct comparison to the planar Pt catalyst. The complete set of characterization data results in the conclusion that Zn-rich Pt-Zn alloys undergo bulk leaching of Zn under the electrochemical tests. The post-leaching, stable film is highly porous and consists of a slightly Zn-rich PtZn ordered intermetallic phase. The specific activity of the film toward the oxidation of methanol is equivalent to that of planar Pt at low current density which most likely corresponds to a Pt coating of the PtZn phase. The underlying ordered intermetallic may alter the electronic properties of the surface Pt making the catalyst more tolerant to catalyst poisons.

5.2.6 Conclusions

High-throughput evaluation of composition spread thin film catalysts is achieved by employing a parallel fluorescence screening followed by local electrochemical testing of the most active regions. An experimental technique for catalyst pretreatment that emulates fuel cell stack start-up has been developed and validated. The need for localized measure of the catalyst specific surface area has been demonstrated. Our reported protocols are compatible with high-throughput studies: less than an hour is needed to perform an entire testing program that includes electrochemical pretreatment, repeated fluorescence assays (to ensure reproducibility) and the measurement of specific oxidation current density of the most promising catalyst composition.

The utility of the experimental techniques is shown through the characterization of a Pt-Zn composition spread both by traditional thin film characteriza-

tion techniques and by our high-throughput, purely electrochemical techniques. The Zn-rich alloys leach Zn into solution until a stable PtZn catalyst with a presumed Pt-rich skin layer forms. Carefully accounting for the increased surface area of the resulting porous catalyst reveals that this catalyst has specific activity that is comparable to Pt below 650 mV vs. SHE and better than Pt at higher overpotentials.

5.2.7 Acknowledgments

This work made use of the SEM, EDS, and XRD facilities of the Cornell Center for Materials Research Facilities with support from the National Science Foundation Materials Research Science and Engineering Centers (DMR-0520404). Primary funding for this work is provided by the Cornell Fuel Cell Institute with support from the Department of Energy (ER06-02-13022-11751-11792).

5.3 *Supplementary Information:* High throughput evaluation of dealloyed Pt-Zn composition spread thin films for the oxidation of methanol

5.3.1 The area dependence of the fluorescence onset potential in the characterization of methanol oxidation catalysts.

A model of fluorescence evolution

Consider an electrode (or an approximately homogeneous region of a composition spread electrode) with known specific surface area ratio r. Electrochemical characterization of this electrode as a methanol oxidation catalyst consists of the measurement of the fluorescence intensity F, and geometric current density I as a function of electrode potential E using a linear current sweep at rate v. Subsequently, the specific surface area current density $\mathbb{I}$ is determined. At a given potential in the sweep, a total protonic charge Q per geometric surface area has been released into solution. Supposing containment of this charge in a solution thickness τ above the electrode, the average pH in the solution layer is

$$p = -\log_{10}\left(Q\,\tau^{-1}\,\mathrm{mol}^{-1}\,L\right). \tag{5.6}$$

Assuming a diffusion constant of approximately $10^{-4}\mathrm{cm}^2\mathrm{s}^{-1}$, the lower limit of τ after 100s (the approximate length of a single voltage sweep) of proton diffusion is $100\mu\mathrm{m}$[1]. During a fluorescence experiment, Q and F increase and p de-

[1]Imaging of the evolving fluorescence from a camera position in the plane of the substrate using a quartz cell indicates that fluorescent layer is confined to approximately this thickness. The efforts of Valerie Wiesner and Maxim Lobovsky were crucial in this study

creases monotonically, with fluorescence intensity reaching a detectable value when the critical charge density Q^* is reached at the fluorescence onset potential E^*. If the nominal length scales of the structural features of a given catalyst electrode are much smaller than τ and the microstructure of the electrode permits the rapid diffusion of released protons to the geometric electrode surface, the value Q^* has a universal value for a given apparatus.

Nernstian fluorescence onset potential

We consider the case of methanol oxidation in the absence of oxidation products with a single electron rate-limiting step. The potential E at which the oxidation proceeds with current density $\mathbb{I}$ is given by the Nernst equation,

$$E = E_{1/2} - f \ln\left(\frac{\mathbb{I}_l - \mathbb{I}}{\mathbb{I}}\right), \tag{5.7}$$

where $\mathbb{I}_l$ is the mass transport limited current density, $E_{1/2}$ is a catalyst-specific potential and f=59.1mV at ambient temperature. Inversion of Eq. 5.7 yields the current density as a function of electrode potential,

$$\mathbb{I} = \frac{\mathbb{I}_l}{1 + \mathrm{Exp}\left(f^{-1}\left(E_{1/2} - E\right)\right)}. \tag{5.8}$$

For small current densities, we assume that $\mathbb{I}_l$ is proportional to the accessible electrode surface area, regardless of the electrode microstructure. For a linear voltage sweep at rate v starting at a voltage $E_{-\infty}$ at which $\mathbb{I}$ is negligibly small, the accumulated geometric charge density Q at time t is given by

$$Q = r \int_{-\infty}^{t} \mathrm{d}t' \, \mathbb{I}, \tag{5.9}$$

where the prefactor r is for conversion from specific surface area to geometric surface area. In our approximations $\mathbb{I}$ is a property of the catalyst (independent

of microstructure). Substitution of Eq. 5.8 into Eq. 5.9 and integration via a variable transformation yields

$$\begin{aligned} Q/r &= \int_{-\infty}^{t} \mathrm{d}t' \, \frac{\mathbb{I}_l}{1 + \mathrm{Exp}\left(f^{-1}\left(E_{1/2} - v\,t'\right)\right)} \\ &= \mathbb{I}_l \, f \, v^{-1} \int_{-\infty}^{f^{-1}\left(v\,t - E_{1/2}\right)} \mathrm{d}y \, \left(1 + \mathrm{Exp}\left(-y\right)\right)^{-1} \\ &= \mathbb{I}_l \, f \, v^{-1} \, \ln\left(1 + \mathrm{Exp}\left(f^{-1}\left(E - E_{1/2}\right)\right)\right). \end{aligned} \tag{5.10}$$

The critical protonic charge is then given by

$$Q^* = r \, \mathbb{I}_l \, f \, v^{-1} \, \ln\left(1 + \mathrm{Exp}\left(f^{-1}\left(E^* - E_{1/2}\right)\right)\right), \tag{5.11}$$

and solving for the fluorescence onset potential yields

$$E^* = E_{1/2} + f \, \ln\left(\mathrm{Exp}\left(Q^* \, v \, f^{-1} \, r^{-1} \, \mathbb{I}_l^{-1}\right) - 1\right). \tag{5.12}$$

Determination of critical protonic charge required for detectable fluorescence

Define the fluorescence intensity scale such that the noise in F is 1 when averaging over a many mm^2 of geometric surface area (elimination of high frequency noise). The fluorescence onset potential E^* is that at which F reaches a value distinguishable from the noise. Consider also the potential E_{10} at which the fluorescence reaches a more substantial value of 10. We note that for all discussed experiments, E_{10} is well below the potentials at which transport limitations are evident.

For the 10nm and 50nm Pt-Zn films, F and $\mathbb{I}$ are measured by the fluorescence assay and local testing, respectively. The protonic charge (Eq. 5.9) at E^* is of order 0.1mC/cm^2 and at E_{10} is approximately 1mC/cm^2 for both films[2].

[2]The current at and before E^* is very small and thus the current dataset can only provide an order of magnitude estimate.

With the assumption that the catalyst surfaces have equivalent specific catalytic properties, the invariance of these charge densities with surface area ratio r is in agreement with the model of Sec. 5.3.1.

At v=5mV/s, we approximate that the diffusion time for protons released prior to detectable fluorescence is of order 1s and thus the pH (Eq. 5.6) at E^* is approximately pH 4[3]. It follows that the pH at E_{10} is slightly below pH 4.

The approximate local pH of the solution during the fluorescence assay is essential for thermodynamic interpretation of fluorescence results as it is pivotal in the conversion of the Ag/AgCl and RHE potential scales to SHE. The value of pH 4 was assumed in the above comparison of fluorescence assay voltage scale with Ag/AgCl electrode to the pH1 methanol oxidation current acquired using an RHE electrode.

5.3.2 Determination of specific surface area ratio from ferrocene linear voltammetry

The 0.73cm^2 region analyzed in the manuscript is on the border between the region that experienced bulk leaching and the region that experienced either surface or no leaching. As such, a fraction of the 0.73cm^2 region was approximately planar compared to the highly porous remainder of this film area. We chose this region to demonstrate the severity of the bulk leaching even within a few at% of the critical Zn concentration for bulk vs. surface leaching. Also, we were

[3]This value is in agreement with that resulting from the intuitive argument alluded to in the manuscript: the pH at visible fluorescence cannot be pH7 because the quinine would not fluoresce. The pH must be lower than pH7 and not too much lower than the critical pH for quinine protonation (approximately pH4). The logarithmic nature of the pH scale dictates that the answer is near pH4

interested in studying the PtZn ordered intermetallic which we expected to be at highest concentration at this substrate position. While the Pt-Zn binary composition spread affords the analysis of a more uniformly leached region, higher order (e.g. ternary) composition spreads may contain critical borders for bulk leaching with more complicated shape due to the absence of equi-stoichiometry contours (in a ternary composition spread, each substrate position has a unique stoichiometry).

To calculate the surface area ratio in this situation, consider a testing area A (=0.73cm^2) with a porous fraction β and planar fraction 1-β. An absolute area Z is measured by ferrocene linear voltammetry (or other method) and the specific surface area to geometric (planar) surface area ratio r of the porous fraction is to be determined. The specific surface areas are $A\,(1-\beta)$ for the planar fraction and $A\,\beta\,r$ for the porous fraction. The sum of these areas is the measured area Z, and thus the specific area ratio is

$$r = 1 + \left(\frac{Z}{A} - 1\right)/\beta \tag{5.13}$$

The area ratios of the manuscript's Figure 7 are derived from Eq. 5.13.

The large uncertainty of the surface area ratios in Figure 7 reflect the uncertainty in β, variation in the ferrocene oxidation peak height with repeated tests, and possible error introduced by the approximation that the 1-β fraction is planar.

It is important to note that the area ratio of Eq. 5.13 is the meaningful quantity for analysis of the fluorescence onset; for equal specific activity, the porous fraction fluoresces first. However, for the analysis of the measured oxidation currents (Figure 8), the measured absolute area Z is the meaningful quantity as the oxidation current is averaged over the planar and porous fractions in the

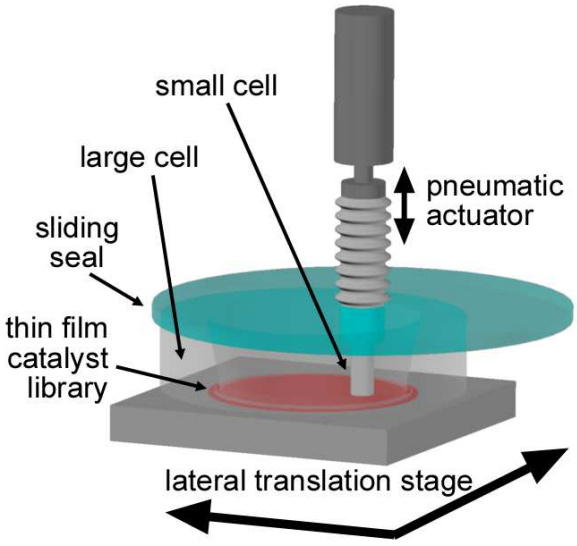

Figure 5.10: An illustration of the apparatus for the acquisition of cyclic voltammograms of small substrate regions. The translation stage and pneumatic actuator allow for automated rastering of the substrate region.

same manner as the ferrocene oxidation current.

5.4 Raster echem and minicell

After employing the fluorescence assay to quickly identify promising methanol catalysts, additional testing is required to determine the fluorescent active regions catalytic properties under fuel cell conditions. To acquire such data, we use so-called minicells, PTFE cells with 3 to 10mm inner diameter that seal on the film surface and allow for testing of the enclosed film. With such cells, cyclic voltammograms can be acquired in low pH solutions. Figure 5.10 shows the apparatus we are developing for automated acquisition of this type of data at a set of substrate positions. So far we have only demonstrated analysis of single substrate positions. The composition spread is contained in a large PTFE cell that

is similar to that of the fluorescence apparatus. The entire film is exposed to solution and pretreatment steps can be applied to the entire composition spread. The lowering of the minicell isolates the solution within the cell from the rest of the solution. While the entire film is still a common electrode, the effective working electrode is only the film exposed to the solution within the minicell. We are currently using a $\sim$6mm diameter cell which contains a coiled Au wire (counter electrode) and two capillary tubes, one for gas flow and the other for the reference electrode. The reference electrode tubing is filled with solution at the pH of the testing solution (usually pH=1) and provides a conducting pathway from a reference electrode bath to the minicell (the precludes the need for small form factor reference electrodes). A sliding seal provides atmosphere control even during substrate movement with respect to the minicell. The gas inlet within the minicell will eventually provide for oxygen reduction testing once a Pt counter electrode is installed (an O_2 flow rate of $\lesssim$0.1 L/minute into the minicell is sufficient).

CHAPTER 6

ANALYSIS OF ELECTROCHEMICAL FLUORESCENCE METHODS

6.1 Image processing and fluorescence intensity

Traditional analysis of electrochemical tests involve analysis of the working electrode current as a function of the applied voltage. For the continuous composition spread thin films, this current does not provide position-(or composition-)dependent information. As described in Section 5.1, we obtain composition-dependent data through detection of electrochemically-induced fluorescence. In this chapter we discuss the interpretation of this and other data obtained in parallel screenings. For the fluorescence assays, a series of CCD images are acquired, and Figure 6.1 outlines the simple image subtraction technique used to extract the fluorescence intensity images used in further analysis.

The high-throughput processing of the electrochemical fluorescence data is performed using a Labview program developed within the group. Many details of the program are in the manual (Appendix), but to get an idea, a screen shot taken during an analysis session is shown in Figure 6.2. The basic analysis procedure is to define a region of interest and calculate the average fluorescence intensity in the region (Figure 6.3a). A voltage-dependence that is exponential over $>$100mV indicates a voltage-driven reaction which could be either oxidation of the fuel (what we are looking for) or oxidation of the film (false positive). Removing the fuel and repeating the experiment addresses the false positive issue. The fluorescence onset potential is defined as the potential at which the fluorescence intensity crosses some critical value, with some additional qualifiers (monotonic, positive curvature). Figure 6.3 shows an example of the onset

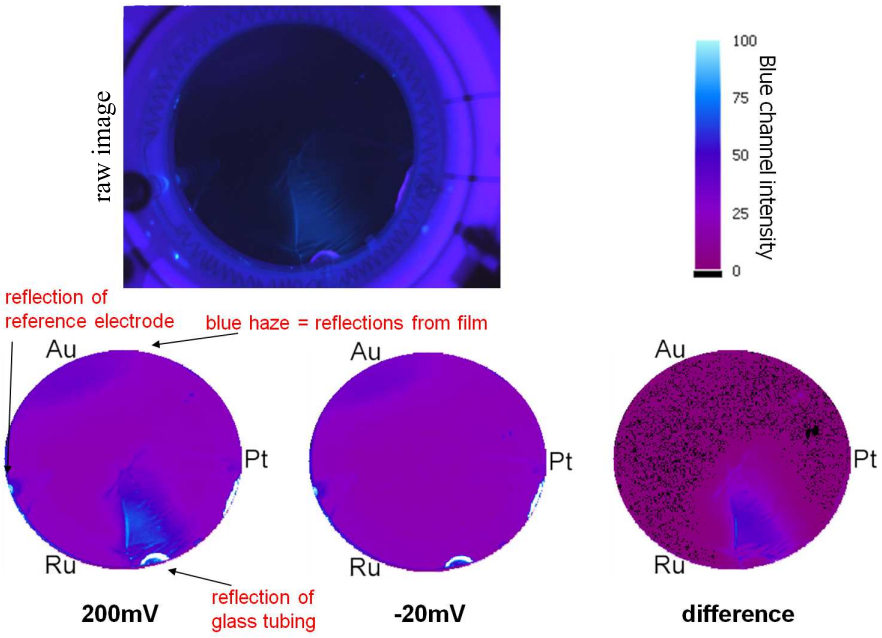

Figure 6.1: An image acquired by the CCD during a fluorescence assay of methanol oxidation for a Ru-Pt-Au composition spread thin film and the basic image processing. The bottom images are cropped versions of the raw image with the blue channel intensity plotted in false color. Image subtraction of the background image from the beginning of the scan (acquired at -20mV) from an image containing electrochemical fluorescence (acquired at 200mV) yields a map of the electrochemical fluorescence which is used for further analysis.

potential for an active region. The onset potential can also be calculated point by point and mapped onto a ternary composition diagram (Figure 6.3b) using composition maps(Chapter 3 or 4).

6.2 Modeling of fluorescence assay data

Section 5.2.4 includes a model for the evolution of fluorescence due to fuel oxidation in a linear sweep voltammetry experiment. The resulting general func-

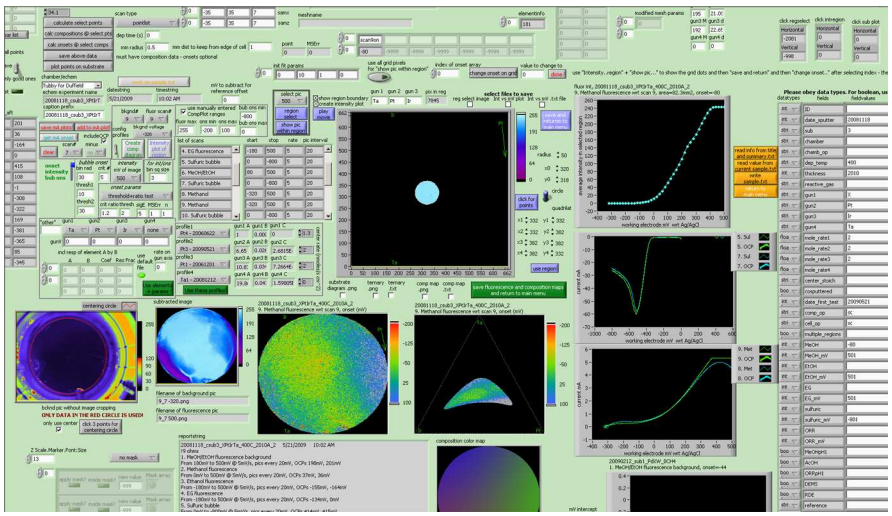

Figure 6.2: A screen shot of a fraction of the front panel of the Labview program used for analysis of fluorescence assay experiments.

tional form for the fluorescence intensity is

$$F = A\, n\, \ln\left(1 + \mathrm{Exp}\left(\left(E - E_{1/2}\right)\, n/\alpha\right)\right), \tag{6.1}$$

where F is the fluorescence intensity, E is the applied potential and α=59.1 mV at ambient temperature. The prefactor A, half-wave potential $E_{1/2}$, and number of electrons n in rate-limiting reaction are model parameters.

Determination of these parameters for a given catalyst-fuel system may provide insight into the reaction pathway. For example, the accepted models of methanol oxidation on Pt and Pt-Ru alloy catalysts reveal that the mechanism for the oxidation of adsorbed CO differs significantly for these two catalysts. This reaction is the rate limiting step for Pt and at high overpotentials occurs via reduction of water in an n=2 process. Hydroxyl species adsorbed on Ru in the alloy catalyst facilitate the oxidation of CO at lower overpotentials in an n=1 reaction. These mechanisms are reflected in the fluorescence assay of Pt-Ru alloy catalyst. Figure 6.4 shows the $E_{1/2}$ and n parameters determined from a fluorescence assay of a continuous Pt-Ru composition spread thin film. With

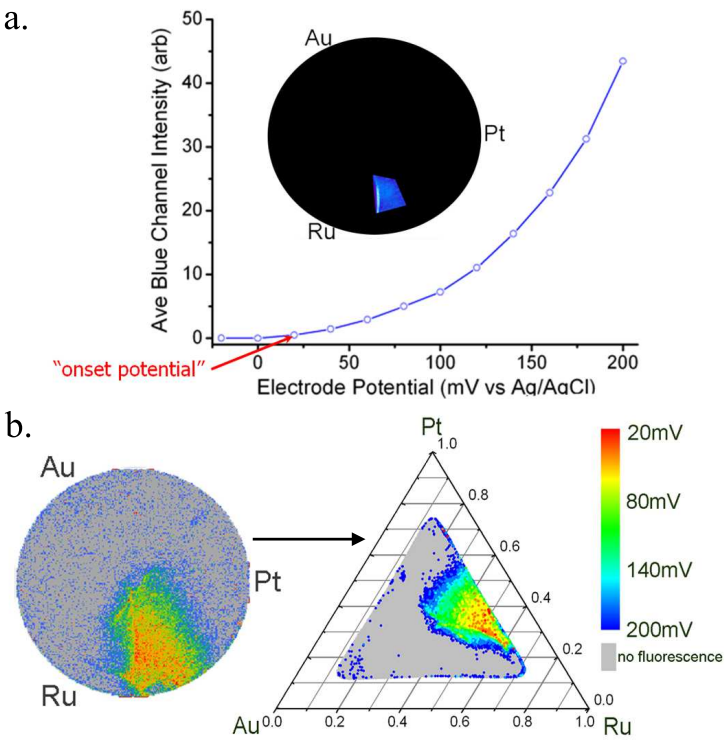

Figure 6.3: a. The fluorescence intensity profile for the active region of the dataset of Figure 6.1. The inset shows the substrate region with the selected active region. The plot is the average blue channel intensity in this regions as a function of applied potential with the points noting the mV values of image acquisition. b. The fluorescence onset potential is calculated as a function of substrate and mapped onto a ternary composition diagram. (All potentials are with respect to Ag/AgCl).

increasing Ru concentration, both $E_{1/2}$ and n decrease, with n remaining in the 1 to 2 interval. Thus, the fit data is consistent with the accepted models of catalysis in this chemical system. Expanding this type of analysis to new catalysts (i.e., plotting n as a function of composition) may help identify the rate limiting step in the reaction and in general help classify types of catalysts. However, further investigation of the fitting procedure, covariance among the parameters and sensitivity of the fitted values to data acquisition details are necessary to verify that this high level of interpretation of the fluorescence data is robust.

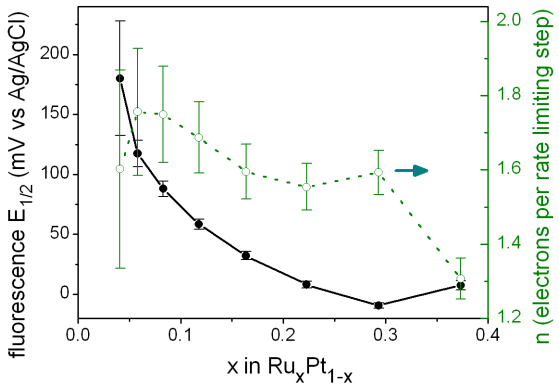

Figure 6.4: The fitted values of the half wave potential $E_{1/2}$ and effective number of electrons in the rate limiting reaction n are plotted as a function of composition for methanol oxidation in the Pt-Ru system. In a single methanol oxidation experiment, the fluorescence intensity of select compositions are fitted to Equation 6.1 and two of the three fit parameters are plotted with error bars calculated from the diagonal of the covariance matrix.

6.3 Analysis of bubbles of evolved gas

As mentioned above, the pretreatment sweep can also be viewed as a H_2 evolution experiment. As with the fluorescence assays of fuel oxidation, the current collected over the entire composition spread can tell you when a reaction started happening but it does not tell you where. After the H_2 evolution proceeds for a while, enough H_2 is created that bubbles form on the film surface and sometimes even stream into solution. One possible way of extracting a position-dependent figure of merit is to count the bubbles. The CCD images of the substrate taken during the potential sweep are analyzed for bubbles (Labview "blob" counting) and the positions of the bubbles are used to create number of bubbles vs potential plots for each region in a hexagonal tiling of the substrate. These plots are very similar to the fluorescence intensity profiles discussed above. Thresholding with a critical number density of bubbles provides

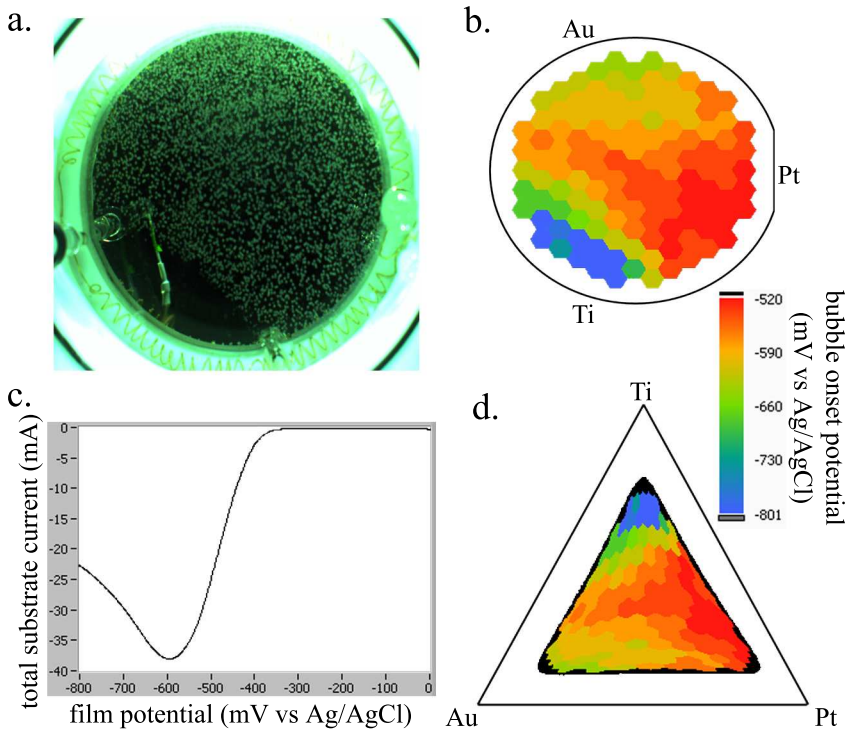

Figure 6.5: Analysis of H_2 bubbles for characterizing the catalysis of H_2 evolution in a pretreatment scan. The raw CCD image (a.) is segmented into hexagonal regions for bubble detection, which provides a bubble onset map (b.) that is mapped onto a ternary composition diagram (d.). This map provides the position dependence of the reaction with the onset potential of the best catalyst noted by the sharp onset of reduction current near -360mV.

the extraction of the "bubble onset potential". An example of the results of this process is shown in Figure 6.5. The results give the intuitively correct conclusions that the Pt-rich region contains the best catalysts and the Ti-rich region contains poor catalysts. The H_2 evolution current is shown in Figure 6.5c, the peak at -600mV is due to mass transport limitations; these could be the coverage of active catalyst sites by bubbles but I think it is the local void of H^+ in solution (this is done at pH=2 and the evolution current is really high).

This technique has some significant issues which have impeded its routine

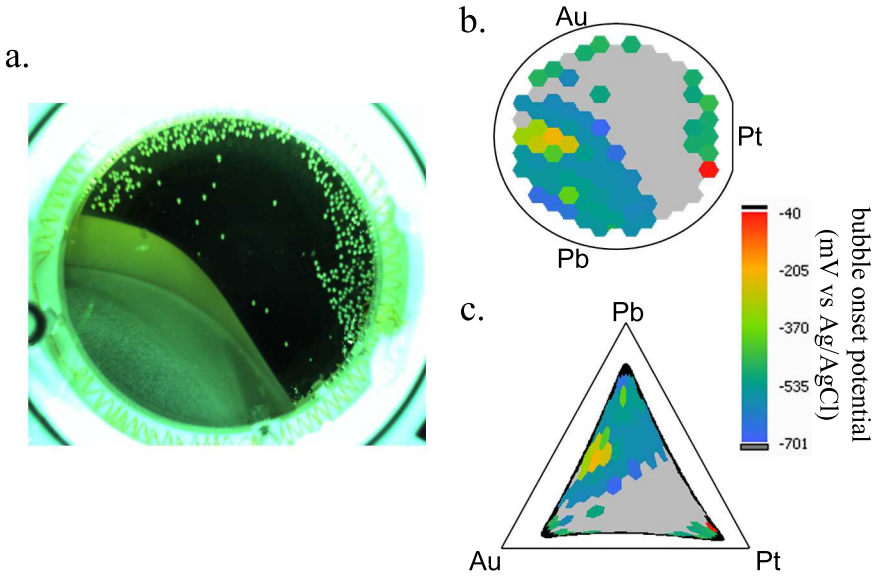

Figure 6.6: The same analysis outlined in Figure 6.5 is presented for a Pb-Pt-Au system, which highlights nucleation-based artifacts.

use in the high-throughput catalyst studies. First, if the desired figure of merit is onset potential, the bubble detection is a not an ideal approach as the bubbles form well after the onset of H_2 evolution. The catalysts with highest onset potential may be the first to show bubbles, but this is not guaranteed. The main issue is that the distribution of bubble nucleation sites (as a function of substrate position) can dominate the bubble onset profile. Figure 6.6 shows the bubble onset analysis of a Pb-Pt-Au system where the relatively great bubble onset of the Pb-rich region is most likely due to the plethora of nucleation sites available on this visibly rough surface. SEM images of such regions have shown 1 to 50μm mounds on the surface. A close look at Figure 6.5a reveals a high density of bubbles in the Au-rich region. Due to Pt-Au phase segregation, the Au-rich regions of Pt-Au-B films typically contains surface islands. We toyed with the idea of dispersing a powder on the film surface to even the playing field but decided the information gain is not worth the mess and possible resulting complications

during further testing of the film.

This technique could potentially be applied for the detection of CO_2 in formic acid oxidation studies (formic acid is an acid and is thus not conducive to study by electrochemical fluorescence).

CHAPTER 7

CATALYST SYSTEMS OF INTEREST

7.1 Overview of Pt-A-B

Based on the finding of high catalytic activity of ordered intermetallics PtPb and PtBi[27, 28] toward the oxidation of formic acid, an initial and lasting goal of the combinatorial subgroup of the CFCI was to search binary and ternary Pt-containing systems for new catalysts. While oxidation of formic acid continues to be studied, the oxidation of methanol is in some ways more interesting. So, details aside, the goal is to search Pt-A and Pt-A-B systems for methanol oxidation catalysts. While most of the samples I prepared belonged to this class of material, this dissertation contains detailed testing results for a only a few of these materials. Many of the systems show catalytic activity for methanol oxidation, but few of the systems were sufficiently characterized to provide an understanding of what makes that catalyst better than others. From the samples I have made, there are tens of thousands of fluorescence intensity images (I personally acquired much less than half of those). It is not enlightening to simply tabulate raw images so I will instead provide a brief summary of this project.

7.1.1 Choosing a set of elements

The first task in this project was to decide which elements to include in the Pt-A-B study, so I will start by noting that the initial thinking and game plan is included in Mark Prochaska's dissertation. One criterion is to rank the elements by their known Pt chemistry. That is, if A is known to be immiscible with Pt and

A is known not to be a catalyst then it is hard to imagine that mixing Pt and A at different ratios will lead to catalyst discovery. If Pt and A form a solid solution then we have something to work with. In fact this is the case for the world's most favorite catalyst system, Pt-Ru. If Pt and A form ordered intermetallics then that may provide further opportunities to identify energetic phenomena. If A is immiscible with Pt but B forms intermetallics with A and Pt, we might still consider the Pt-A-B system.

Pt-A and Pt-A-B ordered intermetallics are an interesting systems to study for a few reasons. Empirically, it is known that two members of this class, PtPb and PtBi, are excellent catalysts for formic acid oxidation. Such ordered intermetallics might lead to a radically different catalytic behavior due to the possibility of having a well-ordered surface in which the Pt atoms are in a geometry that has never before been explored. More practically, the enthalpy of mixing of Pt and A is generally much larger than if Pt and A formed an alloy with random site assignment. The high enthalpy of mixing, which can be estimated using the Miedema models[114], provides catalyst stability. For use in fuel cells this suggests that the catalyst may not degrade over time. For our electrochemical testing, this means that the element A may be stabilized with respect to oxidation and possibly leaching. For almost every metal, the oxidation potential in acidic media is lower than fuel cell anode operating potentials. Thus, on its own the metal will likely oxidize and will leach if the oxide is soluble. If the metal is incorporated into an intermetallic, we have a better chance of making meaningful measurements of catalytic activity as a function of composition. As we'll see in Section 7.3, some oxidation of A isn't necessarily bad.

7.1.2 The ones that have been tried

The Pt-A-B systems that have been studied from 2004-2008 are shown in Figure 7.1 (Pt-A binaries are on the diagonal). These 561 films were deposited by Mark Prochaska, Maxim Kostylev or myself (or associated undergraduates). Nearly every composition spread noted in this figure was deposited from two or three elemental metal targets such that the central region of the composition space was realized in the composition spread thin film. That is, most of the binary films were sputtered with 1:1 molar ratio of Pt:A resulting in a $\approx$ 0.1 to 0.9 range in the atomic fraction of A in the composition spread thin film. Some films were deposited to obtain a 2:1 ratio at substrate center, resulting in a $\approx$0.05 to 0.7 range in the atomic fraction of A. The study of more dilute concentrations of alloying elements in Pt is presented in the next section.

Most chemical systems were studied with 1 to 3 films usually deposited with identical composition range and different substrate temperatures. The systems with 4-10 films (indicated in Figure 7.1) most likely exhibited fairly good catalytic activity or modest activity on a Pt-poor region of the composition spread. That is, duplicate films were made to test repeatability or to allow for more detailed electrochemical or other characterization. The creation of more than 10 films in the same chemical system generally indicates the detailed study of new equipment or experimental processes rather than the detailed study of that chemical system. For example, new catalyst evaluation techniques are typically tested with a recently-deposited Pt-Ru film to demonstrate the viability of the test. In particular, the studies of differences in film properties resulting from deposition in Tubby vs. deposition in Gilgamesh were performed using Pt-Ti-Pb films.

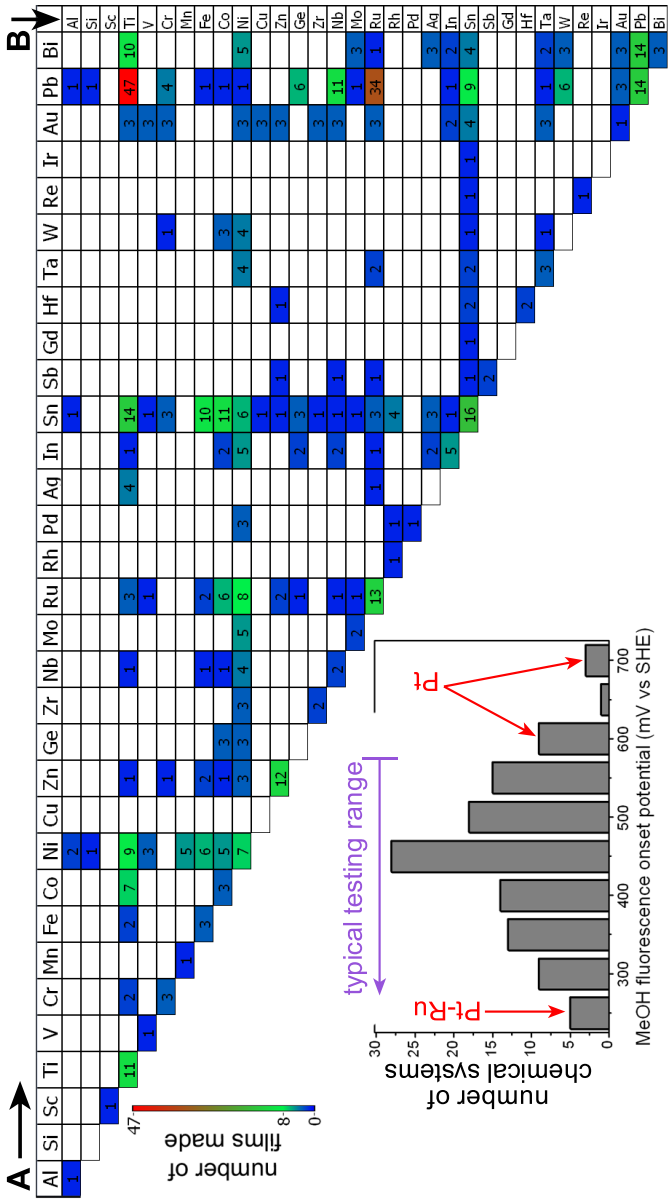

Figure 7.1: A summary of Pt-A-B composition spreads. For a given chemical system, the color scale and number indicate the number of films that have been prepared. The inset is a histogram that summarizes the electrochemical fluorescence results for these samples.

The inset of in Figure 7.1 is a histogram of the fluorescence onset potential for most of the electrochemical fluorescence tests for methanol oxidation performed on the Pt-A-B systems. There is a lot of information in this histogram; there are also a lot of issues. The basic message is that we have discovered a lot of chemical systems that are modestly horrible methanol oxidation catalysts. We have found a few chemical systems which are competitive with Pt-Ru but nothing that is paying the down payment on a direct methanol fuel cell company. The Pt and Pt-Ru labels show which bin those chemical systems belong to. Pt is associated with two bins because a Pt film that is treated the same as any of the other films goes into the higher onset potential bin and a Pt film that is cleaned in sulfuric acid and then immediately tested performs a bit better.

A superficial interpretation of the histogram might be that it is really hard to design a chemical system that is as bad as Pt and nearly impossible to add an element to Pt and make it worse than Pt. Well, as indicated by the purple arrow, most films were tested only to modestly high potentials (So if the onset potential is $>$600mV we never find out and the system is not represented in the histogram). Thus the high-potential region of the histogram is not an accurate representation of the distribution of behavior in Pt-A-B catalyst systems.

A more subtle complication with this figure is that not all of the chemical systems were tested under identical conditions protocols, and thus the catalyst test results can not be directly compared. Our research group has used 3 different electrochemical fluorescence testing systems over the years and only the most recent one has atmosphere control. The addition of the electrochemical pretreatment to the protocol step was made $\approx$ August 2007; many chemical systems show no methanol oxidation activity when this pretreatment step is omit-

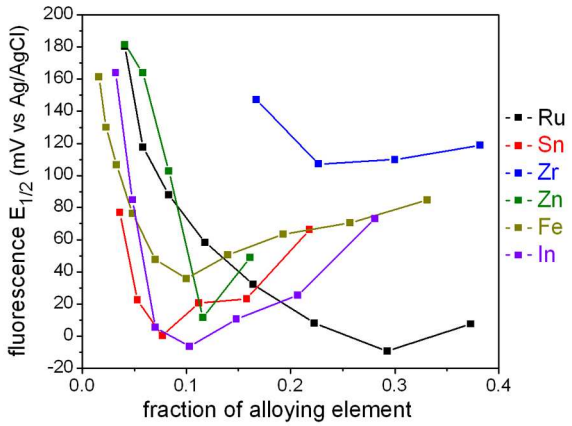

Figure 7.2: The electrochemical fluorescence-determined $E_{1/2}$ for the oxidation of methanol is shown as a function of the concentration of A in Pt-A systems.

ted. This means that some of the chemical systems, upon retesting, would end up in lower-potential bins. On the other hand, very few of the fluorescence onset potentials have been corrected for electrochemically-induced alterations to surface area. Applying this correction would result in some chemical systems moving to higher potential bins.

A final comment regarding this figure is that it says nothing about the composition of the active region in the chemical system. Obviously there is a difference in research value of a $Pt_{0.85}A_{0.15}$ catalyst and a $Pt_{0.2}A_{0.4}B_{0.4}$ catalyst with the same onset potential. The bottom line: combinatorial research that includes evolving research techniques makes for a very challenging data mining and data representation problem.

7.2 Binary fcc-Pt alloys

We have also looked at a lot of Pt-A and a few Pt-A-B systems at Pt concentrations 0.02 to 0.6. The original motivation for looking at this composition range came from Maxim Kostylev's work in the Pt-Sn system. He made films with substantial activity for the oxidation of methanol and other fuels. The most active films had a columnar structure with platelets that were Pt-rich on one side and Pt-poor on the other. This unique structure is the result of some poorly understood film growth conditions. To get a more easily studied film, we went to higher Pt:Sn ratio at substrate center and ≈300°C deposition temperature. As we will see, such a film is catalytically active and seemed to be more active for lower Sn concentrations where the phase is fcc-Pt and not the intermetallic Pt_3Sn. This result prompted a re-evaluation of the assumption that Pt-A intermetallics will likely be superior to Pt-A alloys (which originated from the PtPb and PtBi work). The question then arose "Are there certain elements that when alloyed into fcc-Pt significantly improve its activity and if so what are the distinguishing characteristics of these elements?"

Twenty elements A were chosen for the study of Pt-A composition spread films with center stoichiometry near 10at.% A. Figure 7.2 shows how the electrochemical fluorescence-determined $E_{1/2}$ for methanol oxidation changes as a function of composition for select Pt-A systems. The plots clearly demonstrate the existence of a single minimum in $E_{1/2}$ for each chemical system. Comparison of this data with known bulk phase diagrams leads to the hypothesis that the optimal concentration is the solubility limit of A in fcc-Pt. As discussed in Section 4.1 for the case of Pt-Ru, the solubility limit of A in Pt-A thin films may differ from the bulk thermodynamic equilibrium value. High energy XRD and

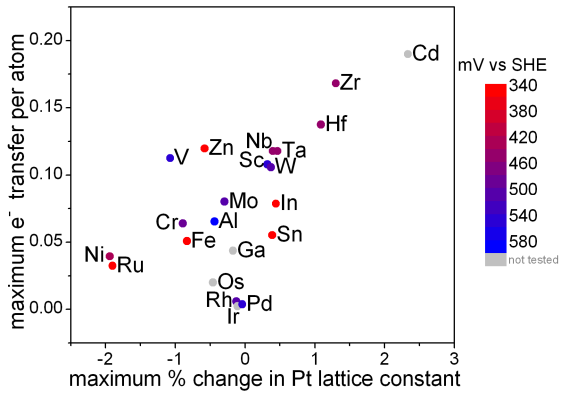

Figure 7.3: The electrochemical fluorescence-determined $E_{1/2}$ for the most active region of Pt-A films is plotted in the color scale. Each Pt-A system is plotted as a function of calculated material properties of the alloy at the solubility limit of A in fcc-Pt.

XRF measurements have been acquired on Pt-A for A=Pd, Rh, Pd, W, V, Hf, In, Ta, Ru, Sc, Ni, Fe, V, Ti, Zn, Cr, Mo, Nb, Zr. If A has a molar volume (for fcc 12-fold coordination) that differs significantly from Pt then tracking the fcc lattice constant as a function of composition will allow for determination of the solubility limit. If there is little shift in this parameter, the detection of the volume fraction of the most Pt-rich ordered intermetallic and extrapolating to zero will also work. If the solubility limit hypothesis is true then future work should involve investigation of ternary Pt-A-B systems where the solubility limit of A+B exceeds that of A or B in the binary systems.

Figure 7.2 also indicates that the catalytic activity is not solely a function of the solubility of A in fcc-Pt. We are considering a few other possibilities for governing parameters. One possible parameter that could be governing the catalytic activity and could really limit our ability to draw conclusions about the electrochemical properties of Pt-A is thin film fiber texture. A pure Pt film is highly fiber-textured in the (111) direction. My understanding is that Pt nanoparticles are typically more catalytically active for a given reaction due

to the high surface density of step edges. However, I have not found a study comparing methanol oxidation rates on different facets of single crystal Pt. Possibly, the role of small amounts of A in Pt-A alloys is to introduce facets that are more active than Pt(111) to the film surface. This possibility will also be investigated with the XRD data. The other possible parameters we are considering are chemical properties of A. For example, we know that the solubility limit is important and think that the electronegativity difference between Pt and A is important so maybe an important parameter is the product of these two quantities, the total change in electronegativity averaged over the fcc phase. Figure 7.3 shows the variation in the best $E_{1/2}$ for Pt-A as a function of the maximal change in lattice constant (product of solubility limit and difference in molar volume) and maximum electron transfer from Pt (product of solubility limit and electron transfer of an atom of A in Pt). The solubility limits are determined from phase diagrams. The differences in molar volume are calculated from indexed Pt-A XRD data[3]. The electron transfer per A is calculated using the Miedema model[114]. Clearly, these parameters do not sufficiently represent trends in the electrochemical data. Unless chemistry is as arbitrary as it sometimes seems, there must be other parameters or some details of the thin film surfaces that we do not understand (have not yet thought about).

Our implementation of combinatorial methods in catalyst studies has produced a database of electrochemical data that allows for data-driven hypotheses to be generated. The subsequent correlation of measured catalytic activity with measured and known film properties presents the possibility of empirically determining the governing parameters of catalytic activity and thus may be the best way to get into the tricky business of catalyst design.

7.3 *Manuscript, submitted:* Improved Fuel Cell Oxidation Catalysis in $Pt_{1-x}Ta_x$

7.3.1 Abstract

Sputter co-deposition of platinum and tantalum is used to generate catalyst libraries of $Pt_{1-x}Ta_x$ with 0.05<x<0.9. Extensive characterization of the libraries by high-energy x-ray diffraction reveals the presence of several ordered intermetallic phases as a function of composition and deposition conditions. Assessment of the activity for the oxidation of methanol and formic acid is achieved through a fluorescence-based parallel screening followed by detailed testing of the most promising catalysts. Correlations among the electrochemical results, the inferred phase fields and x-ray photoelectron spectroscopy characterization provide an understanding of the catalytically active surface and highlight the utility of composition spread thin films in catalyst research. The observations suggest that the interaction between Pt and Ta sub-oxides is important and enhances the catalytic activity of Pt.

7.3.2 Introduction

Fuel cells, in particular polymer electrolyte membrane fuel cells (PEMFCs), represent an attractive technology to meet future energy needs due to their potentially high efficiency in converting stored chemical energy to electrical energy. However, their widespread deployment has been hampered by materials limitations, as exemplified in the catalysts by their high cost, intolerance to fuel

contaminants and degradation leading to short fuel cell lifetimes. The possible use of methanol and other small organic molecules (SOMs) as PEMFC fuels is promising due to their high energy density and ease of transport, compared to H_2. Presently, one of the setbacks for implementation of SOM PEMFCs has been the lack of an anode catalyst that effectively overcomes the kinetic barriers for complete oxidation (to CO_2) of these complex molecules. Theoretical models that describe the complete oxidation of SOMs incorporate several adsorption and charge transfer steps that are optimized by surface atomic and electronic structure properties unique to the catalyst[52, 94]. During this oxidation process, CO formation (as an intermediate) is likely, and thus CO tolerance of catalysts is an implicit factor in oxidation catalysis studies using such fuels. CO tolerance is a particularly relevant property as it is also of importance for the anode catalyst in H_2 fuel cells. The poisoning of Pt catalysts by CO impurities associated with H_2 production from hydrocarbon reformation is a quintessential issue in catalysis. To address this issue, searches for new catalysts often involve modification of Pt by alloying with less-noble metals (including Pt-based ordered intermetallics)[26], creating layered structures with various elements[93, 146], and replacing the standard carbon support for Pt nanoparticles. Since the interfaces among electrode components often play an important role in catalysis and the electrode surface may be altered during operation as a catalysts, these ideal electrode archetypes are rarely distinctly realized. The influence of electrode modification on catalytic activity is most directly determined by characterization of the surface during catalysis, a notoriously difficult task. In the present work, we present an ensemble of characterizations that, when applied to a library of catalysts in the Pt-Ta system, provide insights into the composition and structure of the most catalytically active surface.

Tantalum Incorporation in Fuel Cell Catalysts

Recently, several methods of Ta inclusion in PEMFC electrode materials have been investigated. Ishihara et al.[80] demonstrated activity of partially oxidized tantalum carbonitrides for the oxygen reduction reaction (ORR) and noted the importance of the degree of surface oxidation. ORR catalysis was also studied on electrodes containing Vulcan carbon, Pt colloids and TaO_y formed by oxidation of Ta after its reduction from $TaCl_5$. The addition of Ta_2O_5 increased the area-specific ORR activity for only certain Pt-Ta_2O_5-C configurations, suggesting that any improvement in catalytic activity is related to the interfaces of the three components. $Pt_{1-x}Ta_x$ alloys have also been investigated as possible PEMFC cathode materials[21]. Composition spread thin films covering the entire composition range were found to be quite stable at oxidizing potentials in acidic media, but the catalytic activity for oxygen reduction dropped sharply and monotonically with increasing Ta content.

Studies of H_2 and CO oxidation have also been performed on TaO_y-modified Pt/C electrodes. CO oxidation on commercial Pt/C electrodes partially coated with Ta_2O_5 showed a 150 mV negative shift in the peak potential for oxidation of adsorbed CO[180]. Similar experiments were performed on Pt+TaO_y and PtRu+TaO_y electrodes[159]. The former electrode was made by coreduction of $Pt(NO_2)_2(NH_3)_2$ and $TaCl_5$ on Vulcan carbon. While the inclusion of TaO_y only lowered the CO oxidation peak by 70 mV (50 mV for PtRu+TaO_y), the authors also studied the time dependence of CO adsorption onto the electrodes and found that the inclusion of TaO_y significantly reduced the adsorption rate. This behavior indicates that the role of TaO_y in improving the CO tolerance of Pt is distinct from that of alloyed Ru. While surface Ru serves as a source of active

oxygen and thus enhances CO oxidation, TaO_y diminishes the adsorption of CO, possibly through a decrease in the Pt-CO bond strength. The Ta oxidation state was not characterized in these materials, but Lesnyak et al.[96] found that the use of a similar material as a gas phase H_2 oxidation catalyst resulted in partial reduction of the Ta_2O_5 support. The electrode, consisting of Pt nanoparticles on a Ta_2O_5 support, was characterized by XRD, electron diffraction and x-ray spectral micro-analysis both before and after use as a catalyst for oxidation of H_2 in a fuel stream with 20:1 O_2:H_2. The catalysis test resulted in a decrease in the oxygen stoichiometry from y=1.4 to 1.3, with both values slightly smaller for TaO_y regions adjacent to Pt particles. This partial reduction of the Ta resulted in the surface of the highly crystalline Ta_2O_5 support transforming into a nanocrystalline Ta_2O_5 + TaO_2 composite.

CO oxidation on $Pt_{1-x}Ta_x$ alloy thin films[148] and bulk Pt_2Ta and Pt_3Ta ordered intermetallics[37] has also been studied. The latter work found that the oxidation of adsorbed CO was shifted to more positive potentials for the intermetallic compounds compared to pure Pt. This shift could be due to an increase in Pt-CO binding energy and underscores a difference in the role of Ta in these materials and that of the Pt-TaO_y composites. The thin film $Pt_{1-x}Ta_x$ catalysts[148] were deposited on water-cooled substrates, and XRD characterization of the films indicated that the low deposition temperature kinetically stabilized Ta-rich bcc and Pt-rich fcc alloys. In addition, a nanocrystalline (or possibly amorphous) alloy (NCA) was observed for x >0.3. The thin film samples with 0.3< x <0.7 exhibited CO stripping onset potentials up to 50 mV lower than that of pure Pt and a corresponding small decrease in onset potential was observed for the oxidation of H_2 in the presence of CO. We studied $Pt_{1-x}Ta_x$ composition spread thin films deposited at elevated temperatures,

which enables the synthesis and electrochemical characterization of the ordered intermetallic phases. These films do contain an NCA region, and methanol oxidation on the as-deposited NCA demonstrates a similar negative shift in oxidation potential. However, we demonstrate further improvement in methanol oxidation activity via a catalyst pretreatment step. In addition, our study of methanol oxidation as a continuous function of composition, combined with the XRD mapping of the libraries, reveals important trends in catalytic activity.

Pt-Ta Material Properties

The equilibrium phase diagram for the $Pt_{1-x}Ta_x$ system is comprised of several ordered intermetallic phases. The phases discussed in the present work are listed in 7.1 but we note the existence of a low-symmetry Pt_4Ta phase as well as a high temperature (>1630°C) TaPt phase. Giessen et al.[58] present the phase behavior of $Pt_{1-x}Ta_x$ for x <0.5 and discuss isomorphism of the two orthorhombic Pt_2Ta phases highlighted in our discussion of electrochemical results.

Detailed XPS studies of TaO_y electrodes by Kerrec et al.[89] demonstrated the existence of several kinetically stabilized Ta oxidation states denoted by their oxygen stoichiometry and distinguished by Ta $4f_{7/2}$ binding energies. Binding energies of 23.5±0.4 eV, 26.1±0.4 eV, and 27.1± 0.2eV were associated with y=1, $1 < y \leq 2$, and y=2.5, respectively.

Table 7.1: Documented Crystallographic phases in the Pt-Ta system

Nominal Stoichiometry	PDF Entry	Crystal System	Abbreviation in Present Work
Pt	04-0802	Cubic	Pt-fcc
Pt_3Ta	18-0974	Monoclinic	βPt_3Ta
Pt_3Ta	03-1465	Orthorhombic	orth-$Pt_{1-x}Ta_x$
Pt_2Ta	03-1464	Orthorhombic	orth-$Pt_{1-x}Ta_x$
Pt_2Ta	18-0975	Orthorhombic	orth-$Pt_{1-x}Ta_x$
$PtTa_4$	04-1727	Tetragonal	$PtTa_4$
Ta	04-0788	Cubic	Ta-bcc

7.3.3 Experimental

Composition Spread Deposition

Films were prepared in a custom built combinatorial sputter deposition system described previously[65]. Each $Pt_{1-x}Ta_x$ library was created by first depositing an adhesion layer (underlayer) onto a 76.2mm-diameter Si substrate. During and after this deposition, the substrate was radiatively heated and maintained at the library deposition temperature. Elemental Pt and Ta (>99.9% purity) were co-deposited from separate magnetron sputter sources (Angstrom Sciences) in an atmosphere of 0.66 Pa Ar. With the aid of a cryoshroud[65], the background pressure during deposition remained in the 10^{-5} Pa range. The geometrical relation of the deposition sources with respect to the Si substrate provided a deposition gradient from each source that upon codeposition resulted in a continuous variation in composition across the substrate. The Pt and Ta deposition rates at substrate center were measured with a quartz crystal monitor just prior

to deposition of the library.

The range of x represented in a given library is dictated by the deposition profiles of the individual sources but may be shifted to the Pt-rich or Ta-rich range by control of the relative power delivered to the independent sources. Given the constant deposition rates, the film thickness is determined by deposition time, but the thickness at each substrate position is determined by the local deposition rates and chemical mixing of the elements. In the present work, three $Pt_{1-x}Ta_x$ libraries are discussed; they are distinguished by the underlayer, deposition temperature, thickness at substrate center ("library thickness") and stoichiometry at substrate center. Library A was generated with a 12nm Ti underlayer, 400°C deposition temperature, 160nm library thickness and x=0.25 at substrate center. Library B was generated with a 12nm Ta underlayer, 550°C deposition temperature, 160nm library thickness and x=0.5 at substrate center. Library C was generated with a 30nm Ti underlayer, 450°C deposition temperature, 35nm library thickness and x=0.33 at substrate center.

We note that Ti and Ta were chosen as underlayer materials due to their good adhesion of all elements commonly used in library depositions and demonstrated utility as a diffusion barrier to library contamination by Si. We also note that none of the $Pt_{1-x}Ta_x$ leached during electrochemical testing, and thus their catalytic properties were independent of film thickness.

Thin Film Characterization

We calculated the spatial map of composition in the libraries using verified models and measured deposition profiles for the Pt and Ta sources. The calcu-

lation also includes alterations in the deposition rates induced by resputtering events[63, 64]. The estimated uncertainty in the calculated values of x is $\lesssim 15\%$, comparable to that of common thin film characterization techniques. Within a given library, the relative composition accuracy is much better.

XRD characterization of the libraries was performed with a high-throughput crystallography setup which will be described in detail in a separate publication. Briefly, monochromatic 60keV x-rays impinge the thin film and the diffraction image is attained in transmission geometry by a 345 mm diameter image plate (Mar Research). The high x-ray energy affords detection of scattering wavevectors inaccessible with standard Cu Kα radiation, as evident in 7.4c. The diffraction patterns of the underlayer and Si are present in each diffraction image and are subtracted from each image as the first step in image processing. Subsequent analysis includes the integration of diffraction images to attain intensity vs. $|\mathbb{Q}|$, the magnitude of the scattering vector. These profiles are compared to patterns of known phases in the Powder Diffraction File (PDF)[3] and a phase map of the library is constructed.

Due to unique growth rates for each crystal facet, metallic thin films commonly acquire fiber texture during deposition. The resulting film consists of crystallites which are randomly oriented with respect to substrate azimuth but aligned with respect to substrate normal. Thus, a given reciprocal lattice vector occupies distinct values of χ, the angular displacement from substrate normal. The $50° < \chi < 140°$ range intercepted by the image plate is incomplete, and as a result the diffraction patterns used for phase identification may be missing peaks. Upon phase identification, the χ distribution of indexed peaks can be used to extract the average crystallite orientation in the film. This orientation

is important as it dictates the crystal facet at the film surface, which may ultimately determine surface chemistry and reactivity.

XPS spectra were obtained using a Surface Science Instruments SSX-100 with a 1 μPa base pressure. Sample orientation provided a 55° emission angle. Survey scans were performed with 150V pass energy from 0-600eV at 1eV/step. High resolution scans were performed with 50V pass energy from 15eV to 85eV at 0.065eV/step. $In\ situ$ cleaning of the film surface was performed by 15 s impingement of 4 keV Ar at 3 μA/cm^2 but minor residual surface contamination by hydrocarbons was inferred from the presence of a weak C 1s peak. While such contamination has negligible effect on the analysis of the Ta and Pt, the likely presence of oxygen in the contaminant layer confounds the measurement of oxygen in the film.

The 15 eV to 85 eV spectra were fit with one set of Pt 4f doublet peaks and either two or three sets of Ta 4f doublet peaks using the CasaXPS software package. We used the Shirley line shape to model the background and an asymmetric-Lorentzian peak shape, which we previously found to be appropriate for our sputter deposited thin metal films. For fitting procedures, the doublet peaks were constrained by the known binding energy shifts and area ratios.

Fluorescence Assay

In the last decade, a number of publications have presented combinatorial high-throughput methods for efficient exploration of the wide range of possible anode catalysts for direct methanol fuel cells (DMFCs). The fluorescence assay

used to screen catalysts was first employed by Reddington [127] and further adapted for thin films by Prochaska, et al [121]. The entire film is used as the working electrode in a specially designed electrochemical cell[66]. In the screening process, a pH-sensitive fluorescent indicator is used to identify catalytically active regions in a combinatorial library [121]. The potential applied to the film is swept to positive potentials, up to 500 mV vs. Ag/AgCl, at a scan rate of 5 mV/s with a large area Au coil as the counter electrode. The testing solution consists of 5 M methanol, 3 mM quinine, and 0.1 M potassium triflate as supporting electrolyte. The solution begins at neutral pH and as increasingly high overpotentials are applied to the film and methanol is oxidized, the released protons cause a decrease in pH below 5. Protonation of the quinine ensues and in this condition the quinine is fluorescent under UV illumination. Although the entire library is a common working electrode, the local generation of protons allows measurement of catalytic activity with $\lesssim$1 mm resolution via optical detection of fluorescence. Images are taken at 20 mV intervals with a charge-coupled device (CCD) camera, and at a given region of the library, image processing provides a fluorescence intensity voltammogram.

We previously presented[66] a model of this fluorescence profile of a Nernstian oxidation reaction:

$$F = A\, n\, \ln\left(1 + \mathrm{Exp}\left(\left(E - E_{1/2}\right)\, n/f\right)\right), \tag{7.1}$$

where F is the fluorescence intensity, E is the applied potential and f=59.1 mV at ambient temperature. The prefactor A, half-wave potential $E_{1/2}$, and number of electrons n in rate-limiting reaction are model parameters. In the present work we fix n=2 and extract the figure of merit $E_{1/2}$ through least squares fitting of the measured profiles.

Typical measurements of methanol oxidation by a pure Pt film result in an $E_{1/2}$ ≈340 mV vs Ag/AgCl. However, testing of a Pt film immediately after extensive electrochemical cleaning in a 0.1M H_2SO_4 solution results in an $E_{1/2}$ as low as 250 mV.

In addition to the routine fluorescence tests, a pretreatment of the film is performed to possibly reduce surface oxides that are formed upon air exposure and remove other surface contaminants. This pretreatment entails a linear voltage sweep from 0 to -800 mV vs. Ag/AgCl in an aqueous solution of 0.01 M H_2SO_4 with 1 M Na_2SO_4 as supporting electrolyte[66].

Localized Electrochemical Characterization

While the fluorescence assay allows us to efficiently identify the nominal compositions of promising methanol catalysts, additional testing is required to determine the catalytic properties under fuel cell (low pH) conditions. Localized electrochemical testing is enabled with a 6-mm inner diameter Teflon cell that isolates a 0.32 cm^2 film region. A 70-mm diameter cell seals on the edge of the substrate and is filled to expose the entire library (working electrode) to testing solution. The 6-mm cell contains counter and reference electrodes, and positioning the cell at a chosen spot on the substrate allows for testing of catalysts within a 5 at.% composition range. In the present study, this technique is used to acquire cyclic voltammograms (CVs) of select catalyst regions in solutions at a pH of 1. CVs acquired in the absence of fuel provide further characterization of the catalyst, and CVs acquired in the presence of fuel verify the activity of the catalysts in an environment that approaches fuel cell conditions.

To facilitate comparison of oxidation current densities, specific surface area measurements are performed on select catalysts. Due to surface roughness, the active surface area may be much larger than the projected geometric area. As previously described[66], a linear sweep voltammogram using 1 mM ferrocenemethanol in an aqueous solution of 0.1 M potassium triflate (supporting electrolyte) is used for determining the specific surface area of films. While this technique provides the true electrode surface area available to molecules comparable in size to ferrocenemethanol, the absolute area of Pt surfaces is quantified through analysis of hydrogen adsorption and desorption in 0.1M H_2SO_4.

7.3.4 Results and Discussion

Structural Characterization

The XRD spectra obtained from the high-throughput crystallography experiments are represented in 7.4. For Libraries A and B, the set of substrate positions characterized in the XRD experiments are shown as solid black dots on a composition map of the substrate. These diffraction spectra and their corresponding compositions are used to create an interpolated map of diffraction intensity vs. $|\mathbb{Q}|$ over the composition range of the library. Inspection of these maps reveals several phase boundaries as well as differences in the phase behavior of the two libraries. As seen in the plotted individual spectra and PDF patterns, the $Pt_{1-x}Ta_x$ ordered intermetallic phases exhibit a large number of reflections. The typical crystalline grain size of $\lesssim$10 nm results in a relatively broad diffraction peak line widths of $\gtrsim$0.7 nm^{-1}. Consequently many of the reflections overlap both within a given phase and among other phases, which

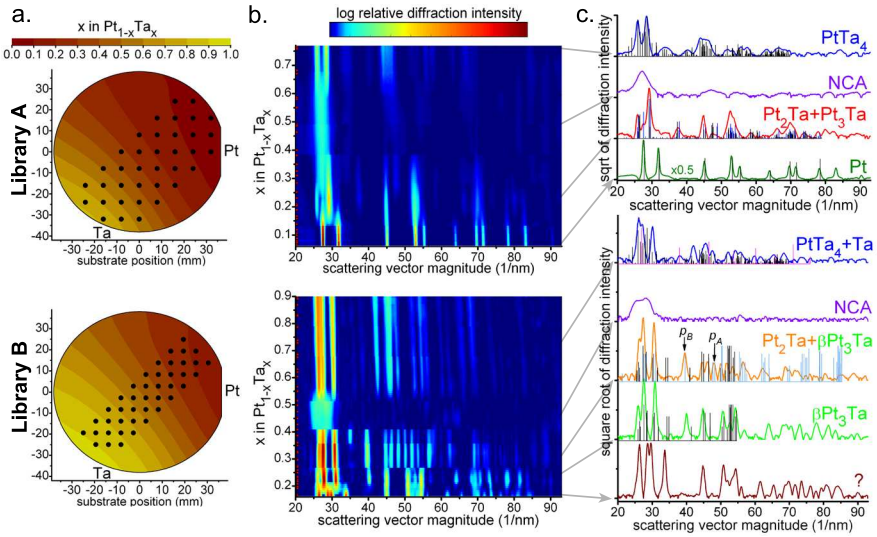

Figure 7.4: The composition and XRD mapping of Libraries A (top row) and B (bottom row) are shown. a. The value of Ta fraction x as calculated from deposition profiles plotted over an outline of the substrate. The element labels indicate the orientations of the deposition sources with respect to the substrate. The substrate positions analyzed by XRD are denoted by black points. b. X-ray diffraction intensities (color scale) as a function of scattering vector (horizontal axis) for measurements taken at various positions (indicated in a.), plotted with interpolation as a function of the corresponding x (vertical axis). The observed compositional ranges of peak sets outline the phase fields of the library. The specific compositions for which spectra were obtained are noted by small red markers on the composition axis. c. Representative spectra from each phase field are plotted to demonstrate phase identification. Reference PDF peaks for labeled phases (7.1) are plotted in black where relevant. For the Pt_3Ta + Pt_2Ta spectrum, PDF 03-1465 is shown in blue and 03-1464 in black. For the Library B $PtTa_4$+Ta spectrum, the Ta PDF peaks are shown in gray. For the Pt_2Ta + βPt_3Ta spectra, the Pt_2Ta (PDF 18-0975) lines are shown in blue with lattice constant reduced by 6% and the βPt_3 lines are shown in black with lattice constant increased by 2%. Relative diffraction intensities are on the same square-root scale across all compositions except that the plot corresponding to fcc-Pt has been multiplied by 0.5.

confounds rapid phase identification. The preferred orientation of the crystallites (see fiber texture discussion above) creates an additional complexity in interpreting the phase behavior of the libraries. However, analysis of both the correlated shifts in $|\mathbb{Q}|$-values of peaks and the appearance or disappearance of peaks as a function of composition assists in phase identification.

For Library A, the identification of the fcc-Pt (the pure phase for x <0.14) and $PtTa_4$ (the pure phase for x >0.67) phases is straightforward. From x=0.14 to 0.44, the set of reflections indicates the presence of an orthorhombic phase. As evident in the PDF patterns, orthorhombic Pt_2Ta and Pt_3Ta are distinguished by low-intensity peaks which are observed in all spectra in this composition range. While the relative concentrations of the two phases likely change as a function of x, in the present work we simply designate this phase region as orth-$Pt_{1-x}Ta_x$. This library also contains a phase with little diffraction intensity, other than a broad peak near 27 nm^{-1}. Similar diffraction spectra in this composition range have been presented for films deposited at low temperature[148, 21]. While this unidentified phase may consist of nm-scale grains of the high temperature phase PtTa, the lack of substantial grain growth even at our elevated deposition temperature suggests the possibility that this system forms a metallic glass [145]. Pending further study of this phase we denote it NCA (nanocrystalline alloy).

All phases except the NCA phase exhibit strong fiber texture with sharp peaks in the diffraction intensity distribution as a function of angular displacement χ from substrate normal. For the orth-$Pt_{1-x}Ta_x$ phases of Library A, this peak width is ≈10°, and analysis of the strongest reflections and their χ-distributions indicates that one or more of the following crystallographic planes

are oriented parallel to the film surface: Pt_3Ta (100), Pt_2Ta (010), Pt_2Ta (001).

Library B also contains the $PtTa_4$ intermetallic and an NCA phase but exhibits different phase behavior in the Pt-rich half of the library. For x <0.2, the XRD spectra indicate the presence of an ordered intermetallic phase but the pattern does not match any Pt-Ta entries in the reference literature[3]. Instead of the orthorhombic Pt_3Ta found in Library A, Library B contains monoclinic βPt_3Ta. The cause for this difference in phase behavior is not understood. The orthorhombic phase is believed to be stabilized by interstitial impurities such as oxygen[58]. Oxygen contamination should increase with the higher background pressure associated with increased deposition temperature, yet the orthorhombic phase is found in the library deposited at lower temperature. A more likely cause is an influence from the underlayer. At the start of the composition spread deposition, the Ta underlayer of Library B may nucleate a different phase than the Ti underlayer of Library A; once nucleated, the metastable phase can grow indefinitely.

While βPt_3Ta is present from x=0.19 to above x=0.4, as x increases beyond 0.27 the lattice constant discontinuously increases. At this phase boundary, several new peaks appear, such as the peak labeled p_A in 7.4c. These peaks are matched by a different orthorhombic structure of Pt_2Ta (03-1464 instead of 18-0975 used for Library A) after a 6% decrease in lattice constant is applied. This pattern also matches well with the peak labeled p_B, but this peak is present for x <0.27 and is the only peak in these βPt_3Ta spectra that does not match the monoclinic PDF pattern. The appearance of several new peaks in the spectrum of an ordered intermetallic suggests the addition of a second phase rather than ordering within the existing phase. We thus assert that orthorhombic Pt_2Ta is

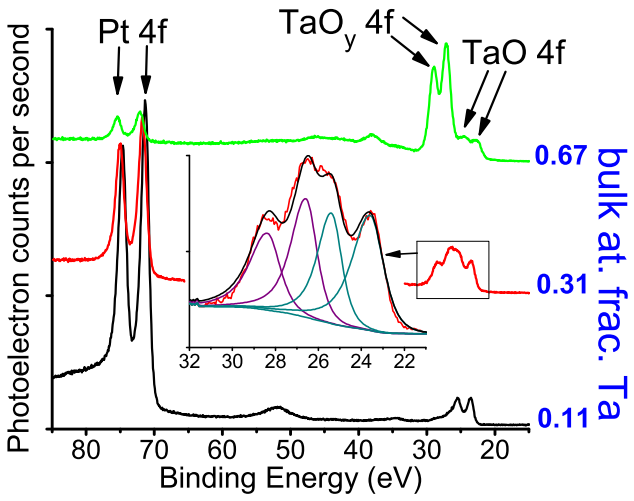

Figure 7.5: The XPS spectra obtained for three $Pt_{1-x}Ta_x$ samples. Each spectrum is labeled on the right with the respective value of x. The inset shows the Ta 4f region of the x=0.31 spectrum with the modeled background and four fitted peaks.

present on the Ta-rich side of this phase boundary but note that full understanding of phase behavior in Library B will require further analysis.

XPS Characterization

XPS characterizations (Figure 7.5) were performed on Library C. After electrochemical testing by the fluorescence assay (including pretreatment), the library was diced, and pieces centered at x=0.11, 0.31 and 0.67 were used for analysis. An additional x=0.31 piece was extracted from a library sputtered under identical conditions but not electrochemically tested. The peak energies and compositions extracted from peak areas are given in Table 7.2.

The values for the non-tested (as-deposited) x=0.31 film are not listed since the difference in each measured quantity from that of the tested x=0.31 film is well within the uncertainty of the measurement. The fact that there is negligi-

Table 7.2: Results of the XPS characterization of Library C.

bulk: x in $Pt_{1-x}Ta_x$	bulk phase	XPS: x in $Pt_{1-x}Ta_x$	XPS: mol frac. TaO_y /(TaO+TaO_y)
0.11	fcc (Pt)	0.13±0.03	0.26±0.08
0.31	orth-$Pt_{1-x}Ta_x$	0.42±0.05	0.45±0.12
0.67	NCA	0.89±0.03	0.88±0.08

bulk: x in	binding energies (eV)		
$Pt_{1-x}Ta_x$	Pt $4f_{7/2}$	TaO $4f_{7/2}$	TaO_y $4f_{7/2}$
0.11	71.3±0.3	23.6±0.3	25.9±0.5
0.31	71.7±0.3	23.6±0.4	26.6±0.4
0.67	72.1±0.3	22.6±0.8	25.1±0.5, 27.1±0.2

ble difference between tested and non-tested films indicates that any chemical surface modification that occurred during electrochemical testing was reversed upon re-exposure to ambient conditions. This result is in agreement with the observation discussed in the next section that the electrochemical properties of the active $Pt_{1-x}Ta_x$ catalysts are reproduced upon repeated testing with the effects of air exposure reversed by the electrochemical pretreatment.

The XPS measurements indicate that the film surface is enhanced in Ta compared to the bulk, which suggests that the chemical potential gradient provided by surface oxidation of Ta is sufficient to cause nm-scale diffusion of Ta to the surface. This effect is driven by the high heat of formation of TaO_y compared to PtO_z and was also observed in the $Pt_{1-x}Ta_x$ thin films of Bonakdarpour et al.[21].

The binding energy of the Pt $4f_{7/2}$ peak increases with increasing x and ex-

ceeds the 70.9 eV value for pure Pt, indicating partial charge transfer from Pt or a lattice strain effect. We note that in the event that the d-electron density decreases via e^- transfer to TaO_y, the Pt-CO binding energy would increase.

The Ta 4f binding energies also shift to positive potentials, but we consider the effect of e^- transfer with Pt to be negligible compared to Ta-O interactions. The lower binding energy Ta $4f_{7/2}$ peak listed in 7.2 is associated with the Ta^{II} chemical state. TaO has been identified in Ta electrodes with varying overall oxygen content[89] and is also found in our partially oxidized $Pt_{1-x}Ta_x$ electrodes over a wide composition range.

The XPS spectra indicate that for all x some of the Ta in the top few nm of the film exists in a higher oxidation state (higher binding energy) than TaO. The spectra from the $x = 0.11$ and $x = 0.31$ samples were both well fit by one set of high energy peaks while the $x = 0.66$ spectrum required two sets of such peaks to account for the observed data. The energies of the Ta $4f_{7/2}$ peaks are given in the last column of 7.2 and show that all three spectra have a peak associated with $1< y <2.5$. Only the x=0.66 sample has a peak in the y=2.5 range (i.e. Ta^{V}). The fraction of Ta in this highest oxidation state is 0.63 ± 0.1. For all three films, the fraction of Ta with any oxygen coordination $y>1$ is given in 7.2 and increases as expected with x. Pure Ta (x=1) is known to oxidize to form Ta_2O_5 (y=2.5).

Methanol Oxidation Activity by Fluorescence Assay

Fluorescence assays were performed on the libraries both before and after electrochemical pretreatment. For Libraries A and B, the results are summarized in 7.6, and we note that these results were comparable for all three libraries. The

fluorescence images reveal contours that correspond closely to the composition contours of 7.4a, and thus the activity of each library can be represented simply by its variation with composition (7.6c,f). The composition ranges associated with the ordered intermetallic phases (identified above) are also indicated in 7.6c,f. Dramatic correlation between the phase boundaries and the catalytic activity are apparent. The materials with highest methanol oxidation activity are found in Library A and have the orth-$Pt_{1-x}Ta_x$ structure with 0.24$< x <$0.32. A region with $x \approx$0.3 was chosen for further electrochemical testing as described in the following section. We focus further discussion of the fluorescence assay results on materials from Library A.

Without the reducing pretreatment, the section of the library with only orth-$Pt_{1-x}Ta_x$ is largely inactive for methanol oxidation. The fcc region as well as the orth-$Pt_{1-x}Ta_x$ + NCA two-phase region have slightly lower $E_{1/2}$ compared to a typical Pt film. After the pretreatment, the pure-Pt phase region exhibits a 60 mV decrease in $E_{1/2}$, the pure NCA region exhibits a 90 mV decrease in $E_{1/2}$, and the pure orth-$Pt_{1-x}Ta_x$ region exhibits a decrease in $E_{1/2}$ of over 300 mV, making it by far the most active catalyst in the library. After exposing the library to air for several days, we repeated the fluorescence assay tests and found that the same activity profile is observed both before and after pretreatment. This experiment was also performed several times on Library B with similar results. We therefore infer that the activity in the orth-$Pt_{1-x}Ta_x$ catalyst is related to the reduction of the surface from its air-stable state and that the reduction and re-oxidation are reversible and reproducible.

In the first anodic sweep after pretreatment, the orth-$Pt_{1-x}Ta_x$ region also fluoresces weakly in solution containing no methanol. The level of fluorescence

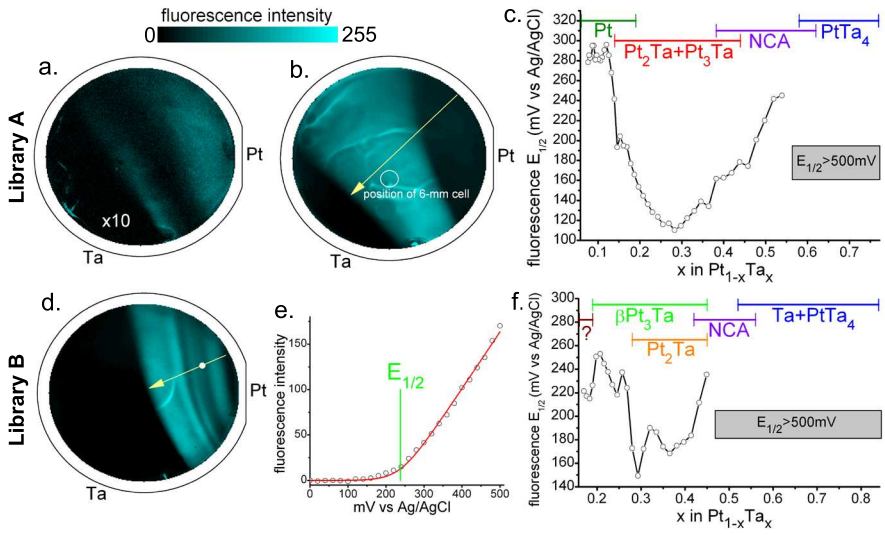

Figure 7.6: The fluorescence assay measurements of methanol oxidation activity are illustrated for Libraries A (top row) and B (bottom row). Figures a., b. and d. show images of the fluorescence intensity across the libraries in an outline of the Si wafer. All three images were acquired at 400 mV during a 5mV/s anodic sweep. Images b. and d. were acquired on pretreated libraries and show bright fluorescence from the active regions. Image a. was acquired with Library A after days of exposure to air and exhibits much lower fluorescence intensity (the intensity has been increased ten-fold for plotting). The sharp lines of brightest fluorescence (most evident in b.) are due to thermally-driven convection. The fluorescence intensity profile obtained by averaging the intensity over a 0.5 mm diameter regions (position of white dot in image d.) is plotted in e. along with the fitted profile (red curve) and fitted value of $E_{1/2}$ (green line). Values of $E_{1/2}$ were also acquired at 1.2 mm spaced points along the yellow lines shown in b. and d. These values are plotted in c. and f. along with the composition range occupied by each identified ordered intermetallic phase.

intensity is consistent with the release of ca. 2 H^+ per surface metal atom. While H^+s in this scan are possibly being released from the film, we believe the fluorescence is due to surface reoxidation. However, the surface must not completely reoxidize during this step because if the testing environment is kept under inert atmosphere, subsequent tests of methanol oxidation repeat the optimized activity profile.

In 7.6c, the variations of $E_{1/2}$ with composition are striking, but we note that the most Pt-rich composition with $E_{1/2}$ <200 mV is x=0.15 in Library A and x=0.28 in Library B. In Library A, this composition corresponds to the phase boundary of orth-$Pt_{1-x}Ta_x$ and the same is probably true in Library B (as discussed above). Apparently the existence of orth-$Pt_{1-x}Ta_x$ in the film results in a surface that has unique electrochemical behavior. While the XPS characterization demonstrates that the top few nm of the x=0.31 air-stable film contain approximately equal concentrations of two Ta sub-oxides, the electrochemical tests indicate that the most active surface is further reduced.

Further Electrochemical Study of Optimal Composition

A $Pt_{0.7}Ta_{0.3}$ region of Library A (outlined in 7.6b) was characterized by local electrochemical tests. In 7.7, the CVs of a pure Pt sample and the $Pt_{0.7}Ta_{0.3}$ sample are shown for pH=1 solutions containing no fuel, methanol, and formic acid. Comparison of the CVs obtained for each film in the three solutions provides insights into the chemical state and morphology of the $Pt_{0.7}Ta_{0.3}$ surface. The CV of $Pt_{0.7}Ta_{0.3}$ in the 0.1M H_2SO_4 solution contains the redox waves and hydrogen adsorption/desorption waves similar to those of a pure Pt electrode, in stark contrast to well-studied Pt alloys such as Pt-Ru. As expected, these features are

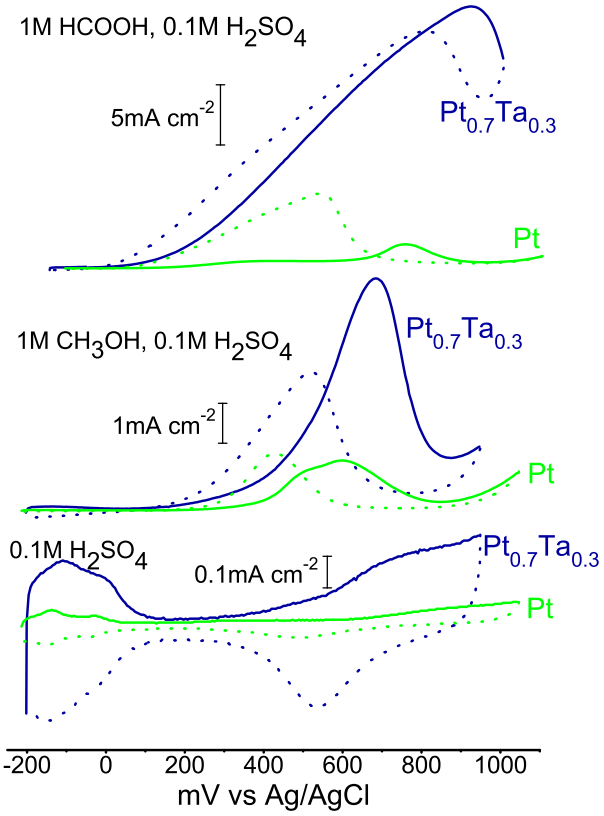

Figure 7.7: The cyclic voltammograms of Pt and $Pt_{0.7}Ta_{0.3}$ in 1 M formic acid, 0.1 M sulfuric acid; 1 M methanol, 0.1 M sulfuric acid; and 0.1 M sulfuric acid with a unique current density scale bar for each fuel. The forward scans are shown with solid lines and the reverse scans with dotted lines. The CV of $Pt_{0.7}Ta_{0.3}$ in 0.1 M sulfuric acid is indicative of a polycrystalline Pt electrode. The ensemble of characterizations indicate that this electrode contains a high density of Pt islands surrounded by TaO_y.

also seen in the Pt film CV, and for both films the hydrogen adsorption and desorption waves are used to calculate electrochemical surface areas of 0.23±0.06 and 1.15±0.1 cm^2 for Pt and $Pt_{0.7}Ta_{0.3}$, respectively. Compared to the film area accessed by the 6-mm cell (0.32 cm^2), these measurements imply specific surface area ratios (roughness factors) of 0.72 and 3.6. We have not identified the reason for the sub-unity value of the specific surface area of the Pt film, but for the present discussion we note that the $Pt_{0.7}Ta_{0.3}$:Pt area ratio determined by hydro-

gen adsorption is approximately 5:1. The surface area ratio between the same region in the Library A and the same Pt film was also measured via linear sweep voltammetry with a ferrocenemethanol redox couple as described above. This surface area ratio, 1.02±0.16, corresponds to an approximately equivalent surface area accessible by the ferrocenemethanol molecule on the two electrodes. Assuming a unit specific surface area ratio for the Pt film, this result suggests two possible surface morphologies of $Pt_{0.7}Ta_{0.3}$: completely flat and "conducting" (in the sense that all surface sites allow the charge transfer associated with the ferrocenemethanol redox reactions) or composed of electrochemically insulating material and "rough" conducting material such that the total area of the conducting material equals that of a flat conductor. Given the likely phase segregation of Pt and TaO_y, the latter morphology is plausible. The hydrogen adsorption measurement measures the surface area of "conductive" material within the assumption that all such material adsorbs H^+ with the same area density as Pt. While surface TaO_y may alter the surface capacity of adsorbed H^+, the ensemble of measurements advocates a model of the surface in which Pt and TaO_y are segregated at or below the nm scale and that the Pt regions contain sub-1.4 nm features (smaller than ferrocenemethanol molecule) which lend to an increased absolute surface area. Nevertheless, for calculating the oxidation current densities of small organic molecules, we may assume a unit specific surface area ratio.

On the anodic sweep, the methanol oxidation onset potential of the $Pt_{0.7}Ta_{0.3}$ catalyst is $\lesssim$80 mV lower than Pt, a smaller improvement than anticipated from the fluorescence results. The strong effect of the pretreatment step in the fluorescence testing and its assumed influence on nature of the surface oxide raises the question of whether this discrepancy is due to a difference in the pretreated sur-

face oxide in pH=1 vs pH=4 testing solution. While further investigation of the electrochemical properties of Pt-Ta surfaces may address this issue, the CVs of methanol and formic acid oxidation confirm that the presence of the surface oxide results in higher oxidation current densities. In addition, application of the model of Manoharan and Goodenough[103] to the CVs in methanol and formic acid indicates that a higher fraction of the fuel is being completely oxidized. That is, in contrast to those of Pt, the CVs on $Pt_{1-x}Ta_x$ demonstrate a greater forward oxidation peak height than reverse peak height. This difference is indicative of a diminished accumulation of carbonaceous species on the surface from incomplete fuel oxidation.

The model of sub-nm surface structure proposed to explain the surface area measurements and the strong correlation between fluorescence onset potential and the presence of orth-$Pt_{1-x}Ta_x$ present the possibility that the partially oxidized surface maintains a structure dictated by the underlying lattice. Future catalyst characterization by surface-sensitive (grazing incidence) XRD and scanning tunneling microscopy characterization will provide insight into this matter, and surface conductivity mapping via the latter technique may provide a better understanding of the Ta suboxide. However, we note that the desired surface condition is one that may be difficult to reproduce outside of the electrochemical environment.

7.3.5 Conclusions

Catalytic activity in the Pt-Ta system was investigated through extensive structural and electrochemical characterization. Thin film libraries containing Pt-Ta

ordered intermetallics, a nanocrystalline phase and an fcc-Pt alloy were tested as methanol oxidation catalysts with a parallel screening method. The included pretreatment step, which is similar to typical fuel cell start-up procedures, significantly improved the activity of the catalysts for methanol oxidation. The correlation of activity with the inferred phase fields suggests that the formation of a bulk orthorhombic structure facilitates the partial reduction of the surface TaO_y. The most active catalyst surface appears to be a Ta sub-oxide and Pt composite with $\lesssim$1 nm structure, and the interaction between these species results in less Pt contamination by carbonaceous species during the oxidation of methanol and formic acid.

7.3.6 Acknowledgements

This work was performed under the Cornell Fuel Cell Institute funded by the Department of Energy (ER06-02-13022-11751-11792). This work made use of the XPS facility of the Cornell Center for Materials Research with support from National Science Foundation (NSF) award DMR-0520404. The diffraction experiments were conducted at the Cornell High Energy Synchrotron Source (CHESS) which is supported by NSF award DMR-0225180. The authors thank Jon Shu for assistance with the XPS experiments and Darren Dale and Alexander Kazimirov for assistance with the diffraction experiments.

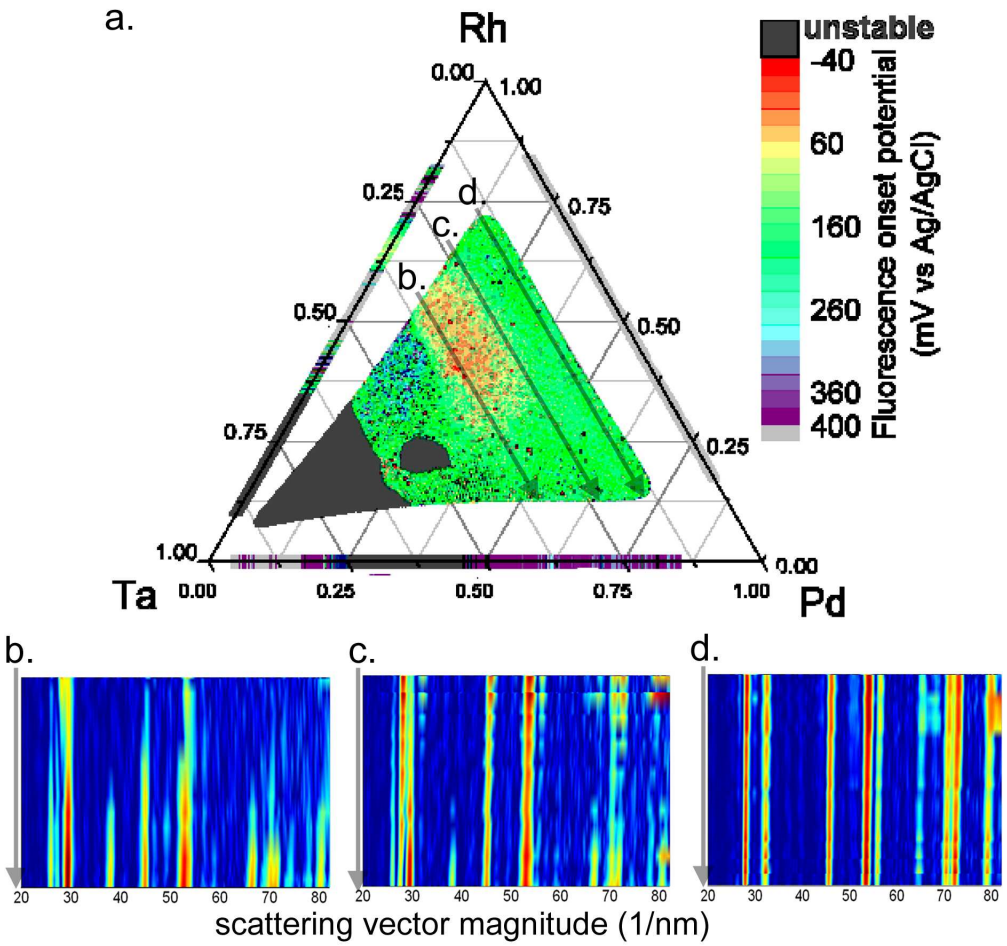

Figure 7.8: The fluorescence onset potential for the oxidation of methanol is plotted on a Pd-Rh-Ta ternary composition diagram. The results are compiled from three binary and one ternary composition spread. The most active region is located near the middle of the composition diagram. For the three indicated arrows, plots of diffraction intensity as a function of position along the arrow are shown for the same range of scattering vector magnitude.

7.4 Ordered intermetallics (A,B)$_1$Ta$_x$ with 0.25$< x <$0.4

During the initial high energy XRD experiments, I applied some intuition and some knowledge of binary phase diagrams to choose some ternary systems with unknown phase behavior that I thought could be interesting (possibly contain a ternary phase because I think phase discovery by composition spreads is cool). One such system was Rh-Pd-Ta. I still haven't finished analyzing the data to determine if I made a new phase, but fortune has it that this system contains one of the few decent catalysts with zero Pt content. The methanol oxidation data from the fluorescence testing is shown in Figure 7.8 and shows that $Rh_{0.68}Ta_{0.32}$ is a methanol catalyst and that much better catalysts exist in the $Rh_{0.40}Pd_{0.25}Ta_{0.35}$ region of composition space. Figure 7.8 also shows some diffraction intensity maps from the ternary system along lines of constant Ta concentration. The most Ta-poor diffraction map shows an fcc alloy at all Pd:Rh. The other two diffraction maps straddle the most active region and show correlation between catalytic activity and an ordered intermetallic phase that has not yet been identified.

While $Rh_{0.40}Pd_{0.25}Ta_{0.35}$ is not a fantastic catalyst and is very expensive due to primarily to the cost of Rh and Pd, this finding provides hope that good non-Pt catalysts are out there. By learning the mechanisms responsible for catalysis in this and other systems, we can formulate some potentially active non precious metal systems to try. Blindly poking around the incredibly large composition space of non-precious metal alloys does not seem prudent - we need leads.

Maybe there is a scientific explanation for the fact that the best catalysts in the Pt-Ta and Rh-Pd-Ta systems are ordered intermetallics with similar Ta stoi-

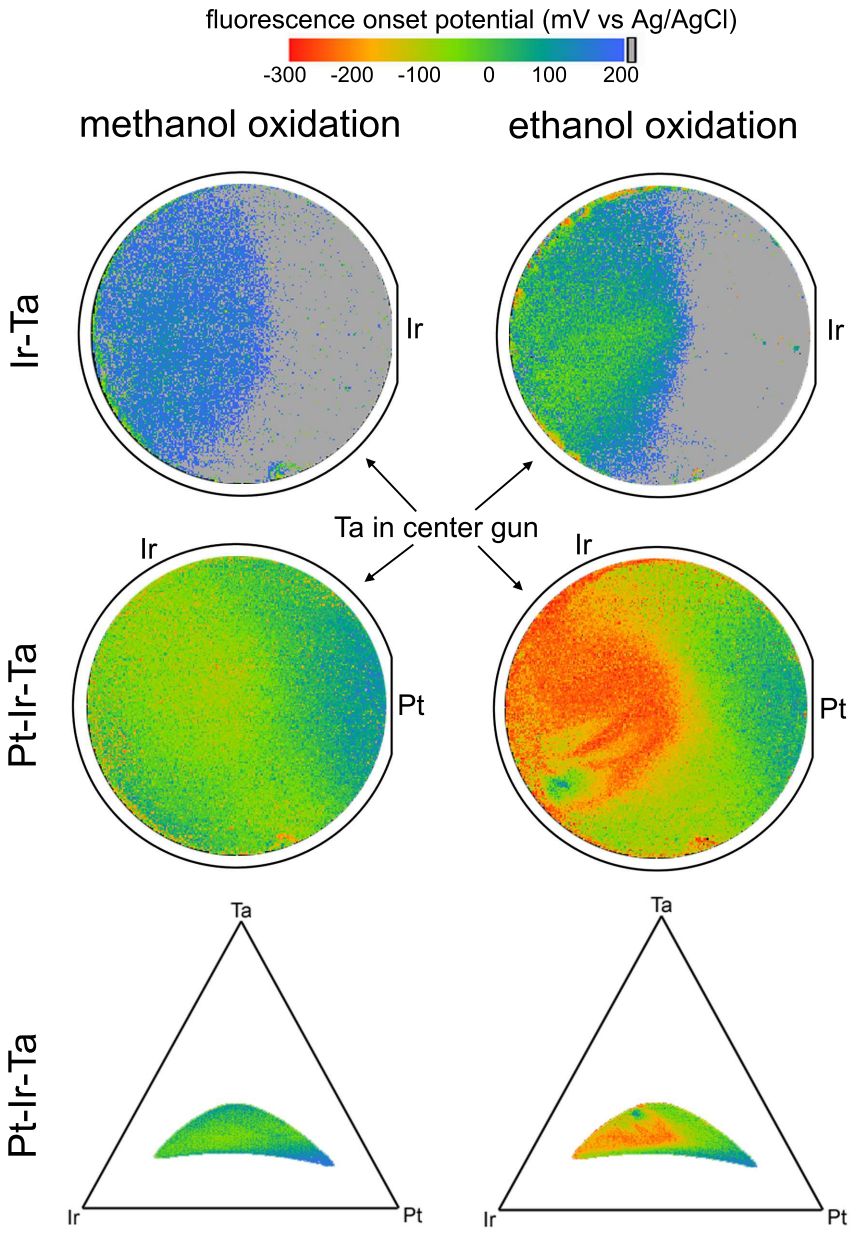

Figure 7.9: The fluorescence onset potential for the oxidation of methanol and ethanol. The Ir-Ta film (top row) has 3:1 center stoichiometry and the onset potential is plotted in the outline of the substrate with the Ir label indicating the orientation of the Ir source. Similarly, the onset potential for a Pt-Ir-Ta film with 1.5:1.5:1 center stoichiometry is plotted both within the substrate outline (middle row) and as a function of composition in the ternary composition diagram (bottom row).

chiometries. The answer may come from further analysis of these systems and other systems of the type (A,B)$_1$Ta$_x$ with 0.25$<$ x $<$0.4. Several such systems have been sputtered and analyzed both by high energy XRD and fluorescence assays. Almost none of the XRD data has been analyzed although some of the electrochemical data has been analyzed. The two systems that exhibit the most interesting electrochemical properties are Ir-Ta and Pt-Ir-Ta (Figure 7.9). These systems were deposited with Ta in the center gun to achieve the composition range 0.25$<$ x $<$0.4 (Figure 7.9). Further work is needed to understand these systems, but I will note that the ethanol fluorescence onset in Pt-Ir-Ta is about the lowest we've seen and is certainly the lowest in this range of Pt concentration.

A final note about these systems is that several A_3Ta phases (A is a precious or semiprecious metal) are known and the set of phases contains a few different structure types. Pretreatment is important for all the systems presented in this section, just as it was for Pt-Ta. From the Pt-Ta characterization I think it is safe to assume that the surface Ta in the active regions is oxidized, but clearly the existence of an underlying ordered intermetallic is important.

7.5 Transition metal carbides and their precious metals alloys

To branch out from the Pt-A-B catalysts, we ventured into mixtures of precious metals and transition metal carbides. We had two heuristic arguments for studying transition metal carbides as oxidation catalysts. First, carbides such as TaC and WC are used as catalysts in commercial high temperature gas reforming processes and are believed to have electronic structures that in some ways

resemble that of Pt. Also, there is a rule of thumb in catalysis that I interpret as the following: in catalysis you need a molecule to adsorb in a certain way to the surface and it might be helpful have an element in the catalyst that is also in the molecule. The more practical reasons to explore thin film carbides are: these materials have not been looked at very closely for fuel cell anode applications; we were pretty sure we could make them in sputtering and could easily mix them with precious metals (more easily than via traditional chemistry methods); the carbides are refractory and are known to have decent chemical stability which gives hope for the creation of robust catalyst with low or no precious metals.

In designing the study we were faced with the options of a dozen carbon-loving transition metals, a few interesting carbon stoichiometries for each transition metal, and a few precious metals to mix with the carbides. The idea of mixing the carbides with precious metals is that the two classes of materials may optimize different parts of the fuel oxidation and could together be phenomenal catalyst; this makes sense only if one assumes that the codeposition results in nm-scale phase segregated carbide and precious metal (see below for evidence that this is a bad assumption). We focused on pseudobinary systems A-B-C, where A is a precious metal (Pt, Pd, Ru), B is an early transition metal (W, Ta, Mo, Ti, V) and C is actually just carbon. The carbon stoichiometry is determined by the concentration of the carbon source CH_4 in the deposition atmosphere. Ti and V have not yet been extensively explored, so for the current discussion B=(W, Ta, Mo).

W, Ta and Mo each have a few known carbide phases, generally of the B_2C and BC stoichiometries with one or two structure types per stoichiometry. To make hydrogen incorporation in the film as thermodynamically unfavorable

as possible, all depositions were performed at elevated temperature (usually 400°C), and in our heaters' range, temperature is not expected to dramatically affect growth of the refractory carbides (T_m >2500K). Thus, CH_4 concentration is the main parameter we have to control carbide phase and the expectation is that it governs only carbon stoichiometry (that is, we have no independent control of structure type). Trying three different CH_4 concentrations gives us 4x3x3=36 composition spreads to explore A-B-C and B-C systems. This assumes we can astutely pick the methane concentrations without $a\ priori$ knowledge - we couldn't - this took many additional experiments.

The summary of the project is that due to some surprises (see below discussion of phase behavior) and some learning about how to deposit these materials, we made 70 films and tested nearly all of them for methanol, ethanol and ethylene glycol oxidation. Out of the 36 chemical systems, the films covered all of the A-B systems, except for a couple of the B=Mo systems. None of the tested A-B-C systems demonstrated better catalysts than the corresponding A-B system. I think the materials should be revisited for oxygen reduction studies as well as H_2 oxidation in the presence of CO. I would be wary about using the same films after all that has been done to them, especially since W oxides are soluble in the pH range of the fluorescence testing but are not soluble at the more interesting range of pH$\lesssim$1. We still learned a lot about the carbides and phase behavior in A-B-C systems and the remainder of the section will describe some of the interesting properties.

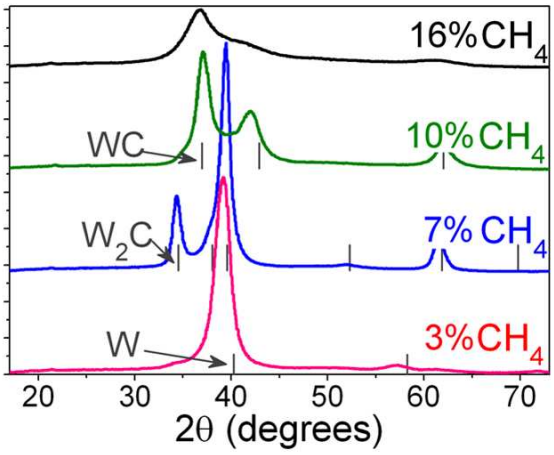

Figure 7.10: Diffraction spectra are shown for films deposited from a single W source with the labeled concentration of CH_4 (balance is Ar) in the deposition atmosphere. The indexed peaks for the bulk carbide phases[3] are also shown.

7.5.1 Carbide phase control and electrochemical stability

For the B-C systems (no precious metal), phase control was achieved through variation of the CH_4 concentration for each B=(W, Ta, Mo). The total sputter pressure was always kept at 5mT with gas composition controlled by the flow rates of Ar and CH_4. For B=W, diffraction spectra at four CH_4 concentrations are shown in Figure 7.10. At low carbon content, the material is carbon interstitially dissolved in the bcc-W lattice (evident by increased lattice constant). At higher carbon content, the W_2C and WC phases are acquired. Further increase in carbon content likely increases carbon stoichiometry in the fcc WC_{1-x} phase with the XRD signature being the decrease in grain size. Similar phase behavior is seen for B=Ta and B=Mo. The Mo films were not as extensively characterized. While the B=W films seemed to be phase pure everywhere in the thin film with some evolution in fiber texture and slight lattice constant shifts, the mid-range carbon concentration B=Ta films showed different phases as a function

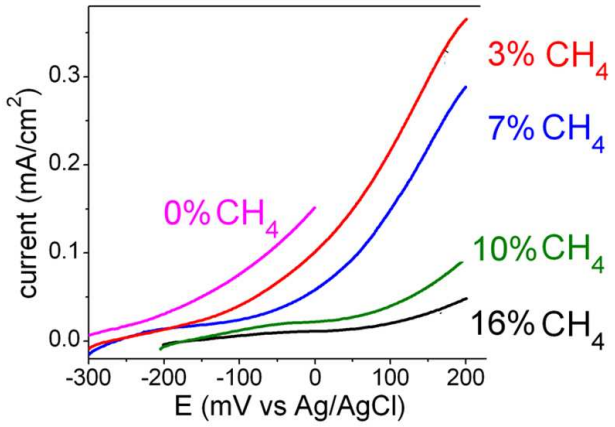

Figure 7.11: The current from the entire composition spread during a 5mV/s anodic sweep in aqueous 3mM quinine, 1M potassium triflate solution. The oxidation current is likely due to the oxidation of the W in these approximately constant composition films with different carbon concentrations due to deposition in different (labeled) concentrations of CH_4.

of distance from the Ta gun. Such variations are likely due to differing carbon concentrations as a function of angle from the deposition source and complicate systematic studies of composition in A-B-C systems (measurements of carbon stoichiometry in thin films are confounded by relatively low signal to noise and other possible sources of the carbon signal, such as pump oil in vacuum systems).

During electrochemical testing in the fluorescence setup, the stability of the B-C films clearly increased with increasing carbon content. Electrochemical fluorescence was produced during each experiment, regardless of the presence of a fuel. Thus, the fluorescence and corresponding oxidation current must be due to oxidation of the film. As indicated in Figure 7.11, the voltage required for a given oxidation rate increases with carbon content, indicating that the stability of WC_{1-x} increases with x. The only source of uncertainty in this result is that we have not sufficiently demonstrated that the reduced oxidation currents are

not due to graphitic carbon agglomeration on the film surface, which would protect the underlying film from oxidation (graphitic carbon oxidation is kinetically slow).

A final note on carbide electrochemical results is that for all A-B-C systems, the thin films were found to be stable in all electrochemical fluorescence testing for C:B$\gtrsim$0.5 and A:B$\gtrsim$0.2. Thus, precious metal - transition metal carbide composites pass a basic test for fuel cell compatibility, but none of the compositions we tested are good catalysts.

7.5.2 Phase behavior of cosputtered carbides

As mentioned above, the initial expectation for the phase behavior of cosputtered precious metals was that they would phase segregate. As it turns out, lots of interesting things happen in the small sections of the ternary A-B-C phase diagrams we explored. Two illustrative systems are the pseudobinary systems Pt-TaC_{1-x} and Pt-WC_{1-x}, where the three different end members have fcc structure type.

The phase behavior of thin film Pt-Ta was presented in Section 7.3. A Pt-TaC_{1-x} sputtered in 10% CH_4 was analyzed by the same high energy XRD technique. Comparison of Figures 7.12a. and 7.12b. demonstrate that the presence of carbon strongly influences the phase behavior. The Pt-Ta system contains a few ordered intermetallic phases, but the Pt-TaC_{1-x} system contains only the end member fcc phases. The detailed view of fcc {111} reflections in Figure 7.12c. show that there is no peak shifting due to lattice constant shifts as a function of composition. Figure 7.12d shows that both fcc phases have lattice con-

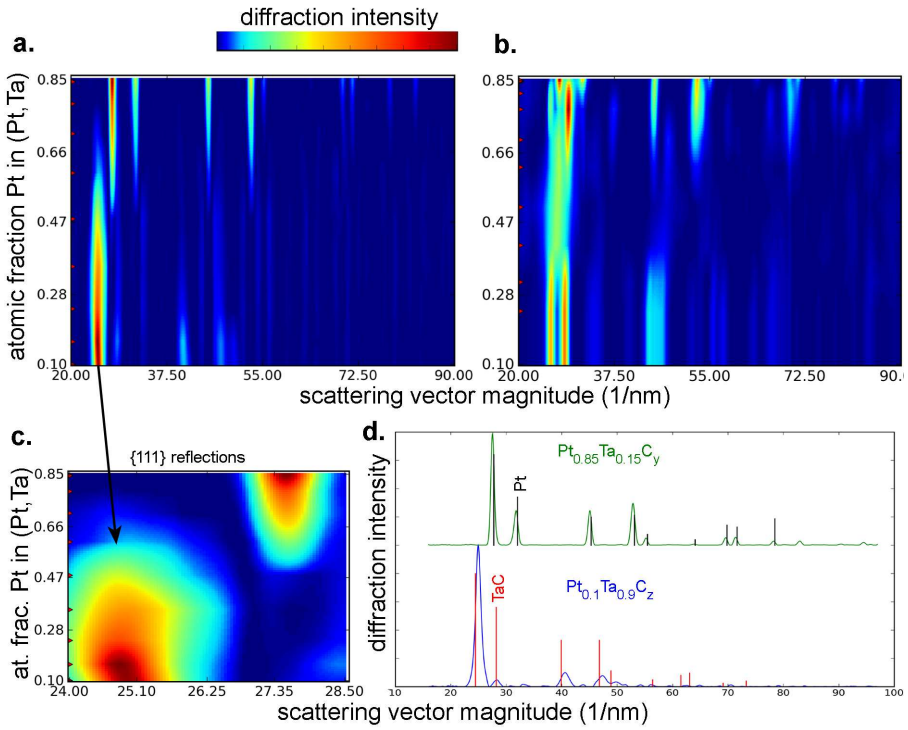

Figure 7.12: a. XRD intensity plotted as a function of the scattering vector magnitude and concentration of Pt. The composition spread thin film contains Pt, Ta and C, but the plotted Pt concentration is the Pt/(Pt+Ta) atomic fraction. b. For comparison, diffraction data for a Pt-Ta thin film is plotted in the same axes. c. An expanded view of (a.) shows only the fcc-{111} peaks and demonstrates the lack of a lattice parameter shift as a function of composition. d. The most Pt-rich and Pt-poor line profiles from the data in (a.) are shown along with the indexed[3] powder patterns for Pt and TaC.

stants shifted from their bulk equilibrium value. The larger TaC lattice constant may be due to the sub-stoichiometric carbon concentration (carbon is interstitial in TaC). However, the lattice shift is also consistent with a $\lesssim$10% solubility of Pt in TaC. Similarly, the deviation of the $Pt_{0.85}Ta_{0.15}C_y$ diffraction peaks from the Pt pattern suggest solubility of $\lesssim$10% TaC in Pt (this TaC may be very carbon poor). In this type of limited solubility system, the Pt and TaC phases should coexist at all compositions between the solubility limits. However, each phase

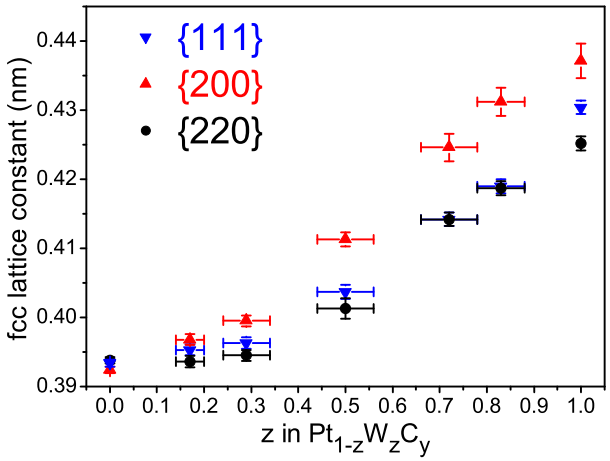

Figure 7.13: Peaks in the XRD line profiles of Pt-WC_{1-x} films at the noted Pt:W compositions were used to calculate the fcc lattice constant through assignment of the indicated fcc reflection.

is undetectable for a significant fraction of that composition range. This may be due to the fact that a dilute segregated phase has little chance to form large grains and may be undetectable by these XRD experiments (In GADDS spectra, a 5° peak at 2θ=30° would be undetectable; by the Debye-Scherrere equation, this would correspond to a ~2nm grain size.). High energy XRD or electron diffraction may resolve crystalline phases with small coherence lengths.

Very different phase behavior is found in the Pt-WC_{1-x} system. Films in-line with this chemical system have not been investigated by high energy XRD but several films deposited in 16% CH_4 and varying Pt:W stoichiometry ranges have been characterized on the GADDS instrument. The diffraction images indicate that the film structure characteristics measured in the diffraction experiment all vary smoothly across the entire Pt:W composition range. WC_{1-x} prefers (100) fiber texture while Pt prefers (111) fiber texture and the films evolve between these fiber textures and become equiaxed in the central composition region. The grain size ($\sim 1/$peak width) decreases monotonically with WC_{1-x} content, and

the peak positions shift monotonically with WC_{1-x} content. Using the three measured fcc reflections, the fcc lattice constant was calculated as a function of composition and the results plotted in Figure 7.13. These results indicate complete solid solubility in the Pt-WC_{1-x} system. However, we do note two atypical phenomena shown in Figure 7.13. First, while the three independent calculations of lattice constant at fixed Pt:W provide comparable results for high Pt content, these numbers diverge with increasing W content. The 10% CH_4 line profile in Figure 7.10 shows that this is a real effect. I do not understand what is going on. The other atypical property of this system is that the lattice constant does not shift linearly with composition, a deviation from Vegard's law. This is likely due to a variation in the value of y as a function of z in $Pt_{1-z}W_zC_y$. At z=0, y=0 and y is most certainly monotonic in z and remains $<$1. Assuming the carbon is interstitial and the effective volume per carbon is constant, if y is linear in z then the lattice constant shift should be linear in z. However, with $decreasing\ z$, the Pt coordination of each C increases, which may lead to a super-linear decay in y. In the approximation of constant effective molar volume of C, this phenomenon could give rise to the super-linear trend in Figure 7.13. Also, the chemical bond strength among Pt and W may change as a function of z, especially if y is varying significantly, and this change in bonding can also give rise to curvature in the alttice constant profile. The composition in the figure is calculated from deposition profiles. Measurements of both z and y would certainly help understand the film properties, but as noted above, such measurements are experimentally difficult.

While these thin films may contain materials that are far from equilibrium, all of these results are important for the fuel cell cathode research involving Pt on WC and related catalysts [133, 176]. In particular, the alloying of Pt and

WC has implications for the microstructure of electrodes synthesized by co-precipitation of Pt and WC.

CHAPTER 8

THE SEMICONDUCTING SCN-YN SYSTEM

The deposition of high quality films of these nitrides require a high deposition temperature and a very low partial pressure of reactive gasses (O_2, H_2O) in the vacuum system, conditions accessible in Tubby. ScN and YN were known to be indirect semiconductors with high absorptivity in the visible range, but the phase behavior of the ScN-YN system had not been explored. The discovery of a direct-gap semiconductor in the ScN-YN system would give these materials great potential as absorbers in photovoltaics. As it turns out, we did not find a direct-gap material, but we did find that ScN and YN form a solid solution with a remarkably high ≈9% change in lattice constant. Also, our optical data suggests that the calculated band structure of YN needs revisiting (only a small amount of moderate-quality work is published on YN and there are discrepancies with our results).

8.1 *Manuscript:* High Mobility, Single Crystalline ScN and Single-Orientation Epitaxial YN on Sapphire via Magnetron Sputtering

8.1.1 Abstract

The mechanical, chemical, and electronic properties of the lanthanoid nitrides give this class of materials many potential applications. While ScN research activity has sharply increased recently, investigations of growth methods for opti-

mizing structural and, more importantly, electronic properties are still needed. YN has received some theoretical but very little experimental attention. We present results of x-ray diffraction and atomic force microscopy analysis of film structure as well as Hall effect measurements of electronic properties for sputter-deposited ScN and YN. Films are deposited at select values of sputter gas stoichiometry, gas pressure and substrate temperature, and optimal values are suggested. Additionally, the role of deposition geometry is investigated. Grown under optimal conditions, ScN films are single crystalline and YN films are singly oriented with both nitrides exhibiting the same epitaxial relation to α-$Al_2O_3(1\bar{1}02)$ substrates. Our films also exhibit the highest documented electron mobility for the respective materials, despite their high carrier concentration.

8.1.2 Introduction

Transition metal nitrides have been incorporated in numerous commercial applications. For example, TiN, which crystallizes in the rock-salt (B1) structure type, has been extensively studied and is commonly used as a protective coating due to its chemical stability and high hardness. However, the neighbor transition metal nitride, ScN, has only recently been receiving significant attention. Furthermore, its 4d analogue, YN, is almost completely unexplored. Both ScN and YN crystallize in the same rock-salt structure as TiN and have similarly high melting temperatures in excess of 2500°C [154, 49, 87]. Measurements on sputtered ScN indicate that its hardness of $\sim$21 GPa rivals that of TiN[54].

Recent theoretical work indicates that both ScN and YN are indirect semiconductors[123, 147, 158, 56]. Experimental characterization of ScN films

by optical techniques[56] and optical techniques combined with scanning tunneling spectroscopy[5] have suggested minimum gap values of 1.3±0.3eV and 0.9±0.1eV respectively. A measured indirect gap has not been reported for YN, though recently the gap values have been calculated to be 0.85eV[147] and 0.54eV[158]. The measured optical gaps of ScN and YN are 2.15eV and 1.5eV respectively[5, 43].

Semiconductor applications of ScN in junctions such as ScN/GaN or in alloy semiconductors such as $Ga_{1-x}Sc_xN$ are currently under investigation[41, 97, 34], and similar applications for YN have also been proposed[36]. ScN may also have applications as a host for magnetic transition metals. Recent density functional calculations[75] indicate that $Sc_{0.97}Mn_{0.03}N$ may be a dilute magnetic semiconductor (DMS) at room temperature, and up to 25% solubility of MnN in ScN has been experimentally achieved[7]. YN may also be a useful DMS material as demonstrated by magnetism in Gd-doped YN[169, 168].

The potential electronic applications of ScN and YN promote interest in thin film deposition techniques that optimize crystalline and electron transport properties. Growth of single crystalline ScN is also of interest for use as a seed layer for GaN[110, 85]. The high melting point of these nitrides makes the formation of single crystalline films by an annealing process impractical, and thus the choice of substrate and of deposition parameters are crucial in obtaining films of high crystal quality. We present structural and electrical characterization of single crystalline ScN and single-orientation epitaxial YN films deposited by reactive magnetron sputtering on α-$Al_2O_3(1\bar{1}02)$. To provide perspective, both previously employed growth methods of ScN and YN and previously reported electronic measurements on ScN films are first discussed.

Growth methods and structural properties

Although there have been recent advances in the growth of ScN nanoparticles[59] and bulk ScN[115], our discussion is focused on vacuum deposited thin films. Dismukes et al.[43, 42] used a halide vapor transport method to deposit both YN, ScN and other nitrides on α-$Al_2O_3(1\bar{1}02)$ with film thickness up to 20μm. Detailed structural characterization was only performed for ScN and the authors concluded that different processing conditions resulted in ScN films of different orientation and level of epitaxy. One observed epitaxial relation was $[001]_{\mathbf{ScN}}$ || $[1\bar{1}02]_{\mathbf{Al_2O_3}}$, $[111]_{\mathbf{ScN}}$ || $[0001]_{\mathbf{Al_2O_3}}$ (further discussion in Section 8.1.4). Fiber textured films (see Sec. 8.1.3) with $[321]_{\mathbf{ScN}}$ || $[1\bar{1}02]_{\mathbf{Al_2O_3}}$ were also obtained and an SEM image of one such film showed micron-scale mounds.

YN films have also been grown by reactive laser ablation onto Si substrates[36]. Composition analysis indicated that although the films were deposited in an ultra high vacuum (UHV) system, the films contained $\sim$10% oxygen substitution for nitrogen. With such high oxygen content, the films were observed to be metallic.

Studies of the pseudobinary nitride systems $Gd_xY_{1-x}N$ and $Nb_xY_{1-x}N$ included the reactive dc magnetron sputtering of YN on sapphire substrates[169, 168, 163].

Moustakas and Dismukes[113] used electron cyclotron resonance Molecular beam epitaxy (MBE) to grow polycrystalline, (111)-oriented ScN films on α-$Al_2O_3(0001)$ with an AlN seed layer. MBE deposition of (111)-oriented ScN was also achieved by Moram et al.[109] by growth on Si(111). The latter work presented extensive analysis of the temperature dependence of film epitaxy and

reported the lowest rocking curve line widths for thin film ScN.

Bai et al.[12] grew ScN thin films on amorphous and single crystal substrates using multiple techniques and studied a wide substrate temperature range. ScN films varying from amorphous to textured polycrystalline were observed.

A significantly different deposition technique was employed by Zheng et al.[69], who deposited ScN on W foil by a high-temperature sublimation-recondensation method.

Gall et al.[55] deposited ScN on MgO(001) by magnetron sputtering in a pure N_2 atmosphere. Transmission electron microscopy (TEM) images and electron diffraction revealed that the film grew with both (001) and (111) orientations. However, above a thickness of $\sim$40nm, the film was purely (111) fiber textured due to growth kinetics. The film had a columnar structure with column width 30nm$\pm$5nm. ScN films with similar structural properties were also grown with a TiN seed layer[53]. TEM images in these films revealed nanopipes along the growth direction.

The role of ion bombardment in ScN deposition was discussed in [54] using the substrate and basic deposition technique of [55]. By both employing a Tesla coil to magnetically unbalance the magnetron sputter discharge and controlling substrate bias, the authors created a high flux of ion bombardment (primarily N_2^+) at the growing film's surface. The flux ratio of N_2^+ ions to deposited Sc was kept at approximately 13 while 345nm ScN films were grown on 750°C MgO substrates with 13V, 20V and 50V bias. Bombardment by 13eV ions yielded polycrystalline films with both (001) and (111) orientations as in [55]. The films with higher energy ion bombardment had the single (001) orientation, but the

50eV N_2^+ bombardment resulted in significant (interstitial) N implantation and thus a high strain, high defect density film. TEM images revealed a surface of regular, smooth mounds with width 30nm and height 5nm for the 20V bias and width 50nm and height 10nm for the 50V bias film. Thus, the 20eV ion bombardment removed the kinetic barrier associated with the competing fiber textures of [55] but the low substrate temperature with respect to the ScN melting point afforded kinetic surface roughening.

Finally, Al-Brithen, et al.[4] controlled the orientation of MBE-grown ScN films by varying the single-crystalline substrate. Deposition on α-Al_2O_3(0001) yielded ScN(111) and deposition on MgO(110) yielded ScN(110). The most extensive ScN characterization was performed on (001)-oriented (epitaxial) ScN films deposited on MgO(001). Atomic force microscopy (AFM) images of these ScN films revealed a surface of pyramids and plateaus approximately 100nm wide and several nm tall. Scanning tunneling microscopy analysis indicated that the top surface of the plateaus were atomically smooth. Similar growth techniques were also used to investigate ScN growth in both Sc-rich and N-rich conditions[139, 6].

Electronic properties

Previously reported electronic measurements indicate that as-deposited, single-phase ScN is n-type with carrier concentration varying from 10^{18} to 10^{22} cm^{-3}[42, 113, 5]. In [5], ScN electronic properties were extracted from Drude model curve fitting of the thin film optical absorption, resulting in a carrier concentration of 4.8x$10^{18}$$cm^{-3}$ and electron mobility of 48 $cm^2V^{-1}s^{-1}$. Hall measurements of the MBE grown films of [113] resulted in comparable carrier con-

centrations but with electron mobilities below 10 $cm^2V^{-1}s^{-1}$.

Hall measurements of chemical vapor-deposited films were presented in [42], and the data for the highest quality films are plotted in Figure 8.4. Additionally, the authors found that annealing ScN films in Mg vapor reduced carrier concentration and correspondingly increased electron mobility.

8.1.3 Experimental Method

ScN and YN films were reactively sputtered from metal targets in one of two magnetron sputter deposition systems with deposition parameters provided in Table 8.1. All ScN films and one YN film (films A through G) were deposited in a deposition system (system 1) described previously[65] using 99.9% pure metal targets. This deposition system contains both on-axis and tilted deposition sources (Angstrom Sciences ONYX-2), and the substrate may be placed at varying angular displacements γ from target normal[65] (see Figure 1 in [63]). Sc was deposited from a tilted source operated at 475mA (310V) for deposition of films at γ=35° and 50°. Sc was also deposited from an on-axis source at 420mA (280V) to obtain the sample at γ=15°, and we note that in this geometry the presence of the substrate heater caused regular arcing of the Sc source. Y was deposited from a source at 120mA (260V) with substrate at γ=35°. The chamber was pumped to the 10^{-5}Pa range and deposition base pressure was approximately 10^{-4}Pa. As discussed in [65], the partial pressure in the deposition region is significantly lower due to our use of a gettering technique. The films from system 1 were the only films used for structural and epitaxial analysis. Electrical data is presented for YN films (films H through N) deposited

using a different deposition system (system 2) with a 99.999% pure Y target.

All films were deposited onto 10mm x 10mm or 5mm x 10mm single crystalline α-$Al_2O_3(1\bar{1}02)$ (r-plane sapphire) substrates. A Mo film was deposited on the back side of the substrates and served as an absorption layer for radiative heating of the substrates in a custom built heater. No substrate processing prior to deposition was performed other than a 10 minute heating ramp prior to deposition. During this preheating, the targets were sputtered in pure Ar atmosphere for at least 1 minute and then in the Ar/N_2 atmosphere for at least three minutes while the mass deposition rate was measured with an Inficon crystal deposition monitor. The variation in deposition rate as a function of γ was determined via crystal monitor movement[65]. The mass accumulation rates were assumed to be due exclusively to the accumulation of stoichiometric (Y,Sc)N and the bulk nitride densities were used to calculate film thickness.

While ScN is stable in moist air, YN is highly reactive[43] and thus a $\sim$10nm (presumably nanocrystalline) AlN layer deposited below 200°C was used to protect the YN films from corrosion. ScN films both with and without this AlN layer and an additional AlN film deposited directly onto Al_2O_3 were tested to ensure that this layer did not affect the electrical measurements. To prepare films for Hall measurements, we covered the nitride films with photoresist, chemically etched away the Mo layer, diced the substrate into 5mm square segments (removing segments of the substrate that were shadowed by the substrate holder during deposition), chemically removed the photoresist, and applied $\sim$0.2mm diameter In solder contacts onto the four corners of the square sample.

Electrical van der Pauw[161] measurements were made on a custom built

Hall station with a 1.5 Tesla electromagnet, a Keithley 181 nanovoltmeter and a Keithley 224 current source. Hall coefficients were measured using both magnetic field polarities, resulting in a Hall field of 3 Tesla. Film contacts were routinely confirmed to be ohmic by noting a linear current response to a dc voltage sweep. Measurements made with inverted current polarities and over the course of the experiment were averaged to remove thermal voltages and drift. Furthermore, Hall coefficients measured with both geometrical permutations were compared to ensure experimental accuracy .

Analysis of film crystal structure and orientation were performed by x-ray diffraction on a Bruker AXS general area diffraction detector system (GADDS). For detected Bragg reflections, a single GADDS image provides not only the length of the scattering vector, but also the angle ψ between the scattering vector and substrate normal. The orientation of a crystalline grain is uniquely defined by ψ and the azimuthal direction ϕ of the scattering vector. An image taken under full azimuthal substrate rotation (average over ϕ) provides an intensity distribution of ψ for each Bragg reflection. While this distribution is flat for equiaxed films, films exhibiting fiber texture contain a preferred orientation of the crystalline grains marked by a peak in the ψ distribution. The fiber texture direction is defined by the scattering vector whose ψ distribution is peaked at substrate normal. All of the analyzed ScN and YN films of the present work exhibit well-defined (001) fiber texture. The quality of the texture is quantified by the fraction of (Y,Sc)N (002) diffraction intensity associated with the peak about ψ=0 (substrate normal). The integrated intensity of the peak at ψ=0 gives the intensity from the textured (002) planes. The integrated intensity over $\sim$50° of the remaining ψ range is normalized to the full 90° range of ψ (under the 4-fold cubic symmetry) to give the intensity of the equiaxed planes. The ratio of the

textured intensity to the sum of the textured and equiaxed intensities defines the quantity we refer to as "texture fraction".

Additional analysis of the ϕ distribution of the Bragg reflections is required for analysis of the epitaxial relation of the film to the underlying substrate. GADDS diffraction images taken at 5° intervals of ϕ are used to create partial pole figures (maps of diffraction intensity as a function of ψ and ϕ) for both (Y,Sc)N and substrate reflections. The interpolated pole figures are used to assess the nature and quality of film epitaxy. Diffraction images are also integrated over ψ to attain 2θ spectra which are further analyzed with Jade (Materials Data Inc.) software. The relation of substrate peak positions and the known α-Al_2O_3 pattern[79] are used as an internal calibration of the 2θ scale, and the nitride diffraction peaks are used to calculate the rock-salt lattice constant.

8.1.4 Results and Discussion

Film structure

Six ScN films and a single YN film were analyzed via x-ray diffraction. Diffraction images indicated that all films crystallize into a single-phase rock-salt structure as indicated by the scattering angle diffraction spectra of Fig. 8.1a. The lattice constants calculated from the (002) and (022) reflections are approximately equal, yielding values of 0.451(1)nm and 0.491(3) for ScN and YN respectively (slightly larger than the literature values of 0.450nm[95] and 0.489nm[2]). All films are epitaxial with substrate relation $[001]_{\mathbf{(Sc,Y)N}}$ || $[1\bar{1}02]_{\mathbf{Al_2O_3}}$, $[100]_{\mathbf{(Sc,Y)N}}$ || $[11\bar{2}0]_{\mathbf{Al_2O_3}}$, as determined by the nitride (002) pole figure and the relation of the nitride {202} and Al_2O_3 $\{1\bar{2}13\}$ pole figures (Figure 8.1).

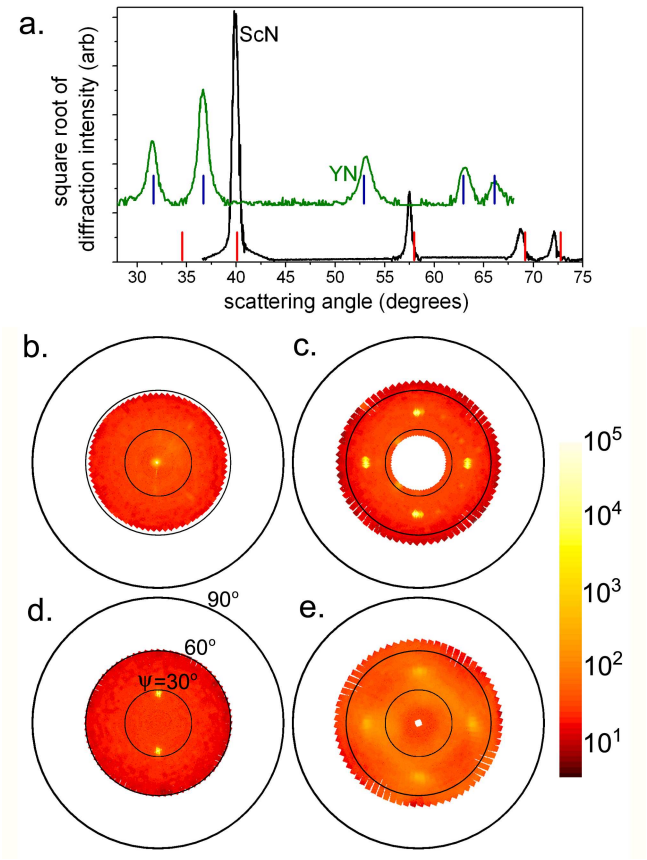

Figure 8.1: The GADDS images integrated over ψ give the diffraction intensity as a function of scattering angle. For both ScN and YN, the accepted peak positions are marked and the shift of the measured patterns to lower scattering angles is evident, especially for ScN. The absence of the ScN (111) reflection and the relative intensities of the peaks are due to the limited extent of the area detector and the use of the subset of the area detector without substrate reflections. The pole figures of b. ScN(002), film B; c. ScN{202}, film B; d. Al_2O_3 $\{1\bar{2}13\}$ and e. YN{202}, film G are plotted to demonstrate the epitaxial relation of the nitride films to the Al_2O_3 substrate. The pole figures share a common azimuthal orientation and (arbitrary) logarithmic diffraction intensity scale. The peak splitting (which is especially apparent in c. and d.) is an artifact of the interpolation.

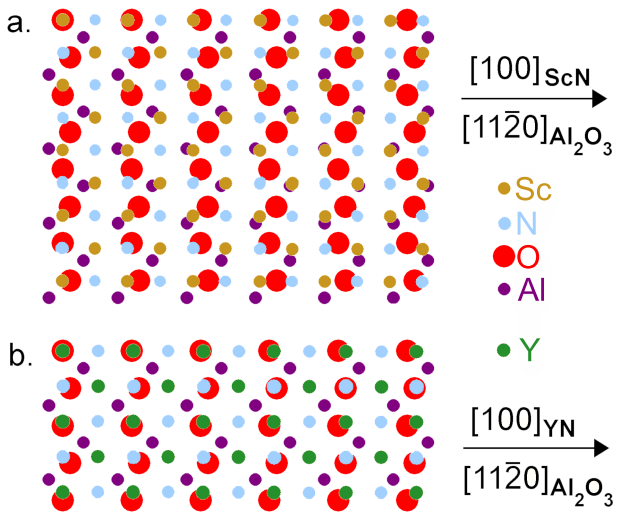

Figure 8.2: A model for the epitaxial relation of a. ScN and b. YN on α-$Al_2O_3(1\bar{1}02)$ is given assuming a non-reconstructed substrate surface and non-strained nitride. A single layer of oxygen atoms are shown with the 15pm subsurface Al atoms. A single layer of nitride is shown with the arbitrary alignment of the metal and oxygen atom in the upper-left corner. Note that symmetry permits interchangeability of the metal and nitrogen atomic assignment.

The only previous reports of ScN deposition on Al_2O_3 $(1\bar{1}02)$ are those of Dismukes et al.[43, 42]. The quoted epitaxial relation (Section 8.1.2) involves the same ScN(001) fiber texture. Given the $[1\bar{1}02]Al_2O_3$ || [001]ScN, the angle between $[111]_{\mathbf{ScN}}$ and $[0001]_{\mathbf{Al_2O_3}}$ is minimized at 2.9° with the azimuthal alignment of these crystalline directions. The implied epitaxy differs from that demonstrated in Fig. 8.1 by a 45° azimuthal shift.

Figure 8.2 presents a model of the atomic arrangement implied by our epitaxy, assuming a non-reconstructed, oxygen-terminated Al_2O_3 surface. The rectangular sublattices of the surface oxygen and sub-surface aluminum imply a lowest lattice mismatch of 5% for both ScN and YN. We find no lattice match to either nitride (111) surface. We conclude that the two-fold symmetry of the

$Al_2O_3(1\bar{1}02)$ surface results in the energetic preference of the formation of a four-fold symmetric (001) nitride monolayer over the three-fold symmetric (111) configuration.

The pole figures indicate that each nitride film has a single epitaxial orientation, and additionally Figures 8.1b and 8.1c demonstrate that the ScN film is single crystalline (texture fraction $>$0.999 and single azimuth orientation). Figure 8.1e indicates that the YN film has an equiaxed polycrystalline fraction, which is quantized by the texture fraction of 0.54. While the texture fraction for film A with γ = 15° is $>$0.98, the value for film F with γ = 50° is 0.7.

The ψ-width of the peaks in pole figures are analogous to rocking curve line widths. The angular resolution of the pole figures in Fig. 8.1 is much poorer than that of typical rocking curve experiments, and in fact the line widths of the (002), (202), and (222) reflections of ScN (film B) are resolution limited ($<$1°). The line widths of the same YN (film G) reflections are approximately 5°.

The ScN films deposited at different γ positions also exhibit different surface morphologies. AFM images of the three different surfaces are presented in Figure 8.3. AFM line scans (Figure 8.3d) show that films at γ = 15° and 35° have 4nm$\pm$2nm high mounds. The mounds of the γ = 15° film are smooth (resembling those of the ScN film grown under 20eV ion bombardment in [54]) while the γ = 35° film has regular, aligned pyramid mounds. These two mound morphologies coexist in the film of [4]. The γ = 50° film has a significantly different surface morphology that appears atomically smooth with a few smooth mounds per square micron that are approximately 5nm high and 200nm wide. At this high γ, we suspect that these mounds may be due to target ejecta.

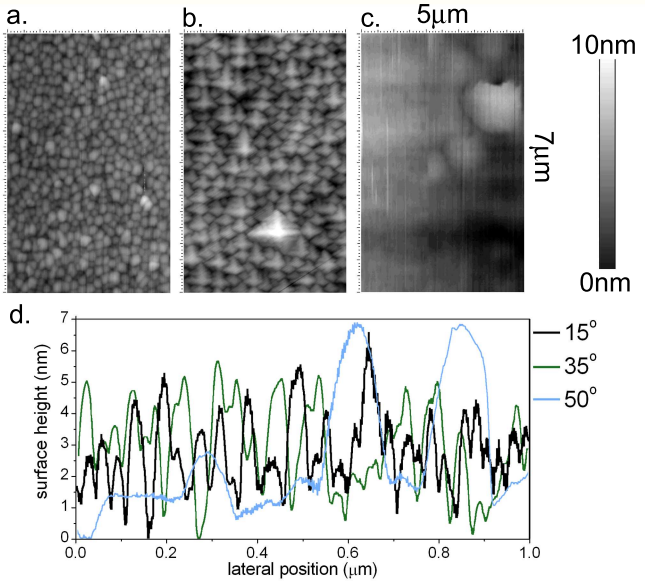

Figure 8.3: AFM images (5μm x 7μm) of ScN film surfaces are shown for a. film A with γ = 15°; b. film D with γ = 35°; and c. film F with γ = 50°. d. AFM line scans taken from the three films are plotted. The line scans are not a subset of the AFM images. Note that these films have different thicknesses and do not have an AlN capping layer.

The differences in ScN morphology as a function of γ may be caused by a combination of a number of co-varying process parameters. The lower deposition rate of film F (compared to films A and D) corresponds to a 70% higher surface diffusion length, which could explain its relatively high smoothness. However, the significant differences in the surface morphology of films A and D, despite the similarity of their deposition rates, suggests the presence of a different physical phenomenon. One possible candidate is the angle of incidence of accumulating material at the substrate surface. This angle changes with γ, the orientation of the deposition source, and gas-phase scattering phenomena. The AFM images indicate that the varying morphologies are not caused by shadowing effects. Thus, the angle of incidence is not likely responsible for the changes in surface morphology. We conjecture that the process parameter of greatest

Table 8.1: Deposition parameters are given for all films analyzed. Films A through G were deposited in system 1 while films H through N were deposited in system 2. Values of γ are not directly comparable between the two systems and are not provided for films H through N. A single deposition geometry was used for all films from deposition system 2.

film	type	Dep.R. (nm/m)	Thick. (nm)	Dep.T. (°C)	(%N_2 in Ar)	Gas Pres. (Pa)	γ
A	ScN	11	160	820	20	0.67	15°
B	ScN	10	150	720	20	0.67	35°
C	ScN	10	160	820	20	0.67	35°
D	ScN	10	480	820	20	0.67	35°
E	ScN	10	430	820	20	0.67	35°
F	ScN	3.6	140	820	20	0.67	50°
G	YN	11	150	820	20	0.67	35°
H	YN	5.2	260	850	20	0.67	
J	YN	5.2	260	800	20	1.0	
K	YN	6.6	330	650	15	0.67	
L	YN	6.8	340	650	12.5	0.67	
M	YN	6.6	330	770	18.7	0.64	
N	YN	5.6	280	880	22	0.67	

relevance may be film bombardment by energetic gas molecules. The energy imparted to film surface atoms through such bombardment varies significantly with deposition geometry and may lead to significant changes in morphology (as demonstrated in [54]). A more detailed discussion of film bombardment is available in the Appendix.

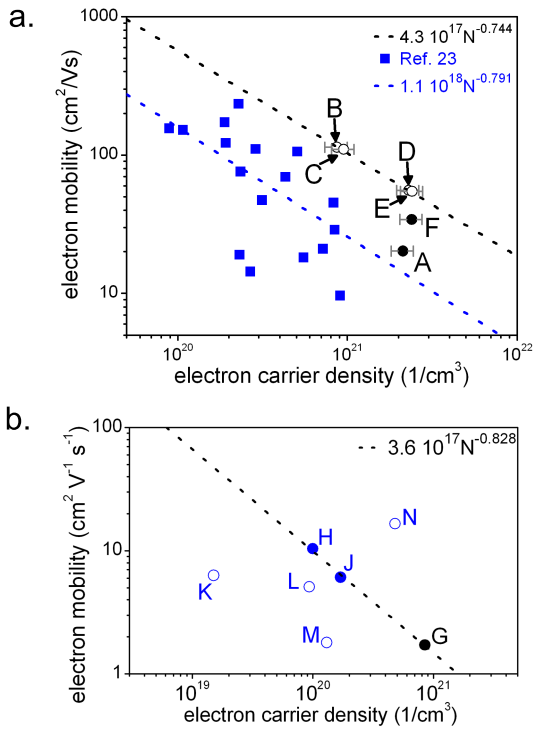

Figure 8.4: a. ScN mobility is plotted as a function of carrier concentration for films from the present work (black symbols) and from [42] (blue symbols). The power law relation obtained from the γ=35° films (films B through E) is plotted (black line) along with the power law plotted in [42] (blue line). b. YN mobility is plotted as a function of carrier concentration for films G through N. Blue symbols denote films from deposition system 2. The three solid points denote the films with most similar deposition conditions which are used to suggest a possible power law relation (black line).

Electrical properties

All films in Table 8.1 were analyzed using the Hall effect. Thickness measurements obtained from the deposition rate monitor are used to calculate carrier concentration from the van der Pauw sheet resistance, providing a carrier concentration(N)-mobility(μ) datum for each film (Figure 8.4).

The highest ScN mobility is obtained with γ=35°. Films B through E were

deposited in this geometry at the same deposition rate and have nearly indistinguishable crystalline properties as analyzed with x-ray diffraction. Electronic measurements indicate that the thin, lower temperature film (film B) has the lowest carrier concentration. The higher deposition temperature causes a slight increase in carrier concentration while the higher thickness (increased deposition time) causes a significant increase in carrier concentration. The mobility decreases with the increased carrier concentration as described by the μ=c N^b (where b and c are material-dependent constants) power law presented in Figure 8.4. The changes in carrier concentration at constant deposition geometry suggest that higher substrate heater power and longer heater operation may cause increased outgassing, which would lead to increased film contamination through reactions with water vapor, hydrocarbons and other desorbed molecules. This phenomenon would also explain the generally high carrier concentrations found in all films deposited in system 1, which is not capable of UHV operation.

The ScN film deposited at γ=15° (film A) has a mobility well below that expected from the proposed power law, which is possibly related to the surface roughness shown in Figure 8.3a. This surface roughness may indicate the presence of a columnar growth structure and fibrous voids (such as those reported in [53]) which would hinder lateral electron mobility. The ScN film deposited at γ=50° (film F) also has a relatively low mobility which is most likely due to unaligned grains as characterized by the 0.70 texture fraction.

The carrier concentration of the YN film G is comparable to (10% lower than) that of the ScN film C grown under the same conditions. However, the mobility is a factor of 65 lower, which is partially due to the relatively low texture fraction

of 0.54 but also suggests a fundamental lower electron mobility in YN compared to ScN.

While we do not present the γ dependence of YN films, we note that films H through N were all deposited at the same geometry. Table 8.1 and Figure 8.4 indicate the variations in electrical properties with various deposition parameters. We use the electrical measurements of the YN film from the system 1 (film G) and the two other YN films with the most similar deposition conditions (films H and J) to suggest a possible mobility power law for YN (Figure 8.4b).

As discussed above, the high carrier concentration of these films is most likely due to contamination by reactive gases in the deposition. The primary mechanism of donor electron generation by a contaminant atom is via oxygen substitution on nitrogen lattice sites. Assuming that this is the only contribution to carrier concentration, the fraction of nitrogen sites occupied by oxygen can be calculated to be from 2% to 5.5% for ScN films and a maximum of 2.5% for YN films.

Previous measurements on highly doped YN demonstrated metallic behavior[36], most likely due to a very high density of defect states. We performed Hall measurements on one YN film while varying temperature from 4K to 300K. The carrier concentration increased by 40% over the temperature range, reaching a value of $1.8\text{x}10^{19}\text{cm}^{-3}$ at room temperature, which is consistent with the assertion that YN is a semiconductor. Further characterization of low carrier concentration YN is needed to verify that YN is in fact a semiconductor as indicated by ab initio calculations.

8.1.5 Conclusions

We describe the reactive magnetron sputtering of ScN and YN onto α-$Al_2O_3(1\bar{1}02)$ single crystal substrates that results in a single-orientation epitaxy that was not previously reported. The crystallinity and surface morphology of ScN varies with deposition geometry but the surface roughness is comparable to the smoothest ScN films of previously reports (see Section 8.1.2). The measured mobilities of ScN indicate that for single crystalline films, mobility is not significantly altered by a 100°C change in deposition temperature. However, we find that YN mobility increases with deposition temperature and depends significantly on N_2:Ar sputter gas stoichiometry (optimal near 1:4) and slightly on total gas pressure (optimal near 0.66Pa).

Our study of ScN films indicates that variation in deposition geometry can alter both structural and electrical properties, but the physical mechanism responsible for these variations remains under investigation. We speculate that film bombardment by gas atoms may be important, suggesting that thus higher quality films may be obtained by optimizing ion bombardment with a mechanism such as that of [55].

While our films have relatively high carrier concentration, higher purity ScN films have been made by other methods (see Section 8.1.2). We believe low carrier concentration films may be made with our technique using targets of higher purity and an UHV deposition system to avoid oxygen contamination. The presented mobility power laws for ScN and YN suggest that these materials may demonstrate very high mobility at low carrier concentration.

8.1.6 Acknowledgments

The authors wish to thank Nathan Gabor and Maxim Noginov for assistance in acquisition of AFM images. Also, we thank Maura Weathers for guidance in our use of the Cornell Center for Materials Research facilities supported by the National Science Foundation under Award Number DMR-0520404.

8.1.7 Appendix

During deposition, the substrates are electrically grounded, and thus negative ions and electrons in the sputter plasma may bombard the growing film's surface. Additionally, the growing film may be bombarded by energetic gas neutrals which reflect from the metal targets. This phenomenon and its importance in determining film composition was recently modeled for the deposition system 1[63, 64]. Using the model of [63], yield data of [68] and reflections dynamics data of [45], we calculate nominal values of reflected gas neutrals to sputtered metal (at the quoted operating voltages) to be 0.07 Ar:Sc, 0.05 N_2:Sc, 0.30 Ar:Y and 0.11 N_2:Y. This calculation considers the number of impinging gas atoms required to remove a metal atom and the reflection probability of those atoms. It also includes the approximations that the target bombardment gas stoichiometry is that of the sputter atmosphere (They are not equal due to differing ionization dynamics in the plasma.) and that the target surface is metallic (It is partially nitrided.). At γ=15° we anticipate that the film bombardment by ions and electrons is more significant than that of reflected neutrals. At higher angles, neutral gas bombardment is more significant but the flux profile is unknown. However, the modest values of the flux ratios suggest that spatial varia-

tions in their values may result in significantly different film bombardment and thus different energetics of the surface film atoms.

8.2 *Letter:* Structural, Electronic and Optical Properties of (Sc,Y)N Solid Solutions

8.2.1 Abstract

The refractory nitrides ScN and YN are candidate semiconductors for optoelectronic and DMS applications. Studies have included alloying ScN with other III-V semiconductors such as GaN to engineer the electronic, optical and structural properties. We suggest that ScN-YN and higher order alloys will lead to further control of these properties. We demonstrate complete solid solubility in the ScN-YN system through analysis of sputter deposited composition-spread thin films. Characterization of electrical, optical and structural properties is presented as a function of composition, demonstrating excellent epitaxy, high mobility, high absorptivity and high energy optical gap across the entire composition range.

8.2.2 Letter

The refractory IIIA-VB semiconductors ScN and YN have many potential applications due to their high mechanical strength[54], high optical gap[5, 43, 36] and equilibrium rock-salt (B1) crystal structure that is uncommon among ni-

tride semiconductors. The most recent experimental (for ScN) and theoretical (for ScN and YN) studies indicate that these nitrides are indirect semiconductors with minimum gap at $\Gamma \rightarrow X$ and optical gap at the X point. The indirect gap of ScN has been measured to be 1.3$\pm$0.3 eV[56] and 0.9$\pm$0.1 eV[5], in reasonable agreement with recent band structure calculations[56, 123, 158]. Measurements of the direct gap vary from 2.1 eV to 2.4 eV as summarized in [5]. The most recent calculations of the YN band structure have yielded indirect gaps of 0.85 eV[147] and 0.54 eV[158] and a minimum direct gap near 1 eV. No measurement of the YN indirect gap has been reported. Dismukes et al.[43] measured an optical gap of 1.5 eV for YN, but both the present work and that of [36] indicate that YN has a higher energy optical gap. De la Cruz et al.[36] report spectroscopic ellipsometry characterization of YN that, through Lorentz oscillator analysis, suggests YN has no direct gap less than 2.6 eV. Our analysis of the optical absorption inferred from the ellipsometry data[36] suggests an optical gap at 2.3 eV.

The shared crystal structure and differing gap energies of ScN and YN suggest that the alloy nitride $Sc_{1-x}Y_xN$ ($0 \leq x \leq 1$) is a semiconductor with tunable indirect band gap and optical gap. Mn-doped ScN[75, 7] and Gd-doped YN[169, 168] have been identified as interesting dilute magnetic semiconductor (DMS) materials, and magnetic atom substitution into $Sc_{1-x}Y_xN$ introduces the prospect of a class of DMSs with tunable band gap.

Band gap engineering has been demonstrated in $Sc_xGa_{1-x}N$[97], generating significant interest in optoelectronic applications of this compound semiconductor, as proposed by [41]. Both indirect and direct semiconductors exist in this pseudobinary system due to the composition dependence of the equilibrium

crystallographic phase, and similar behavior is anticipated in the $Sc_xIn_{1-x}N$ system[33, 34, 124, 125, 126, 111]. Incorporation of YN into these and other compound nitride systems will afford further control of electronic, optical, and structural properties.

Other studies of Sc- and Y-containing IIIA-IIIB-N compound nitrides include investigations into the equilibrium phase behavior of the Y-Al-N and Sc-Al-N systems which have demonstrated immiscibility of YN and AlN and of ScN and AlN[130]. Also, the (metallic) ternary perovskites Sc_3AlN[90] and Sc_3InN[77] have been synthesized. In the Sc-Y-N system, Sc and Y solubility has been demonstrated[19], the Y-YN[24] and Sc-ScN[95] phase boundaries have been investigated, and in the present work we demonstrate a complete solid solution in the pseudobinary system $Sc_{1-x}Y_xN$.

Cherchab et al.[31] have calculated that the material formed by alternating bilayers of rock-salt ScN and YN is a semiconductor with a small direct gap. Other recent theoretical work has provided the core energy and electronic structure of metastable ScN and YN phases[31, 50, 102, 138, 38, 100, 8, 9], several of which show a direct band gap or an indirect gap slightly below the optical gap. A wide-gap semiconductor of this type with absorptivity and electron mobility comparable to those presented in this work would make a very promising absorbing medium for photovoltaic applications. The additional prospect of a composition-tuned band gap merits continued investigations into Sc- and Y-containing compound nitride semiconductors.

We recently reported single crystalline ScN and single-orientation epitaxial YN films that demonstrate the highest recorded electron mobility for the respective materials[61]. The films discussed in this letter are fabricated with the same

magnetron sputter deposition system by using two confocally tilted sources[65] containing Y and Sc metal targets to create a continuous composition spread. Discrete nitride stoichiometries are studied by analysis of diced 5mm square samples, but we note that the metal composition gradient of $\lesssim$1 at%/mm implies that the characterized samples are not completely homogeneous. We present data on pure ScN and YN films as well as films from two $Sc_{1-x}Y_xN$ composition spread depositions: deposition A contains $Sc_{1-x}Y_xN$ samples ranging from x=0.05 to 0.55 and deposition B from x=0.17 to 0.8. Both depositions were performed in 0.66 Pa of 20% N_2 in Ar onto 720°C α-$Al_2O_3(1\bar{1}02)$. The Sc source was operated at 475 mA, 305 V for both depositions while the Y source was operated at 125 mA, 240 V and 265 mA, 270 V for depositions A and B, respectively. The Y power was chosen to attain the desired composition ranges. Film composition and thickness ($\sim$150 nm for deposition A and $\sim$300 nm for deposition B) are determined from single-source rate profiles[61, 65].

While ScN is stable in air, YN is air-sensitive[43]. Visual observation of a polycrystalline $Sc_{1-x}Y_xN$ composition spread deposited on SiO_2 indicates that the $x<0.45$ nitrides are stable in air for over a year. To prevent corrosion, all Y-containing films are capped with a 10 nm AlN layer, which was confirmed to be electrically insulating and optically transparent over the energy range of interest. Further details concerning sample processing and characterization methods are provided in [61].

Xray diffraction analysis indicates that all films crystallize into a single rock-salt phase with lattice constant as a function of composition given in Fig. 8.5. The linear discrepancy in lattice constant demonstrates complete solubility of YN and ScN despite the large (>8%) variation in lattice parameter. Analysis of

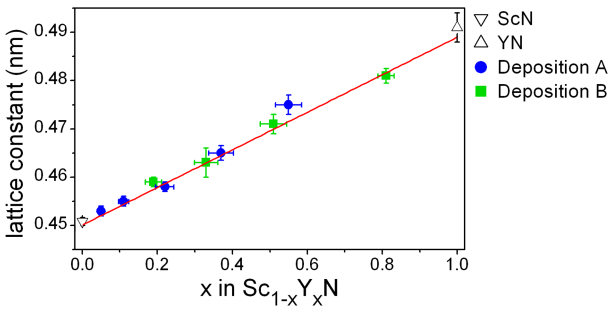

Figure 8.5: The rock-salt lattice constant of $Sc_{1-x}Y_xN$ films are plotted for the binary end members as well as ternary nitrides from the deposition of two composition spreads. The line connecting the accepted binary nitride lattice constants[95, 2] is shown in red, and the agreement with the measured lattice constants demonstrates solid solubility of YN and ScN.

pole figures reveals that all films are epitaxial with $[001]_{(\mathbf{Sc,Y})\mathbf{N}}$ || $[1\bar{1}02]_{\mathbf{Al_2O_3}}$, $[100]_{(\mathbf{Sc,Y})\mathbf{N}}$ || $[11\bar{2}0]_{\mathbf{Al_2O_3}}$. We quantify the quality of the fiber texture by the fraction of the [002] intensity in the fiber texture orientation. A rigorous definition of this quantity, which we refer to as "texture fraction", is given in [61], and the measured values for the nitride films are given in Fig. 8.6. We also measure the crystal quality of the epitaxial fraction of the films by the line widths (FWHM) of fiber plots of the (002), (202), and (222) reflections (analogous to rocking curve line widths). The peak widths are instrument limited for ScN and Sc-rich mixed nitrides but increase to 3° to 4° for 0.5<x<0.8 and reach 5° for YN.

Solid solubility in $Sc_{1-x}Y_xN$ should lead to smoothly varying indirect and optical gaps as a function of composition. The indirect gaps of intrinsic $Sc_{1-x}Y_xN$ are likely obscured by defect states and thus we investigate only the direct gap behavior of this pseudobinary system. The optical transmission fraction T and reflection fraction R of ScN, YN and compound nitride films (from deposition B) were measured in a Shimadzu UV-3101PC spectrophotometer and

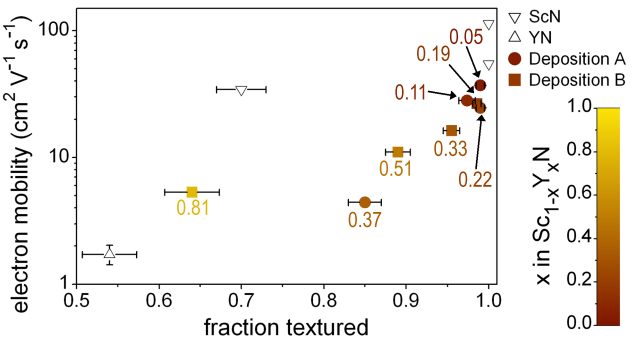

Figure 8.6: The electron mobility measurements of Fig. 8.8a. are plotted against the (002) texture fraction. The data points corresponding to ternary $Sc_{1-x}Y_xN$ films are colored according to the composition color scale at right.

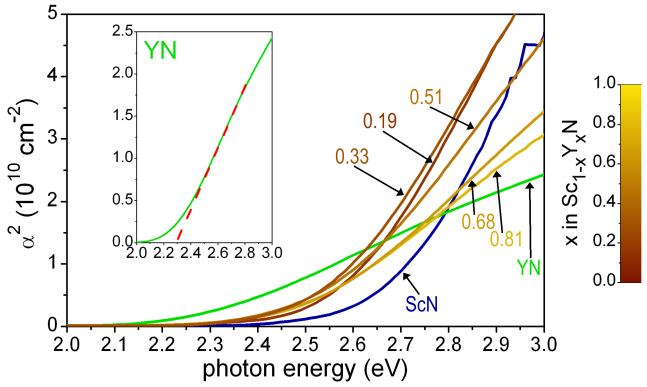

Figure 8.7: The square of the measured optical attenuation coefficients for seven nitride films are plotted against photon energy. The data from the composition spread B films are colored according to the composition color scale at right. The inset plot shows the YN data in the same coordinates axes and includes an extrapolation (dashed red line) to an intercept near 2.3 eV. The approximate film thicknesses are 450 nm for ScN, 150 nm for YN and 300 nm for composition spread B.

used to calculate the absorption coefficient $\alpha = -\tau^{-1}\ln(T/(1-R))$, where τ is the film thickness. Plots of α^2 as a function of photon energy are given in Fig. 8.7 and indicate that the YN gap of 2.3 eV is the smallest optical gap in the composition range. The ScN data lack a well-defined linear region but suggests a direct gap above 2.6 eV, larger than previously reported values. As expected, the optical gap continually decreases with increasing Y content, but the variation is only $\sim$0.1 eV over the entire composition range. This small change in gap energy implies a YN optical gap in excess of 2 eV.

While different calculation techniques for determining the ScN band structure result in a wide range of band gaps, the most recent calculations based on the GW method[123] are in best agreement with the experimental data. Many of the same techniques have been employed to calculate the YN band structure and have resulted in comparable variability. The GW value for the direct gap of YN is 1 eV[158]. This value is less than half of that indicated in Fig. 8.7, which is comparable to that resulting from the measurements of [36] discussed above. Further theoretical and experimental work are needed to accurately determine the band structure of YN and resolve this striking discrepancy.

We also note that the calculated band structures for ScN and YN reveal that both the direct and indirect gaps involve the conduction band with minimum at the X point[56, 123, 158]. For both materials, this band is fairly parabolic for a 2 eV range over which no other band exists. Thus, even at our high doping level, it is not surprising that (for all but one sample) α^2 varies linearly with energy within 1 eV above the direct gap. The unique electronic structure of these materials allows the extraction of band gaps from Fig. 8.7 despite the high carrier concentrations, though the band gap values may reflect small Burstein-

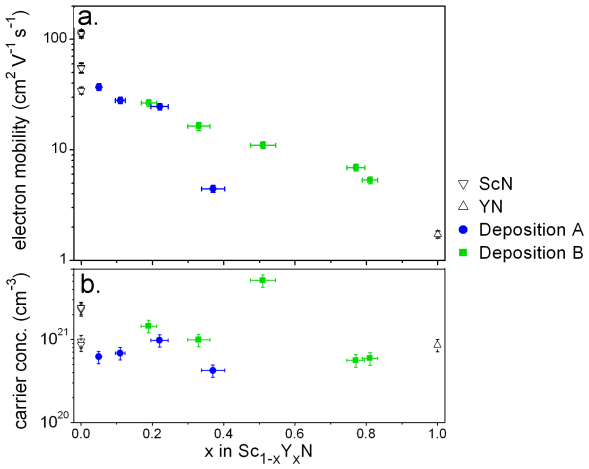

Figure 8.8: Hall probe measurements of (a) mobility and (b) carrier concentration in $Sc_{1-x}Y_xN$ films are plotted for binary nitrides and ternary nitrides from the deposition of two composition spreads.

Moss shifts whose exact values cannot be determined without information on the density of states in the conduction band. Future investigation of higher purity samples will permit a more detailed investigation of the optoelectric properties of $Sc_{1-x}Y_xN$.

The optical data also indicate that for all compositions the absorption coefficient above the optical gap is in excess of 10^5 cm^{-1} and that the absorption length increases with Y content. The absorptivity of these materials is remarkably high and is in agreement with previous optical characterizations of ScN[5, 56].

All films are n-type and mobility and carrier concentration are plotted as a function of composition in Fig. 8.8. Although we do not have a quantitative direct measure of nitrogen or oxygen concentrations, we argue in [61] that the high carrier concentrations are due to oxygen substitutions on nitrogen sites at the level of a few at%. We assert that the oxygen impurities affect the electronic

and optical properties solely through electron doping, as discussed above.

In addition to the mobility dependence on cation stoichiometry evident in Fig. 8.8 and the mobility dependence on carrier concentration presented in [61], we find a strong dependence on crystal quality, as indicated by Fig. 8.6. The nature of the composition spread mandates that deposition geometry changes with film stoichiometry. This results in variations in energetic gas bombardment of the growing film as a function of substrate position[63]. The effects of these variations on film properties are discussed in [61], and we suggest that the low texture fraction (Fig. 8.6) and mobility (Fig. 8.8a) of the x=0.37 film are due to low bombardment.

We emphasize that deposition in an atmosphere with lower partial pressures of contaminant gases will result in nitride films with lower carrier concentration. Our studies indicate a significant increase in mobility with reduced carrier concentration (reduced scattering by ionized impurities)[61], but the limit to the room temperature mobility from phonon scattering is not known. Growth of these compound nitrides in an UHV environment under optimal ion bombardment should result in single crystal films with very high electron mobility. These desirable structural and electronic properties combined with the possibility of band gap engineering make the compound nitride semiconductor $Sc_{1-x}Y_xN$ a promising material for electronic and optoelectronic applications.

The authors wish to acknowledge Felix Lee and George Scopelianos for assistance in data acquisition and Prof. Richard Hennig for helpful discussions. Additionally we acknowledge support from the facilities of the Cornell Center for Nanoscale Systems (supported by NSF contract EEC-0117770) and Cornell Center for Materials Research (supported by NSF contract DMR 0520404).

CHAPTER 9

ADDITIONAL PROJECTS

During the last four years I have also been involved in several projects which have never been a focus of my research. However, I have devoted some time and effort to their development and want to share some thoughts and results. The bulk of the work on each of these projects was performed by a collaborator. The first two projects were performed by undergraduates under my (and Bruce's and sometimes Sara Barron's) supervision: Leo Small and José Fonseca, respectively. The nitrides project was conceived and organized by Akira Muira. The carbon nanotube catalyst project is in collaboration with the nanotube experts in the John Hart group at the University of Michigan.

9.1 Oxide electrolytes for SOFCs

This project is aimed at creating a platform for high-throughput discovery of new solid electrolytes for O^- conduction. A lot of effort is being put into raising the operating temperature of PEM fuel cells above 100°C. Significantly less effort is being put into lowering the operating temperature of solid oxide fuel cells (SOFCs) below 700°C. The balance between temperature-driven improvements to fuel cell kinetics and ease of engineering suggests a target range of 150°C to 250°C. With some create engineering, especially in small form-factor (low power) fuel cells, the upper range can be pushed to 400°C. The general neglect of SOFC in the research community seems to suggest that everyone is betting that PEM fuel cells will get into this range before SOFCs. I'm beginning to think this may not be true, and I'll also bet that once the desired operating temperatures are reached, the solid oxide electrolytes are going to be a lot more

robust than the polymer ones. The remainder of this section is extracted from a letter being prepared by Leo Small and describes our evaluation of the composition dependence of the phase behavior and ionic conductivity in the yttria-zirconia system. Algorithms for robust extraction of ionic conductivity from the impedance spectra are being developed, but the data clearly demonstrates our ability to use these techniques to characterize thin film electrolytes at low temperature at high enough throughput to be useful for materials optimization and discovery.

Unlike traditional ceramic electrolytes with μm-sized grains, ceramic thin films typically possess grain sizes on the order of 10 nm. The nanocrystallinity may signify a departure from the equilibrium phase behavior and corresponding ionic conduction of a given electrolyte material. Nanocrystalline films of the classic ionic-conducting system (Zr,Y)O_y were studied by Mondal et al.[108] who found enhanced grain boundary conductivity in $Zr_{1-x}Y_xO_y$ with x = 0.0085 and 0.0145. Hertz and Tuller[74] investigated thin films of $Zr_{0.91}Y_{0.09}O_y$ with 5-10 nm grains and found a decrease in the activation energy for grain boundary conduction. Huang et al.[78] have demonstrated successful operation of SOFCs containing thin film $Zr_{0.84}Y_{0.16}O_y$ consisting of 20-30 nm grains.

In $Zr_{1-x}Y_xO_y$, substitution of Y^{3+} on Zr^{4+} sites creates oxygen vacancies to maintain charge balance, resulting in $y = 2 - x/2$. The vacancies are relatively mobile and lead to a substantial ionic conductivity at elevated temperature. For low Y concentrations, the conductivity increases with increasing Y content. Above a critical concentration, further addition of yttria proves deleterious due to association of the vacancies with immobile Y cations, restricting ionic conduction below 550°C[70, 11]. Thus, the YSZ composition with the

greatest conductivity at temperatures near 300°C could differ significantly from that at 800°C (i.e., $Zr_{0.85}Y_{0.15}O_y$). We present the composition dependence of the electrical conductivity of thin film YSZ at temperatures from 300-500°C. All compositions were synthesized in a single experiment in order to isolate composition-dependent effects.

The $Zr_{1-x}Y_xO_y$ thin film was integrated to form Pt-electrolyte-Pt test structures on an SiO_2-coated Si wafer. The electrolyte film was deposited by 90° off-axis rf co-sputtering using elemental Zr and Y targets in a vacuum system with a base pressure of $\sim 10^{-3}$ Pa. Gas flows of 10 sccm O_2 and 15 sccm Ar were used to establish a sputtering pressure of 4 Pa. A forward power of 103 W was applied to the Zr target, while 50 W was applied to the Y target, providing the $0.04 \leq x \leq 0.16$ part of the pseudobinary system over 35 mm of substrate. In order to obtain dense films, a rf bias was applied to the substrate such that a constant -50 V DC bias was maintained during sputtering[15]. The substrate was not intentionally heated. A 100 minute deposition gave a center thickness of 189 nm as measured with a crystal monitor. The $Zr_{1-x}Y_xO_y$ composition spread was flash annealed in inert atmosphere at 700°C for 90 s to preclude significant further structural evolution during measurements up to 500°C. Finally, counterelectrodes were deposited by evaporating a ~40 nm Pt layer through a shadow mask consisting of a square array of dots 0.2 mm in diameter.

Analysis of film properties was performed by Scanning Transmission Electron Microscopy (STEM). The bright field STEM image of Fig. 1a shows the cross section of a test structure without the counterelectrode, revealing that the $Zr_{0.92}Y_{0.08}O_y$ film is composed of grains ranging in size from 3 to 15 nm. Analysis of the corresponding annular dark field STEM image indicates a void density

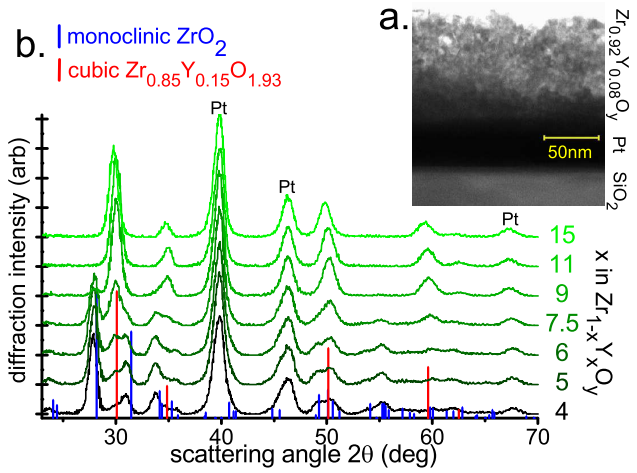

Figure 9.1: a. Cross section of a $Zr_{0.82}Y_{0.08}O_y$ film, showing the presence of equiaxed grains with diameter ranging from 3 to 15 nm. The film surface has been removed by polishing so this image does not represent the as-deposited surface. b. X-ray diffraction spectra plotted for seven values of x. Cataloged diffraction patterns[3] are shown for comparison.

of $\sim$0.2 vol.%.

The relation between wafer position and cation composition was determined using deposition profiles for ZrO_2 and Y_2O_3, which were acquired under similar deposition conditions in the same deposition chamber. The absolute uncertainty in the cation fraction at x=0.1 is estimates to be $\pm$0.02.

Prior to deposition of the counterelectrodes, the phase behavior of the composition spread was assessed by x-ray diffraction (XRD) using an area detector (Bruker GADDS). The diffraction images indicate that the films are composed of equiaxed grains up to $\sim$10 nm in diameter. The XRD spectra are plotted in Fig. 1b and demonstrate that the composition spread contains pure monoclinic, pure cubic and combined phase regions. The lattice constants of the monoclinic phase are expanded by up to 1.4% compared to ZrO_2 due to substitution of Y^{3+} on Zr^{4+} sites[11]; in the cubic phase region, the lattice constant increasing with

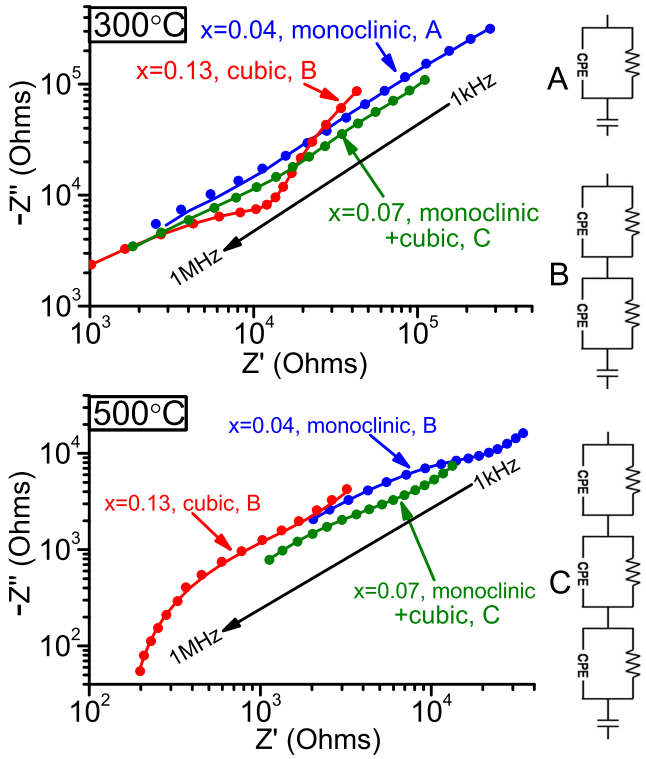

Figure 9.2: Impedance spectra (dots) of representative test structures acquired at 300°C and 500°C are plotted with the fitted spectra (lines) from equivalent circuit A, B or C. Impedances from frequencies between 100 Hz and 1 kHz have been omitted to reveal detail at higher frequencies. Equivalent circuits at 500°C include an additional 150 Ω series resistor (not shown) to account for increased resistance of the Pt back contact.

x as expected. Analysis of the composition dependence of the monoclinic and cubic peak intensities indicates that the phase boundaries are at x=0.05 and 0.11. The x=0.05 solubility limit of the monoclinic phase is consistent with the literature. However, the cubic phase region extends well below the x=0.17 phase boundary observed in microcrystalline $Zr_{1-x}Y_xO_y$[131]. Reduced grain size is known to stabilize the higher symmetry tetragonal phase of ZrO_2[57], and our expanded range of cubic symmetry is consistent with a mechanism associated with grain size.

The impedance response $\tilde{Z}(\omega) = Z'(\omega)+\mathrm{i}Z''(\omega)$ of the test structures were obtained with a HP 4284 LCR meter using 100 mV ac excitation and frequencies from 100 Hz to 1 MHz. The substrates were mounted on a heated probe station with thermal paste, and the temperature determined using a thermocouple cemented to a mounted substrate. The counterelectrode of the desired test structure was contacted by a Pd needle.

The impedance spectra of all test sites were fitted with equivalent circuits using a complex nonlinear least squares fitting program[22]; results are illustrated in Fig. 2. Bauerle's equivalent circuit of three resistor-capacitor networks linked in series[70, 18] does not represent these impedance spectra. The Pt electrodes used in this study are blocking electrodes, corresponding to the replacement of the final resistor-capacitor network of Bauerle's circuit by a single capacitor. Also, the nanocrystallinity of the films results in significant variations in the relative sizes of grains and grain boundaries. To account for the corresponding dispersion of relaxation times, the capacitors in the intragrain and grain boundary networks of the circuit are replaced by constant phase elements (CPE), creating circuit B in Fig. 2. Most acquired spectra were adequately modeled by this equivalent circuit, with the two R-CPE networks representing intra- and inter-grain conductivities. The association between circuit component and conduction mechanism was made by matching the active frequency range of the CPE with the characteristic frequencies of intragrain ($\sim$10 kHz) or grain boundary ($\sim$1 kHz) ionic conduction.

9.2 Thin Film SOFC fabrication for material evaluation

The above project which aims to identify potentially interesting oxide electrolytes using high throughput experiments motivates the development of a complementary medium-throughput technique for evaluating the performance of the electrolytes under fuel cell operating conditions. In an effort to develop such a technique, the van Dover group hosted NNIN-REU student José Fonseca. The details of the project are available in his report[51]. The idea is to be able to deposit composition spreads which are identical to those deposited in the high-throughput project of the previous section, but to then use the films in a micro-fuel cell testing station. The strategy is to use photolithography to create electrically isolated thin film fuel cells. The thin film membranes (Figure 9.3) are square with order 100μm side and thus each contains a homogeneous oxide electrolyte. In a single deposition, fuel cells with widely varying composition and/or thickness are fabricated, which allows for systematic investigation of fuel cell performance with respect to these parameters.

There are several problems with chemically compatible processing and aversion of mechanical destruction of the membranes, some of which have been solved. The other aspect of the research plan is to develop techniques for rapid fuel cell testing at 500°C. Based on the quite fancy testing apparatus developed by the Prinz group[78], I made a quite inexpensive testing apparatus (Figure 9.4) which I have used to heat membranes to over 500°C with an atmosphere of H_2 on one side and air on the other. Combined with a common bottom contact and a Pd probe needle top contact, this setup should allow for the testing of thin film membrane SOFCs, but such an experiment has yet to be (successfully) performed.

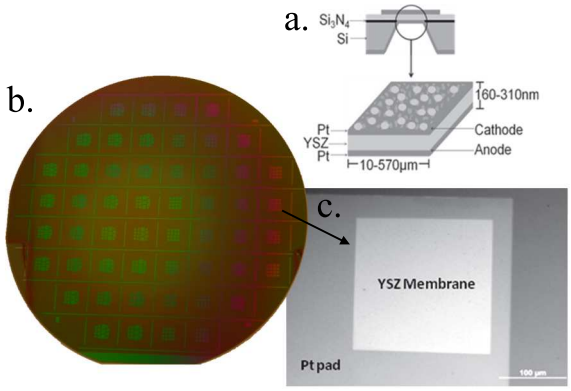

Figure 9.3: a. Cartoon of a micro-fuel cell consisting of two porous Pt electrodes separated by a sputter-deposited oxide electrolyte. This stack has a ≈1000 aspect ratio and is thus essentially a membrane suspended on a Si wafer. b. A plan view of a 3 in. wafer with a thickness spread of YSZ deposited on top of templated Pt pads. The template includes arrays of membranes of several sizes placed at the center of 8mmx8mm chips. c. An optical micrograph showing a plan view of a 400μm square Pt-YSZ-Pt membrane. The Pt electrode is larger than the membrane to allow for probe needle contact.

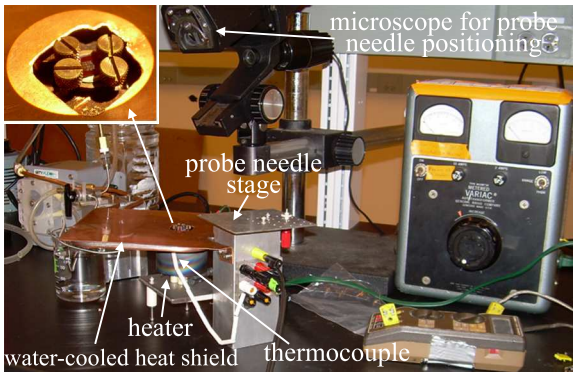

Figure 9.4: A photograph of the apparatus for testing thin film membrane SOFCs. The membrane is heated primarily through H_2 which flows through a stainless steel chamber mounted on a US-Inc resistive heater. The upper-left inset shows a top view of a 8mm square Si chip bolted to the chamber with the patterned Pt as shown in Figure 9.3.

9.3 Complex nitrides synthesis from transition metal thin films

Metastable nitrides can be quite stable due to large kinetic barriers to oxidation. Such materials are ubiquitous in many disciplines and despite valiant (and continuing) efforts, Frank DiSalvo has yet to study every single nitride phase. His postdoc Akira is expanding the list of nitrides that have been made in the DiSalvo labs and had the idea of making some particularly tricky nitrides (high temperature phases) by reacting metal thin films with NH_3. I'm the thin film resource in the project and so far A_2Mo_3N with A=Pt,Pd,Ni have been attempted with demonstration of nice, phase pure Pt_2Mo_3N and some less-nice other nitride phases. The high temperature nitride phases are being tested for stability under fuel cell operating conditions and catalytic activity for oxidation of methanol, formic acid, and hydrogen in the presence of carbon monoxide. This project also sets a platform for discovery of new high temperature nitride phases and may already comprise the most extensive research of nitride research for fuel cell applications.

9.4 Catalysts for growth of carbon nanotubes

Carbon nanotubes are commonly grown through decomposition of a carbon-containing gas at high temperature on nanoparticle metal catalysts with an oxide support. While the process parameter space of the gas composition, flow, and temperature has been extensively explored, a handful of different metal catalysts and oxide underlayers have been tried. The ultimate goals of chirality selectivity and indefinite growth seem far from being realized. So we (Bruce, John Hart, his students and I) designed some catalyst systems to explore with

the purpose of gaining insight into the mechanisms responsible for chirality nucleation and growth termination. $In\ situ$ characterization of the catalysts and growing nanotubes are performed by the Hart group with a setup amenable to 1-D catalyst composition or thickness spreads[173].

CHAPTER 10

APPENDIX

10.1 Details of the crystal monitor determination of deposition profiles

Figure 10.1 contains an outline of the substrate, the coordinate axes are inches from the substrate center and the position of the relevant gun is marked in grey. These properties are shared with most of the figures in the section. Also, in the below contour plots, squares denote points at which WDS or EDS data were taken. Colored contours are not plotted beyond the Cartesian boundaries implied by the set of data points. All contours are calculated using Origin 7.5 default interpolation algorithms for random (x,y) data sets. Commonly, deposition rates (or equivalently film thicknesses) are normalized to the value of the center of the substrate. Also, plots of deposition rate as a function of the radial gun coordinate are typically "angle adjusted". This simply involves dividing the deposition rate by the azimuthal-coordinate term in Equation 3.1.

Figures 10.2, 10.3 and 10.4 summarize the analysis of a tantalum film sputtered from gun 3. The Ta thicknesses measured on this film were all between 160$\mathring{A}$ and 1400 $\mathring{A}$, perfectly within the useful range implied by Figure 3.2. It is worth noting that at the thicker end of the substrate, small errors in the measurement of k-raw values give large errors in film thickness due to the steep slope at k-raw>90%. There is a measurement error of k-raw values of at least ±0.03. However, this error is mainly due to differences in material properties between bulk and sputtered Ta and is thus systematic. Systematic errors do not

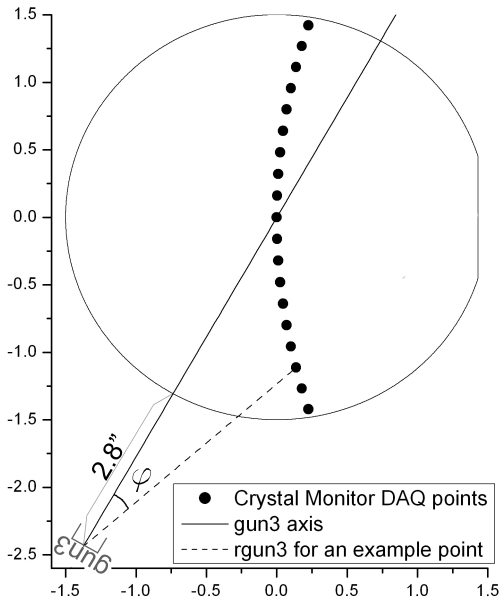

Figure 10.1: The deposition region is outlined by the shape of a 3″ wafer. This is a bird's eye view in Tubby so this would be the $back$ side of the wafer. The position of gun 3 is shown as well as the projection of the gun 3 axis in the substrate plane. The crystal monitor positions commonly used for deposition profiling are shown. These substrate positions are parameterized in polar coordinates in the substrate plane with the origin determined by projecting the gun center in the direction normal to this plane.

alter the profile very much in the linear regime of Figure 3.2, which covers most of the substrate.

The contours of figure 10.2 certainly provide qualitative verification that this technique for characterizing thickness profiles is legitimate. First assume that the angular term in 3.1 is correct. Then the crystal monitor must be divided by $\sqrt{cos\,(\varphi)}$ prior to fitting to the functional form of 3.2, and to compare with this fitted function, WDS data must also be divided by the angular term. The raw crystal monitor data, fitted function, and WDS data divided by the angular term are plotted in Figure 10.3. The data used for the function fitting were cor-

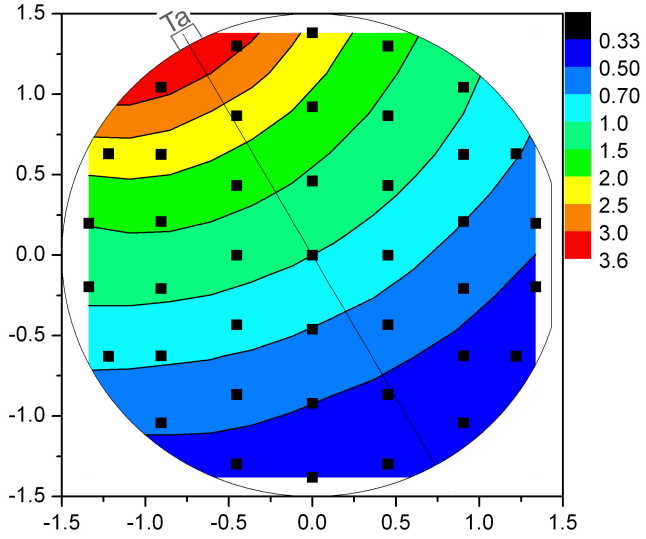

Figure 10.2: Contour plot of the thickness of a tantalum film sputtered from gun 3 as determined by WDS measurements applied to the fit function of Figure 3.2. The thicknesses are normalized to the thickness measured at the center of the substrate.

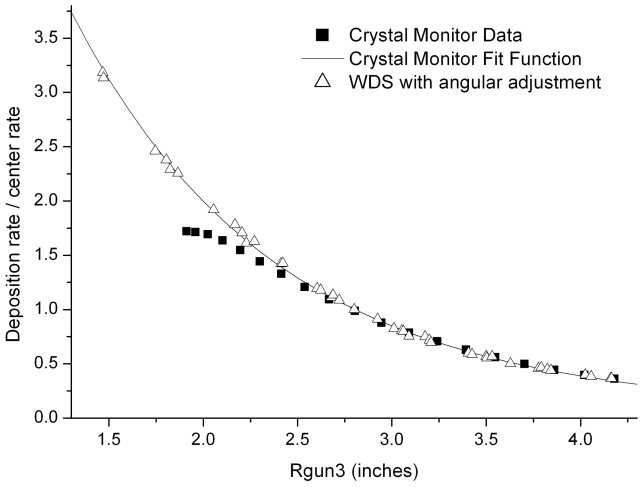

Figure 10.3: The raw crystal monitor data, angular adjusted WDS data, and function fitted to angular and shadow corrected crystal monitor data are shown as a function of $rgun3$. All data sets are independently normalized to the center value.

rected by more than the angular term. Clearly, the crystal monitor raw data has a dependence on $rgun3$ that seems unphysical as the slope suddenly dies with $r3gun$ <2″. The angular correction helps in this regard but for this dataset I believe the deposition rates also need to be corrected for shadowing of the crystal from the Ta sputtered material. This shadowing was evident upon visual analysis of the crystal after deposition. To correct for the shadowing, I fit an empirical form for the supposed shadowing affect so that crystal monitor data is shadow corrected by the transformation

$$depositionrate \rightarrow depositionrate\left(0.95 + \frac{1.95}{(rgun/inch)^{3.38}}\right). \tag{10.1}$$

Note that the shadow correction value is unity at $rgun$=2.8″ so that normalization to the center rate is not compromised. While Figure 10.3 suggests that $rgun$ is a reasonable variable and that Equation 3.2 is a reasonable functional form, the shadow correction somewhat forced that result. Regardless, the fractional error between measured and calculated profiles,

$$\frac{DepRate_{wds} - DepRate_{calculated}}{DepRate_{wds}}, \tag{10.2}$$

is given as a contour plot in Figure 10.4 and indicates that we are on the right track.

Figure 10.5 gives the contour plot of the thickness profile of a Pt film sputtered from gun 1 and measured with WDS. Figure 10.6 shows the raw and angle adjusted crystal monitor data for Pt in gun 1. The inability to obtain crystal monitor data for 1.3″< $rgun$ <1.7″ and corresponding need to extrapolate crystal monitor data for a sizeable fraction of the substrate make the angular correction necessary for compliance with measured data.

Figure 10.7 is a contour plot of the error (Equation 10.2) of the crystal monitor fit function and demonstrates the validity of the deposition profile model.

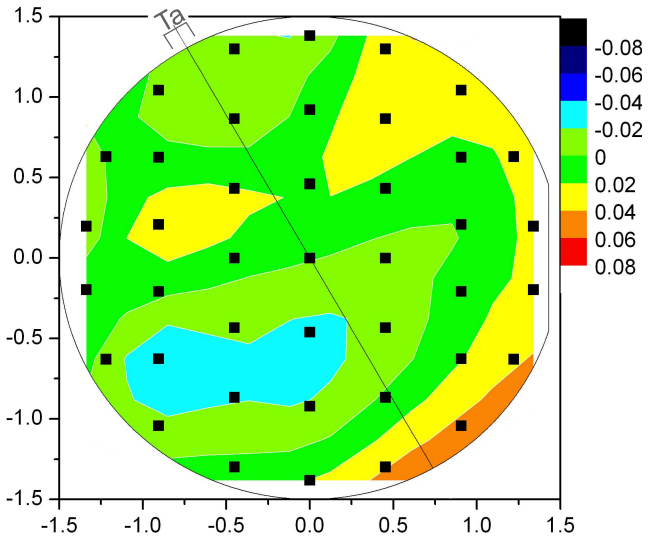

Figure 10.4: The error between the WDS data of Figure 10.2 and the crystal monitor fitted function of Figure 10.3 (including the angular adjustments of Equation 3.1).

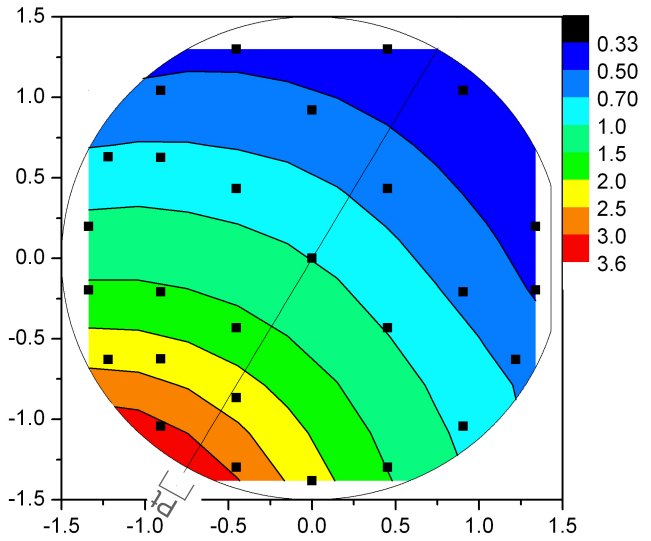

Figure 10.5: Contour plot of the thickness profile of a Pt film sputtered from gun 1 and measured with WDS

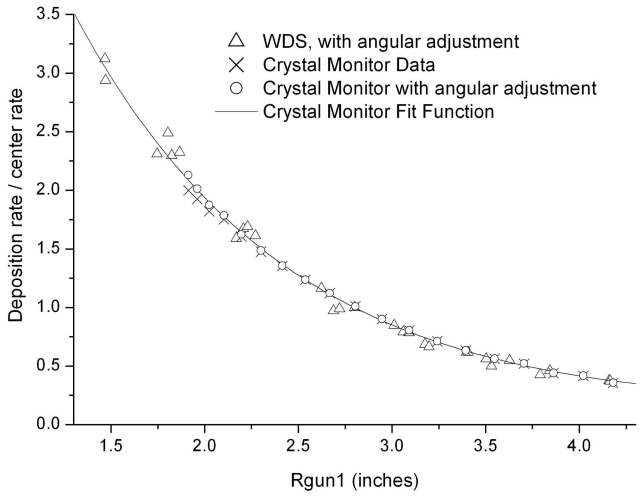

Figure 10.6: The raw and angle adjusted crystal monitor data, angular adjusted WDS data, and function fitted to angular and shadow corrected crystal monitor data are shown as a function of $rgun1$ for deposition of Pt. All data sets are independently normalized to the center value.

For this sample, no shadow correction was needed. I propose the following technique for applying shadow corrections for crystal monitor data that lacks other thickness measurements for comparison: Mix the shadow adjusted data (computed using 10.1) and non-shadow adjusted data with weightings that preserve deposition rate at substrate center and that, when fit to the functional form of Equation 3.2, minimize the least-squares goodness-of-fit parameter. That is, choose the level of shadow correction that makes the data most like the proposed functional form that has been verified by WDS profiles. This algorithm yields the weightings already used in Figures 10.3 and 10.6.

The remaining obstacle is to characterize profiles for gun 2. In principle, for a given target element, the profile should be identical to a gun 1 or gun 3 profile under coordinate transformation. Using the Ta, gun3 and Pt, gun1 profiles above, comparisons were made with Pt and Ta films sputtered from gun 2 and analyzed with WDS. The results are in Figures 10.8 and 10.9. Unfortunately,

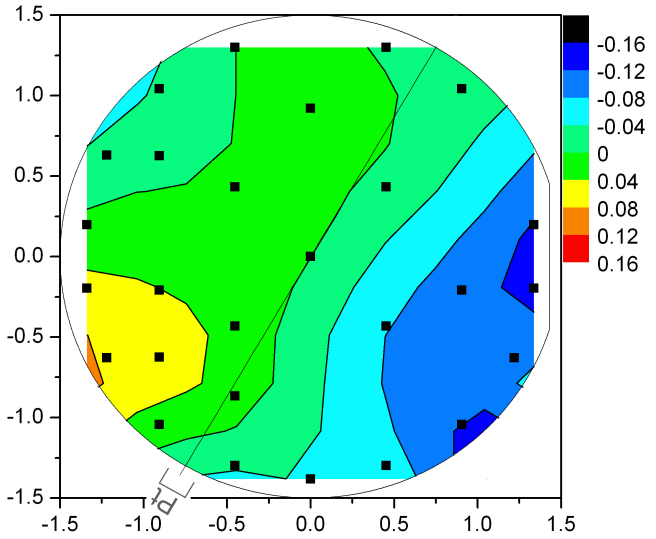

Figure 10.7: The error between the WDS data of Figure 10.5 and the crystal monitor fitted function of Figure 10.6 (including the angular adjustments of Equation 3.1).

the orientation of gun 2 is visibly different from guns 1 and 3 due to imperfect manufacturing of the gun mount. Thus, differences in profile may be anticipated. The Ta sample certainly indicates significant differences in the profiles as the calculated deposition rates differ by as much as 20% from measured rates. The Pt sample shows better compliance with better than 10% agreement over most of the substrate. Also, the structure of the error surface of Figure 10.9b is indicative of the substrate having shifted and rotated from its home position before deposition. Such substrate shifting was evident upon visual analysis of the substrate after deposition. Thus, while the profile of gun 2 remains to be carefully documented, most sputtered samples are made with Pt from gun 2, so the profile only needs to be well understood for this single case.

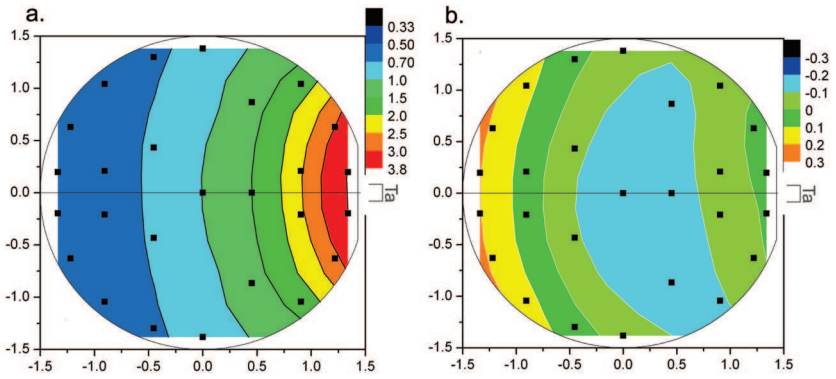

Figure 10.8: a. Contour of Ta film thickness as measured by WDS. The black points denote measurement positions. b. The fractional deviation of a. from the gun 2 deposition profile inferred from appropriate geometric transformation of crystal monitor-determined Ta gun 3 profile.

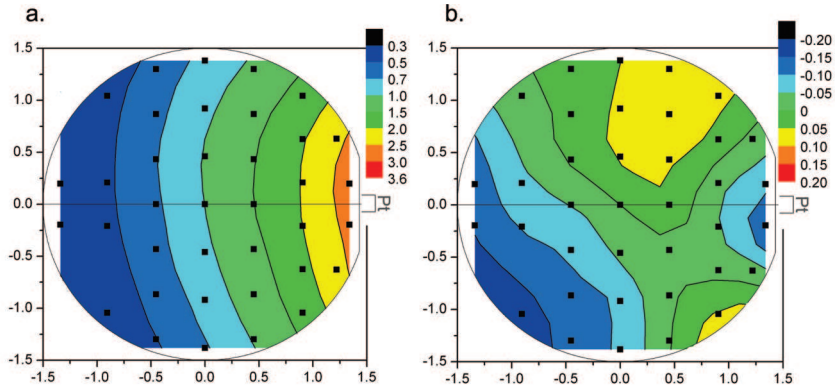

Figure 10.9: a. Contour of Pt film thickness as measured by WDS. The black points denote measurement positions. b. The fractional deviation of a. from the gun 2 deposition profile inferred from appropriate geometric transformation of crystal monitor-determined Pt gun 1 profile.

10.2 Algorithms for phase identification by analysis of XRD correlation maps

In the CHESS experiments, diffraction images are taken on a regular rectangular grid of substrate positions with spacing d_{grid}. The physical extent of the m row, n column grid extends beyond the substrate with data collected at points within the composition spread. The dataset X consists of images acquired at a set of substrate positions denoted by their ordinal index, $X \subset \{0, 1, \ldots, m\,n-1\}$. For a given $k \in X$, the diffraction image ${}_k\mathbb{I}$ is analyzed in polar coordinates ρ and γ with

$$\rho = L\ \tan(2\theta), \tag{10.3}$$

where L is the substrate-detector separation and 2θ the scattering angle.

The substrate is not rotated during acquisition, precluding the study of single crystalline films. The films are assumed to be either equiaxed or fiber textured, with the detector azimuth γ capturing a wide range of the texture angle χ. This inclusion of this wide range of χ is facilitated by a substrate tilt of α=46°as evident in the geometric relation

$$\chi = \cos^{-1} \tag{10.4}$$
$$\left(\tfrac{2\pi}{Q\lambda}\left[\cos\alpha - \left(1-\sin^2(2\theta)\,\sin^2\gamma\right)^{1/2}\,\cos\left(\alpha - \tan^{-1}\left(\tan(2\theta)\,\cos\gamma\right)\right)\right]\right),$$

which reveals that for a given detector azimuth γ, χ is weakly dependent on the Bragg angle and strongly dependent on the substrate tilt.

The use of a single-crystalline (e.g. Si) substrate results in the detector capture of relatively intense thermal diffuse scattering of Si Bragg reflections. Lead blocks are used to protect the detector from the brightest of these substrate reflections and the more diffuse intensity must be subtracted from ${}_k\mathbb{I}$. A mask image $\mathbb{K}$ is used to zero the pixels surrounding the lead blocks from analysis.

Given the counts per incident photon ${}_k\mathbb{I}_i$ in pixel i at position k, define an image with pixel values

$$\mathbb{M}_i = min\left\{{}_k\mathbb{I}_i\right\}_k . \tag{10.5}$$

By design, $\mathbb{M}$ contains the diffraction spectra from the substrate and any other uniform layers. The image also contains detector counts from x-ray fluorescence and diffraction for amorphous material, most notably air. There are some algorithms for modification of $\mathbb{M}$, but for the present purposes we use this image as the background image for the entire dataset:

$${}_k\mathbb{B} \approx {}_k\mathbb{A}. \tag{10.6}$$

Diffraction spectra analogous to powder spectra are obtained by integration of the images,

$${}_kI \propto \int \mathrm{d}\chi \; \mathbb{K}\left({}_k\mathbb{I} - {}_k\mathbb{B}\right) \tag{10.7}$$

and analyzed as functions of the magnitude Q of the scattering vector. Unlike that of conventional diffraction data, the "background" of a given ${}_kI$, i.e. the Q-variation of intensity not from film Bragg reflections, may have sharp features and several changes in curvature. Polynomial fitting of this background is not appropriate due to the high order that would be needed to capture the high local curvature. Instead, background subtraction is performed by an $ad\ hoc$ method:

at a given Q value, the background intensity is maximized with the constraints that it may not surpass ${}_kI$ and the curvature of the background must remain above -16/nm^2, a value corresponding to the minimum curvature of a diffraction peak with height near the detectability limit and width corresponding to a 2nm grain size. Redefining ${}_kI$ to be the 1-d intensity after this background subtraction, the dataset is now prepared for higher level analysis.

Define the intensity self-correlation image for point k,

$$ {}_kQQ(Q_a, Q_b) = {}_kI(Q_a){}_kI(Q_b), \tag{10.8} $$

where $Q_a \geq Q_b$. The Q-Q correlation image from the entire dataset is

$$ QQ(Q_a, Q_b) = \sum {}_kkQQ(Q_a, Q_b). \tag{10.9} $$

The intensity along the image diagonal (Q_a=Q_b) will peak at Q values where there is a film Bragg reflection from any position in X. Off-diagonal (Q_a>Q_b) peaks correspond to Bragg reflections at Q_a and Q_b which coexist in any diffraction image. The most basic interpretation of the peaks is that if Bragg reflections are witnessed at scattering vectors Q_a and Q_b from the same phase then there will be intensity at QQ. There may not necessarily be a peak at this position as this intensity may be part of a broader peak. Still, the set peak positions, ${}^{QQ}P$, contain information concerning the phase grouping of the witnessed Bragg reflections. To estimate the extent of a given peak in ${}^{QQ}P$, we find the values ${Q_a}^-$, ${Q_a}^+$, ${Q_b}^-$, ${Q_b}^+$ at which the value of QQ drops to half the maximum value or begins increasing (the latter criterion separates overlapping peaks). The resulting rectangle surrounding the maximum value is the approximate extent of the peak.

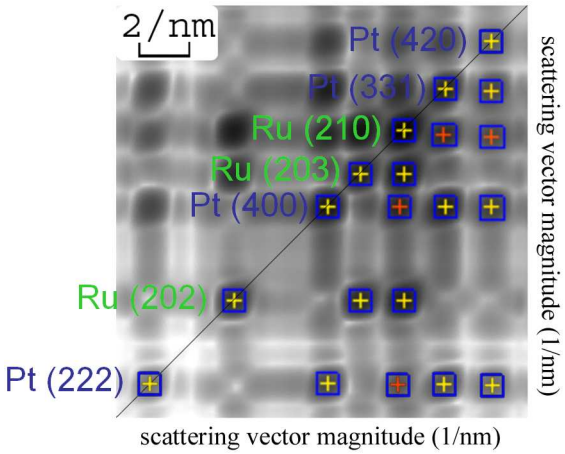

Figure 10.10: A small section of the calculated QQ for a Pt-Ru composition spread thin film is plotted. A colored cross indicates the position of a detected peak and its $\overline{QQ}$ value (yellow is high, orange is low). The blue box indicates the calculated "extent" of the peak. The indexed reflections are labeled and the off-diagonal peaks only have appreciable intensity at Q_a, Q_b values corresponding to Bragg reflections from the same phase.

Define a normalized QQ

$$\overline{QQ}(Q_a, Q_b) = QQ(Q_a, Q_b) \,/\, \left(QQ(Q_a, Q_a)\; QQ(Q_b, Q_b)\right)^{1/2}. \tag{10.10}$$

By definition, $\overline{QQ}$ will be unity on the diagonal. Off-diagonal, $\overline{QQ}$ will take values between zero and unity. For Q_a and Q_b where the intensity remains in the same ratio for all ${}_kI$, $\overline{QQ}$ will be unity. Deviations from a constant ratio will result in smaller values and in the limit where there is never intensity at both Q_a and Q_b in the same image but there is intensity at both Q_a or Q_b at some point in X, $\overline{QQ}$ will be zero. Generally, the values of $\overline{QQ}$ are only meaningful where QQ is significantly above the noise. Treating QQ as a probability density function in the rectangular region described above, the expected value of $\overline{QQ}$ is calculated for each peak in ${}^{QQ}P$. If this expected value exceeds some critical value (≈0.7), the corresponding Q_a and Q_b are considered to be correlated; that

is a Bragg reflection at Q_a in a given ${}_k\mathbb{I}$ is commonly accompanied by a Bragg reflection at Q_b. For the study of powders, this critical value may be set close to unity, but for thin films a smaller value is desired due to variations in the maximum intensity ratios of single-phase Bragg reflections (as measured by the detector) due to evolution of the fiber texture of that phase.

Consider a list of peaks ${}_k{}^{I}\mathcal{P}$ in the 1-d spectrum ${}_kI$. A pair of peaks at q_a and q_b may be associated with a peak in ${}^{QQ}\mathcal{P}$ at Q_a, Q_b if q_a, q_b lies within the full extent of the peak, defined as twice the FWHM extent described previously. This definition of "association" is appropriate for q_a, q_b shifting from the ${}^{QQ}\mathcal{P}$ values due to alloying under the assumption that the density of analysis points in X is high enough that alloys peaks sum to form wide continuous peaks in QQ and not a series of smaller peaks with distinguishable maxima. This approximation also implies that the shifting alloy peaks result in a single correlation peak in ${}^{QQ}\mathcal{P}$. If this FWHM extent is not available due to overlapping peaks, "association" can be defined by appropriate proximity of q_a, q_b and Q_a, Q_b. The difference in magnitude of alloy versus anisotropic lattice parameter shifts suggests a critical deviation that is directional in the Q_a-Q_b plane. For example, if q_a=Q_a, then q_b must be within $r_{aniso}Q_b$ of Q_b, where r_{aniso} is the maximum fractional anisotropic lattice parameter shift. The maximum deviation occurs for a perfect alloy shift with q_a=(1+r_{alloy})Q_a, q_b=(1+r_{alloy})Q_b where r_{alloy} is the maximal fractional shift in lattice parameter due to alloying. The quadratic (in Q_a and Q_b) curve of maximum deviation with these constraints is not a conic section but can be visualized as a distorted ellipse with major axis at an angle $\tan^{-1}(Q_b/Q_a)$ from the Q_a axis. The liberal association of pairs of peaks in ${}_k{}^{I}\mathcal{P}$ with a correlation peak in ${}^{QQ}\mathcal{P}$ results in possible multiple associations but ensures that lattice parameter shifts are handled appropriately. For the Pt-Ru example in Figure

10.10, this association algorithm according to the $\overline{QQ}$ value leads to the correct grouping of the peaks into the Pt and Ru phases.

A given subset of peaks in ${}_k{}^I\mathcal{P}$ may belong to a phase ${}_j\mathcal{P}$ if and only if every q_a, q_b pair is associate with a correlation peak with acceptable $\overline{QQ}$ value. In principle, this should provide for the deconvolution of the set of detected Bragg reflections into a list of phases and their intensity at a given substrate position (essentially, a phase diagram of the composition spread). These algorithms have only been implemented up to the calculation of $\overline{QQ}$.

10.3 Manual for Tubby control

This manual is not contain step-by-step instructions for depositing films and contains no lessons on vacuum depositions. It is more of a reference manual for the equipment, especially custom-made equipment. Familiarity with vacuum and sputtering equipment is assumed.

10.3.1 PVD equipment and chamber dimensions

A description of the deposition system and the associated Figure 2.2 were given in Section 2.2.3. This section contains the layout of the PVD equipment in the chamber.

Figure 10.11 serves 2 purposes. It shows the orientation of the PVD equipment, including the numbering of the guns in the 4-gun assembly. Also, it labels the useful dimensions of the chamber. The bottom of the chamber is curved with

Table 10.1: Dimensions of Figure 10.11. These are all measured or derived from geometrically-related measurements - these measurements are difficult and have $\gtrsim$0.01″ uncertainty. Third decimal place is best guess.

label	inches	description
a	8.875	half of chamber ID
b	2.875	radius of the 3 bottom port holes
c	1.375	distance from bottom port hole to chamber wall
d	4.25	distance from center of bottom port hole to chamber wall
e	8.011	length of equilateral triangle connecting port holes
f	5.135	minimum dist. from center of port hole to edge of another
g	2.261	minimum distance between edges of port holes
h	4.625	radius of circle containing port hole centers

3 conflat ports. All the dimensions are in the plane of the conflats - curvature is ignored. Note that the 4″ gun and the ion gun are not at the center of their port holes. The substrates are intended to lie on a circle at the 4.625″ diameter of the port holes. The feedthroughs for the 4″ gun and ion gun are not in the center of their conflats.

10.3.2 Electronic equipment and computer interfacing

The figures and tables give the brief descriptions of all of the equipment. Here are some more notes:

U1 is 4 pressure gauges in 1 unit. The convectron pressures are always displayed and only 1 ion gauge can be operated at any given time. It's pressure

Table 10.2: Partial list of Tubby equipment

U1	Convectron and ion gauge controller
U2	Custom valve, interlock control unit
U3	Butterfly valve controller
U4	Barratron gauge, linked to U3
U5	cryopump temperature
U6	Omega 6 channel temperature controller
U7	auxiliary cryopump convectron gauge
U8	Sycon crystal monitor controller
U9	auxiliary cryopump ion gauge controller (2 gauges)
U10-U14	MDX500 supply, typically for guns 1-4
U14	IonTech ion gun controller
U15	ENI pulsed DC supply, typically for 4" gun
U16	cryoshroud type K thermocouple reader
U17	MKS 4-channel Mass Flow Controller
U18	*broken*Residual Gas Analyzer
U19	RS232 hub
U20	NIDAQ breakout box: many DVMs
U21 and U22	timer and variac for heat tape power
U23	timer for sorption pump heater
U24	"Big" variac for all 3 substrate heaters
U25	"Small" variac for sub2 heater
U26	isolation transformer for sub2 heater
U27	relay+transformer board for heaters

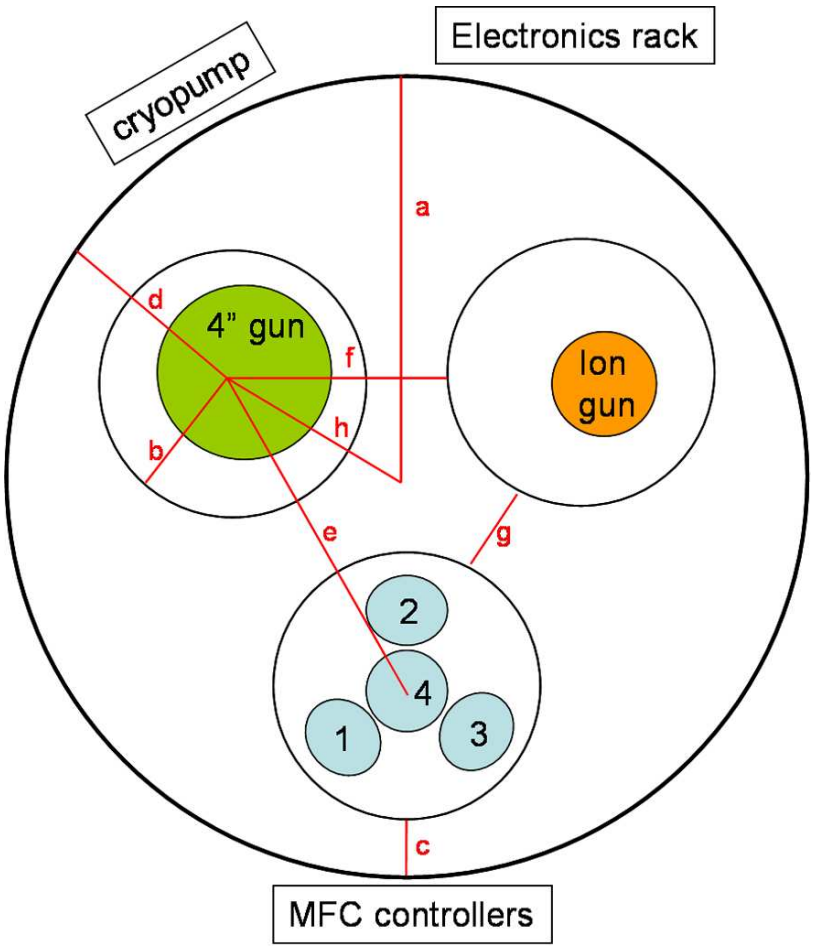

Figure 10.11: Bird's eye view of the inside floor of Tubby. Not to scale. The three conflat ports assumed to be identical and to lie on a circle concentric with the chamber.

is the top line. All pressures are scientific notation in Torr. Ion gauge channel has analog output to computer. Chamber convectron has analog output to comparator circuit (see next section).

U2 contains a lot of switches on the front and a lot of custom electronics on the back. The electronics provide safety interlocks both for users and for the equipment. See next section.

U3 is the butterfly valve controller and U4 is the gauge for the capacitance

manometer. This controls sputter pressure. Make sure U4 reads zero when ion gauge shows ¡0.1mT pressure. U3 effectively controls pumping speed based on the comparison between the voltage output from U4 and the voltage set by the user using the upper-left knob (ignore knob units). The lower-right selector and switch on U3 are used to set valve as open, feedback-controlled or closed (closed is not air-tight).

U5 displays cryopump cold stage temperature. For regen this should be brought above 300K and then cooled down to $\sim$14K.

U6 controls the substrate heaters and reads the heater temperatures. The heater temperature is NOT the substrate temperature. See calibrations for the conversion. I somehow broke channel 3 in the first week. Usually channels 1,2,4 are used for substrates 1,2,3. This unit has relay outputs that control the relays in U27 and thus attempts to maintain the heater temperature at the programmed setpoint using the duty cycle. Reasonable PID parameters are set in the Labview software. RS232 controlled.
NOTE: During sputtering or ion gun operation the temperature can go nuts - watch out.

U7, U9 are additional gauges. Not exactly same place as U1 gauges (some are other side of butterfly valve) but these are generally used when there is a problem with U1.

U8 due to low profile, the crystal monitor is Inficon, but due to friendly computer interface the electronics are Sycon. The Labview includes a library for updating elemental parameters so that A/s reads correctly. But since day 2, the controller has been set so that A/s is really 10^{-8}g/s/cm^2. Virtually all recorded

crystal monitor measurements are in these units. RS232 controlled.

U10-U13. DC power supplies, analog outputs for current and voltage to computer.

U14, U15, U17 Computer interface never setup.

U16 analog output to computer.

U18 The display is broken. RS232 is setup and I tried operating through the computer. Something else is wrong, apparently hardware-related.

U20: NOTE: all analog outputs to computer are calibrated to an accuracy of several %. There is usually negligible analog noise EXCEPT during pulsed DC operation. The goal is to monitor the equipment during sputtering case there are any "jumps" - absolute accuracy could be achieved by careful calibrations.

U21 and U22 power whatever heat tape is plugged into U22. This is usually heat tape to warm N_2 going to the cryoshroud or the cryopump. It has also been heat tape for warming the chamber walls. The heat tape is designed for 120VAC operation but 60VAC to 90VAC is recommended. EXCESSIVE HEATING DURING CRYOPUMP REGEN COULD RESULT IN MELTING OF INDIUM SEALS, DESTROYING THE CRYOPUMP. Forty minutes at 70VAC is a good schedule for warming the cryoshroud. The pressure may skyrocket during this process so only do this after the substrates sufficiently have cooled.

U23 Sorption pump is only used for cryopump regen. If the interlocks are overridden, the mechanical pump could pump the cryopump through the chamber but this usually results in the dislodging of the screen covering the cryopump inlet. 2 hours of heat is enough o clear the sorption pump. After 1

hour, the plug needs to be manually pulled because the pressure never builds up enough to blow it out.

U24-U27. Each substrate heater is partially independently powered: each has a U6-controlled relay and TWO transformers in series.
NOTE: A "36V" transformer is a transformer that is meant to take 120VAC down to 36VAC; more aptly it is a 3:1 transformer.
U24 steps the 120VAC wall voltage down for all 3 heaters. It also contains an ammeter. If you become familiar with typical heater currents you can tell how many are operating. Especially if only one heater is on, one can tell that a bulb has lost electrical contact by noticing that the current is 67% of its normal value. Bulb filaments draw a lot of current when their circuit is closed so make sure to have this big variac on the high current 10A setting even though the normal operation may be at low current.
The 3 relays are attached to the output of the big variac, thus providing independent operation of the 3 heaters. Sub1 and sub3 have additional 3:1 transformers in series, so sub1 and sub3 are at the same voltage during simultaneous operation. The 3:1 transformer for sub2 is still on U27 but is fried. SAFETY PROBLEM: The heaters, especially sub1 and sub3 should have 6A slow burn fuses!!! If the 2 heater wires get shorted in the chamber, the 3:1 transformers will melt before the big variac fuse blows. This is what happened to the sub2 transformer.

Sub2 has its own variac. The 3:1 transformers also serve as isolation transformers but variac does not isolate so there is 1:1 isolation in series. This setup is somehow "lossy", i.e. the voltage to the heater is 10 to 20% less than that expected from the 2 variac settings. The HIGHEST heater power used in nor-

mal operation is at 30VAC, 5.4A. This corresponds to a big variac operation of 90V, 1.8A. The bulbs are obviously meant to operate at 120VAC so the heaters could potentially be operated at much higher power. The integrity of the bulb will likely be compromised. ALSO, the current rating of the 3:1 and isolation transformers is 5 or 6A so we are already pushing the limit of the voltage supply electronics.
NOTE: The power strip in U27 is NOT WALL POWER. It is the output of the big variac.

10.3.3 Custom valve, interlock controller

Valves

The valve controller is a passive controller using only switch logic to provide safety to the vacuum equipment. The circuit diagram is in 10.16. Basically, each PSV needs 120VAC to open the solenoid that provides the compressed air for opening the valve. Each PSV has a switch for turning on that voltage except the voltage is not always available at the switch. Voltage is supplied to all switches if the override C9 is switched to the left. Otherwise, the following logic is in place. "Activated" means that switch actually has the ability to do something, like open a valve. "Up"="On"="valve open".

C6 does not control a valve but activates a bank of PSV switches. In the center position no valve switches are activated; in the up position C2-C5 are activated; in the down position C7 is activated. This keeps the cryopump from being open to the chamber vent or to the chamber rough pump. Additionally it means that the cryopump vent and rough (sorption) pump, which are used

during cryopump regen, can only be opened if gate valve is closed.

C5 is only activated if C4 is down so that during regen one cannot forget to close the N_2 and inadvertently fill the sorption pump.

Similarly, C3 is only activated if C2 is down. Additionally, C3 is only activated if C1 is on. The intention is that the roughing valve cannot be opened to expose an evacuated chamber to a non-operating pump, which would result in pump oil streaming up the foreline and potentially into the chamber.
ISSUE: This, like many of the interlocks, are passive and assume the equipment is working. The interlock requirement is that voltage is being supplied to the pump, not that the pump is actually pulling vacuum. Occasionally, the pump reveals its age as the motor pulls too much current, causing the breaker to trip. The breaker is reset on a large grey box on the back of the electronics rack. If this happens, CLOSE C3 ASAP!

NOTE: the valve opening/closing is not as instantaneous as the switch, especially for C7 gate valve. So for example if C2 and C7 are up and C6 is rapidly switch from down to up, the action will start closing the gate valve but before it closes the vent valve will open and will slightly vent the cryopump.

Interlocks

This is an active interlock controller so that hoist can only be operated with the chamber pressure is high (protect hoist/chamber) and sputter power supplies can only be operated when cooling water is flowing (protect the targets) and the chamber pressure is low (protect user from potentially fatal electrocution).

The interlocks and safeties are wired as shown in 10.17. The solid state switches provide electrical isolation of the interlocks for the power supplies and hoist. The 4 MDX power supplies are electrically identical.

C9 and C10 provide overrides of the interlock logic. Normal operation is C9 to the left and C10 to the center and this is assumed in the logic described below. DO NOT SWITCH C9 AND C10 AT THE SAME TIME - I THINK THIS CREATES A PROBLEM - I HAVEN'T INVESTIGATED. Switching C9 to the right closes the interlocks for the MDXs and IonTech. Switching C10 to left closes ENI interlock and to the right closes hoist interlock.

NOTE: U17 is interlocked so that one cannot inadvertently fill the room with CH_4 or O_2. I don't remember how this is done. This is not included in the circuit diagrams or below description of interlock logic.

NOTE: C12 and C13 indicator LEDs are parallel pairs of LEDs so that in the unlikely case that one burns out, no electronics modification is necessary.

Circuit actions:
C13 is illuminated if the Proteus leads are shorted.
C12 is illuminated high(low) if the U1 chamber convectron voltage is above(below) the voltage across a voltage divider - voltage adjusted by C11 potentiometer. Due to U1 drift and/or power supply drift, this needs to be adjusted occasionally. This involves a comparator circuit whose state is referred to below as "high pressure" or "low pressure".
ISSUE: The U1 convectron voltage has a slope ~ 0.01mV/Torr near atmospheric pressure so making the comparator circuit sensitive to exactly atmospheric pressure is beyond the resolution of the electronics. WHEN THE STATUS IS "PRES-

SURE HIGH" THE PRESSURE IS NOT NECESSARILY AT ATMOSPHERIC PRESSURE. THE TELL TALE FOR THE USER SHOULD BE THE RELEASE OF NITROGEN FROM THE CHAMBER SEAL!

MDX and ENI interlocks leads are shorted if the Proteus leads are shorted AND status is low pressure.

IonTech interlock leads are shorted if status is low pressure.

Hoist is given wall power if status is high pressure.

ISSUE: "infinite" op amp resistance is actually $\sim$1.5kΩ. In the comparator this needs to be "high impedance" so the voltage divider must comprise a relatively low impedance. Originally, a 9V battery was used but the current draw of the low-resistance voltage divider makes this impractical. Thus, a 9V consumer-grade AC/DC converter is used. This is not a voltage-regulated supply which means the actual voltage depends on current draw and the current draw is different in the high pressure status and the low pressure status. THE RESULT IS SHOT NOISE WHICH AT HIGH FREQUENCY MAY EFFECTIVELY ALLOW BOTH PRESSURE STATUSES. You can replace the 9V supply with a voltage-regulated equivalent if this becomes a problem.

10.3.4 Labview programs

There are a set of programs for communicating with each instrument. Typically these are not used. The special cases would be if you want to play with the positioning or if the PID parameters need to be reset on U6 due to a communication error (this latter issue occurs about once per year). There is also a program for deposition profiling. The primary program has a front panel (Figure 10.18).

Figure 10.12: Top of Tubby electronics rack.

Roughly, the top half of the front panel provides control over instruments and the bottom half reports to the user so that you do not need to be looking at all the instruments simultaneously. The left three graphs are the 3 heater temperatures over the last minute. The bottom-right graph allows the user to select which parameter to plot and the time interval. This is most useful for watching a pumpdown or to see if a gun voltage is drifting during sputtering.

THE TOP ROW: The program is designed to make all the readings and write all the commands once every 2 seconds. If there are a lot of such routines or a communication issue, this will take more than 2 seconds and the upper-left indicator will light purple. The output files have one line per iteration and the time at each line is not recorded. These ">2sec" iterations compromise the ability to make parameter vs time plots from the log files.

The next box allows the user to give the log files a name and then has the

Figure 10.13: Bottom of Tubby electronics rack. At the very bottom (not shown) is the power distribution box which has separate circuit breakers, mostly 120VAC.

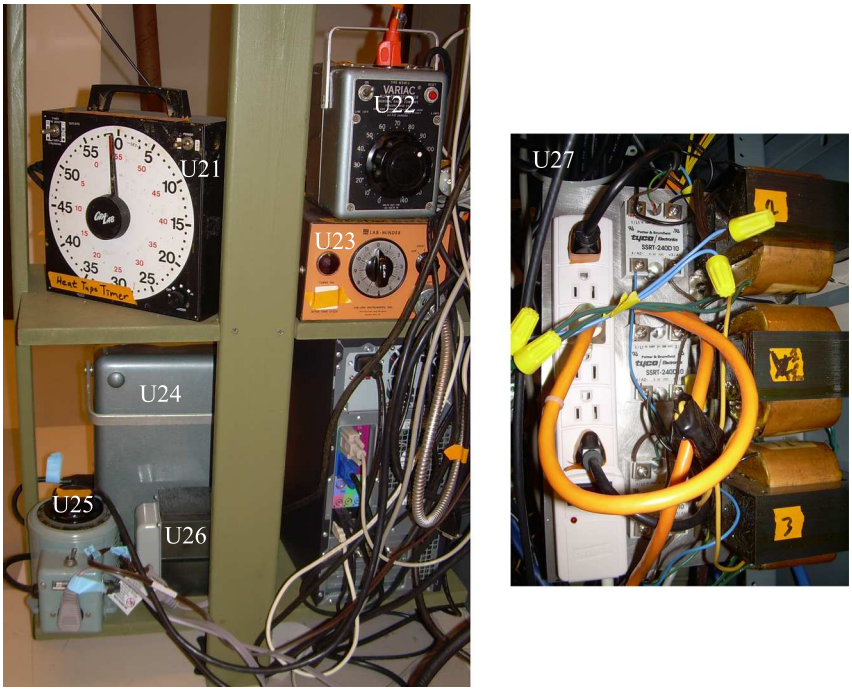

Figure 10.14: Timers+transformers at bottom of Tubby computer electronics rack (left) and transformers+relays at back of Tubby electronics rack (right).

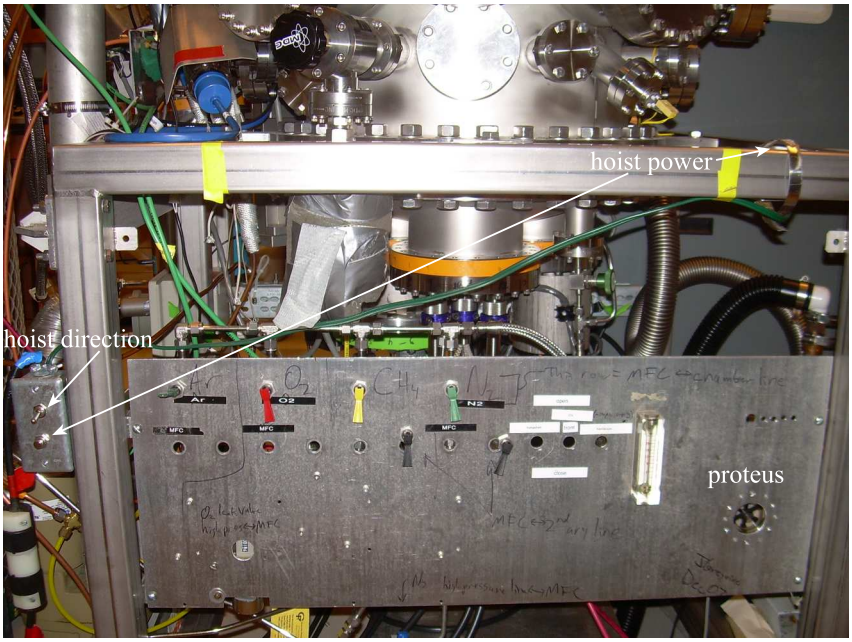

Figure 10.15: Tubby gas and hoist controls

Table 10.3: Controls (and indicators) on Tubby valve+interlock control board, PSV=switch for actuating Pneumatic Solenoid Valve (all valves have normally closed action)

C1	Power to mechanical (roughing) pump
C2	PSV: house nitrogen to chamber
C3	PSV: roughing pump foreline to chamber
C4	PSV: house nitrogen to cryopump (regen)
C5	PSV: sorption pump to cryopump
C6	power control switch for all PSVs
C7	PSV: chamber to cryopump (gate valve)
C8	valve logic override
C9	MDX, ion interlock override
C10	ENI, hoist interlock override
C11	pot. for pressure comparator
C12	pressure high/low indicators
C13	Proteus water flow indicator

user step though 4 items: start pumpdown, stop pumpdown, start DAQ, stop DAQ. Between the pressing of the first 2, the program records only the U1 ion gauge every 2 seconds and records it to a separate file. It is good practice to record a full pumpdown every once in a while. Between the pressing of the third and fourth buttons, the heating, sputtering etc should occur. The upper-right box allows the user to select which instruments to read from. If the switch is down, there will be no communication with the instrument and the displayed and recorded value(s) will be -1. These can be switched in real time.

THE SECOND ROW: Above I mentioned that U6 channels 1,2,4 are used

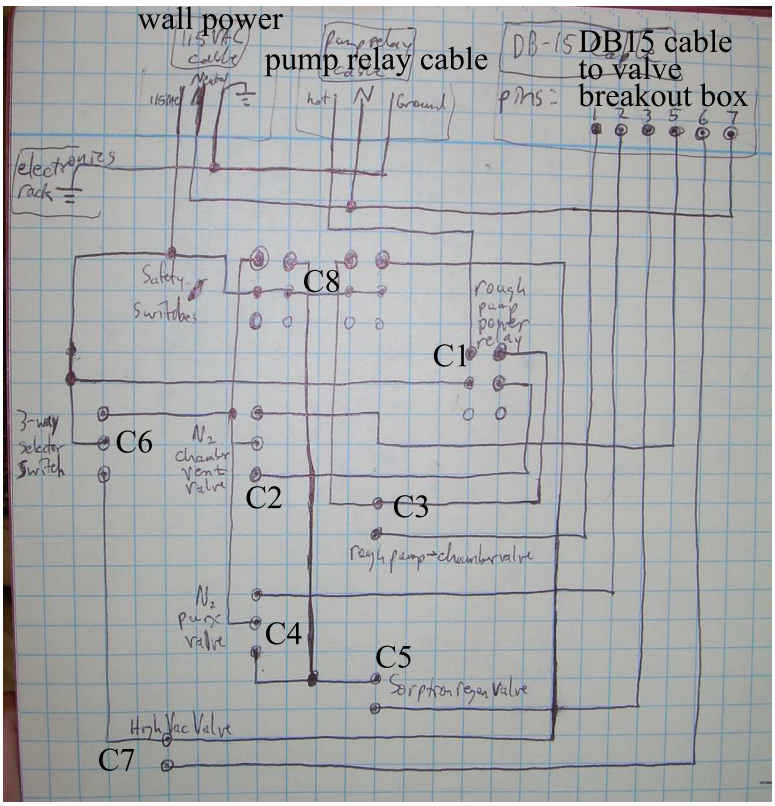

Figure 10.16: Circuit diagram showing valve-switch wiring.

for heaters 1,2,3. That's what this box says. The second box allows changing of the PID parameters. This would need to be done in the middle of a run if for example one substrate had a radiative heater and another had an ohmic heater. This has never happened. The bottom of this box is used for setting the heater setpoints. Generally, 0 means "off" and 9999 means "on" and anything in between is an intended heater temperature.

The next box is for setting crystal monitor parameters - as discussed above this is not used.

Finally, the next box controls the motor. Select the desired motor position and press "Calculate". The blue button given the recommended path to this position and the red button gives an alternate path. The blue option is the short-

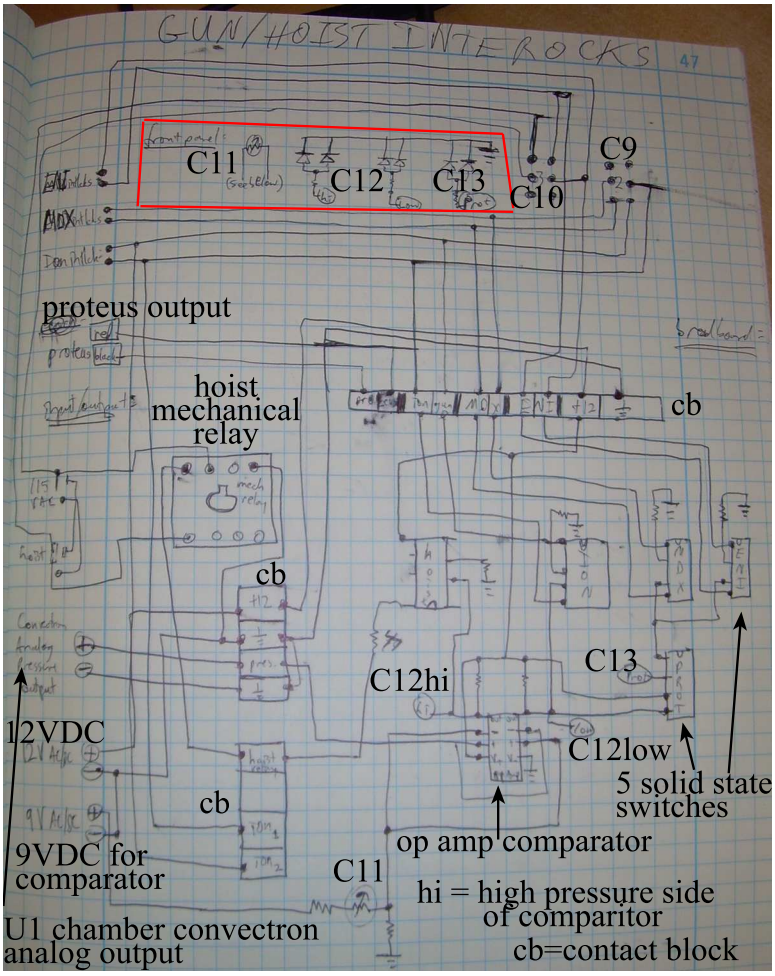

Figure 10.17: Circuit diagram showing interlock-logic wiring. The electronics in the red box are visible from the front panel. All other electronics are on a bread board bolted to the back. The contact blocks provide connectivity to the equipment. The circuit diagram should be accurate with the exception of a recently added U17 interlock which is not included. Also, I'm not so sure about the C9 and C10 wiring.

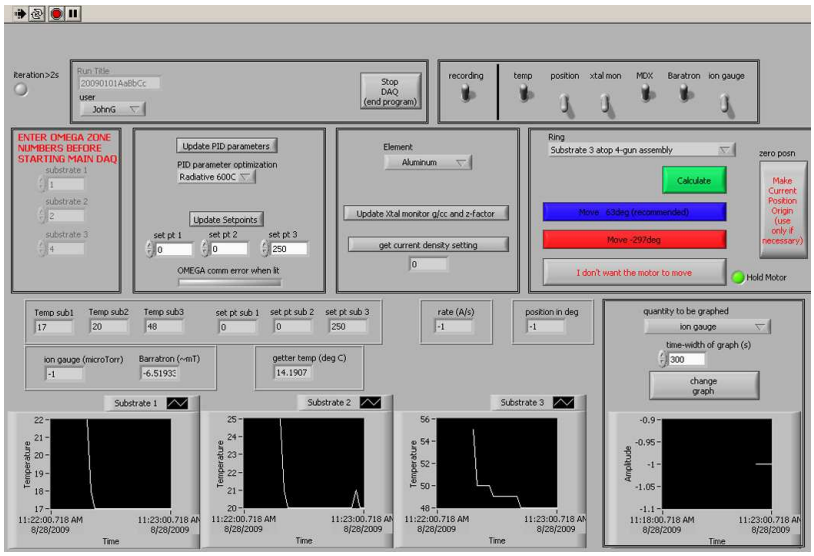

Figure 10.18: Front panel for Labview program that communicates with Tubby instruments.

est unless the gross travel is too large in magnitude which means the wires in the rotary feedthrough might be getting too twisted. IF IN THE MIDDLE OF SPUTTERING, IT IS GENERALLY BEST TO TAKE THE SHORT PATH BECAUSE TAKING THE LONG PATH MEANS MORE THAN ONE SUBSTRATE WILL PASS OVER A DEPOSITION REGION - PLAN YOUR DEPOSITIONS. The "Hold Motor" light is a control for you to use and if it is lit the motor will remain activated after the next communication. You want the motor to be activated during a run but not at all times. The motor gets very hot if it is left activated for hours. The activation is required to keep the small torque from the wires in the feedthrough from spinning the stage. The first step should be to have the motors activated, manual position the stage to the zero position, select "Hold Motor" and then press "Make Current Position Origin".

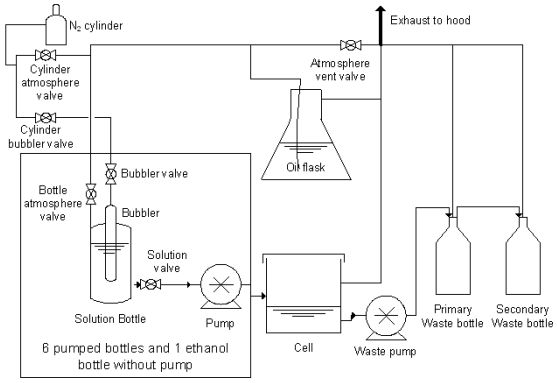

Figure 10.19: Schematic of the plumbing for the apparatus for electrochemical fluorescence testing of thin films.

10.4 Manual for electrochemical fluorescence apparatus

This description of the electrochemical fluorescence assay apparatus is based on a manual originally prepared by Maxim Lobovsky. The testing of a thin film composition spread starts with sample mounting and cell preparation. Then, a series of fluorescence assays are performed, possibly including electrochemical pretreatment(s). For this manual, we will assume the operation of an atmosphere-controlled testing cell (cell with quartz lid - most plastics absorb UV) with a standard three electrode potentiostat. Familiarity with the potentiostat language is assumed and the language particular to this apparatus is mostly described in the next section.

10.4.1 Cell plumbing

The testing solutions are stored in custom made glass vessels which provide capability of deaeration and storage under N_2 pressure (to keep the O_2 content of the solutions low). Figure 10.19 shows the plumbing for N_2 and for filling

and emptying the cell with solution. The figure shows a single bottle with testing solution; additional bottles are plumbed similarly with common N_2 inlets, common gas vent and individual cell-filling pumps.

10.4.2 A couple important issues commonly overlooked

Only apply voltages when the cell is ready

The potentiostat should have a "Dummy" setting in which the three external electrodes are electrically floating. Electrodes should be set to Dummy unless all three electrodes are contacting the solution. This is easily forgotten so let's consider two examples. Usually the reference electrode has to be removed to open the cell - so if droplets need to be wiped from the quartz cell the first step is switching the potentiostat to Dummy. When changing the testing solution, the cell is drained, which should result in loss of contact among the electrodes - switch to Dummy first.

If the potentiostat also has a galvanostat mode, the open circuit potential (OCP) is typically measured prior to each voltage sweep (measure voltage with galvanostat current set to zero amps). Switching from the OCP measurement to the start of the voltage sweep involves switching the mode from galvanostat to potentiostat and changing the control number from zero amps to some start voltage. Performing these 2 steps sequentially has consequences. Switching to potentiostat first will apply zero volts which vs Ag/AgCl is often high enough to drive an oxidation reaction - the typical interpretation of the data assumes there is negligible oxidation current at the start of the scan. Dialing in the "voltage" first will result in the application of some voltage (possibly several volts) to

drive some reaction at the dialed in current. The appropriate action is to switch the cell to Dummy, switch to potentiostat mode, dial in the initial voltage, and switch back to normal electrode configuration.

Electrical contact to the thin film

Typically electrical contact to the thin film is made at three points. Only one point is necessary, but having two points is nice for the following measurement; having three points is nice in case one part of the substrate has a thick oxide layer and cannot be electrically contacted. For the parallel electrochemical test, all thin film positions must be sufficiently electrically contacted to the potentiostat working electrode terminal. The two main issues to keep in mind are contact to the thin film and lateral conduction through the thin film. The former issue effects the ability to test the entire composition spread and the latter issue contends the validity of the parallel measurement. To expand on the latter issue, let's assume a thin film sheet resistance of 100Ω. Consider an experiment in which the edge of the thin film has a low resistance contact to the working electrode and the catalysts at substrate center are driving an oxidation reaction such that there is a 1mA net current (we could never determine if this current comes only from the substrate center catalysts but let's assume this). The voltage drop from the center of the substrate to the edge will be $\sim$100mV (very significant); the potential of the substrate center catalysts is different from the intended voltage by this amount and the experiment is faulty. Before performing electrochemistry, one should test that the resistance across contacts on opposing sides of the substrate is less than $\sim$20Ω. Then, the minimum contact resistance to the thin film must be less than half of this and the effective sheet

resistance (the sheet resistance will be different at each substrate position due to thickness and composition gradients) must me less than this.

10.4.3 Generic steps for performing an experiment

1. Mount substrate and measure contact to contact resistances (enter the minimum as a log comment).
2. rinse cell with water and mount reference electrode.
3. Fill cell with the first testing solution, typically "background" solution. When switching from Dummy electrodes for the first time (typically for an OCP measurement), make sure that a reasonable reading is attained. If the "overload" indicator becomes lit on the potentiostat, the voltage is more than a volt (in absolute), the voltage is drifting rapidly or the voltage "jumps", one of the electrodes is not sufficiently contacted to the potentiostat.
4. Start a "background" fluorescence scan. After the OCP is read, adjust starting voltage (generally to 20 mV below OCP). Do not exceed 200mV (vs Ag/AgCl) as ending voltage without good reason.
5. Perform MeOH fluorescence scan.
6. Repeat MeOH fluorescence scan. If fluorescence occurred, set electrodes to dummy and either partially drain and refill the cell, or use a pipet to remove fluorescence before repeating the scan (the latter is preferred). Rinse.
7. Perform sulfuric acid reducing pretreatment.
8. Perform two rinses with quinine rinse solution. During first drain of the cell, turn on UV light and briefly turn on all fluorescent solutions (background, methanol, and ethanol) which may have been contaminated with sulfuric acid splashes. Be sure to not open the cell to air.

9. Perform MeOH scan. Rinse

10. Perform EtOH scan. Rinse

11. Do anything else that might be cool, rinse with water, remove substrate, patent catalyst.

10.4.4 procedures

Cell preparation

With a junk substrate loaded in the cell, turn on each solution pump until solution flows evenly and without spurts into the cell. Rinse cell. Clean lid after this if needed. Get a reference electrode and place it in the cell and connect it to the labeled alligator clip.

Loading a sample

Make sure the cell is drained before lowering the platform below the cell by turning the large knob in front counterclockwise. Dry the platform with a Kimwipe if there is any liquid on it. Place the sample on the platform with the flat side against the rear of the grooved area on the platform. The sides should just fit within the grove. Raise the platform until the sample touches the cell and tighten the knob so that the sample is pressed against the o-ring on the bottom of the cell. If liquid leaks from the bottom of the cell, try tightening this knob more.

Software start/stop

Open the folder on the desktop called echem analysis Labview and double-click echem control.vi. Click the forward arrow icon at the top of the screen. The software will prompt you to enter an experiment name in the upper left hand corner of the screen. This will correspond to the folder name in the echem test data folder on the desktop. To change this name during operation, click the red, stop sign button (or END EXPERIMENT button) to stop the program and press the arrow to begin again.

Cleaning sample

After the testing of the sample is done, it should be dismounted and immediately cleaned with water. If testing solution is allowed to dry on the sample surface, salt will precipitate on the substrate surface, which may confound some surface characterization.

Rinsing cell

The primary method for cleaning a cell to remove any residue or residual chemicals is to use the softwares rinse cycle. If there is reason to believe that repeated use of the rinse cycle may not have cleaned the cell thoroughly, the lid should be removed and deionized water squirted in the cell from a squirt bottle removal of the lid is to be avoided post-sulfuric acid scan. Drain after finishing.

Cleaning lid

Occasionally, the tubes filling the cell may splash liquid onto the bottom of the transparent lid. This can obscure the cameras view of the sample. Remove the lid holding it by the edges. Wipe with a Kimwipe (or clean with solvents) and then replace the lid.

Sample handling

It is extremely important that nothing touch the sample surface prior to the electrochemical experiment. Hold a sample only by the edges with gloves on. A sample may be rinsed with deionized water and then blow dried with N2.

Software-hardware coupling

Occasionally, there may be problems with the camera not taking pictures. Restarting the computer generally fixes this.

If the software prompts you to save changes when closing it, always click dont save.

The green toggle buttons in the right hand corner will not change anything in the apparatus until write! is clicked.

The PINE operating mode drop down box and cell full LED at the top of the screen should match the actual state of both of these variables. If they do not, adjust them accordingly or it is possible to mess up an experiment or overfill the cell the latter concern is particularly relevant if cell filling or draining is performed manually.

Voltage resolution, voltage limits, voltage divider.

Currently there is a 52kOhm resistor in line with the 10kΩ internal resistance of Pine IN. With a 16 bit resolution on the +-10V NI-PCI card, this gives 50 μV resolution for the Pine IN which means continuous scans occur by minimum steps of 50μV. This also means that the program can make the potentiostat operate in the +-1600mV range. Trying to apply a voltage outside this range will cause the program to crash. The resistance in units of 10kOhms must be entered into the program to adjust the NI-BNC-AO1 voltage so that the voltage will be correct after the voltage divider. If you remove the voltage divider, set this resistance to 0. If you find that the voltage being applied by the potentiostat is a few mV different from what it should be, the resistance may have drifted. Here is how you figure out how to change the resistance in the program to get the right number:
. With PINE on Dummy, Potentiostat, apply 1000mV with the program (make sure program set to Potentiostat.
. Set mA/V setting to 0.1 and Meter Select to I1.
. Ideally, the meter now reads 10.00. If it instead reads X and the resistance in the program is currently R (x10kOhms), change that number to (R+1)*10/X-1.

YOU CANNOT USE A MULTIMETER TO ACCURATELY CHECK THE INPUT VOLTAGE TO THE POTENTIOSTAT. THE RELATIVELY HIGH INPUT IMPEDANCE OF THE MULTIMETER WILL AFFECT THE READING.

NOTE: when you change the resistance in the program, it will only save the change when if you right click on the box, select Data Operations, Make Current Value Default and then save the program.

I-V DAQ, scan rates and controlling the time resolution on current readings

Previous to program version 10, the current was read at a period that always corresponded to 1mV in the scan. This put a limit on the scan rate. With version 10, the bottom left hand corner of the control panel has Current Period (ms) with a default of 5mV/s. Thus, for 5mV/s scans, the current will be read every mV. For 50mV/s scans, the voltage will be read every 10mV. If more current readings are desired, this number can be decreased. I probably wouldnt use anything lower than 40ms.

This means that the scan rate can be arbitrarily high. Limitations will still exist when using the camera a pick the mV per pic value carefully for a given scan rate. The best applied voltage resolution is given in Sec. 5 above. This resolution is compromised by high scan rates. Currently, the voltage is updated at 1000Hz. Thus at 50 mV/s, the voltage increase is 50μV, equal to the resolution. At faster scan rates, the voltage steps will increase, e.g. at 100mV/s, the voltage will increase in 0.1mV steps.

Another difference with DAQ in version 10 is that the voltage is read every time the current is read and both are used for plotting and saved in rundata.txt. Thus, if the DAQ gets behind, there will not be as many data points as you might like but at least the data points will be accurate. This also takes care of any error due to the voltage divider calibration being wrong.

You can tell the DAQ is getting behind by the LEDs labeled late. These blink every time the I-V or picture DAQ routines run late. The boxes to the left give the total number of milliseconds the respective routine has been late in the on-going scan. If this number gets to even 1% of the length of the scan something

is wrong.

Electrochemical Tests

For each test, there are several parameters that can be set at the bottom of the screen. Note that the green buttons must be set before the test is started, but the numbers may be changed after the initial OCP is read
During tests, the software will pop-up yellow boxes that instruct the user to change settings on the potentiostat. Follow these instructions carefully and then click on the box to proceed.
A red abort button will appear under the voltage-current plot during operation of a test. This will stop the test ASAP. Additionally, the test will automatically abort if the absolute current reaches the maximum current specified in the left parameter box

Data output

The folder specified at the beginning of the experiment will contain one summary.txt file, one rundata.txt file, and several image files named in the format X_Y Z.png.

X is the ordinal number of the scan that picture was taken during. Y is the type of scan (see Appendix section III-B for list of possible values). Z is the potential in mV that the picture was taken at. The image files are stored in lossless compression PNG format to save space.

Some Y values currently used - these can be changed but the library should

also be updated in the analysis software:

6 background fluorescence scan

7 methanol fluorescence scan

8 ethanol fluorescence scan

Summary.txt contains a list of the experiments run in the order they were run in. The first number is the type of the experiment (same as Y in the image name). The following numbers are the parameters for the experiment. Starting mV, end mV, sweep rate, mV between pictures and the camera control number (see Appendix A). Rundata.txt contains the same information as summary.txt except for the camera control number. It also has the open circuit potential (OCP) and current data taken at equal time intervals (usually corresponding to 1mV intervals).

current readings at constant voltage

It is sometimes useful to apply a constant voltage for a while. The 2sec mA button is for this. Make sure you have 2 boxes filled out first: the mV value to apply in apply mV/mA and the mA/V pine setting. Upon pressing the2sec mA button, the mV value will be applied and immediately current readings will be made every 2 secs until the stop button that appears in place of the 2sec mA button is pressed. At that time, the data is written to its own text file. The name of the text file is unique to the preceding scan number and the mV value so dont try to do this twice with those same values. There is not reporting of the read values on the front panel look at the potentiostat if you want to watch the current.

cyclic scans

Cyclic voltammograms are currently only supported for the acid scans. Due to significant local change in pH during fluorescence scans, cyclic scans with fluorescence solutions are deemed uninterpretable. So for the acid row in the scan properties the hold V and gas at end is the selector for cyclic scans. This means that doing a one way scan and holding the voltage at the end is not possible for acid scans. If cyclic scan is select,d the number of repetitions is specified in number of cyclic scans. Regardless of the selection of get OCPs, there will be no OCP read at the end of the scan (this is the same action as hold V and gas at end).

Shutdown

Rinse the cell if the last solution in the cell was not water. Remove the reference electrode from the cell, rinse it, and replace it in its proper storage bottle. Turn off the potentiostat and if the setup is not to be used for a while, turn off the power strip.

Making solutions

Materials for solutions are stored in the large metal cabinets in Duffield 324. Note that the solution bottles require 300 mL of solution to completely cover the output line and prevent air from entering it. They can hold up to 2.5L of solution.

Methanol/Ethanol background solution: 0.1 M potassium trifluoromethanesul-

fonate, 0.3 mM quinine

Measure 37.72 g of potassium triflate and 194 mg of quinine and pour into 2 L beaker. Fill to 1800 mL of water and sonicate until solid is dissolved (20 min). Fill to 2 L line on beaker. (volumetric flask is optional for this solution). Quinine sulfate can be used in place of quinine to achieve high molarity of the quinine molecule (0.5mM quinine sulfate = ¿mg). In this case the solution must be neutralized (see instructions).

Fuel fluorescence solution: 0.1M potassium trifluoromethanesulfonate, 0.3 mM quinine, 5 M ethanol or methanol (or other fuel)

Measure 37.72 g of potassium triflate and 194 mg of quinine and pour into 2 L beaker. Measure with graduated cylinder either 404 mL of methanol or 584 mL of ethanol. Fill with deionized water to 1800 mL. Sonicate until solids dissolve (20 min). Pour into 2 L volumetric flask and add water to 2L.

Acid pretreatment solution: 0.01 M Sulfuric acid, 1 M Sodium sulfate

Measure 284 g of sodium sulfate and pour into 2 L beaker. Fill with deionized water to 1800 mL. Sonicate until solids dissolve (20 min). Measure with graduated cylinder 20 mL of 1 M sulfuric acid (or 200mL of 0.1M) and pour into beaker. Pour into 2 L volumetric flask and add water to 2L.

ORR fluorescence solution: 0.1M potassium trifluoromethanesulfonate OR sodium sulfate, 0.3 mM umbelliferone

Measure 37.72 g of potassium triflate (OR 28.4g sodium sulfate) and 97.2 mg of umbelliferone and pour into 2 L beaker. Fill with deionized water to 1800 mL. Sonicate until solids dissolve (20 min). Pour into 2 L volumetric flask and add water to 2L. THIS SOLUTION GETS BUBBLED WITH AIR NOT NITROGEN.

Refilling solution bottles

The solution bottles are refilled in place without removing them from their secondary containment vessels (plastic tubs). Shut off the fluid valve and atmosphere valve. Then, disconnect the N_2 line that enters the bubbler (NOTE: be very careful not to apply too much force to the bubbler as it will break. It is usually easiest to disconnect the hose from the fitting that connects the larger tubing to the smaller tubing). Place the bubbler on Kimwipes under the hood to keep it clean. Use a clean funnel to pour solution in. After adding a solution, it should be deaerated (see next section).

Solution bottle bubbling and overpressure

To remove oxygen from solutions that can affect chemistry in the cell, the solution bottles are capable of bubbling N_2 through solutions and maintaining an N_2 atmosphere over the solutions.

Close all valves on bottles not to be deoxygenated
Close Cylinder atmosphere valve
Open Atmosphere vent valve
Open bottle atmosphere valve and bottle bubbler valve for each bottle to be bubbled
Open cylinder bubbler valve to attain desired bubbling rate. All bottles may not bubble evenly depending on fluid level or position in tubing. Adjust bottle bubbler valves or bubble bottles in batches to ensure all bottles are bubbled evenly.
Wait for 15 minutes
Close cylinder bubbler valve

Close bottle bubbler valves

Open cylinder atmosphere valve

Open bottle atmosphere valves on bottles that will be used

Close Atmosphere vent valve

Reduce cylinder atmosphere valve until oil flask bubbles slowly.

10.4.5 Safety notes

MSDS sheets are kept in a folder taped to the inside of the front door.
Concentrated HF is used and stored in this room. Any users of this room should receive HF safety training. Calcium gluconate is stored in the right cabinet below the hood.

Gases

The primary concern with the gases is over pressurizing any of the sealed vessels in the system. While many parts are kept at slight overpressures with respect to the atmosphere to prevent inward leaks, it is important to keep this pressure as small as possible. Always open bottle atmosphere valves prior to opening bottle bubbler valves.

Electrical

The electrical control/pump box contains wiring at 120 VAC. This wiring is covered, but care must be taken when reaching around this box.

All wiring is connected to a single power strip with surge protector mounted on the top of the electrical box on the back of the front plate. There is a red switch on the right side of this strip that will shut off all electrical power to the apparatus except for low-voltage signals from the computer. Familiarize yourself with the location of this switch in case of an emergency.

10.4.6 Additional notes in case you need to know

Camera control number

The software allows you to control several parameters about the camera to adjust the image. These parameters come in the form of a 4 digit number #$$%.
= 0 or 1 for default or high brightness
$$ = 0 to 99 for shutter speed
% = 0 to 6 for gain control
Note that the software will remove leading zeros from a parameter number so a setting of 10 is equivalent to 0010.

Waste bottle labeling

Here is a typical way to film out the form:
BLDG & RM.: Duffield 324
DATE: [leave blank]
NAME: apparently doesn't matter
TEL.#: 45191
CHECK TYPES: Flamm. Solvent

CHEMICAL NAME/Volume or Weight:

Methanol 160 mL

Ethanol 120mL

Sulfuric acid 0.2 mL

Potassium triflate 32 g

Sodium sulfate 60g

Quinine 260 mg

In water

Glossary

OCP open circuit potential

MeOH methanol

EtOH ethanol

Control software echem control.vi the Labview program that controls the experiment

Analysis software echem analysis.vi the Labview program that analyzes experiment data

Pine the potentiostat/galvanostat

Summary of things to watch out for

. overfilling waste solution bottle

. making sure the cell full LED on the computer agrees with the actual state of the cell

. poor reference electrode connection can be fixed by wiggling the reference

electrode around with Electrodes=Dummy

. Cracked waste pump tubing will cause waste solution to leak from the tubing enclosure tube must be replaced at this time

. Potentiostat current/V setting agrees with computer

. N_2 is actually flowing when the valve is open

10.5 Manual for electrochemical fluorescence analysis

This description of the electrochemical fluorescence assay apparatus is based on a manual originally prepared by Valerie Wiesner. Many but not all features of the program are described below. Figures 10.20 and 10.21 show different parts of the front panel to help connect the text of the manual with the program. The figure parts are referred to below as "Image x".

This program helps you analyze echem data and saves the resulting files in the folder EchemAnalysis within the folder that contains the raw echem data. DO NOT DELETE ANY CHARACTERS IN THE DEFAULT FILENAMES WHEN SAVING FILES. For example, if the default name is IntvsmV.txt you can change it to IntvsmVscan2-secondactiveregion.txt but the automatic file handling will search for the IntvsmV string so it needs to stay at the beginning of the filename.

Open the echem analysis Labview folder located on the desktop and open echem analysis.vi. Select the deposition chamber and testing location (upper-left of Image a). Currently, only "Duffield" choices work. The choice of chamber results in different locations of the element labels in graphs and the composition

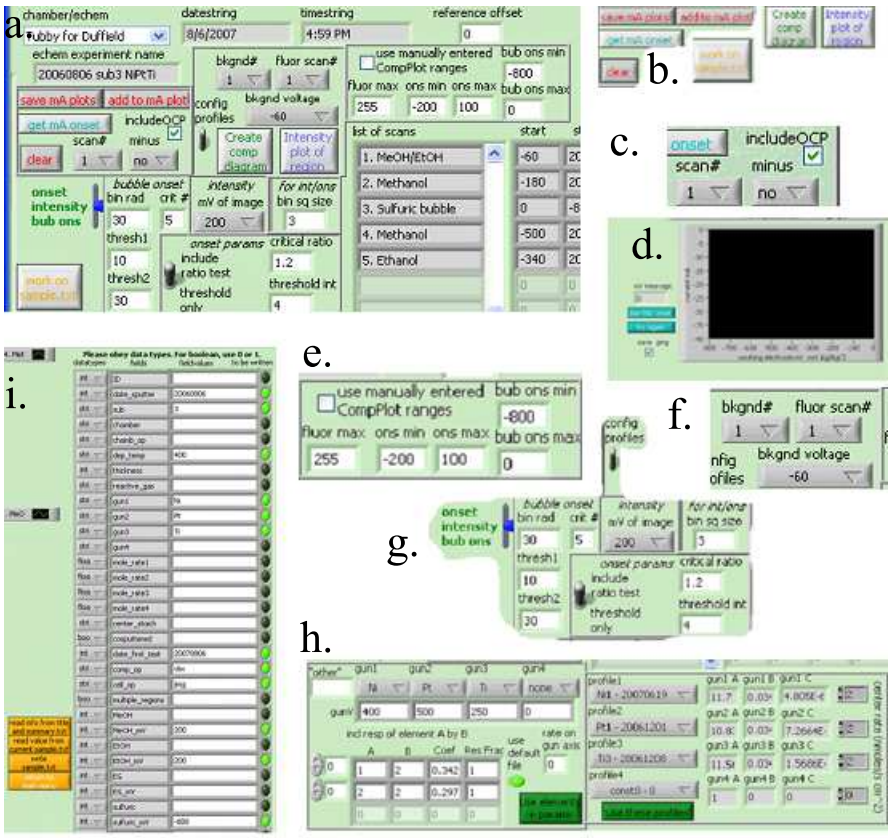

Figure 10.20: Parts of the analysis program front panel.

mapping is only enabled for Tubby. Due to a Labview bug, if the program cannot be started from the front panel, switch to the block diagram (press Ctrl-E) and then press the white RUN arrow in the upper left corner. Ctrl-E will also get you back to the front panel. Select the rundata.txt file which should have been generated automatically by the echem control Labview program. The stop sign in the upper left corner is how you stop the program. If you close the program, DO NOT SAVE ANYTHING always press do not save all. If there is ever a fatal error, Labview will tell you and you select Stop and then restart the program. When the program ends, all unsaved data from previous runs is gone.

Upon selecting the rundata.txt file and returning to the front panel, the echem test info (*echem experiment name*, *datestring*, *timestring*, *list of scans* in Im-

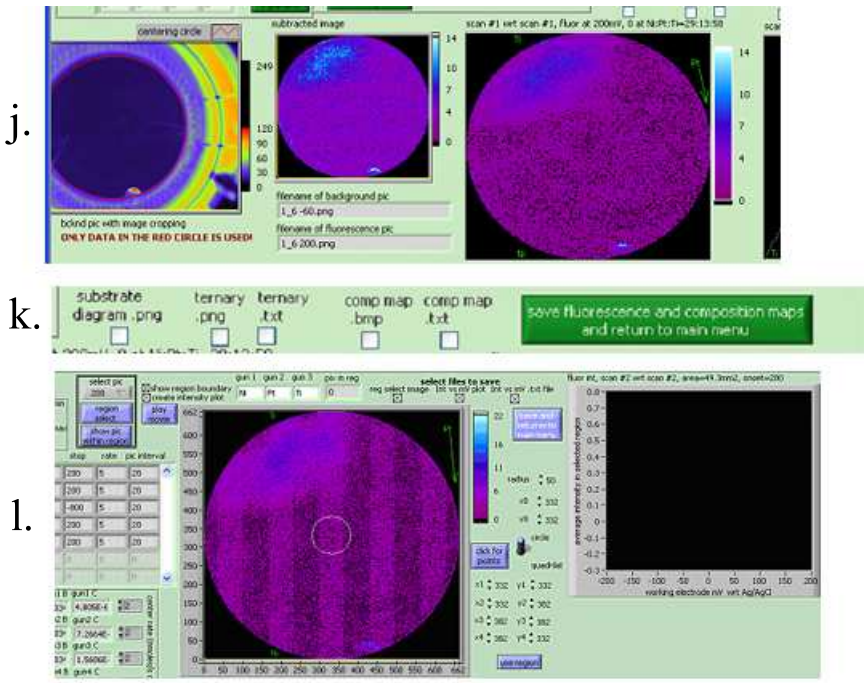

Figure 10.21: More parts of the analysis program front panel.

age a) should all be automatically filled in. You may note that these objects have a dark grey background which signifies that they are indicators and you should not try to change their values. If the background is white you can type in values.

In this control section (Image a) there 7 buttons (Image b) that will perform tasks or send control to other parts of the program. All options and parameters in the control section must be set BEFORE pressing any of these buttons.

The buttons with the red text are for the current vs voltage plots:

The *scan#* pulldown menu (Image c, numbers refer to those in *list of scans*) is for the scan whose current while be plotted. If a scan number is selected in the *minus* menu, the current plotted will be the difference between the two scans. In this case, the voltage range of the plot will be that shared by the two scans, and if the scan is cyclic, only the first leg will be used. *includeOCP* (Image c) will

put a circle at zero current and the OCP before the scan. The legends should update automatically with the scan number and a few other characters. All positive scans get plotted together and all negative scans get plotted together. Individual plots cannot be removed but both graphs can be cleared with the *clear* button. The *save mA plots* button will allow you to save .png pics of the graphs if the graphs are not empty. If you decided you dont want to save the plots after pressing the button, oh well. Pressing cancel on any save menu will kill the program so avoid this.

The other 4 buttons in the main control section will send program control to elsewhere on the front panel. It is important to understand that you can press any button at any time but it will only do something if Labview is ready for it. If you press a button and it looks like it remains pressed (it changes color or appears greyed out), that means you are in the wrong section of the program. Sometimes buttons will flash letting you know what you need to press to get back to the main control part. If you press a button and it remains pressed, you can press it again to unpress it. The sections of the front panel corresponding to these 4 buttons are not well marked, but the color of the text in these buttons corresponds to the background color of the buttons in the section they lead to. Only one of these buttons does not require data entry prior to pressing, *work on sample.txt*. Pressing this button sends you to the far right of the front panel to prepare the fields that will be read into the online database (Image i). You can do this as many times as you like but remember that if the program ends before you save the database fields, you are out of luck because all the entries visible on the front panel will be reset the next time the program is run.

If you already did analysis and saved a sample.txt file or downloaded sam-

ple.txt from the online data system, the *read value from* will fill in all the fields saved there. This will overwrite any existing field values. It is probably a good idea to *read info* from the summary.txt file the first time you press *work on sample.txt*. This file is generated by the echem control program and contains some info that rundata.txt lacks. *Write sample.txt* will write the text file and overwrite any existing one in the sample folder. Only fields that are next to a lit LED in the to be written column will be put in the sample.txt file. You can use these LEDs to avoid writing fields. They should automatically be lit if there is a value in the field. Do not write empty fields You have the ability to type in anything you want to the different fields, but there are no safeguards to enforce data types so you just have to obey the datatypes column when you type in values. This section is the only part of the program that may require you to scroll "off screen". If you do you should scroll back. None of the hyperlinks are active in this program. What you type into the database fields may be overwritten when running other parts of the program.

get mA onset is for determining an onset potential from a current plot. This is most commonly used for sulfuric acid / hydrogen evolution scans. The *scan#* and *minus* menus (Image c) work the same as described above for plotting the current. Once the current is plotted you must click on 4 points on the graph (Image d). Only the mV value of the clicks matters. The clicks must be in INCREASING VALUES OF mV. The first and second pair of clicks will define 2 sets of mV ranges. Each set will undergo linear regression fitting and the intercept will determine the mV onset. If you are not happy with the choice of onset, *try again*. If you are satisfied with the onset calculation, then *use this onset*. For the type of scan (MeOH, EtOH, etc.) selected, the onset potential in the database field menu will be updated automatically if the onset is BETTER than

the current value.

The 2 remaining buttons in Image b(*create comp diagram, Intensity plot of region*) are the complicated ones. They both lead to plotting of fluorescence or bubble data. The plot ranges box (Image e)effects graphs in both of these sections, but mainly the *create comp diagram* section. These values determine the color scale on the plots of intensity (fluor max) and onset. The values in this box will only be used if the checkbox is checked. Otherwise, Labview will choose values that enclose the range of values being plotted. The intent of this section is so you can determine a range of values of interest for all the analysis you will be doing on this sample and then use this manually entered range for all graphs so that the color scales will be the same and they will be directly compared with ease. If a manually entered range exceeds the range of the scan, the excess interval(s) will be greyed in the color scale.

The scan numbers and *bcknd voltage* (Image f) must be selected before pressing either the *create comp diagram* or *Intensity plot of region* button. The blue channel of the background picture will be subtracted from that of the fluorescence scan picture and the result used as the data for these processes. Usually you want the *bcknd#* and *fluor scan#* to be the same and the *bcknd voltage* to be the lowest value of *bcknd#* scan. If you want to look at the picture by picture difference in fluorescence between 2 scans you can select match fluor voltage in *bcknd voltage* but Im pretty sure the 2 scans must have the same number of pictures at the same voltages for this to work. If you want to analyze the absolute (unsubtracted) blue channel of *fluor scan#*, you can select black from *bcknd#*.

Now for the details on *create comp diagram*. All of these options (Image g) must be set:

The most important is the slider bar on the left. It determines what type of analysis will be done. If *intensity* is selected, the analysis consists only of image subtracting. The primary image is the *fluor scan#* picture from the voltage selected in the *mV of image* menu. For both of the onset options, the goal is to go through the pictures from the start voltage to the stop voltage and pixel by pixel or region by region determine onset potential. The onset potential is not interpolated between mV values of images, i.e. the answer will be one of the mV values from a picture.

bub ons will count bubbles in the sequence of images from *fluor scan#*. The *thresh1* and *thresh2* values assign the critical intensity of a group of connected pixels for it to count as a bubble. A search for bubbles is done with each of these values and the bubble counts added together such that groups of pixels with intensities between the values get counted once and the brightest bubbles get counted twice. This works for taking into account the weak pixels from light that hits bubbles, reflects off the quartz lid and reflects of the substrate. This effect can result in an artificially high number of bubbles, but also if this reflected bubble connects the pixels 2 real bubbles, the bubble search will recognize it as one oddly shaped bubble. The algorithm creates a triangular lattice within the echem test region based on *bin radius* and then onset is when the number of bubbles (whose centroid is within *bin radius* of a triangular lattice point) reaches *crit#*. The onset values can then be plotted in false color using hexagons defined by the triangular lattice. High *bin radius* means low spatial resolution in the resulting onset graph, low *bin radius* means noisier data because a couple randomly bright pixels can trigger onset. *crit#* is the number of bubbles that must be in a bin to count as onset.

The *onset* option on the slider is for fluorescence onset. The subtracted blue channel intensity must exceed *threshold int* for onset to occur. Additionally, if *include ratio test* is selected, the ratio of the fluorescence intensity from one pic must exceed that of the previous pic by *crit ratio* for 3 consecutive pictures (the onset is then the voltage of the first of these pics). This constraint is relaxed as necessary when the end of the pictures is reached such that if the last 2 pictures exceed the threshold and the last is a factor of *crit ratio* above the previous picture, the onset will be the voltage of the second to last picture. Recently, additional aoptions were added for performing lest squares fitting of the fluorescence intensity profile. This is still under development and is not described here.

For the *intensity* and *onset* slider options, *bin sq size* values greater than 1 result in analysis of the average intensity of a square of $(bin\ sq\ size)^2$ pixels. This option is for reducing both noise and calculations time. Thus, the number of pixels in the results image is reduced by a factor of $(bin\ sq\ size)^2$. Even values of *bin sq size* will work but for symmetry, odd values make more sense.

For Tubby, regardless of the type of analysis being done (slider value), the resulting substrate image will be mapped onto a ternary phase diagram. If the sample is binary, the substrate image will be mapped to a binary line in the ternary diagram this isnt particularly useful. If the film was made from all 4 guns, the ternary plot will be the projection onto the ternary space of the 3 outer guns. The first time *create comp diagram* is pressed, *config profiles* (middle Image a) must be up/on. It will be set in that position automatically at the beginning of the program. Do not change it until you have run profile configuration at least once. After you are satisfied with the profile, you can switch *config profiles*

off and it will be used until the program ends.

The deposition profile configuration section is shown in Image h. The program will attempt to read the target elements from the folder name. The most commonly sputtered elements are in the pulldown menu. If the film contains an element that is not there, you can select other from the pulldown menu and type the symbol in the *other* text field. This field is used only for labels in the plots. You should type in the voltages (*gunV*) from each of the guns and once each of the 4 guns either have none selected or have a voltage entered, the program will calculate the resputtering coefficients and if any are >0.2 it will sort them from increasing to decreasing and display them into the matrix below *incl resp of element A by B*. In the resputter coefficient array below, the first line indicates that the resputter coefficient for the element in gun 1 (Ni) being resputtered by the element in gun 2 (Pt) is 0.342. Other than entering the correct voltages, the resputtering calculations should require no user interaction. *Res Frac* is the fraction (0 to 1) of the corresponding resputter phenomenon that should be included in composition mapping. Setting this to 0 will remove that calculation. If you would like to see how a Ni target at 400V results in resputtering of Ti, you could enter 3 into column *A* and 1 into column *B* and *Coef* will be calculated and *Res Frac* changed to 1. If there are more than 3 resputter phenomena, the first array index can be used to access more lines. The second index should always remain at 0.

The *use default file* LED should always remain on. This means that the computer will retrieve the file with the rate profile data from its normal location. If using this program on a different computer, you can turn this off and select the file. If you get an error when pressing *use elements + params*, someone moved

the file. Pressing the *use elements + params* will continue to the next section. The computer will find the profiles corresponding to the element, gun# combinations entered in the previous section and will choose the most recent calibration. For gun 2, a gun 1 or gun 3 profile will be selected. If no profiles are found, it will default to Pt from gun 1. Any of these choices can be changed in the pull-down menus. The profile coefficients are displayed but should not be changed without good reason. The molar rates at substrate center for the 4 guns must be entered at the far right. When everything is set, press *Use these profiles*.

At this time, the ternary plot will be made as well as the *composition color map* where the ratios of the RGB channels are the molar rates from the elements, guns 1:2:3 (Image j).

While you are getting the profile parameters right, the program is calculating the fluorescence or onset data. On the far left graph is the background image being used. For fluorescence data you should make sure this picture doesnt contain any fluorescence. You should also make sure that the red circle corresponds to the testing region. If not abort and start asking who screwed up the camera-cell alignment. The parameters describing the relation of the thin film testing region to the CCD images can be adjusted to the left of the Image j panel (not describe here but pretty self explanatory - if you change it and then open an experiment from a previous camera alignment then the adjustment will need to be done again).

The center picture in Image j shows the subtracted images with the file names below and the third graph is the answer. The answer will be plotted in the ternary plot when the profile parameter section is completed. If the elemental labels are not correct, do not save any of the data and rerun the same

routine.

The save check boxes (Image k) must be set as desired before pressing the *save..return* button. When saving the files DO NOT delete any part of the default name. You may enter text after the default name and before the extension to indicate, for example, which scan this corresponds to or if you used a choice of background. In general, do not save the .txt files. The *ternary.txt* option is for saving data where each line corresponds to an image pixel and within the line are tab delimited atomic concentrations and the calculated fluorescence or onset value. This text file can be imported into other programs (Origin or the groups quaternary plotter) for making high quality graphs.

The *Intensity plot of region* application (Image l) allows the user to select a region of the test area and use the average fluorescence intensity from that region to calculate onset potential. The *onset params* and *scan#* and background picture options (see above) are used for this application. There are a couple quirks to get used to. The *select pic* menu is to select the voltage from *scan#* to use for the picture that is displayed in the graph. You usually want this to be the final voltage because that will show the most fluorescence. If you want to select a voltage that is near onset to pick the best onset region you can do so. Once you have picked a voltage you press *region select*. After you have selected a region, you can change the voltage and press *show pic within region*. You have to press *region select* before doing any analysis EVERY TIME you get to this type of analysis from the *Intensity plot of region* button. You can select a circular or quadrilateral shape for the region. The size and location of the shape can be selected by typing in numbers or using the up/down arrows: if circle, the *x0,y0* is the center and *radius* the radius of the circle in PIXELS (see graph axes). The

quadrilat section has the 4 x,y coordinates of the vertices of the quadrilateral. These must be selected in CLOCKWISE order. If *x1,y1* and *x2,y2* are opposite vertices of a quadrilateral, it will not work. The diagonal of the quadrilateral will be shown to help with this. Alternatively, you can press *click for points* and for *circle* you only get to click the center and then have to manually adjust the radius. For *quadrilat* you click all 4 vertices. You can redo this as many times as you need and then you have the right region, click *use region*. You can then click *play movie*. This button can be used to view all subtracted pictures in the scan and the region outline can be overlaid (*show region boundary*). With the region selected you can check *create intensity plot* and the average intensity will be plotted on the right graph as the pictures are analyzed, and when finished the onset potential will be calculated. Once this is done, you can repeat any of the above steps or *save and return to main menu*. Make sure you have checked all the files you would like to save. The *region select image* option will save a .png of the graph used for region select. The elemental labels on this graph are controlled with the text boxes (*gun1,gun2,gun3*) above the graph; they should be automatically read from the folder name. The *pix in region* box will tell you how many pixels were averaged in each picture for creating the intensity plot. This will tell you the area of the region used, which is displayed in the title of the intensity plot.

The .txt file has the format:

1st line : r x y (or x1 y1 x4 y4) in characterization coordinates in mm

2nd line: r x y (or x1 y4) in the coordinate system of the region select graph

3rd line: voltages of pictures in mV

4th line: average subtracted blue channel intensity for regions of pictures (0 to 255)

For the type of scan of *scan*# (e.g. MeOH,EtOH), if the onset potential is BETTER than that currently in the database field, the field will be updated with the calculated value.

Recently, the CHESS XRD/XRF experiments have motivated the addition of features for calculating composition and performing the *Intensity plot of region* routine for a set of points. Also, relatively high-quality graphics for showing the set of points in a substrate outline can be created and saved. The controls are in the upper and upper-left part of the front panel and are not described here.

Finally, There is another part of the program that is not intended to be looked at on a routine basis. It is to the left of the standard front panel and includes the reportstring.png that automatically gets saved every time the program is run. Every time you run the program, any previous repoertstring.png gets overwritten. The data as imported from the echem control files are displayed in the arrays above *reportstring*. The *comments* array gives list of comments on the right and the scan number preceding the entry of the comment on the left. The other arrays are the respective fields read from rundata.txt, one line/row per electrochemical scan.

BIBLIOGRAPHY

[1] Cornell Fuel Cell Institute resputter coefficient calculator at www.cfci.ccmr.cornell.edu/resputter.html.

[2] *National Bureau of Standards (US), Monogr.*, 25(11):131, 1984.

[3] *Powder Diffract. File, JCPDS Internat. Centre Diffract. Data, PA*, 2004.

[4] H Al-Brithen and A R Smith. *Applied Physics Letters*, 77(16):2485, 2000.

[5] HA Al-Brithen, AR Smith, and D Gall. *Phys. Rev. B*, 70(4):45303, 2004.

[6] HA Al-Brithen, EM Trifan, DC Ingram, AR Smith, and D Gall. *Journal of Crystal Growth*, 242(3-4):345, 2002.

[7] HA Al-Brithen, H Yang, and AR Smith. *J. Appl. Phys.*, 96(7):3787, 2004.

[8] B. Amrani and F.E.H. Hassan. Theoretical study of iii-v yttrium compounds. *Comput. Mater. Sci.*, 39(3):563, 2007.

[9] B. Amrani, A. Maachou, and M. Driz. Structural and electronic properties of iii-v scandium compounds. *Physica B*, 388(1-2):384, 2007.

[10] Ermete Antolini, Jose R. C. Salgado, and Ernesto R. Gonzalez. The stability of pt-m (m = first row transition metal) alloy catalysts and its effect on the activity in low temperature fuel cells: A literature review and tests on a pt-co catalyst. *Journal of Power Sources*, 160(2):957–968, 2006.

[11] Y. Arachi, O. Yamamoto, Y. Takeda, and N. Imanishai. Electrical conductivity of the $\mathrm{ZrOLn_2O_3}$ (ln = lanthanides) system. *Solid State Ionics*, 121, 1999.

[12] Xuewen Bai and M E Kordesch. Structure and optical properties of scn thin films. *Appl. Surf. Sci.*, 175-176:499, 2001.

[13] G Barr, W Dong, and CJ Gilmore. PolySNAP a computer program for analysing high throughput powder diffraction data. *J. Appl. Crystallogr.*, 37:658, 2004.

[14] G Barr, W Dong, CJ Gilmore, A Parkin, and CC Wilson. dSNAP: a computer program to cluster and classify Cambridge Structural Database searches. *J. Appl. Crystallogr.*, 38:833, 2005.

[15] SC Barron and RB van Dover. *unpublished*.

[16] S. Bates. Advances is x-ray analysis. *JCPDS-International Centre for Diffraction Data*, 42:251, 2000.

[17] W. Bauer, G. Betz, H. Bangert, A. Bergauer, and C. Eisenmenger-Sittner. Intrinsic resputtering during film deposition investigated by monte carlo simulation. *J. Vac. Sci. Technol. A*, 12(6):3157, 1994.

[18] J.E. Bauerle. Ysz something something. *J. Phys. Chem. Solids*, 30, 1969.

[19] B.J. Beaudry and A.H. Daane. *Trans. AIME*, 227:865, 1963.

[20] D. B. Bergstrom, F. Tian, I. Petrov, J. Moser, and J. E. Greene. Origin of compositional variations in sputter-deposited ti_xw_{1-x} diffusion barrier layers. *Appl. Phys. Lett.*, 67(21):3102, 1995.

[21] A. Bonakdarpour, R. Lbel, S. Sheng, T. L. Monchesky, and J. R. Dahn. *J. Electrochem. Soc.*, 153:A2304, 2006.

[22] A.S. Bondarenko and G.A. Ragoisha. Eis spectrum analyzer. *EIS Spectrum Analyzer, Beta Release*, 2008.

[23] R. Bruce, S. Eicher, and W.D. Westwood. Effect of resputtering on composition of wsix films deposited by multilayer sputtering. *J. Vac. Sci. Technol. A*, 6(3):1642, 1988.

[24] O. N. Carlson, R. R. Lichtenberg, and J. C. Warner. Solid solubilities of oxygen, carbon and nitrogen in yttrium. *Journal of the Less-Common Metals*, 35(2):275, 1974.

[25] C. E. Carlston, G. D. Magnuson, A. Comeaux, and P. Mahadevan. Effect of elevated temperatures on sputtering yields. *Physical Review*, 138(3A):A759, 1965.

[26] E Casado-Rivera, DJ Volpe, L Alden, C Lind, C Downie, T Vazquez-Alvarez, ACD Angelo, FJ DiSalvo, and HD Abruna. *J. Am. Chem. Soc.*, 126:4043, 2004.

[27] Emerilis Casado-Rivera, Zoltan Gal, A. C. D. Angelo, Cora Lind, Francis J. DiSalvo, and Hector D. Abruña. Electrocatalytic oxidation of formic acid at an ordered intermetallic ptbi surface. *ChemPhysChem*, 4(2):193–199, 2003.

[28] Emerilis Casado-Rivera, David J. Volpe, Laif Alden, Cora Lind, Craig Downie, Terannie Vazquez-Alvarez, Antonio C. D. Angelo, Francis J. DiSalvo, and Hector D. Abruña. Electrocatalytic activity of ordered intermetallic phases for fuel cell applications. *Journal of the American Chemical Society*, 126:4043–4049, 2004.

[29] H. Chang, I. Takeuchi, and X. D. Xiang. A low-loss composition region identified from a thin-film composition spread of ($ba_{1-x-y}sr_xca_y$)tio_3s. *Applied Physics Letters*, 74(8):1165–1167, 1999.

[30] H. Chang, I. Takeuchi, and X. D. Xiang. A low-loss composition region identified from a thin-film composition spread of $(ba_{1-x-y}sr_xcay)tio_3$. *Appl. Phys. Lett.*, 74(8):1165, 1999.

[31] Youcef Cherchab, Bouhalouane Amrani, Nadir Sekkal, Mohamed Ghezali, and Khadija Talbi. Structural and electronic properties of bulk yn and of the yn/scn superlattice. *Physica E*, 40(3):606, 2008.

[32] YS Chu, A Tkachuk, S Vogt, P Ilinski, DA Walko, DC Mancini, EM Dufresne, L He, and F Tsui. Structural investigation of CoMnGe combinatorial epitaxial thin films using microfocused synchrotron Xray. *Appl. Surf. Sci.*, 223(1-3):175, 2004.

[33] C Constantin, H Al-Brithen, M B Haider, D Ingram, and A R Smith. *Phys. Rev. B*, 70(19):193309, 2004.

[34] C Constantin, M B Haider, D Ingram, A R Smith, N Sandler, K Sun, and P Ordejon. *J. Appl. Phys.*, 98(12), 2005.

[35] James S. Cooper and Paul J. McGinn. Combinatorial screening of thin film electrocatalysts for a direct methanol fuel cell anode. *Journal of Power Sources*, 163(1):330–338, 2006.

[36] W De La Cruz, J A Diaz, L Mancera, N Takeuchi, and G Soto. Yttrium nitride thin films grown by reactive laser ablation. *J. Phys. Chem. Solids*, 64(11):2273, 2003.

[37] N. de los Santos-Alvarez, L.R. Alden, E. Rus, H. Wang, F.J. DiSalvo, and H.D. Abruna. *J. Electrochem. Soc.*, 626:14, 2009.

[38] R de Paiva, R A Nogueira, and J L A Alves. *Phys. Rev. B*, 75(8):85105, 2007.

[39] Kishori Deshpande, Alexander Mukasyan, and Arvind Varma. High throughput evaluation of perovskite-based anode catalysts for direct methanol fuel cells. *Journal of Power Sources*, 158(1):60–68, 2006.

[40] Y. Ding, T. Nanba, and Y. Miura. *Phys. Rev. B*, 58:14279, 1998.

[41] J P Dismukes and T D Moustakas. *Proc.-Electrochem. Soc.*, 96:110, 1996.

[42] J P Dismukes, W M Yim, and V S Ban. *J. Cryst. Growth*, 13-14:365, 1972.

[43] J P Dismukes, W M Yim, J J Tietjem, and R E Novak. *RCA Rev.*, 31(4):680, 1970.

[44] P. Du, W.A. Kibbe, and S. Lin. *Bioinformatics*, 22:2059, 2006.

[45] W. Eckstein and J. P. Biersack. Reflection of heavy ions. *Z. Phys. B*, 63(4):471, 1986.

[46] C. Eisenmenger-Sittner, A. Bergauer, and A. Wagendristel. Variation of the lead content in sputtered copper-lead films due to resputtering effects. *J. Vac. Sci. Technol. A*, 10(5):3260, 1992.

[47] Jonah Erlebacher. An atomistic description of dealloying. *Journal of the Electrochemical Society*, 151(10):C614–C626, 2004.

[48] Jonah Erlebacher, Michael J. Aziz, Alain Karma, Nikolay Dimitrov, and Karl Sieradzki. Evolution of nanoporosity in dealloying. *Nature*, 410(6827):450, 2001.

[49] C T Horovitz et al., editor. *Scandium: It's Occurence*, volume 165. London, New York: Academic Press, 1975.

[50] N Farrer and L Bellaiche. Properties of hexagonal scn versus wurtzite gan and inn. *Phys. Rev. B*, 66(20):201203, 2002.

[51] J. Fonseca. Fabrication of an array of thin film solid oxide fuel cells. *http://www.nnin.org/doc/2008NNINreuFONSECA.pdf*.

[52] T. Frelink, W. Visscher, and J. A. R. van Veen. On the role of ru and sn as promotors of methanol electro-oxidation over pt. *Surface Science*, 335:353, 1995.

[53] D Gall, I Petrov, P Desjardins, and J E Greene. Microstructural evolution and poisson ratio of epitaxial scn grown on tin(001)/mgo(001) by ultrahigh vacuum reactive magnetron sputter deposition. *J. Appl. Phys.*, 86(10):5524, 1999.

[54] D Gall, I Petrov, N Hellgren, L Hultman, J E Sundgren, and J E Greene. Growth of poly- and single-crystal scn on mgo(001): Role of low-energy n2+ irradiation in determining texture, microstructure evolution, and mechanical properties. *J. Appl. Phys.*, 84(11):6034, 1998.

[55] D Gall, I Petrov, L D Madsen, J E Sundgren, and J E Greene. Microstructure and electronic properties of the refractory semiconductor scn grown on mgo(001) by ultra-high-vacuum reactive magnetron sputter deposition. *J. Vac. Sci. Technol. A*, 16(4):2411, 1998.

[56] D Gall, M Stadele, K Jarrendahl, I Petrov, P Desjardins, R T Haasch, T-Y Lee, and J E Greene. Electronic structure of scn determined using optical spectroscopy, photoemission, and ab initio calculations. *Phys. Rev. B*, 63(12):125119, 2001.

[57] RC Garvie. Occurrence of metastable tetragonal zirconia as a crystallite size effect. *J. Phys. Chem.*, 69:1238, 1965.

[58] B C Giessen, R H Kane, and N J Grant. *Trans. AIME*, 233:855, 1965.

[59] Yu Gong, YanYing Zhao, and Mingfei Zhou. Formation and characterization of the tetranuclear scandium nitride: Sc4n4. *J. Phys. Chem. A*, 111(28):6204, 2007.

[60] A. Gras-Marti and J. A. Valles-Abarca. Slowing down and thermalization of sputtered particle fluxes: Energy distributions. *J. Appl. Phys.*, 54(2):1071, 1983.

[61] J M Gregoire, S D Kirby, G E Scopelianos, F H Lee, and R B van Dover. *submitted*, 2008.

[62] J. M. Gregoire, M. B. Lobovsky, M. F. Heinz, F. J. DiSalvo, and R. B. van

Dover. Resputtering phenomena and determination of composition in codeposited films. *Phys. Rev. B*, 2007.

[63] J M Gregoire, M B Lobovsky, M F Heinz, F J DiSalvo, and R B van Dover. Resputtering phenomena and determination of composition in codeposited films. *Phys. Rev. B*, 76:195437, 2007.

[64] J M Gregoire and R B van Dover. A model for calculating. *J. Vac. Sci. Technol. A*, 26:1030, 2008.

[65] J M Gregoire, R B van Dover, J Jin, F J DiSalvo, and H D Abruña. Getter sputtering system for high throughput fabrication of composition spreads. *Rev. Sci. Instrum.*, 78(7):072212, 2007.

[66] John M. Gregoire, Maxim Kostylev, Michele E. Tague, Paul F. Mutolo, R. Bruce van Dover, Francis J. DiSalvo, and Hector D. Abruna. *J. Electrochem. Soc.*, 156:B160, 2009.

[67] John M. Gregoire, R. B. van Dover, Jing Jin, Francis J. DiSalvo, and Hector D. Abruña. Getter sputtering system for high throughput fabrication of composition spreads. *Rev. Sci. Instrum.*, 78(7):072212, 2007.

[68] IAP/TU Wien Surface Physics Group. A simple sputter yield calculator. *www.iap.tuwien.ac.at/www/surface/script/sputteryield*, 2006.

[69] Zheng Gu, J H Edgar, J Pomeroy, M Kuball, and D W Coffey. Crystal growth and properties of scandium nitride. *Journal of Materials Science: Materials in Electronics*, 15(8):555, 2004.

[70] X. Guo and R. Waser. Electrical properties of the grain boundaries of oxygen ion conductors: acceptor-doped zirconia and ceria. *Prog. Mater. Sci.*, 51, 2006.

[71] J.J. Hanak. The 'multiple-sample concept' in materials research: synthesis, compositional analysis and testing of entire multicomponent systems. *J. Mater. Sci.*, 5(11):964, 1970.

[72] J. M. E. Harper, S. Berg, C. Nender, I. V. Katardjiev, and S. Motakef. Enhanced sputtering of one species in the processing of multielement thin films. *J. Vac. Sci. Technol. A*, 10(4):1765, 1992.

[73] J. M. E. Harper and R. J. Gambino. Combined ion beam deposition and etching for thin film studies. *J. Vac. Sci. Technol.*, 16(6):1901, 1979.

[74] J.L. Hertz and H.L. Tuller. Electrochemical characterization of thin films for a micro-solid oxide fuel cell. *J. Electroceram.*, 13, 2004.

[75] A. Herwadkar and W R L Lambrecht. Mn-doped scn: a dilute ferromagnetic semiconductor with local exchange coupling. *Phys. Rev. B*, 72(23):235207, 2005.

[76] D. W. Hoffman. Intrinsic resputtering-theory and experiment. *J. Vac. Sci. Technol. A*, 8:3707, 1990.

[77] Carina Hoglund, Jens Birch, Manfred Beckers, Bjorn Alling, Zsolt Czigany, Arndt Mcklich, and Lars Hultman. Sc3aln - a new perovskite. *European Journal of Inorganic Chemistry*, 2008(8):1193, 2008.

[78] H. Huang, M. Nakamura, P. Su, R. Fasching, Y. Saito, and F.B. Prinz. High-performance ultrathin solid oxide fuel cells for low-temperature operation. *J. Electrochem. Soc.*, 154, 2007.

[79] T Huang. *Adv. X-Ray Anal.*, 33:295, 1990.

[80] Akimitsu Ishihara, Shotaro Doi, Shigenori Mitsushima, and Kenichiro Ota. *Electrochim. Acta*, 53:5442, 2008.

[81] S. Jayaraman and A. C. Hillier. Construction and reactivity screening of a surface composition gradient for combinatorial discovery of electro-oxidation catalysts. *Journal of Combinatorial Chemistry*, 6(1):27–31, 2004.

[82] S. Jayaraman and A. C. Hillier. Electrochemical synthesis and reactivity screening of a ternary composition gradient for combinatorial discovery of fuel cell catalysts. *Measurement Science and Technology*, 16(1):5–13, January 2005 2005.

[83] Rongzhong Jiang. Combinatorial electrochemical cell array for high throughput screening of micro-fuel-cells and metal/air batteries. *Review of Scientific Instruments*, 78(7):072209–7, 2007.

[84] Jing Jin, Mark Prochaska, Dominic Rochefort, David K. Kim, Lin Zhuang, Francis J. DiSalvo, R. B. van Dover, and Hector D. Abruna. A high-

throughput search for direct methanol fuel cell anode electrocatalysts of type ptxbiypbz. *Applied Surface Science*, 254(3):653, 2007.

[85] M.J. Kappers, M.A. Moram, Y. Zhang, M.E. Vickers, Z.H. Barber, and C.J. Humphreys. Interlayer methods for reducing the dislocation density in gallium nitride. *Physica B*, 401-402:296, 2007.

[86] K Kawasaki and H Iwasaki. RAPID MAPPING OF TEXTURE IN POLYCRYSTALLINE MATERIALS USING AN IMAGING PLATE ON A SYNCHROTRON-RADIATION SOURCE. *J. Synchrot. Radiat.*, 2:49, 1995.

[87] C P Kempter, N H Krikorian, and J C McGuire. *Journal of Physical Chemistry*, 61(9):1237, 1957.

[88] K. Kennedy, T. Stefansky, G. Davy, Zackay V, and E. R. Parker. Rapid method for determining ternary-alloy phase diagrams. *Journal of Applied Physics*, 36(12):3808–3810, 1965.

[89] O. Kerrec, D. Devilliers, H. Groult, and P. Marcus. *Mater. Sci. Eng.*, B55:134, 1998.

[90] M. Kirchner, W. Schnelle, F.R. Wagner, and R. Niewa. Preparation, crystal structure and physical properties of ternary compounds (r3n)in, r=rare-earth metal. *Solid State Sci.*, 5(9):1247, 2003.

[91] Shirlaine Koh and Peter Strasser. Electrocatalysis on bimetallic surfaces: Modifying catalytic reactivity for oxygen reduction by voltammetric surface dealloying. *J. Am. Chem. Soc.*, 129:12624, 2007.

[92] Dmitry A. Kukuruznyak, Harald Reichert, John Okasinski, Helmut Dosch, Toyohiro Chikyow, John Daniels, and Veijo Honkimaeki. High-throughput screening of combinatorial materials libraries by high-energy x-ray diffraction. *Appl. Phys. Lett.*, 91(7), 2007.

[93] H. Lee, S E. Habas, G.A. Somorjai, and P. Yang. *J. Am. Chem. Soc.*, 130:5406, 2008.

[94] J. M. Leger. Mechanistic aspects of methanol oxidation on platinum-based electrocatalysts. *J. of Appl. Electrochem.*, 31(7):767, 2001.

[95] W Lengauer. Investigations in the scandium-nitrogen system. *J. Solid State Chem.*, 76(2):412, 1988.

[96] V. V. Lesnyak, V. K. Yatsimirskii, O. Yu. Boldyreva, and T. D. Kinder. *Theor. Exp. Chem.*, 44:189, 2008.

[97] M E Little and M E Kordesch. Band-gap engineering in sputter-deposited scxga1-xn. *Appl. Phys. Lett.*, 78(19):2891, 2001.

[98] Renxuan Liu and Eugene S. Smotkin. Array membrane electrode assemblies for high throughput screening of direct methanol fuel cell anode catalysts. *J. Electroanal. Chem.*, 535(1-2):49, 2002.

[99] C. J. Long, J. Hattrick-Simpers, M. Murakami, R. C. Srivastava, I. Takeuchi, V. L. Karen, and X. Li. Rapid structural mapping of ternary metallic alloy systems using the combinatorial approach and cluster analysis. *Rev. Sci. Instrum.*, 78(7), 2007.

[100] A Maachou, B Amrani, and M Driz. Structural and electronic properties of iii-v scandium compounds. *Physica B*, 388(1-2):384, 2007.

[101] S. Mahieu, G. Buyle, D. Depla, S. Heirwegh, P. Ghekiere, and R. De Gryse. Monte carlo simulation of the transport of atoms in dc magnetron sputtering. *Nucl. Instrum. Methods Phys. Res. B*, 243(2):313, 2006.

[102] Luis Mancera, Jairo A Rodriguez, and Noboru Takeuchi. First principles calculations of the ground state properties and structural phase transformation in yn. *Journal of Physics Condensed Matter*, 15(17):2625, 2003.

[103] R. Manoharan and J.B. Goodenough. *J. Mater. Chem.*, 2:875, 1992.

[104] N. Matsunami, Y. Yamamura, Y. Itikawa, N. Itoh, Y. Kazumata, S. Miyagawa, K. Morita, and R. Shimizu. A semiempirical formula for the energy dependence of the sputtering yield. *Radiat. Eff. Lett.*, 57(1-2):15, 1980.

[105] N. Matsunami, Y. Yamamura, N. Itoh, H. Tawara, and T. Kawamura. Energy dependence of ion-induced sputtering yields of monatomic solids in the low energy region. *Institute of Plasma Physics Reports*, IPPJ-AM-52:37, 1987.

[106] A. R. Miedema, P. F. de Chatel, and F. R. de Boer. Cohesion in alloys-fundamentals of a semi-empirical model. *Physica B*, 100(1):1, 1980.

[107] M. M. Mohebi and J. R. G. Evans. A drop-on-demand ink-jet printer for

combinatorial libraries and functionally graded ceramics. *Journal of Combinatorial Chemistry*, 4(4):267–274, 2002.

[108] P. Mondal, A. Klein, W. Jaegermann, and H. Hahn. Enhanced specific grain boundary conductivity in nanocrystalline Y_2O_3-stabilized zirconia. *Solid State Ionics*, 118, 1999.

[109] M.A. Moram, T.B. Joyce, P.R. Chalker, Z.H. Barber, and C.J. Humphreys. Microstructure of epitaxial scandium nitride films grown on silicon. *Appl. Surf. Sci.*, 252(24):8385, 2006.

[110] M.A. Moram, M.J. Kappers, T.B. Joyce, P.R. Chalker, Z.H. Barber, and C.J. Humphreys. Growth of dislocation-free gan islands on si(111) using a scandium nitride buffer layer. *J. Cryst. Growth*, 308(2):302, 2007.

[111] M.G. Moreno-Armenta, L. Mancera, and N. Takeuchi. First principles total energy calculations of the structural and electronic properties of scxga1-xn. *Phys. Status Solidi B*, 238(1):127, 2003.

[112] T. Motohiro and Y. Taga. Monte carlo simulation of thermalization process of sputtered particles. *Surface Science*, 134(1):494, 1983.

[113] T D Moustakas, R J Molnar, and J P Dismukes. *Proc.-Electrochem. Soc.*, 96-11:197, 1996.

[114] A. K. Niessen, F. R. de Boer, R. Boom, P. F. de Chatel, W. C. M. Mattens, and A. R. Miedema. Model predictions for the enthalpy of formation of transition metal alloys. ii. *CALPHAD: Comput. Coupling Phase Diagr. Thermochem.*, 7(1):51, 1983.

[115] R Niewa, D A Zherebtsov, M Kirchner, M Schmidt, and W Schnelle. New ways to high-quality bulk scandium nitride. *Chem. Mater.*, 16(25):5445, 2004.

[116] H. Nowotny, E. Bauer, A. Stempfl, and H. Bittner. ber die systeme: Platin-zink und platin-kadmium. *Monatshefte fr Chemie / Chemical Monthly*, 83(1):221, 1952.

[117] H. Oechsner. Sputtering-a review of some recent experimental and theoretical aspects. *Appl. Phys.*, 8(3):185, 1975.

[118] Ryan OHayre, Suk-Won Cha, Whitney Colella, and Fritz B. Prinz. *Fuel Cell Fundamentals*. John Wiley and Sons Inc., 2006.

[119] H. W. Pickering. Characteristic features of alloy polarization curves. *Corrosion Science*, 23(10):1107, 1983.

[120] Marcel Pourbaix. *Atlas of electrochemical equilibria in aqueous solutions*. Cebelcor, Brussels, 1974.

[121] Mark Prochaska, Jing Jin, Dominic Rochefort, Lin Zhuang, Francis J. DiSalvo, Hctor D. Abruña, and R. B. van Dover. High throughput screening of electrocatalysts for fuel cell applications. *Rev. Sci. Instrum.*, 77:154104, 2006.

[122] D. V. Pugh, A. Dursun, and S. G. Corcoran. *J. Mater. Res.*, 18:216, 2003.

[123] A Qteish, P Rinke, M Scheffler, and J Neugebauer. Exact-exchange-based quasiparticle energy calculations for the band gap, effective masses, and deformation potentials of scn. *Physical Review B (Condensed Matter and Materials Physics)*, 74(24):245208, 2006.

[124] V. Ranjan, L. Bellaiche, and E.J. Walter. Strained hexagonal scn: a material with unusual structural and optical properties. *Phys. Rev. Lett.*, 90(25):257602, 2003.

[125] V. Ranjan, S. Bin-Omran, L. Bellaiche, and A. Alsaad. Isostructural phase transitions in gan/scn and inn/scn superlattices. *Phys. Rev. B*, 71(19):195302, 2005.

[126] V. Ranjan, S. Bin-Omran, D. Sichuga, R.S. Nichols, L. Bellaiche, and A. Alsaad. Properties of gan/scn and inn/scn superlattices from first principles. *Phys. Rev. B*, 72(8):85315, 2005.

[127] Erik Reddington, Anthony Sapienza, Bogdan Gurau, Rameshkrishnan Viswanathan, S. Sarangapani, Eugene S. Smotkin, and Thomas E. Mallouk. Combinatorial electrochemistry: A highly parallel, optical screening method for discovery of better electrocatalysts. *Science*, 280(5370):1735, 1998.

[128] R. A. Robinson and R. H. Stokes. *Electrolyte Solutions*. Butterworths, London, 1959.

[129] E. Sawatzky and E. Kay. Cation deficiencies in rf sputtered gadolinium iron garnet films. *IBM J. Res. Dev.*, 13:696–702, 1969.

[130] J C Schuster and J Bauer. The ternary systems sc-al-n and y-al-n. *J. Less-Common Met.*, 109(2):345, 1985.

[131] H. Scott. Phase relations in the zirconia-yttria system. *J. Mater. Sci.*, 10, 1975.

[132] M. P. Seah, C. A. Clifford, F. M. Green, and I. S. Gilmore. An accurate semi-empirical equation for sputtering yields i: for argon ions. *Surf. Interface Anal.*, 37(5):444, 2005.

[133] A Serov and C Kwak. Review of non-platinum anode catalysts for dmfc and pemfc application. *Apply. Cat. B*, 90:313, 2009.

[134] L.R. Shaginyan, M. Misina, S. Kadlec, L. Jastrabik, A. Mackova, and V. Perina. Mechanism of the film composition formation during magnetron sputtering of wti. *J. Vac. Sci. Technol. A*, 19(5):2554, 2001.

[135] S. I. Shah and P. F. Carcia. Spatial dependence of composition in ion beam sputter deposited gdtbfe thin films. *J. Vac. Sci. Technol. A*, 9(3):609, 1991.

[136] Simone C. Sieg, Changwon Suh, Timm Schmidt, Michael Stukowski, Krishna Rajan, and Wilhelm F. Maier. Principal component analysis of catalytic functions in the composition space of heterogeneous catalysts. *QSAR Comb. Sci.*, 26(4):528, 2007.

[137] K. Sieradzki, N. Dimitrov, D. Movrin, C. McCall, N. Vasiljevic, and J. Erlebacher. *J. Electrochem. Soc.*, 149(8):B370, 2004.

[138] A. Simunek, J. Vackar, and K. Kunc. Core energy levels of sc and n and their variation with coordination number in scn. *Phys. Rev. B*, 72(4):45110, 2005.

[139] A.R. Smith, H.A.H. Al-Brithen, D.C. Ingram, and D. Gall. *J. Appl. Phys.*, 90(4):1809, 2001.

[140] Colin J. Smithells. *Smithells metals reference book*. Butterworth-Heinemann, 7th edition, 1992.

[141] Eugene S. Smotkin and Robert R. Diaz-Morales. New electrocatalysts by combinatorial methods. *Annual Review of Materials Research*, 33(1):557, 2003.

[142] Eugene S. Smotkin, Junhua Jiang, Amit Nayar, and Renxuan Liu. High-throughput screening of fuel cell electrocatalysts. *Applied Surface Science*, 252(7):2573, 2006.

[143] L. Smrcok. *Z.Kristallogr*, 214:430, 1999.

[144] L. Smrcok, M. Durik, and A. Jorik. *Powder Diffraction*, 14:300, 1999.

[145] F Spaepen and D Turnbull. *Annu. Rev. Phys. Chem.*, 35:241, 1984.

[146] J.S. Spendelow, G.Q. Lu, P.J.A. Kenis, and A. Wieckowski. *J. Electroanal. Chem.*, 568:215, 2004.

[147] C Stampfl, W Mannstadt, R Asahi, and A J Freeman. Electronic structure and physical properties of early transition metal mononitrides: Density-functional theory lda, gga, and screened-exchange lda flapw calculations. *Phys. Rev. B*, 63(15):155106, 2001.

[148] D. A. Stevens, J. M. Rouleau, R. E. Mar, A. Bonakdarpour, R. T. Atanasoski, A. K. Schmoeckel, M. K. Debe, and J. R. Dahn. *J. Electrochem. Soc.*, 154:B566, 2007.

[149] P. Strasser, Q. Fan, M. Devenney, W. H. Weinberg, P. Liu, and J. K. Norskov. High throughput experimental and theoretical predictive screening of materials - a comparative study of search strategies for new fuel cell anode catalysts. *Journal of Physical Chemistry B*, 107(40):11013, 2003.

[150] Peter Strasser. Combinatorial optimization of ternary pt alloy catalysts for the electrooxidation of methanol. *Journal of Combinatorial Chemistry*, 10(2):216, 2008.

[151] R. V. Stuart, G. K. Wehner, and G. S. Anderson. Energy distribution of atoms sputtered from polycrystalline metals. *J. Appl. Phys.*, 40(2):803, 1969.

[152] R.V. Stuart and G.K. Wehner. Energy distribution of sputtered cu atoms. *J. Appl. Phys.*, 35(6):1819, 1964.

[153] K. Sturm and H. U. Krebs. Quantification of resputtering during pulsed laser deposition. *J. Appl. Phys.*, 90(2):1061, 2001.

[154] J E Sundgren, B O Johansson, A Rockett, S A Barnett, and J E Greene. page 95. 149. American Institute of Physics, 1986.

[155] I. Takeuchi and X.-D. Xiang, editors. *Combinatorial Materials Synthesis*. Dekker, New York, 2003.

[156] H. C. Theuerer and J. J. Hauser. Getter sputtering for preparation of thin films of superconducting elements and compounds. *Journal of Applied Physics*, 35(3):554–555, 1964.

[157] M.W. Thompson. Ii. the energy spectrum of ejected atoms during the high energy sputtering of gold. *Philosophical Magazine*, 18:377, 1968.

[158] Lu Tie-Yu and Huang Mei-Chun. Electronic structure of scn and yn: density-functional theory lda and gw approximation calculations. *Chin. Phys.*, 16(1):62, 2007.

[159] Atsushi Ueda, Yusuke Yamada, Tsutomu Ioroi, Naoko Fujiwara, Kazuaki Yasuda, Yoshinori Miyazaki, and Tetsuhiko Kobayashi. *Catalysis Today*, 84:223, 2003.

[160] M. Cotte P. Walter J. Susini V.A. Solé, E. Papillon. A multiplatform code for the analysis of energy-dispersive x-ray fluorescence spectra. *Spectrochim. Acta*, B62:63, 2007.

[161] L J van der Pauw. A method of measuring specific resistivity and hall effect of discs of arbitrary shape. *Philips Research Reports*, 13:1, 1958.

[162] L.J. van der Pauw. A method of measuring specific resistivity and hall effect of discs of arbitrary shape. *Philips Research Reports*, 13:1–9, 1958.

[163] R B van Dover, B Hessen, D Werder, C-H Chen, and R J Felder. Investigation of ternary transition-metal nitride systems by reactive cosputtering. *Chem. Mater.*, 5(1):32, 1993.

[164] R. B. van Dover, M. Hong, E. M. Gyorgy, J. F. Dillon, and S. D. Albiston. *Journal of Applied Physics*, 57:3897, 1985.

[165] R. B. van Dover and L. F. Schneemeyer. *Macromolecular Rapid Communications*, 25:150, 2004.

[166] R. B. van Dover, L. F. Schneemeyer, and R. M. Fleming. Discovery of a useful thin-film dielectric using a composition-spread approach. *Nature 392*, (6672):162–4, 12 March 1998.

[167] R. B. van Dover, L. F. Schneemeyer, and R. M. Fleming. Discovery of a useful thin-film dielectric using a composition-spread approach. *Nature*, 392(6672):162, 1998.

[168] R B van Dover, L F Schneemeyer, and E M Gyorgy. Magnetic behavior of diluted lanthanoid-pnictide systems. *J. Appl. Phys.*, 61(8):3542, 1987.

[169] R B van Dover, L F Schneemeyer, and E M Gyorgy. Magnetic properties of gd-substituted yttrium nitride. *Met. Res. Soc. Symp. Proc.*, 89:147, 1987.

[170] RB van Dover and LF Schneemeyer. The codeposited composition spread approach to high throughput discovery exploration of inorganic materials. *Macromol. Rapid Commun.*, 25(1):150, 2004.

[171] S Vogt, YS Chu, A Tkachuk, P Ilinski, DA Walko, and F Tsui. Composition characterization of combinatorial materials by scanning Xray fluorescence microscopy using microfocused synchrotron Xray beam. *Appl. Surf. Sci.*, 223(1):214, 2004.

[172] R. A. Waldo, M. C. Militello, and S. W. Gaarenstroom. *Surface and Interface Analysis*, 20:111, 2004.

[173] B.N. Wang, R.D. Bennett, E. Verploegen, A.J. Hart, and R.E. Cohen. Characterizing the morphologies of mechanically-manipulated multi-wall carbon nanotube films by small-angle x-ray scattering. *J. Phys. Chem. C*, 111:17933, 2007.

[174] A. Wee, D. Grayden, Y. Zhu, K. Petkovic-Duran, and D. Smith. *Electrophoresis*, 29:4215, 2008.

[175] G. Wehner. Influence of the angle of incidence on sputtering yields. *Journal of Applied Physics*, 30(11):1762, 1959.

[176] Erich C. Weigert, Daniel V Esposito, and Jingguang G Chen. Cyclic voltammetry and x-ray photoelectron spectroscopy studies of electro-

chemical stability of clean and pt-modified tungsten and molybdenum carbide (wc and mo2c) electrocatalysts. *J. Power Sources*, 193:501, 2009.

[177] Jay F. Whitacre, T. Valdez, and S. R. Narayanan. Investigation of direct methanol fuel cell electrocatalysts using a robust combinatorial technique. *Journal of the Electrochemical Society*, 152(9):A1780, 2005.

[178] Bin Xia, Yong S. Chu, and Wayne L. Gladfelter. Use of a synchrotron X-ray microbeam to map composition and structure of multimetallic metal oxide films deposited by combinatorial chemical vapor deposition. *Surf. Coat. Technol.*, 201(22-23):9041, 2007.

[179] X.-D. Xiang, X. Sun, G. Briceno, Y. Lou, K.-A. Wang, H. Chang, W. G. Wallace-Freedman, S.-W. Chen, and P. G. Schultz. A combinatorial approach to materials discovery. *Science*, 268:1738–1740, June 1995.

[180] Yusuke Yamada, Atsushi Ueda, Hiroshi Shioyama, and Tetsuhiko Kobayashi. *Appl. Surf. Sci.*, 223:220, 2004.

[181] Roswitha Zeis, Anant Mathur, Greg Fritz, Joe Lee, and Jonah Erlebacher. Platinum-plated nanoporous gold: An efficient, low pt loading electrocatalyst for pem fuel cells. *Journal of Power Sources*, 165(1):65, 2007.